SEISMIC SAFETY EVALUATION OF EARTH DAM AND POSSIBLE REHABILITATION METHODS(Dissertation_全文)

AUTHOR(S):

Bhuddarak Charatpangoon

SEISMIC SAFETY EVALUATION OF EARTH DAM AND POSSIBLE REHABILITATION METHODS

BHUDDARAK CHARATPANGOON

2014

ABSTRACT

Earth dams are the most common type of dams because of their cost effectiveness. Many earth dams have been built throughout Japan for irrigation water supply, flood mitigation, and hydropower. Given that Japan lies in one of the most seismically active areas of the world, seismic safety is one of the main issues in dam construction and management in the country. Therefore, to ensure dam safety, appropriate safety evaluation of such dams is crucial. This study aimed to understand and explain the dynamic behavior of dams during earthquakes, as well as investigate the failure of the Fujinuma dam. We performed site investigation, fact finding operation, laboratory experiments, numerical simulations, as well as suggested possible rehabilitation methods, and implemented the finite–strain finite element code.

The site investigation showed that the dam body could be divided into three layers according to their properties—top, middle, and bottom. The middle and bottom layers were found to contain clayey soil, while the top layer was constituted of cohesionless soil. At the site, no obvious evidence such as sand boils could be found to confirm the occurrence of liquefaction. Furthermore, the material in the middle and bottom layers did not seem to be prone to liquefaction. From the experimental results, it can be summarized that both the middle and bottom layers consisted of a high percentage of fine particles, whereas the upper part consisted mainly of sandy material. Accordingly, both the middle and bottom layers were not susceptible to liquefaction.

A microtremor observation was conducted in this study to determine the site predominant period and the natural frequency of the dam. The results show that the natural frequency of the remainder of the main dam is 2–5 Hz in the upstream–downstream direction. Similarly, a modal analysis of the remaining dam using the finite element method showed that its natural frequency is about 2.35 Hz in the upstream–downstream direction, which is in good agreement with the microtremor observation. Thus, the material properties are suitable for modeling the original dam and performing dynamic analysis of the dam.

To determine the causes of dam failure, a dynamic analysis of the dam was performed using numerical simulation. The results obtained using the 2011 Tohoku eaerthquake ground motion recorded show that the dam was subjected to a high–amplitude, long–duration earthquake that characterized by a wide band, which possibly induced resonance in the dam. Thus, the dam experienced significant amplification throughout its body, and this led to large inertial driving forces. In addition, owing to shaking for a long duration, pore pressure was built–up within the dam's body, especially in the lower portion of the downstream side. Although the excess pore pressure was not adequate to match the effective stress and trigger liquefaction at those particular locations, the shear strength of the soils might have decreased at locations where the effective stress was small. Accordingly, a large shear strain was observed initially in the top portion of the dam, and later, the large shear strain can be observed on the downstream side. Regarding the sliding patterns seen in the top portion and on the downstream slope, the dam was settled and the plastic deformation was then accumulated. The deformation accumulation rose until the dam's crest reached the reservoir level. Therefore, the dam failed owing to the loss of freeboard, which might have led to breaching of the dam. Furthermore, in all cases, large

shear strains were observed initially in the upper portion of the upstream slope, followed by large shear strains on the downstream side. These, together with tension cracks, may have caused the dam slope's sliding failure. In addition, the sliding patterns exhibit good agreement with the facts gathered from field observations.

In this study, to prevent dam failure, we introduce the following five retrofitting techniques: 1) Retrofit 1, adding downstream berm equaling half the dam's height; 2) Retrofit 2, adding downstream berm equaling the dam's height; 3) Retrofit 3, enlarging the dam and increasing dam height; 4) Retrofit 4, lowering reservoir level; and 5) Retrofit 5, applying geogrid reinforcement layers. All retrofit models were analyzed using simulated motion because it is difficult to compare the results using the observed motion.

The results indicate that Retrofit 3, 2, and 5 are effective for reducing the risk of failure of the studied dam. Among all, Retrofit 3 was found to be the most effective method in case of the studied dam, especially for the existing dam, owing to its simplicity and because the resulting crest settlement was the lowest among the values achieved by the other techniques. By raising the dam height and adding downstream berm, it was ensured that the retrofit dam could safely resist the simulated motion. Retrofit 5 or the geogrid reinforced model, too, was found to be a good measure. However, for the existing dam, Retrofit 2 and 3 are more appropriate because they are easier to execute than geogrid reinforcement.

In reality, when a dam experiences a long–duration earthquake such as the observed motion used for studying the actual dam's failure, the use of only one mitigation measure might be inadequate to prevent dam failure. A combination of the aforementioned retrofitting techniques may be necessary for ensuring seismic safety of a dam and its resistance to energetic quakes. The measure proposed in this study is a combination of various techniques. The actual dam was enlarged by a 3.5 m increase in the crest height, doubling of the crest width, and adding a downstream berm and geogrids in the dam body. In addition, to reduce the effect of build–up pore pressure, which may reduce shear strength, a seepage cut–off wall was built at the dam centerline along the dam's height. The results show that the proposed model can withstand the massive power of the observed motion because crest settlement was not adequately high to cause overtopping failure (freeboard length = 5.3 m). However, the dam might experience a large shear strain, which may subsequently cause slope instability and cracking. Although the results show that the dam did not fail, a large settlement did take place, which might damage structures based on the proposed dam model.

Eventually, a finite–strain finite element code for coupled solid–fluid suitable for dynamic problems was proposed. The governing equation, finite element formulation, and its matrix form are presented in this paper. As a preliminary step, the code was developed only for the elastic regime. Moreover, the proposed code was verified using static and dynamic problems. In the static problem, the soil column model was analyzed and the results were compared with those of the analytical solution of the one–dimensional consolidation problem. For small loads, the two sets of results are in good mutual agreement, and for larger loads, the code yields a great approximation with certain assumptions. For dynamic problems, a harmonic wave was applied to the soil column model. The results show that

both finite–strain and small–strain finite element code yield very good agreement in all aspects.

Thereafter, the proposed code was used to estimate the response of the Fujinuma dam when subjected to the generated harmonic wave. A dynamic analysis was performed to estimate the dam's response and compare with the finite element code for the infinitesimal strain. The comparison indicates that the maximum crest settlement, horizontal displacement, acceleration and excess pore pressure obtained from the finite–strain finite element code are in good agreement with the values obtained using the small strain finite element code.

As the proposed code is incomplete as yet, some parts such as the damping term are not included in it. Additionally, incorrect parts or mistakes must be found and addressed to provide a reliable code that can be used for further studies related to this field. In addition, in future works, material nonlinearity or other advanced constitutive laws and proper fluid–structure interaction should be considered for describing other possible failure mechanisms. Therefore, the development of an advanced constitutive law and the application of this code to determine dam failure mechanism will be the objectives of future work.

The results of this study indicate that the people living near the dam site, especially on the downstream side, are always at risk. The Fujinuma dam was constructed in times when modern seismic design was not yet established. Moreover, a seismic safety evaluation of this dam using the state of the art techniques was not conducted. In fact, this study presents only one case; there are many existing fill dams whose seismic safety needs to be evaluated to ensure the safety of people and their properties. Therefore, seismic safety evaluation of existing dams is crucial and indeed urgent. Otherwise, a future quake might prove to be disastrous for those living downstream of a dam. Thus, this study demonstrates that it is very important to not only design a dam that is capable of withstanding future quakes but also to investigate and mitigate problems in addition to maintaining existing dams for ensuring their seismic safety.

ACKNOWLEDGEMENTS

This dissertation could not possible have been completed without advice and support of individuals or groups that in one way or another have been providing help and their valuable assistance during the time of conducting this study.

Completing my PhD degree is perhaps the most challenging thing in my life ever. Many memorable moments, with smile and sometimes tear, have been shared with many people during this study. These always remind me to walk on with great will even the way does not seem to be existed. Besides, i learnt that how little that one be in this world. The knowledge itself is of course everlasting, also many tasks could not possible be achieved without the help by others. These remind me to keep learning and realizing how important the team is. Especially, in Japan, teamwork is very important key to success so i will always keep in my mind always.

It has been a great privilege to spend several years in the Earthquake and Lifeline Laboratory, Department of Urban Management, Graduate school of Engineering at Kyoto University. The acknowledgement is my deepest sincere to thank for those whom i really would like to express for their collaboration.

First and foremost, my debt of gratitude must go to my advisor, Prof. Junji Kiyono. He patiently provided the inspiration, encouragement and advice necessary for me to proceed through the doctorial course and complete my dissertation. I want to thank Prof. Kiyono for his persistent encouragement, kindness and serving as an exemplar to me as a great mentor. He has been a strong and supportive adviser to me throughout my graduate school career, but he has always given me great freedom to pursue independent work. Also, he is like a father to me during my study in Japan.

I would like to express my deepest appreciation to Assoc. Prof. Aiko Furukawa. She sincerely provided the vision, encouragement and counsel necessary for me to conquer through all obstacles in the completion this research work.

Special thanks to my committee, Prof. Junji Kiyono, Assoc. Prof. Aiko Furukawa, Prof. Takeshi Koike, Prof. Akira Igarashi and Prof. Hiroyasu Ohtsu for their guidance and helpful suggestions. Their comment has served me well and i owe them my heartfelt appreciation.

Members of Earthquake and lifeline Engineering Laboratory, especially, the secretariat Ms. Sayuri Furukawa also deserve my sincerest thanks, their friendship and assistance has meant more to me than i could ever express. I could not complete my work without invaluable friendly assistance of the participants of those.

I should also mention Prof. Mamoru Mimura of Geofront System Engineering laboratory and Prof. Susumu Iai and the member of Geotechnics for Hazard Mitigation laboratory, DPRI for allowing me to conducting the experiment at their laboratory. My thanks and appreciations also go to Assoc. Prof. Sutthisak Soralum for his kind co–operation and encouragement which help me in completion of this project. Also, i would like to express my appreciation to Dr. Chayanon Hansapinyo for his kind co–operation on the conducting this research.

Special thanks go to my friends in Thailand, Japan and other parts of the World whose were sources of laughter, joy, and support. Besides, i would like to thank Mr. Uchida Haruto, Mr. Keita Kojima, Mr. Dohi Yuji and Mr. Tewdoi Singhasenee. I am very happy that, in many cases, my friendships with you have extended well beyond our shared time in Japan.

I wish to thank Mr. Narong, Mrs. Katsanee, Bhuddawat and Pattarawut Charatpangoon, my parents and my Brothers. Their love provided my inspiration and was my driving force. I owe them everything and wish i could show them just how much i love and appreciate them. I would also like to dedicate this work to my lost relatives including Grandma Mrs.Mui–ngek, who left us too soon. I hope that this work makes you proud.

I would like to gratefully acknowledge Mr. Wana Nithiwana, Ms. Nipaporn Pharadee and Ms. Diana Nikolof for providing a great support and great driving force to persuade a scholarship abroad. A special gratitude i would give to Dr. Pennung Warnitchai and Dr. Kyung Ho Park, They continually and convincingly conveyed a spirit of adventure in regard to research and scholarship, and an excitement in regard to teaching. Without the great inspiration from them this dissertation would not have been possible.

Also, the author wishes to express his gratitude to Ms. Piyanan Lerttawiwong, whose love and encouragement allowed me to finish the course so i will just give her a heartfelt “thanks.”

Finally, an honorable mention goes to Japanese Government <MONBUKAGAKUSHO: The Ministry of Education, culture, sports, science, and technology MEXT> for providing the scholarship that allowing me to complete my doctoral course.

TABLE OF CONTENTS

LIST OF FIGURES

LIST OF FIGURES

LIST OF FIGURES

LIST OF FIGURES

LIST OF FIGURES

LIST OF FIGURES

LIST OF TABLES

CHAPTER I

INTRODUCTION

1.1 Background

The damage and loss of life caused by earthquakes are great. This is magnified when there is a collapse of an essential infrastructure, such as a dam or a power plant. These have the potential of destroying entire cities. Dams are essential for the survival of a community providing the needed water and power to supply a community. Not to mention the other benefits that it brings such as tourism and flood control. However, when it fails, the destruction is often deadly causing irreparable damage to the land, the people and the economy.

In general, earth dams are the most common type of dam found because of its cost effectiveness. A number of earth dams exist throughout all over the world for serving multi purposes. In developing countries or even some developed countries such as those in Southeast Asia are not well prepared for the possibility of an earthquake. Perhaps this is due to the fact that only recently was it discovered that earthquakes are probable in these areas. Because of their lack of preparedness, most of the operating dams in these countries were designed and constructed based on static loading. The seismic safety was considered by using the pseudo–static method with 0.1g seismic coefficient (kh), without explicit consideration of dynamic response from the seismic effect. Since, the knowledge of earthquake engineering has improved. Moreover, there is concrete evidence that the dynamic behavior of such structure is far beyond what assumed in the past as psudo static force procedure. Unfortunately, such considerations were not explored when many structures were constructed. Thus, there are numerous infrastructures like dam that their seismic safety was still in doubt. Also, due to increasing of the human population, this caused the city expanded and spread out to the seismic risk area. As a result, these cause concerning people realize that their previously design against earthquake may be not safe from the earthquake as once believed. Since many countries lie in one of the seismically active areas, one of the main issues in the dam management and construction is the seismic safety. Therefore, to assure dam's safety, a proper safety evaluation of such dams is crucial and necessary.

To evaluate the dam safety or the cause of its failure, it is necessary to understand the failure types of an earth dam. There are several main reasons that considered being main causes of any earth dam failure. First, the overtopping or loss of freeboard, this type is mainly based on the magnitude of its deformation. The overtopping is occurred when the embankment crest settles down below the reservoir level therefore the erosion from overtopping could lead the dam to fail. Secondly, crack and internal erosion, if a dam is deformed by earthquake excitation or fault displacement, the deformations can cause cracks in dam and or disrupt internal filters, either of which could lead to failure of the dam by erosion. And slope failure, the seismic wave might cause instability to the embankment

slope that consequence to the slope sliding. Lastly, for the material which is prone to liquefy, during the shaking the liquefaction may take place and causes a huge amount of settlement then lead to the dam failure. Through this information, the seismic safety can be evaluated and also the investigation on the dam failure can be completed.

Although the dam failures are seldom, studies have been conducted based on those events to understand the causes of those failures. For example, the failure of the Teton dam, this earthen dam located in Idaho, United States. It was 93 m high and 355 million m^3 capacity. The dam was failed on June 5, 1976 due to the internal erosion known as "piping" as it was filling for the first time. The failure caused a huge flood that damaged the city at downstream with the total damages cost of about 2 billion us dollars (Bountry and Randle 2001[1], U.S. Department of Interior Bureau of Reclamation USBR[2]). Besides, the Lower San Fernando dam which was a 40 m high hydraulic–fill earth dam located in San Fernando, California, was failed on February 9, 1971, as the San Fernando earthquake struck the southern California. This seismic shaking triggered liquefaction of the hydraulic–fill within the upstream slope of the dam. Therefore, the sliding was found to be induced by the loss of strength in the liquefied soils during earthquake and caused a great damage to downstream (Seed et al. 1975[3]). In Japan, Aratozawa dam is a rock–fill impervious core dam with the height of 74.4 m. The dam is located in Kurihara, Miyagi prefecture, Japan. According to the Iwate–Miyagi Nairiku earthquake in 2008, the huge landslides occurred around the reservoir on the left bank upstream from the dam. It caused settlement of about 20 cm at the core zone however there is no evidence of a severe damage to the dam safety but caused the dam to be nonfunctional (Yamaguchi et al. 2008[4]).

According to the Fujinuma dam failure, Harder LF, Jr et al. 2011[5] visited the Fujinuma dam just only a few weeks after the event. The principal purpose of the visits was to observe and document the failure of the main dam and the upstream slide in the auxiliary dam. The discussions on the failure mechanism and recommendations on the future works made by the authors were also given. In additional, Ono et al. 2011[6] stated that the failure of the Fujinuma dam was only the second of such dam to fail completely in the recorded history of Japan. Also, as official records, there are about 210,000 reservoirs in Japan, at least 20,000 dams are vulnerable to future earthquakes. Therefore, the contributions of this report will raise the awareness for reducing the potential of the dam failure in future catastrophic events. Likewise, Tanaka et al. 2012[7], study on the failure of the Fujinuma dam. Therefore, comments and discussions on the cause of the dam failure have been demonstrated.

Subsequent to the devastating earthquake in the Japan's chronicle on 11 March 2011, seven dams were found to be damaged and the Fujinuma was collapsed due to the baleful force generated by the 9.0–magnitude quake known as the 2011 Off the Pacific Coast of Tohoku Earthquake (hereafter, the 2011 Tohoku earthquake). The Fujinuma dam was constructed to serve as a water supply for an irrigation purpose. The dam was located on a tributary of the Abukuma river, Sukagawa city in Fukushima prefecture, Japan. It had failed following to the 2011 Tohoku earthquake. Therefore, it caused the flood that washed away 19 houses while damaging others, disabling a bridge and blocked roads with debris. One person was

missing and seven bodies were discovered after searches began at dawn. According to these, the failure of the Fujinuma dam found to be a very good example to get insight the failure phenomenon and also to acquire useful information in the field of dam safety.

In the computation of soil structures, coupling behavior between solid skeleton and pore water is crucial. Since, Biot (Biot 1941[8] and Biot 1956[9]) firstly developed a linear theory of poroelasticity, thereafter researchers in this field have established numerous solid–fluid coupling formulations with different assumptions. Those techniques have their own strength in solving different problems. Among all, as the u–p formulation has been established it becomes well–known and widely applied in the field of Geotechnics due to its simplicity. Hence, finite element codes for porous medium are continuously developed by many. Lately, as advanced computational techniques in Geotechnics have been introduced, it is beneficial for researchers (Oka et al. 1994[10], Diebels and Ehlers 1996[11], Lewis and Schrefler 1998[12], Zienkiewicz et al. 1998[13], Li et al. 2004[14], Woodward and Griffiths 1995[15], Kramer 1996[16], Uddin 1999[17], Wieland 2003[18], Tancev 2005[19], Sica et al. 2008[20], Rampello et al. 2009[21], Charatpangoon et al. 2010[22]) to analyze the seismic behavior of dams using those techniques. Consequently, plenty researches have been conducted in the area of the seismic safety of the existing earth dam. Recently, Soralump and Tansupo 2009[23] conducted a dynamic response analysis of the Srinagarind dam using 213 records of 35 earthquake events and the equivalent linear method for the nonlinear behavior of dam materials. Similarly, Fallah and Wieland 2010[24] conducted an evaluation of earthquake safety of the Koman concrete face rockfill dam in Albania using a two–dimensional (2D) finite element (FE) model of the maximum cross–section. It was carried out using the equivalent linear method.

At present, the state of the art in numerical simulation using finite element method for porous media is being developed and extended to large deformation and finite strain in both static and dynamic problems. Accordingly, these make a great contribution to the field of geotechnical earthquake engineering to obtain more reliable results. Also, more advanced constitutive laws can be addressed. Since, both extensions in the finite element at finite strain are now addressed, more extensive behaviors of earth structure can be then further expressed and are able to capture the failure mechanism accurately. All these methods as mentioned above have been applied to evaluate the safety of earth dam. The importance of such research is not only to discover its level of damage or its behavior, but above all to preserve it from the future quakes.

Even, there is much research has been conducted in this field, practically, there are still a number of existing dams were not yet evaluated their safety. Also, the procedure to obtain all necessary parameters used in the analysis is one of the important issues. Those parameters need to be gathered or acquired with proper and systematic way. Furthermore, for the dam that might evaluate as unsafe and prone to fail, there is a need to strengthening it for finding out the mitigations in order to ensure the life and properties of people who live downstream. Accordingly, the systematic procedure to evaluate the seismic safety of the dam and the proper way to find out the cause of the dam failure is needed to be

addressed. Also, the mitigation techniques should be studied to provide the best solution for preventing the loss of life and properties due to the failure of the dam.

1.2 Statement of the problem

As the seismic safety of the dam becomes big issue as it could bring about a great disaster to the life and properties of people who live downstream. Recently, there is much researches provides the proper way for evaluating the seismic safety of the dam, yet these methods have their own strength and drawback. Accordingly, the selection of the method that could be suitable and systematic for applying in the particular case is very crucial. Thus, this study aims to find out the appropriate systematic way to evaluate the seismic safety of the dam and also the proper mitigation for the interested dam. As the occurrence of the 2011 Tohoku earthquake, the Fujinuma dam was an earth dam with 18.5 m height and 6 m crest width was failed following this event. Since, the dam was failed but remaining portion still existed at the site, the remaining dam could provide a large amount of data, evidences and facts. The facts and other information could be obtained by conducting the site investigation and the laboratory experiments. By studying the failure of this dam, it could reveal clues that lead to a better understanding on the failure mechanism and the dynamic behaviour or even prevent the failure to the similar type of dam.

However, this task arises some difficulties due to the procedure and some limitations. As the dam was built long time ago in the past, there is no or limit of data from its design can be found. Yet, the in–situ test and laboratory experiments can be done, it needs to be discussed which method could be used to obtain information and whether they are reliable or not. Also, for the evaluation of the dam safety, which techniques could be properly applied to obtain the results.

Eventually, if the analysis results indicate that the dam is prone to fail and reveal the cause of its failure, which is the best mitigation that could efficiently solve that particular problem. Through this study, how to raise the awareness of the individual or concerned groups is very important as well.

1.3 Significance of the research

From this study, the information, facts and numerical analysis results on the failure of the Fujinuma dam were summarized and discussed. The outcomes will provide a better understanding on the cause of the earth dam failure and its behaviour during the earthquake excitation. In addition, by studying the possible rehabilitation techniques, a better understanding on the problems along with their solutions were obtained and also the advantages and drawbacks for each method were summarised. Hence, these outcomes can be used in order to improve a current design code and also to prevent the other existing earth dams from their failure that may induced by future quakes. Besides, this research will give engineers or other who concerned, proper tools necessary to incorporate the findings into the construction and rehabilitation of earth dams. In short, this study proposes a systematic way to evaluate the seismic safety of earth dam and to propose possible rehabilitation methods for the interested dam. Lastly, this research could raise the people

and concerned groups, awareness on the seismic safety of the dam and make a safety environment.

1.4 Research objectives

The main objective of this research is to develop an appropriate procedure for evaluating the seismic safety of earth dam. Also, this study aimed to find out the cause of the Fujinuma dam failure following the 2011 Tohoku earthquake by conducting the site investigation, laboratory experiment and numerical simulation. Furthermore, to determine the proper method of rehabilitation for particular dam, various mitigation techniques were introduced. Lastly, as it is recognized that in the study of the failure of soil structure, the coupled solid–fluid finite element code at large deformation found to be most suitable for analyzing such problems. Hence, the implementation of such code is also included in the objectives of this study.

The specific objectives are:

- The selection of a dam: it is expected that the selected dam should be accessible, be able to acquire information and data, and be able to conduct in–situ tests or laboratory tests.
- Input earthquake history: the proper earthquake motions will be selected in order to use in this study.
- Evaluation of the material properties: field test and laboratory test will be conducted in order to determine the material properties, and to find out the evidence of the dam failure.
- Evaluation of the seismic safety of the dam: by using numerical simulation, the seismic safety of the dam will be determined. In this case, the numerical simulations were conducted to understand the dynamic behavior of the dam and its possible causes of failure.
- Implementation of the coupled solid–fluid finite element code for solving dynamic problem at finite strain: to obtain better results on a dam's behavior during an earthquake excitation and also to capture its failure mechanism, it is necessary to implement a finite element code at finite strain. Therefore, the coupled solid–fluid finite element code at finite strain will be proposed and verified with the basic geotechnical problem.
- Proposal of seismic rehabilitation of the dam: a number of solutions will be proposed. The comparisons among all rehabilitation techniques will be presented and the most appropriate solution will be suggested.

1.5 Scope of the study

This study aimed to determine the cause of the failure of the Fujinuma dam and find out the possible rehabilitation techniques. First, the study on the dam failure was presented. It deems to get insight the dynamic behavior and find out the cause of failure of the Fujinuma dam. The site investigation and laboratory experiments were conducted to obtain the information and facts on its failure and also to be used in the numerical simulation. For the

site investigations, there are two measurements have been conducted which are; microtremor observation and visual investigation. In case of laboratory experiments, grain size analysis, permeability and triaxial tests were conducted. Thereafter, numerical simulations were carried out under coupled solid–fluid 2D finite element method. The mechanical properties of soil will be described through the simple elastic–perfectly plastic using the Mohr–Coulomb available in the finite element code Plaxis (Brinkgreve and Vermeer 1998[25]). The observed motions and simulated motion were used in order to determine the response of the dam during the excitation. Dynamic analyses were conducted and the overall dam behaviors and the possible failure mechanism of the dam are presented. Also, discussions and comparisons between numerical results and existing facts were expressed. Furthermore, the study of several rehabilitation methods was introduced and the most appropriate technique was presented. Finally, this study is aimed to get insight the failure of earth structure, the large displacement is inevitable. Therefore, the finite element code for coupled solid–fluid at finite deformation was then developed. The proposed code was verified for both static problem and dynamic problem.

1.6 Literature review

1.6.1 Types of dam

According to the construction's material, dam can be divided into 2 main types as follow;

Concrete dam
This type of dam is constructed using reinforced concrete. Concrete dams come in a variety of types and rely on the weight of concrete and/or their shape to hold back the water. Concrete is a relatively expensive material and the construction of concrete dams is usually more labor–intensive than the construction of embankment dams.

- ***Gravity dam***
  In general, concrete dam is constructed for a large water storage structure and also for the dam which serves for generating the hydroelectricity. Concrete dam relies on its shape to withstand the pressure of the water built up behind them. The example is the Three Gorges Dam (181 m high) in China.
- ***Arch dam***
  The arch dam is unique in its design. The arch curves back upstream and the force exerted by the water is transferred through the dam into the valley walls and floor. They are normally constructed in deep gorges and the geological foundations need to be particularly sound. The spectacular concrete arch–gravity, the Hoover dam (221.4 m high) is example of the well–known arch dam.
- ***RCC dam***
  Roller compacted concrete (RCC) as concrete compacted by roller compaction. The concrete mixture in its unhardened state must support a roller while being compacted. Thus RCC differs from conventional concrete principally in its consistency requirement. For effective consolidation, the concrete mixture must be dry enough to prevent sinking of the vibratory roller equipment but wet enough to permit adequate distribution of the binder mortar in concrete during the mixing and vibratory compaction operations.

Embankment dam
An embankment dam is typically constructed by the placement and compaction of a various compositions of soil, sand, clay and/or rock. It can be divided into two major types based on the construction's material as following.

- ***Earth–fill dam***
  Earth–fill dams, also called earthen or simply earth dams, are constructed as a simple embankment of well compacted earth. There are several types of earthen dam which are; a homogeneous earth dam is entirely constructed of one type of material. A zoned–earth dam has distinct parts or zones of different material, generally a locally fill material with an impervious clay core. Modern zoned–earth embankments provided filter and drain zones to improve the drainage system within dam's body and preserve dams from the seepage failure. An interesting type of temporary earth dam occasionally used in high latitudes is the frozen–core dam, in which a coolant is circulated through pipes inside the dam to maintain a watertight region of permafrost within it. Almost construction materials are available on the site, it is hence the most popular dam type in the world. Another type of the earthen dam is hydraulic–fill dam which is now outdated and quite prone to the liquefaction.

- ***Rock–fill dam***
  Rock–fill dams are embankments of compacted granular material with an impervious zone. The earth utilized often contains a large percentage of large particles hence the term rock–fill. The impervious zone can be on upstream side, downstream side, and center in which case it is referred to as a core. The impervious zone could be made of masonry, concrete, plastic membrane, steel sheet piles, low permeability soil, timber or other material. To prevent internal erosion of clay into the rock–fill, a filter is required. Filters are specifically graded soil designed to prevent the migration of fine grain soil particles. An example of a rock–fill dam is New Melones dam in California.

Combined dam
This type of dam is a combination of the 4 types as mention above. For example, earthen dam combined with RCC dam in order to improve the foundation strength.

1.6.2 Mode of failure and past failure events of dams

In order to find the proper method to design or evaluate the safety of dams, it is important to understand its failure mechanism. The several failure types along with real failure events in the past (Wikipedia[26], USCOLD 1994[27], UNEP 2001[28], ICOLD 2001[29], ICOLD 2002[30], ICOLD 2010[31], Wieland 2012[32]) are listed below.

Overtopping of the embankment
Usually, the seismic safety of the embankment dam is evaluated based on the magnitude of its deformation. The overtopping is occurred when the embankment crest settles down below the reservoir level therefore the erosion from overtopping can cause the dam to fail.

When the earth structure subjected to the external applied load such as earthquake, wind etc, sometimes the stress may exceed the strength and cause the permanent displacement to the dam. These permanent deformations normally occurred respect to instant and small in

size however, for the long duration and strong excitation it can be cumulatively large and led to the overtopping failure. Also, during the excitation the rapid change in soil fraction volume could cause an excess pore pressure, this excess pore pressure can significantly reduce the effective stress that causing the loss of soil strength. When soil strength reduces, the greater permanent displacement is expected. Also if the pore pressure becomes large enough to equal the effective stress, then liquefaction could possibly occurred.

The overtopping can be also set off by the following:

- Movement on fault though the reservoir or though the embankment foundation, causing the reservoir elevate to rise above the crest of the dam or dam crest fall below the reservoir surface
- An earthquake induced landslide that displaces a significant volume of water
- A large seiche wave generated by an earthquake

Selected examples of the dam failure of this failure mode in the past are listed as follow; Sweetwater Dam in San Diego County, California (1916) and Lower Otay Dam in San Diego County, California (1916) failed owing to flooding, Laurel Run Dam in Johnstown, Pennsylvania, United States (1977) and Niedow Dam in Lower Silesian Voivodeship, Poland (2010) subjected to heavy rain resulting in over–topped from flooding.

Slope Stability and foundation Failures

Foundation defects due to differential settlement, slides, and slope instability can also cause dam failure. Movement on fault though the embankment foundation may cause a great damage or even the dam breach. For earth dams, there are several types of slope stability failures which are steady–state, seismic, and rapid–drawdown. For the steady–state case, failure occurs on the downstream side of the dam under conditions of steady–state seepage. This type of failure may occur as a result of an increase in pore water pressure in the dam. For the rapid–drawdown case, failure occurs on the upstream side of the embankment as a result of a sudden lowering of the reservoir level. In seismic case, the earthquake excitation is capable of causing the slope instability and lead to mass sliding failure of the embankment slope. Besides, for the dam which constructed using the material that prone to liquefaction or settled on the liquefiable soil, when the excess pore pressure is developed and becomes large enough to match the effective stress, the liquefaction is expected to occur which of course resulting the dam failure.

Selected examples of the dam failure of this failure mode in the past are listed as follow; Gohna Lake dam in India (1894), Aznalcollar Mine Tailings Dam in Spain (1998) was failed owing to the sliding on weak clay foundation, Tokwe Mukorsi Dam in Masvingo Province, Zimbabwe (2014) failed due to the downstream slope failure, Dam in Mianyang City, Sichuan Province, China (2011) tailings dam damaged from landslides caused from heavy rains and Tailing dam in Huayuan County, Xiangxi, Hunan Province, China (2011)

Piping and seepage

Failure due to piping and seepage, these are caused by internal erosion due to piping and seepage, and cracks in the dam structure. If a dam is deformed by earthquake excitation or fault displacement, the deformations can cause cracks in dam and/or disrupt internal filters, either of which could lead to failure of the dam by erosion.

For example, the failure of the Teton dam, this earthen dam located in Idaho, United States. It was 93 m high and 355 million m^3 capacity. The dam was failed on June 5, 1976 due to the internal erosion known as "piping" as it was filling for the first time. The failure caused a huge flood that damaged the city at downstream with the total damages cost of about 2 billion us dollars (Bountry and Randle 2001[1], U.S. Department of Interior Bureau of Reclamation USBR[2]) Recently, Dam in Omai, Guyana (1995), Taum Sauk reservoir in Lesterville, Missouri, United States (2005), Tennessee Consolidated No.1, Grays Creek, TN, USA (1988) were failed due to the internal erosion.

Failure due to problems with conduits and valves

Failure due to problems with conduits and valves is typically caused by the piping of embankment material into conduits through joints or cracks. Should there be conduits through the embankment, deformation of the dam can rupture them or cause joints to separate, leading to erosive failure by either creating an unfiltered exit for seepage or exposing the embankment or foundation to full reservoir head where not intended. Erosion along intact conduits has also caused dam failure.

Other causes

The remaining 6 percent are due to other miscellaneous causes. Many of the historical dam failures in the United States have been secondary results of other disasters. The prominent causes are earthquakes, landslides, extreme storms, massive snowmelt, equipment malfunction, structural damage, foundation failures, and sabotage.

For disaster induced dam's failure, they mostly concern with flood and earthquake. For example; Swift Dam in Montana, United States (1964) which failure caused by heavy rains, Banqiao and Shimantan Dams in China (1975), Shakidor Dam in Pakistan (2005), failed owing to the sudden and extreme flooding caused by abnormally severe rain, Delhi Dam in Iowa, United States (2010), Campos dos Goytacazes Dam in Brazil (2012) failed after a period of flooding and 4000 people displaced. Selected examples for earthquake induced dam's failure cases are; The Lower San Fernando dam which was a 40 m high hydraulic–fill earth dam located in San Fernando, California, was failed on February 9, 1971, as the San Fernando earthquake struck the southern California. This seismic shaking triggered liquefaction of the hydraulic–fill within the upstream slope of the dam. Therefore, the sliding was found to be induced by the loss of strength in the liquefied soils during earthquake and caused a great damage to downstream(Seed et al. 1975[3]), Veta de Agua No.1, Chile (1985) was failure due to liquefaction which triggered by the earthquake, In 1996 Amatista, Nazca, Peru suffered from liquefaction failure of upstream–type tailings dam during earthquake, Shihgang Dam in Taiwan (1999) caused by damage sustained during the 921 earthquake, The Fujinuma was collapsed due to the baleful force generated

by the 9.0–magnitude quake known as the 2011 Off the Pacific Coast of Tohoku Earthquake. The Fujinuma dam was constructed to serve as a water supply for an irrigation purpose. The dam was located on a tributary of the Abukuma river, Sukagawa city in Fukushima prefecture, Japan. According to the Fujinuma dam failure, Harder LF, Jr et al. 2011[4] visited the Fujinuma dam just only a few weeks after the event. The principal purpose of the visits was to observe and document the failure of the main dam and the upstream slide in the auxiliary dam. The main dam was possibly failed owing to the high intensity amplitude along with long durations of shaking while the saddle dam was failed due to the rapid drawdown. The failure caused the flood that washed away 19 houses while damaging others, disabling a bridge and blocked roads with debris. One person was missing and seven bodies were discovered after searches began at dawn.

Poor construction, lack of maintenance and repair, and deficient operational procedures are preventable or correctable by a program of regular inspections. For examples of the dam failure of this failure mode in the past are listed as follow; Dale Dike Reservoir in South Yorkshire, England, United Kingdom (1864), Mill River Dam in Williamsburg, Massachusetts, United States (1874), Hauser Dam in Helena, Montana, United States (1908), Austin Dam in Austin, Pennsylvania, United States (1911), Desná Dam in Desná, Czech Republic (1916), Gleno Dam in Province of Bergamo, Italy(1923), Meadow Pond Dam in New Hampshire, United States (1996). Whilst, South Fork Dam in Johnstown, Pennsylvania, United States (1889), Kantale Dam in Kantale, Sri Lanka (1986), Ka Loko Dam in Kauai, Hawaii (2006) failed owing to the poor maintenance, lack of inspection and illegal modifications.

Terrorism and vandalism are serious concerns that all operators of public facilities must plan for; these threats are under continuous review by public safety agencies. For example, Eder, Möhne Dams in Ruhr, Germany (1943) was destroyed by bombing during Operation Chastise in World War II. Another interesting case was the Hope Mills Dam in North Carolina, United States (2010) which sinkhole caused dam failure. Vajont Dam in Italy (1963) in fact not a dam failure, since the dam structure did not collapse and is still standing. Filling the reservoir caused geological failure in valley wall, leading to 110 km/h landslide into the lake; water escaped in a seiche over the top of dam. Valley had been incorrectly assessed stable.Similarly, In Japan, Aratozawa dam is a rock fill impervious core dam with the height of 74.4 m. The dam is located in Kurihara, Miyagi prefecture, Japan. According to the Iwate–Miyagi Nairiku earthquake in 2008, the huge landslides occurred around the reservoir on the left bank upstream from the dam. It caused settlement of about 20 cm at the core zone however there is no evidence of a severe damage to the dam safety but caused the dam to be nonfunctional (Yamaguchi et al. 2008[4]).

1.6.3 Seismic performance criteria for earth dams

According to ICOLD 2010[31] the performance criteria for the dam body and safety–relevant components and equipment are as follows:

In case of Operating Basis Earthquake (OBE): The OBE may be expected to occur during the lifetime of the dam. No damage or loss of service must happen. It has a probability of occurrence of about 50% during the service life of 100 years. The return period is taken as 145 years (ICOLD 2010[31]).
Dam body should have no structural damage (cracks, deformations, leakage etc.) which affect the operation of the dam and the reservoir is permitted. Minor, repairable damage, is accepted.
For The Safety Evaluation Earthquake (SEE) is the earthquake ground motion a dam must be able to resist without uncontrolled release of the reservoir. The SEE is the governing earthquake ground motion for the safety assessment and seismic design of the dam and safety-relevant components, which have to be functioning after the SEE. For major dams the SEE can be taken either as the Maximum Credible Earthquake (MCE) or Maximum Design Earthquake (MDE) ground motions.
Dam body or Structural damage (cracks, deformations, leakage etc.) is accepted as long as the stability of the dam is ensured and no uncontrolled release of large quantities of water is released from the reservoir causing flooding in the downstream region of the dam.

FEMA (Federal Guidelines for Dam Safety Earthquake Analyses and Design of Dams, 2005[33]) suggested the performance criteria for the earthen dam which located in the seismic prone region, the dam should satisfied criteria which summarized as follow.

- Dam and foundation materials not subject to liquefaction and do not include loose soils or sensitive clays.
- The dam is well built and compacted to at least 95% of the laboratory maximum dry density, or relative density greater than 80%
- The slope of the dam are 3:1 (H: V) or flatter, and /or the phreatic line is well below the downstream slope of the embankment.
- The freeboard at the time of the earthquake is at least 3–5% of the embankment height and not less than 0.9 m. freeboard requirements to accommodate reservoir seiche waves or coseismic movement of faults at the dam site or in the reservoir must be considered as a separate issue.
- No potential cracks that would allow internal erosion.

In addition, according to Tani et al. 2009[34], they summarized the seismic safety of a fill dam based on the performance based design criteria. The basic requirements and the design of a fill dam were firstly described. The performance based standard (ISO 23469) which is established after Hyogo–ken nanbu earthquake was used as the performance based criteria for evaluating the seismic safety of an existing fill dam. The performance criteria was set in order to ensure that no over flow will occur nor breach when a fill dam subjected to the credible earthquake in region. The criterions included the freeboard requirement after the shaking, post shaking slope stability and displacement. It is mentioned also the used of the finite element method in the seismic safety evaluation of a fill dam on its advantages, drawbacks as well as the recommendations. Besides, several rehabilitation techniques were proposed and studied using finite element method. The paper suggested that in case of using the numerical simulation for evaluating the seismic safety of the existing earthen dam, due to uncertainty in the numerical analysis and the material model the safety factor

of 2.0 should be taken into account. Accordingly, it is recommended that the settlement of the crest should not exceed 1.0 m so the allowable settlement should be limited at 0.5 m.

1.6.4 Seismic safety evaluation of earth dam

Equivalent–static forces

In the absence of site–specific estimates of design peak ground, the design seismic inertia forces for equivalent–static slope stability assessment shall be taken as (IS: 1893[35]):

$$FH = (1/3)\ ZISW \qquad \text{(Eq. 1.1)}$$

where FH is the horizontal inertial force, Z is the zone factor given in IS: 1893–part1 (2002) [35], I is the importance factor, S is an empirical coefficient to account for the amplification of ground motion between bedrock and the elevation of the toe of the dam or embankment, and W is the weight of the sliding mass.

If the estimate of design peak ground horizontal acceleration (PHGA) at the elevation of the toe of the dam is available, the design seismic inertia forces for equivalent–static slope stability assessment shall be taken as:

$$FH = (1/3)\ a_{max}W \qquad \text{(Eq. 1.2)}$$

where a_{max} is the design PHGA at the elevation of the toe of the dam. The vertical inertial force during an earthquake may be neglected in the design.

Newmark's method

Newmark's method or Sliding block method of slope stability analysis. This method provides an easy means for approximate estimation of the permanent sliding displacements (Newmark 1965[36]). The method suggests that a failing mass from the slope may be considered as a block of mass sliding on an inclined surface only when the inertial force acting on it, is equal or higher than the force required for causing an embankment slide. The block sliding is initiating when the Factor of Safety (FOS) became equal to 1. It also points out that when the FOS becomes less than 1 "failure" does not mean the total failure of the slope but each time when the FOS falls below unity, the permanent deformations occur which accumulate whenever FOS < 1. Accordingly, by estimating the yield acceleration which causing FOS falls below 1 together with the inertia force, the permanent displacement can be evaluated by integrating twice the difference of the applied acceleration and the yield acceleration with respect to time.

Due to its simplicity, this method is still widely used nowadays in engineering practice to evaluate the seismic slope stability and the permanent displacement of an earth dam. It has been proved a reasonable results and quite comparable to measured data.

However, this method is not taking into account the true dynamic response. The accurate sliding displacements should be estimated from the time history analysis. It also cannot really take into account of excess pore water pressure during cyclic loading which may play an important role on the failure of an earth dam. Currently, Numerical methods such as finite difference and finite element analysis are used which those limitations can be addressed and included the complicated elasto–plastic constitutive models.

Dynamic analysis

Dynamic analysis essentially involves estimation of the deformation behavior of an earth dam or an embankment using the finite element or finite difference method. A complete and detailed dynamic analysis is a major undertaking that requires extensive database and specialized skills. The results of such analyses are sensitive to the input seismologic parameters and engineering properties. Dynamic analysis employing a nonlinear stress–strain relationship provides a rational framework for estimation of deformation of an earth dam or an embankment. The biggest difficulty in employing these models is to obtain soil stress–strain models that are representative of the soil in situ behavior. This approach requires an accurate characterization of the stress–strain behavior of the materials within the body of the earth dam or embankment and foundation. Dynamic analysis of earth dams and embankments also require a suitable earthquake time–histories representing design earthquakes. A wide range of approaches have been utilized to model deformation behavior of earth dams and embankments.

1.6.5 Finite element method

In the past, seismic response of earth embankments was usually analyzed by using pseudo static analyses or displacement methods derived from the Newmark (1965) [36] using rigid block model. However, by using those techniques, it is merely to obtain a good approximation owing to the huge assumption made.

Since, Biot (1941)[6] proposed general theory of three–dimensional consolidation and Terzaghi (1943) [37] introduced the consolidation theory for one–dimensional systems which he investigated a one–dimensional consolidation problem of a horizontal layer with a homogeneous load, their works greatly advanced the knowledge in the geomechanics. In 1956, Biot[7] proposed a two phase system consisting of a solid skeleton and a pore fluid. The theory and the finite element code for coupled three–dimensional consolidation in geomaterial were then well established for example, Morrison 1995[38] finite element code saga, Zienkiewicz and Shiomi 1984[39], Settari and Price 1984[40], Alejano–Monge et al. 1995[41], Chen & Teufel 1997[42], Osorio et al. 1997[43], Koutsabeloulis et al. 1997[44], Chin et al. 1998[45], Gutierrez & Lewis 1998[46].

Hibbitt et al. 1970[47] provided the finite element formulation for problems of large strain and large displacement. In 1975, Bathe et al.[48] introduced the finite element formulation for large deformation dynamic analysis. He described firstly on the necessary concepts from basic to advance of continuum mechanics, motion of body in Cartesian coordinate system. Also, the definition of the total Lagrane formulation and update Largran formulation were given in this study. Therefore, by using those concepts, finite element formulation was proposed in various forms and also the implementation of a finite element code for large deformation dynamic analysis was then introduced. This proposed code then was verified with the exact problem and the close approximation was obtained. This code provided great sources of knowledge and background for coding nonlinear finite element code and it is beneficial for those who concerns to develop the finite element code which include the nonlinearity of both geometric and material.

Later, Bathe and Ozdemir 1976[49] and Gabriel and Bathe 1995[50] included the elasto–plastic constitutive law in the non linear finite element code. Also, many authors published and distributed their material models on this issue such as Bathe 1996[51] and Chrisfield 1997[52]. On early 21 century, as the current solution techniques to solve the nonlinear finite

element are time consuming, much research (Bathe and Baig 2005[53], Chang 2004[54], Pajand et al. 2009[55]) put an effort to finding effective techniques to get rid of an expensive computational time. Bathe and Baig 2005[53] provided the methods for solving finite element equation in nonlinear analysis problem. The solution procedures are implemented and the guideline is given. This paper introduced various techniques for solving FE problems and stated out their effectiveness and drawback. Those methods include full Newton, Newton–Rapson, modified Newton and quasi Newton method BFGS were applied and checked with field examples in both static and dynamic problems. In additional, the proper convergence criteria were discussed and recommended.

After the coupled finite element code have been widely implemented and applied in both research and practice. However, in some point of view, such codes still have limitations in which could provide a good approximation only in a small strain problem. Hence, to implement the formulation for finite element of porous media at finite strain is required. Simon et al. 1984[56] and De Boer et al. 1993[57] proposed the analytical solution for wave propagation in coupled system, many authors (Li et al. 2004[14], Heider 2012[58], Sun et al. 2013[59]), proposed and introduced a finite formulation for dynamic porous media at finite strain and applied those analytical as a verification problem. Especially, Li et al. 2004[14] established the paper which aimed to set up the finite element formulations at finite strain for coupled solid–fluid in dynamic problem. They firstly provide a basic understanding of continuum mechanics in large deformation and large–strain in both total Lagrane and update Lagrane form. Also, necessary knowledge on the mechanic of porous media was introduced. Therefore, the governing equation of motion, momentum and mass consideration for this problem were proposed. The finite element formulation was then established in various forms and the finite element code was developed by using its matrix form. Finally, the verification of the finite element code was made through several problems. The discussions and recommendations of this code were also given. Since, many materials concerning this topic are widely distributed, then the implementation of the code which capable of dealing with the geometrical nonlinearity were established.

Later, much research advanced the constitutive law by including the material non linearity using various techniques. For instants, Owen and Hinton 1980[60], Borja and Alarcon 1995[61], Diebels and Ehlers 1996[11], Carter et al. 1997[62], and Borja et al. 1998[63] have contributed their works in this field.

In addition, recently more advanced techniques for calculating the advanced constitutive law at finite–strain has been introduced. The multicative approach has been implemented in finite element code by Voyiadjis and Kattan 1990[64], Armero1998[65], F. Auricchio and Taylor 1999[66], Dodds and Healy 2001[67], Dunne and Petrinic 2004[68], Khoei et al. 2004[69], and Regueiro and Ebrahimi 2010[70]. According to Regueiro and Elbrahimi 2001[70], they introduced three–dimension finite element formulation and implemented finite element code for inelastic biphasic mixture at finite strain using a simple geomaterial. Firstly, it is similar to the study of Li et al. 2004[14] as they both gave a brief knowledge on finite–strain and the necessary materials required for governing the finite element formulation for particular problem. However, in this paper, they did verify the problems not only with the small–strain FE code but also the analytical solution in dynamic problems. Moreover, the

implementation of the nonlinear materiality using the multiplicative–decomposition of deformation gradient was introduced. The behaviors of mixture using these techniques together with the Drunker–Prager and cap–plasticity model were studied. Therefore, the discussions and recommendations of this study were summarized.

1.6.6 Finite element analysis of earth dam

Recently, various approaches to the dynamic response analysis of earth dams have been applied. Cascone and Rampello 2003[71], Fallah and Wieland 2010[24] applied the equivalent linear method to account for nonlinear soil behavior for the two–dimensional finite element (FE) dynamic analyses of an earth dam. They accounted for synthetic and real acceleration histories as the input motions. Similarly, Z. Feng et al. 2010[72] conducted the study on the numerical earthquake response analysis of the Liyutan earth dam in Taiwan by applying the equivalent linear method.

On the other hand, many researchers applied different constitutive laws in the numerical simulation of the dam. For elasto–plastic constitutive law; Lacy and Prevost 1987[73] studied on nonlinear seismic response analysis of earth dams, Woodward and Griffith 1995[15] studied on the Influence of viscous damping in the dynamic analysis of an earth dam using simple constitutive models, Siyahi and Arslan 2007[74] conducted a nonlinear dynamic finite element simulation of Alibey earth dam, Sica et al. 2008[20] dealt with the influence of past loading history on the seismic response of earth dams, Psarropoulos and Tsompanakis 2008[75] evaluated a tailing dam using a FEM code, PLAXIS, to study static and seismic loading, and Rampello et al. 2009[21] analyzed the dynamic response for the dam using the finite element method with a hardening soil model, and they back–analyzed the earth dam construction. Lately, Khoei et al. 2004[69] conducted dynamic analysis of earth–and rock–fill dams using nonlinear finite element code with material nonlinearity and applied the advanced constitutive law to their study.

1.7 Summary and outline

The structure of this thesis consists of six chapters which yields most information on work done in this research. These works included the site investigation, laboratory experiments, numerical simulations, retrofitting methods and the developing of finite element code for coupled solid–fluid at finite–strain. The content on each chapter can be briefly described as follow.

Chapter 2, provided information on both field investigation and laboratory experiment. Firstly, the results of visual investigation were presented through the overall picture of the Fujinuma dam at a moment, the failure, the affected area followed by the visual examination of fill materials. For the laboratory experiment, physical properties, the particle size test and triaxial test were expressed. The earthquake records of the 2011 Tohoku earthquake obtained from the observed stations around the site also studied and presented. Eventually, the summary and discussions for possible failure mechanism from fact finding were expressed.

Chapter 3, provided information on the microtremor test conducting at site, the contents present the short description of this test on the introduction, methodology and results. The results of the microtremor test provided an understanding on the natural frequency and mode shape of a remaining dam and also the site's predominant period. The comparison between the modal analysis and ambient vibration test of the remaining dam was described in this chapter.

Chapter 4, the numerical simulation using finite element at small strain is presented. The formulation, the description of the model and input parameters were presented. Then, dynamic analyses of the Fujinuma dam were conducted using both the observed and simulated motions. The results explain through its acceleration, stress–strain, displacement, excess pore pressure and the possible failure mechanism. In addition, the retrofitting techniques were proposed to determine the most suitable mitigation for improving the dam safety in this study. The description of strengthening methods is presented and the comparison on results by applying various techniques also demonstrated and discussed.

Chapter 5, the numerical simulation using finite element at finite–strain was presented. The formulations, the description of the model and input parameters also were provided. Then, verification of the code with analytical solution and small–strain code were made. The dynamic analysis of earth dam using a proposed code was presented and compared with the results obtained from the small–strain finite element code.

Chapter 6, the conclusion, discussion and recommendation of this research were presented.

REFERENCES

[1] J. A. Bountry, T. J. Randle, Upstream impact after the 1976 failure of Teton dam, proceedings of the seventh federal interagency sedimentation conference, Reno, Nevada, (2001).

[2] U.S. Department of Interior Bureau of Reclamation (USBR). [Online]. Available: / www.usbr.gov/pmts/sediment/projects/teton River/TetonRiver.html [accessed 03.06.12].

[3] H. B. Seed, I. M. Idriss, K. L. Lee, F. I. Makadisi, Dynamic analysis of the slide in the lower San Fernando dam during the earthquake of February 9, 1971. ASCE, Journal of Geotechnical Engineering Division, GT9 (1975) 889–911.

[4] Y. Yamaguchi, T. Iwashita, S. Mitsuishi, Preliminary investigation of dams stricken by the iwate–miyagi nairiku earthquake in 2008, Proceedings of the 5th east Asian regional dam conference international symposium on co–existence of environment and dams, (2008).

[5] L. F. Harder Jr., K. I. Kelson, T. Kishida, R. Kayen, Preliminary Observations of the Fujinuma dam failure following the March 11, 2011 Tohoku Offshore Earthquake, Japan, Geotechnical reconnaissance of the 2011 Tohoku Japan Earthquake, GEER Association 25e (2011).

[6] K. Ono, S. Kazama, S. Kawagoe, Y. Yokoo, L. Gunawardhana., Possible earthen dam failure mechanisms of Fujinuma reservoir due to the Great East Japan Earthquake of 2011, Hydrological Research Letters 5 (2011) 69–72.

[7] T. Tanaka, F. Tatsuoka, Y. Mohri, Earthquake Induced failure of Fujinuma Dam, International symposium on dams for a changing world, ICOLD, Kyoto, Japan, 6 (2012) 47-52.

[8] M.A. Biot, General theory of three-dimensional consolidation, Journal of Applied Physics, 12 (1941) 155-164.

[9] M.A. Biot, Theory of propagation of elastic waves in a fluid saturated porous solid. I. low-frequency range, Journal of the Acoustical Society of America, 28(2) (1956) 168–178.

[10] F. Oka, A. Yashima, T. Shibata, M. Kato, R. Uzuoka, FEM–FDM coupled liquefaction analysis of a porous soil using an elasto–plastic model, Applied Scientific Research, 52(1994) 209–245.

[11] S. Diebels, W. Ehlers, Dynamic analysis of a fully saturated porous medium accounting for geometrical and material non–linearities, International Journal for numerical methods in Engineering, 39 (1996) 81-97.

[12] R. W. Lewis, B. A. Schrefler, The finite element method in the static and dynamic deformation and consolidation of porous media, John Wiley and Sons, New York, 1998.

[13] O.C. Zienkiewicz, A.H.C. Chan, M. Pastor, B.A. Schrefler, T. Shiomi, Computational geomechanics with special reference to earthquake engineering, John Wiley and Sons, Chichester, 1998.

[14] C. Li, R.I. Borja, R.A. Regueiro, Dynamics of porous media at finite strain, Computation Methods in Applied Mechanics and Engineering, 193 (2004) 3837–3870.

[15] P.K. Woodward, D.V. Griffiths, Influence of viscous damping in the dynamic analysis of an earth dam using simple constitutive models, Journal of Computers and Geotechnics, 19(3) (1995) 245–263.

[16] S.L. Kramer, Geotechnical Earthquake Engineering, The United States of America, Prentice Hall, Inc., 1996.

[17] N. Uddin, A dynamic analysis procedure for concrete-faced rockfill dams subjected to strong seismic excitation, Journal of Computers and Structures, 72 (1999) 409–421.

[18] M. Wieland, Seismic Aspects of Dams, Commission International Des Grands Barrages, Switzerland, 2003.

[19] L. Tancev, Dam and Appurtenant Hydraulic Structures, Taylor & Francis, London, 2005

[20] S. Sica, L. Pagano, A. Modaressi, Influence of past loading history on the seismic response of earth dams, Journal of Computers and Geotechnics, 35 (2008) 61–85.

[21] S. Rampello, E. Cascone, N. Grosso, Evaluation of the seismic response of a homogeneous earth dam, Journal of Soil Dynamics and Earthquake Engineering, 29 (2009) 782–798.

[22] B. Charatpangoon, K. H. Park, C. Hansapinyo, P. Warnitchai, Seismic Safety Evaluation of Mea Kuang Udomthara Dam, Proceedings of the 3rd ASIA Conference on Earthquake Engineering ACEE, Bangkok, Thailand, (2010).

[23] S. Soralump, K. Tansupo, Safety analyses of Srinagarind dam induced by earthquakes using dynamic response analysis method, Proceedings of the International Conference on Performance–based Design in Earthquake Geotechnical Engineering IS–Tokyo, (2009) 987–994.

[24] H. Fallah, M. Wieland, Evaluation of Earthquake Safety of Koman Concrete Face Rockfill Dam in Albania, Proceedings of the 3rd Asian Conference on the Earthquake Engineering ACEE, Bangkok, Thailand, (2010).

[25] R. B. J. Brinkgreve, P. A. Vermeer, Plaxis ver. 7, Material models manual, Balkema, Rotterdam, 1998.

[26] Wikipedia. [Online]. Available: /http://en.wikipedia.org/wiki/Dam_failure. [accessed 07/01/12]

[27] USCOLD , Tailings Dam Incidents, U.S. Committee on Large Dams – USCOLD, Denver, Colorado, ISBN 1–884575–03–X, 1994.

[28] ICOLD, Tailings Dams – Risk of Dangerous Occurrences, Lessons learnt from practical experiences, Bulletin 121, Published by United Nations Environmental Programme (UNEP) Division of Technology, Industry and Economics (DTIE) and International Commission on Large Dams (ICOLD), Paris 2001.

[29] ICOLD, Design features of dams to effectively resist seismic ground motion, Bulletin 120, Committee on Seismic Aspects of Dam Design, International Commission on Large Dams, Paris, 2001.

[30] ICOLD, Earthquake design and evaluation of structures appurtenant to dams, Bulletin 123, Committee on Seismic Aspects of Dam Design, International Commission on Large Dams, Paris, 2002.

[31] ICOLD, Selecting seismic parameters for large dams, Guidelines, Revision of Bulletin 72, Committee on Seismic Aspects of Dam Design, International Commission on Large Dams, Paris, 2010.

[32] M. Wieland, Seismic Design and Performance Criteria for Large Storage Dams, Proc. 15th World Conf. on Earthquake Engineering, Lisbon, Portugal, Sep. 24–28, (2012).

[33] FEMA Federal Guidelines for Dam Safety Earthquake Analyses and Design of Dams, 2005

[34] S. Tani, S. Tsukuni and T. Shiomi, Performance of a fill dam based on the performance–based design concept and study of a seismic retrofitting method, Journal of Soils and foundations, 49(6) (2009) 841–851.

[35] IS 1893–1 (2002): Criteria for Earthquake Resistant Design of Structures, Part 1: General Provisions and Buildings, 2002.

[36] N. M. Newmark, Effects of earthquakes on dams and embankments. Geotechnique, 15 (2) (1965), 139–160.

[37] K. Terzaghi, Theoretical Soil Mechanics, John Wiley and Sons, New York, 1943

[38] C. S. Morrison, The development of a modular finite element program for analyses of soil–structure interaction, Doctoral Dissertation, Geotechnical Engineering Division,

Department of Civil Engineering, Virginia Polytechnic Institute and State University, Blacksburg. 1995

[39] O. C. Zienkiewicz and T. Shiomi, Dynamic behavior of saturated porous media; The generalized Biot formulation and It's numerical solution, International Journal for Numerical and Analytical Methods in Geomechanics, 8(1984) 71–96.

[40] A. Settari and H. S. Price, Simulation of hydraulic fracturing in low permeability reservoirs, SPE Journal, (1984) 141–152.

[41] L.R. Alejano Monge, P.R. Oyanguren, and R.D.L. Fuente, Method to predict final subsidence basins by means of a finite difference computer code, Proceedings of the 5th International Symposium on Land Subsidence, Hague, Neth. IAHS Publication (International Association of Hydrological Sciences) IAHS, Wallingford, Engl. n 234 (1995) 251–258.

[42] H.Y. Chen and L.W. Teufel, Coupling fluid-flow and geomechanics in dual–porosity modeling of naturally fractured reservoirs, Proceeding of the SPE Annual Technical Conference and Exhibition, San Antonio, Texas, 5–8 October, (1997).

[43] J.G. Osorio, H.Y. Chen and L.W. Teufel, Fully coupled fluid–flow geomechanics simulation of stress–sensitive reservoirs, Proceeding of the Reservoir Simulation Symposium, Dallas, Texas, USA, 8–11 June, (1997).

[44] N.C. Koutsabeloulis, B.G.D. Smart, K. Bratvedt and C. Buchholz, A 3–D 3–phase stress dependent reservoir simulator, Proceeding of the SPE Reservoir Simulation Symposium, Dallas, Texas, USA, 8–11 June, (1997).

[45] L.Y. Chin, R. Raghavan and L.K. Thomas, Fully-coupled geomechanics and fluid–flow analysis of wells with stress–dependent permeability, Proceeding of the SPE International Conference and Exhibition, Beijing, China, 2–6 November, (1998).

[46] M. Gutierrez and R.W. Lewis, The role of geomechanics in reservoir simulation, Proceeding of the SPE/ISRM Eurock'98, Trondhelm, Norway, 8–10 July, (1998).

[47] H. D. Hibbitt, P. V. Marcal and J. R. Rice, A finite element formulation for problems of large strain and large displacement, International Journal for Solids Structures, 6 (1970) 1069–1086.

[48] K.J. Bathe, E. Ramm and E.L. Wilson, Finite Element Formulations for Large Deformation Dynamic Analysis, International Journal for Numerical Methods in Engineering, 9 (1975) 353–386.

[49] K.J. Bathe and H. Ozdemir, Elastic–Plastic Large Deformation Static and Dynamic Analysis, Computers & Structures, 6 (2) (1976) 81–92.

[50] G. Gabriel and K.J. Bathe, Some Computational Issues in Large Strain Elasto–Plastic Analysis, Computers & Structures, 56 (2/3) (1995) 249–267.

[51] K. J. Bathe, Finite Element Procedures, Prentice-Hall, MA: Klaus–Jürgen Bathe, 1996

[52] M. A. Crisfield Non–linear finite element analysis of solids and structures, volume 2, John Wiley & Sons Ltd, Baffins Lane, Chichester, England, 1997.

[53] K. J. Bathe and M. M. I. Baig, On a Composite Implicit Time Integration Procedure for Nonlinear Dynamics, Computers & Structures, 83(2005) 2513–2534.

[54] S. Y. Chang, Studies of Newmark method for solving nonlinear systems: (i) basic analysis, Journal of the Chinese Institute of Engineers, 27(5) (2004) 651–662.

[55] M. Rezaiee–Paj, M. Tatar and B. Moghaddasie, Some geometrical bases for incremental iterative methods, IJE Transactions B: Applications, 22(3) (2009) 245.

[56] B. R. Simon, O. C. Zlenklewlcz, D. K. Paul, An analytical solution for the transient response of saturated porous elastic solids, International Journal for Numerical and Analytical Methods in Geomechanics, 8 (1984) 381–398.

[57] R. de Boer, W. Ehlers and Z. Liu, One–dimensional transient wave propagation in fluid–saturated incompressible porous media, Archive of Applied Mechanics, 63 (1993) 59–72.

[58] Y. Heider, Saturated Porous Media Dynamics with Application to Earthquake Engineering, Yousef Heider's Dissertation Report No II–25, University of Stuttgart, Stuttgart, Germany, 2012.

[59] W. C. Sun, J. T. Ostien and A. G. Salinger, A stabilized assumed deformation gradient finite element formulation for strongly coupled poromechanical simulations at finite strain, International Journal for Numerical and Analytical Methods in Geomechanics, (2013) Published online in Wiley Online Library (wileyonlinelibrary.com). DOI: 10.1002/nag.2161

[60] D. R. J. Owen and E. Hinton, finite elements plasticity: Theory and Practice, Pineridge Press Limited 91 West Cross Lane, West Cross, Swansea U.K. 1980

[61] R. I. Borja, E. Alarcon, A mathematical framework for finite strain elasto–plastic consolidation Part 1: Balance laws, variational formulation, and linearization, Computer Methods in Applied Mechanics and Engineering, 122 (1995) 145-171.

[62] J. P. Carter, J. R. Booker and E. H. Davis, Finite deformation of an elasto–plastic soil international. Journal for Numerical and Analytical Methods in Geomechanics, 1(1977)25–43.

[63] R. I. Borja , C. Tamagntm , E. Alarcon, Elastoplastic consolidation at finite strain Part 2: Finite element implementation and numerical examples Computer Methods in Applied Mechanics and Engineering, 159 (1998) 103–122.

[64] G. Z. Voyiadjis and P. I. Kattan, A coupled theory of damage mechanics and finite strain elasto–plasticity–ii damage and finite strain plasticity, International Journal of Engineering Science, 28(6)(1990) 505–524.

[65] F. Armero, Formulation and finite element implementation of a multiplicative model of coupled poro–plasticity at finite strains under fully saturated conditions, Computer Methods in Applied Mechanics and Engineering, 171 (1999) 205–241.

[66] F. Auricchio, R.L. Taylor, A return-map algorithm for general associative isotropic elasto–plastic materials in large deformation regimes, International Journal of Plasticity, 15 (1999) 1359–1378.

[67] R. H. Dodds, Jr. and B. E. Healy, Large strain plasticity model for implicit finite element analyses, civil engineering studies structural research series, 558(1991).

[68] F. Dunne and N. Petrinic, Introduction to Computational Plasticity Oxford University press, Oxford University, UK, 2004

[69] A. R. Khoei, A. R. Azami, S. M. Haeri. Implementation of plasticity based models in dynamic analysis of earth and rockfill dams; A comparison of Pastor–Zienkiewicz and cap models. Computers and Geotechnics, 31(2004) 385–410.

[70] R.A. Regueiro, D. Ebrahimi Implicit dynamic three–dimensional finite element analysis of an inelastic biphasic mixture at finite strain Part 1: Application to a simple geomaterial, Computer Methods in Applied Mechanics and Engineering, 199 (2010) 2024–2049.

[71] E. Cascone, S. Rampello, Decoupled seismic analysis of an earth dam, Journal of Soil Dynamics and Earthquake Engineering, 23(5)(2003) 349–365.

[72] Z. Feng, P. H. Tsai, and J. N. Li, Numerical earthquake response analysis of the Liyutan earth dam in Taiwan, Natural Hazards and Earth System Sciences, 10(2010) 1269–1280.

[73] S. J. Lacy and J. H. Prevost, Nonlinear seismic response analysis of earth dams, Soil Dynamics and Earthquake Engineering, 6(1)(1987).

[74] B. Siyahi and H. Arslan, Nonlinear dynamic finite element simulation of Alibey earth dam, Environmental Geology, 54(2008) 77–85.

[75] P. N. Psarropoulos, Y. Tsompanakis, Stability of tailings dams under static and seismic loading, Canadian Geotechnical Journal, 45(5)(2008)663–675.

CHAPTER II

SITE INVESTIGATION AND LABORATORY TEST

2.1 Introduction

This chapter provides data and information on the materials used in the construction of an embankment body. The geotechnical and engineering properties of these materials, such as unit weight, particle size, and shear strength parameter, are provided. These properties were obtained from previous studies of Ono et al. 2011[1] , Tanaka et al. 2012[2] and from the experiments conducted in this study. In this study, a field investigation and laboratory experiments were conducted to extract the necessary information that may be useful for further studies related to dam failure. This chapter provides a brief introduction to dam materials, visual investigation, the laboratory experiments, and ends up with the results and discussions on fill material properties. In addition, possible failure mechanisms of the dam and the motions recorded near the dam site are presented.

In this study, the Fujinuma dam was selected as a case study. The dam was an earth–fill embankment dam near Sukagawa, Fukushima prefecture, Japan (Fig. 2.1). It was established on the Ebana River, a tributary of the Abukuma River, 16 km west of the city office of Sukagawa (37°18′07″N, 140°11′41″E).

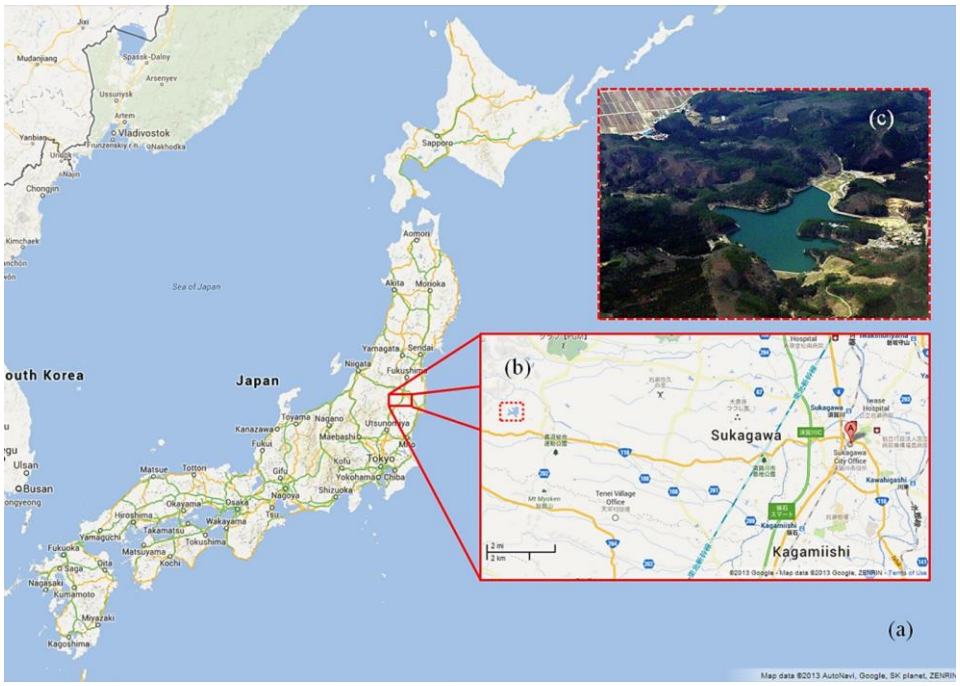

Fig. 2.1 (a) Location of the Fujinuma dam (©2013 Google. Map data. © Google. ZENRIN). (b) Sukagawa and the dam site (Map data ©2013 AutoNavi. Google. SK planet. ZENRIN). (c) Fujinuma dam

The dam construction began in 1937 and it was completed in 1949 after construction was halted during World War II. The primary purpose of the dam was water supply for

irrigation. The dam was an embankment type, 18.5 m high and 133 m long with a structural volume of 99,000 m^3 and a crest width of 6 m. On the upstream face, the concrete frames and panels were installed in order to protect the dam from the erosion. However, there are gaps between these panels so these panels were not served as the impervious layer and still penetrable. In addition, there was an auxiliary dam with a height of about 6 m and a length of approximately 60 m. The dam was at the head of an 8.8 km^2 drainage area giving a reservoir capacity of 1,504,000 m^3 (Wikipedia[3]). Following the devastating earthquake in Japan on 11 March 2011, the Fujinuma dam collapsed owing to the force generated by the 9.0–magnitude earthquake, known as the 2011 Off the Pacific Coast of Tohoku Earthquake (hereafter, the 2011 Tohoku earthquake). The failure caused a flood that washed away 19 houses and damaged others, disabled a bridge, and blocked roads with debris. Seven bodies were discovered after searches began at dawn and one person was declared missing.

Fig. 2.2 Pond after failure

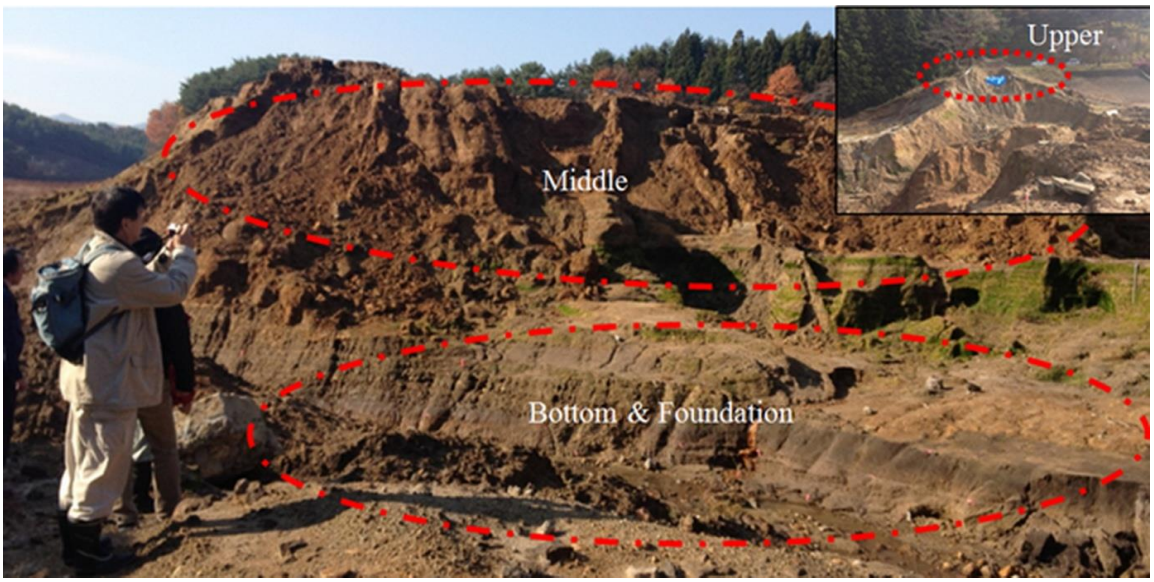

Fig. 2.3 Remaining dam

2.2 Visual investigation

Following the dam failure, most of the upper portion of the dam was washed away; the severe damage or breach location can be seen at the maximum cross section near the left abutment from downstream. On the opposite side, the remaining dam body consisted of the compacted fill materials. The foundations of the dam were exposed to ground level on the downstream side. From visual inspection, the dam body can be classified into three parts: upper, middle, and bottom. In addition, the investigation of the remains dam, reservoir's rim, auxiliary dam, pond (Fig. 2.2) and their vicinity has been conducted. From the survey's results, there is no strong evidence to affirm the occurrence of liquefaction.

The upper layer comprises the top 6–8 m to the dam crest. Unfortunately, most of the upper layer was flushed away when the dam failed. However, on the left abutment, a portion of the upper embankment remains. Visual observation was performed on this section, which revealed that the fill material consists mainly of coarse sand of light color varying from light brown to gray (Fig. 2.3).

The middle portion is about 7–9 m thick. This layer can be seen clearly in the remaining portion of the dam. From visual observation of this portion, this layer appears to have been filled with brownish cohesive soil containing yellowish–gray silt, loam–type clay, and humic silty sand (Fig. 2.3). Moreover, traces of compacted layers can be identified, each approximately 20–30 cm thick.

The bottom layer is between 4 and 6 m thick. This portion consists mainly of layers of loam–type clay and humic silty sand ranging from black to dark gray (Fig. 2.3). In addition, previous investigators (Ono et al. 2011[1] and Tanaka et al. 2012[2]) have indicated that some parts of the bottom layer consist mainly of dark brown sand and gravel. The black foundation material of the dam consists of organic residuals mixed with clay and silt.

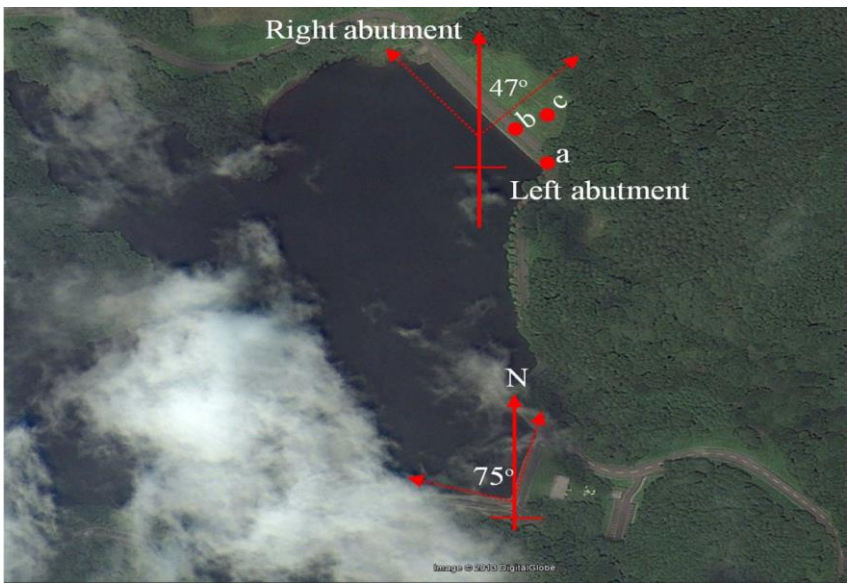

Fig. 2.4 Soil samplings location

2.3 Laboratory experiment

To facilitate the numerical simulation and study the cause of the dam failure, several laboratory experiments have been conducted to obtain the necessary information. Thirteen undisturbed cylinder samples were collected at the site. These samples can be defined based on their origin and testing purpose, as shown in Table 1. For each embankment layer, 4 samples were taken, which gave 12 samples in total for the entire dam body. As shown in Fig. 2.4, the soils samples were taken from locations a, b, and c, corresponding to the upper, middle, and bottom layers, respectively. These samples were tested to acquire the basic soil properties, particle size distribution, and other parameters used in the analysis. The 13th sample, taken from the middle portion, was tested to establish the coefficient of permeability.

Table 2.1 Soil sample

Type of Testing	Number of samples	Site	Condition	Date of test
Permeability test	1	Fujinuma dam	Undisturbed	24/01/12
Triaxial CU test	11(12)	Fujinuma dam	Undisturbed	1–24/04/12
Bottom layer	4	Fujinuma dam	Undisturbed	1–24/04/12
Middle layer	4	Fujinuma dam	Undisturbed	1–24/04/12
Top layer	3(4)	Fujinuma dam	Undisturbed	1–24/04/12
Total	13			

2.3.1 Permeability test

The falling head permeability test is a common laboratory testing method used to determine the permeability of fine grained soils with intermediate and low permeability such as silts and clays. (BS 1377–5:1990 Methods of test for soils for civil engineering purposes Compressibility, permeability and durability tests [4])

The falling head permeability test involves flow of water through a relatively short soil sample connected to a standpipe which provides the water head and also allows measuring the volume of water passing through the sample. Before starting the flow measurements, the soil sample must be saturated and the standpipes are filled with de–aired water to a given level. The test then starts by allowing water to flow through the sample until the water in the standpipe reaches a given lower limit. The time required for the water in the standpipe to drop from the upper to the lower level is recorded. Often, the standpipe is refilled and the test is repeated for couple of times. The recorded time should be the same for each test within an allowable variation of about 10% (Head 1982[5]) otherwise the test is failed. On the basis of the test results, the permeability of the sample can be calculated as

$$k = \frac{2.30\,aL}{At}\log_{10}\left(\frac{h_1}{h_2}\right) \qquad \text{(Eq. 2.1)}$$

Where h_1 = initial head, h_2 = final head, t = time interval, a = cross–sectional area of the liquid stand pipe, A = cross-sectional area of the specimen, L= length of specimen.

Table 2.2 parameters for permeability test

Parameter	**h_1 (cm)**	**A (cm^2)**	**a(cm^2)**	**L (cm)**
value	74.5	28.27	0.82	4.28

In this study, only one soil sample which taken from the middle portion of the dam was tested (Fig. 2.5). The size of soil sample was shown in Table. 2.2. The results were taken from 3 permeability tests and the average permeability is $5.55x10^{-5}$ cm/s. the permeability shows that the material is could be low in water conductivity which is satisfactory for structure of this type. And it indicated the good quality of construction material and compaction at this fill layer. The classification of this material could be possible range from silt to clay.

a) Test's sample b) Falling head method

Fig. 2.5 Permeability test falling head method. a) Sample. b) Instrumental setting

2.3.2 Sieve analysis

A sieve analysis is a practice or procedure used to assess the particle size distribution of a granular material. The size distribution is often of critical importance to the way, the material performs in use. A sieve analysis can be performed on any type of granular materials including sands, crushed rock, clays, granite, feldspars, coal, soil, a wide range of manufactured powders, grain and seeds, down to a minimum size depending on the exact method (BS 1377–2:1990[6], Head, 1982[5], Geotechdata[7]). Being such a simple technique of particle sizing, it is probably the most common. In this study, the sieve number used in the analysis is between sieve numbers 4 to 200 (Fig. 2.6).

The results show that both the middle and bottom layer consist of a high percentage of fine particle sizes (Fig. 2.7). Furthermore, about 30–40% of the particles in these layers are smaller than 0.1 mm, whereas the upper part is shown to consist mainly of sandy materials. Regarding to the Unified Soil Classification System, the upper portion can be classified as poorly graded soil (SP). Although, the middle and bottom portion could not classified using this criterion due to lacking of data of fine particles, by considering the particle size distribution, they should be range between sand to silt or clay. However, the information on the distribution of small particles was obtained from the study of Tanaka et al. 2012[2]. The results show that both the middle and bottom layer consist of a high percentage of fine particle sizes (Fig. 2.7). It can be seen that for particles that smaller than 5 μm, the middle and bottom soil samples are found to be about 36% and 16% respectively. Also, the clay content (particles smaller than 2 μm) of the middle and bottom portions is about 30% and 10%, respectively. Whilst, the upper part is consist mainly of sandy materials. The boundaries for potentially liquefiable soil (b–b) and boundaries for most liquefiable soil (a–a) are shown in Fig. 2.7 (Japan port and Harbor Association 1999[8], Numata and Mori 2004[9]). Generally, to judge the liquefiability of soil, more than one criterion is required.

For clayey soils, Seed and Idriss 1982[10] stated that these soils could be susceptible to liquefaction only when all of these three conditions are met: 1) the soil that contained less than 15% of 5 μm and finer particles. 2) liquid limit is less than 35 and 3) water content/liquid limit is greater than 0.9. Similarly, Andrews and Martin 2000[11] summarized that soils are susceptible to liquefaction if they contain less than 10% finer than 2 μm and liquid limit less than 32, soils are not susceptible to liquefaction if they contain greater or equal to 10% finer than 2 μm and liquid limit greater or equal to 32, and further study is required for soils that meet one, but not both, of these criteria. According to the Seed and Idriss 1982[10] criteria's first condition, both the middle and bottom parts are not met so the soils are not being vulnerable to liquefaction. Also, by considering Andrews and Martin 2000[11], both the middle and bottom are not susceptible to liquefaction. However, the further study should be conducted in order to obtain more accurate results including liquid limit.

Fig. 2.6 Sieve analysis

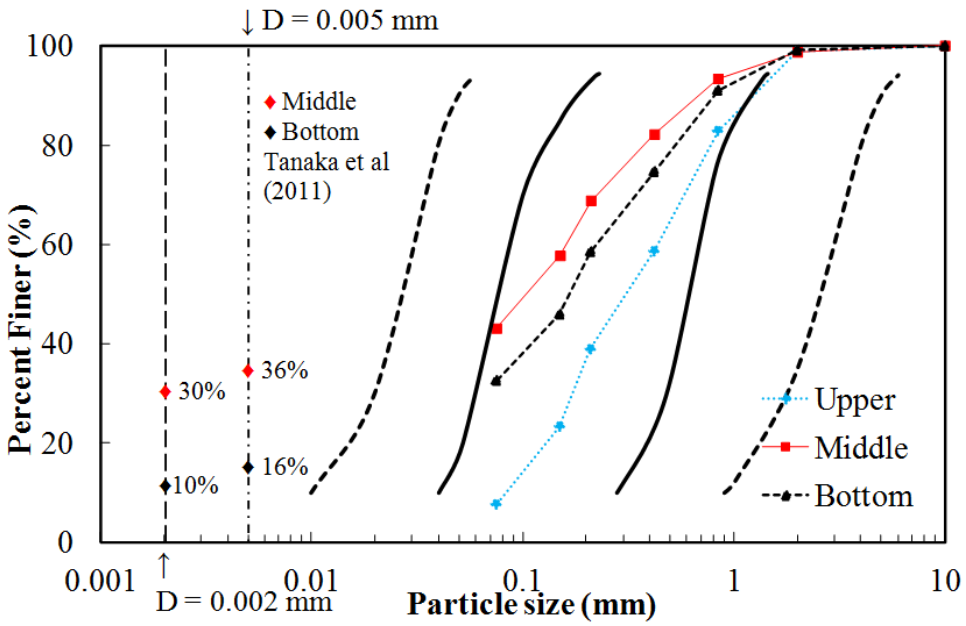

Fig. 2.7 Particle sizes

2.3.3 Triaxial test

Triaxial test is a common laboratory testing method that widely used for obtaining shear strength parameters for a variety of soil types under drained or undrained condition (BS 1377– (1, 6, 7 and 8):1990[12-15], ASTM D4767 [16]). Triaxial test involves subjecting a cylindrical soil sample to confining pressure and controlled increases in axial stresses or axial displacements. The cylindrical soil specimen is usually a 50 mm diameter and 100 mm high. The specimen in vertically enclosed in a thin rubber membrane and placed between two rigid ends inside a pressure chamber. The upper plate can move vertically and apply vertical stresses to the specimen. The axial strain/stress of the sample is controlled through the movement of this vertical axis. Also, the confining pressure is controlled by the water pressure surrounding the sample in the pressure chamber. The volume change of the sample is also controlled by measuring the exact volume of moving water. The type of triaxial test conducted in this study is carried out using Consolidated – Undrained (CU) with 50, 100, 150 and 200 confining pressure.

In case of consolidated test, the test methodology can be seen pictorially as shown in Fig. 2.8. The test was then carried out by a first stage of preparing the sample. The sample was trim to make a 50 mm diameter and 100 high and after that the size and weight of the sample is measured. When complete sizing, the sample was then covered by membrane. Thereafter, the sample is installed to the test chamber together with all instruments set then procedure start by applying confining pressure in the pressure chamber and allowing drainage of the sample. This stage corresponds to the consolidation of the sample. The deviatoric load was then applied through the vertical axis. The deviatoric stress is indeed the difference between the vertical stress and the confining stress. During the deviatoric compression, the drainage valves were closed. Triaxial test data, in general, include

evolution of axial and volumetric strain, deviatoric and isotropic stress, and pore pressure evolution. From the triaxial test results, it is possible to deduce the shear strength parameters, namely friction angle, cohesion, dilatancy angle and the other dependent parameters.

In this study, there are 12 samples being test for this study in order to determine the necessary data used in the latter analysis (Fig. 2.9). The sample numbers 1 to 4 are taken from the dam base. The color is range from dark grey to brown (Figs. 2.9–2.11). The samples taken from the middle portion of the dam are numbered as sample 4 to 8. This material is blown stiff in texture. The last set of sample is taken from the top portion numbered as sample 9 to 10. As can be seen, the samples had shown a light grey in color and sand contained material.

a) Sample preparation

b) Sample preparation

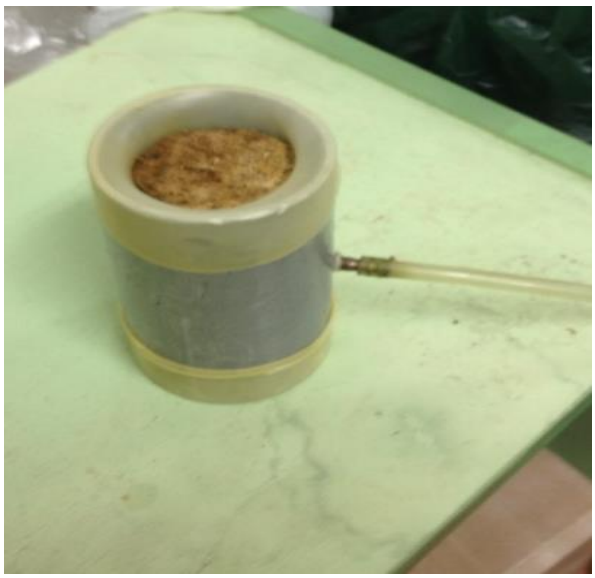

c) Membrane covering

d) Sample installation

Fig. 2.8 Triaxial test methodology

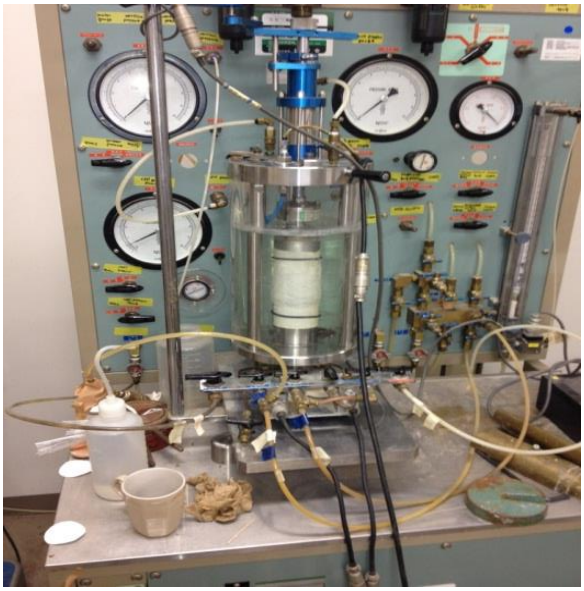

e) Triaxial test f) Failure of the sample

Fig. 2.8 Triaxial test methodology

a) Before b) After

Fig. 2.9 Sample No.1

Fig. 2.10 Sample No.2 (after)

Fig. 2.11 Sample No.3 (after)

a) Before b) After

Fig. 2.12 Sample No.4

a) Before b) After

Fig. 2.13 Sample No.5

a) Before b) After

Fig. 2.14 Sample No.6

a) Before b) After

Fig. 2.15 Sample No.7

a) Before b) After

Fig. 2.16 Sample No.8

a) Before b) After

Fig. 2.17 Sample No.9

a) Before b) After

Fig. 2.18 Sample No.10

Fig. 2.19 Sample No.11

Fig. 20 Sample No.12

The triaxial test results of the shear strength parameters—friction angle, cohesion, and other parameters—are presented in Table 2.3. Also, each parameter used in the analysis can be described as following. The dry and saturated unit weight defined the mass for the element located in dry and saturated areas, respectively. Permeability or hydraulic conductivity described the fluid movement through porous media. In the elastic range, the modulus of elasticity E indicated the relationship between stress and strain within the elastic region, and Poisson's ratio υ provided information on the effect of the load in one direction in relation to the deformation in other directions. The shear strength parameters cohesion c' and friction angle ϕ' were used to form the Mohr–Coulomb's yield surface. Finally, by considering slight compressibility of water, the rate of excess pore pressure was defined as K_w/n, in which K_w is the bulk modulus of water and n is the soil porosity.

The modulus of elasticity used herein was obtained from a triaxial test under 100 kPa of confining pressure, and the initial stiffness was selected as the representative stiffness of the fill material. Therefore, the representative stiffness values of the bottom, middle, and top soil layers are 50 MPa, 30 MPa, and 17.5 MPa, respectively (Figs. 2.21–2.23). To determine the shear strength parameters of the soil samples, the effective normal stress and the ultimate effective shear stress were plotted. The curves show that the cohesion parameter and friction angle of the bottom, middle, and top soil layers are 18.4 kPa and 31°, 7.8 kPa and 32°, and 0.0 kPa and 37°, respectively (Figs. 2.24–2.26).

These values show that the bottom and middle portions of the dam contain cohesive soil, but the upper portion contains loose material. Furthermore, the elasticity modulus values reveal that as the deeper the soil layer is, the higher is its modulus of elasticity. The top portion of the dam was found to have a relatively small modulus of elasticity than that expected of fill materials.

It is should be noted that by taking samples from the remaining of a collapsed dam represents a difficult task and raises many questions on the reliability of the representativeness of the material properties of the retrieved samples. Therefore, the analyzed results obtained using these data and the further used of this study, should be recognized and aware of this limitation.

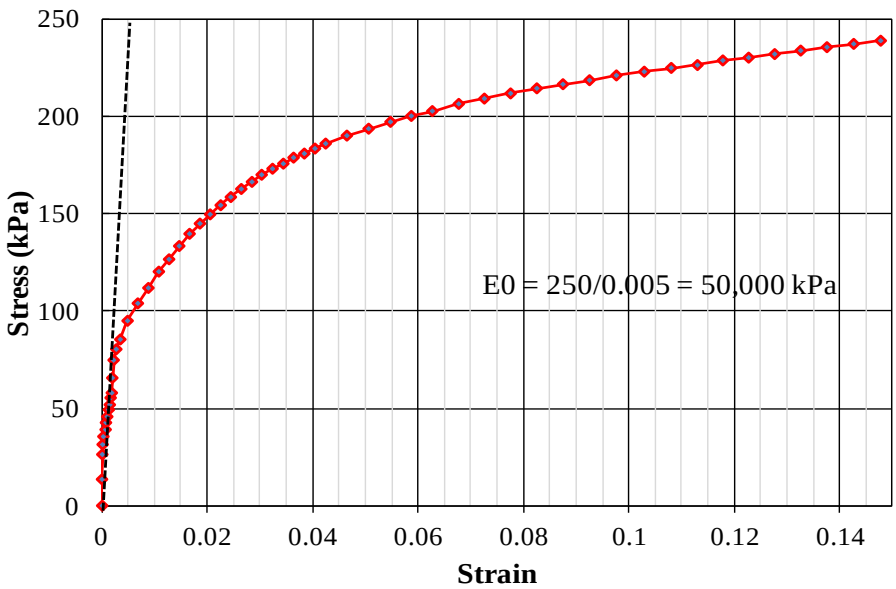

Fig. 2.21 Stress–Strain curve of the bottom soil sample obtained by triaxial test (100kPa)

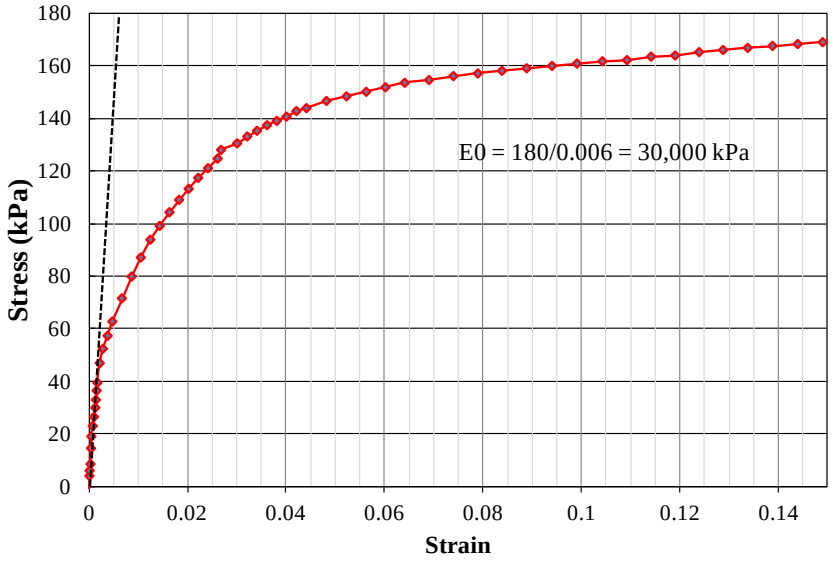

Fig. 2.22 Stress–Strain curve of the middle soil sample obtained by triaxial test (100kPa)

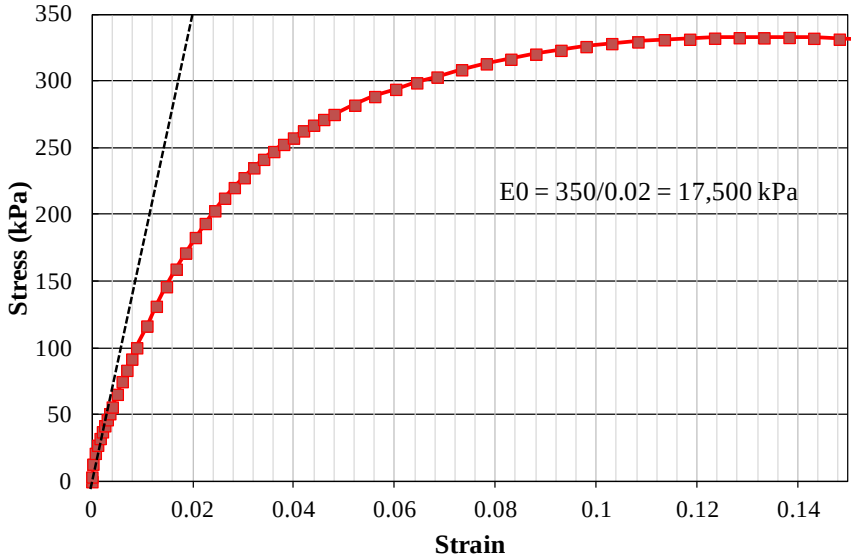

Fig. 2.23 Stress–Strain curve of the top soil sample obtained by triaxial test (100kPa)

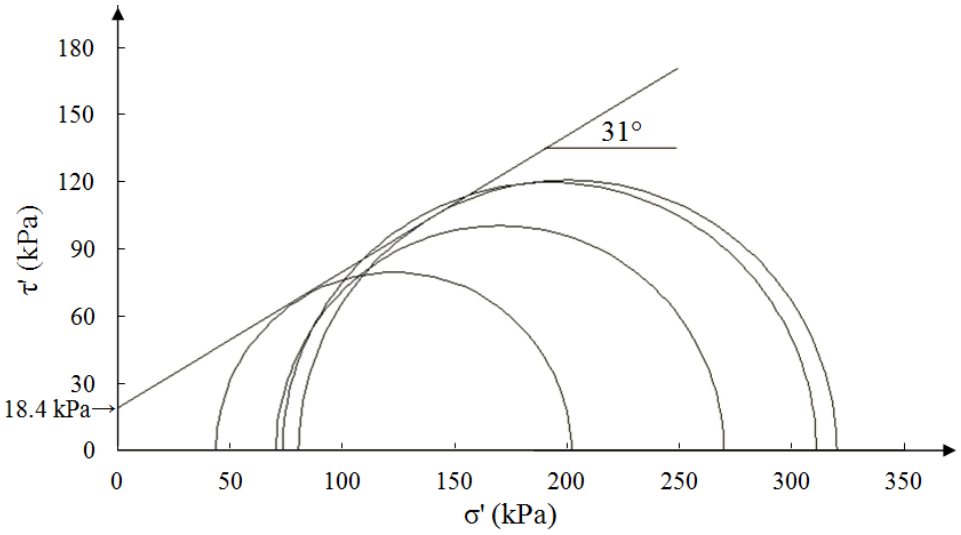

Fig. 2.24 Failure surface of the bottom soil

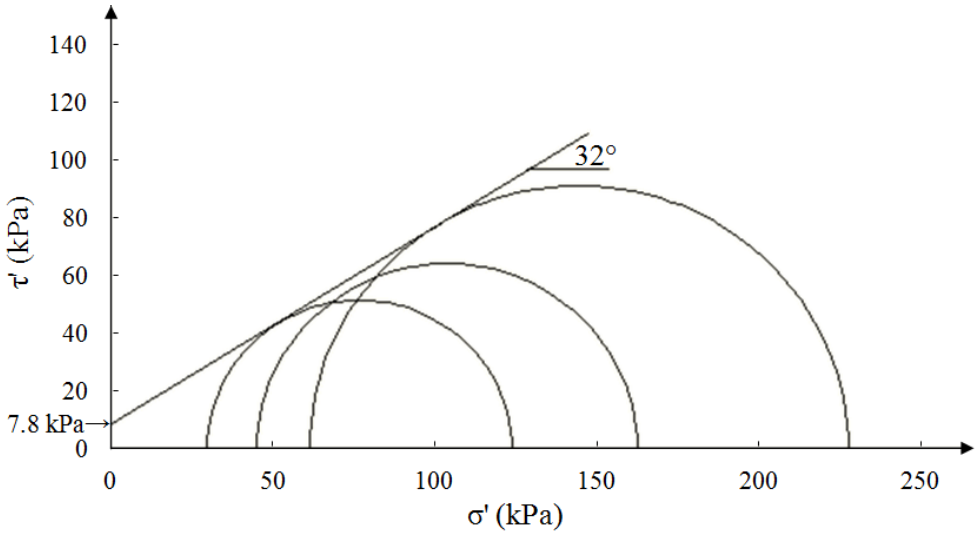

Fig. 2.25 Failure surface of the middle soil

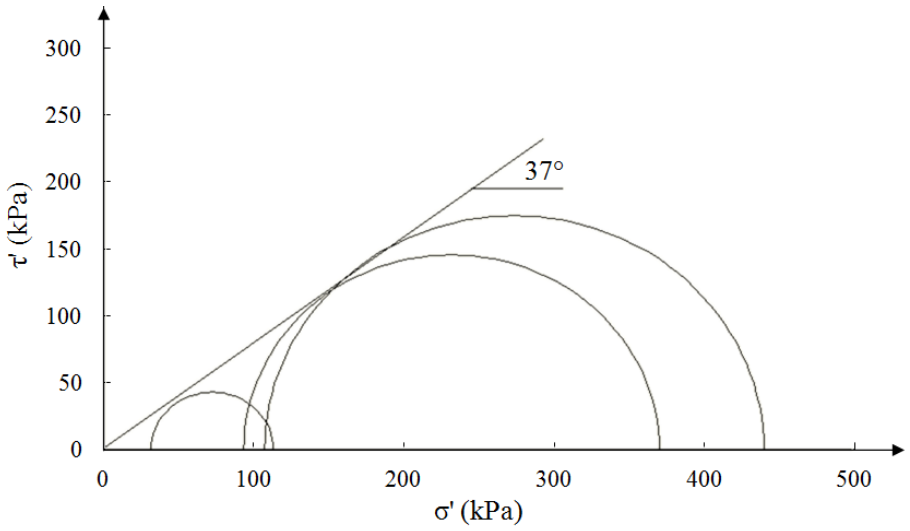

Fig. 2.26 Failure surface of the top soil

Table 2.3 Triaxial test results

Materials	**Layer**	γ_{dry} **(kN/m^3)**	γ_{sat} **(kN/m^3)**	***E*** **(MPa)**	***c'*** **(kPa)**	***ϕ'*** **deg**
Dam body	Bottom	16.0	18.00	50.0	18.4	31
	Middle	14.0	16.00	30.0	7.80	32
	Upper	16.0	18.00	17.5	0.0	37

2.4 Possible failure mechanism of the Fujinuma dam

To identify the cause of Fujinuma dam failure, a site investigation was performed. The facts and other evidences gathered from the site are presented herein, and the important points are discussed. The information is presented in the following order: investigation of the remaining main dam, auxiliary dam, rim, reservoir, and the damaged area downstream. In addition, the facts obtained from this study are compared with results of previous studies. Then, by gathering all information, the important facts and possible failure mechanisms are highlighted. To find out the cause of the dam failure, Prof. Junji Kiyono, Bhuddarak Charatpangoon, and Prof. Mamuro Mimura constituted the team for the first investigation. The second investigation was performed by Bhuddarak Charatpangoon, PyiSoe Thein, Prof. Junji Kiyono, Dr. Suttisak Soralumpand, and Zaw Linkyaw (Fig. 2.27 from left to right).

Fig. 2.27 Investigation team

2.4.1 Investigation of the remaining main dam

Investigation of the main dam is central to this study because it is necessary to gather as much evidence as possible for describing the dam failure mechanism. The investigation consists of a survey of the remaining dam, breach location, and observation of the downstream and upstream slopes, the surrounding area, foundation and the remaining fill material of the dam. The outcomes of this investigation along with their descriptions are shown in Figs. 2.28–47.

Fig. 2.28 Main dam typical section and topographic view

- The dam was breached at its maximum cross section, which is located at the same the location as the river channel. This is expected owing to the huge weight and volume of that portion, which makes it the most vulnerable.

Fig. 2.29 Location of the dam breach at maximum section

- There is no evidence of sand boil at embankment. This is because either liquefaction did not occur or it occurred but the overflow water already washed away the evidence. Notably, the material in the middle and bottom layers seemed to be robust against liquefaction.

- The structural components of the protective face of the dam such as reinforced concrete beams and panels were found on both sides. Concrete beams were found in the pond on the upstream side as well, which can be an evidence of the occurrence of sliding failure on the upstream slope, which might lead to be the trigger of dam failure.

Fig. 2.30 Reinforce concrete beam on the upstream slope

Fig. 2.31 Remains part of slope protection concrete beams on the upstream side

- As per observations of the remainder of the dam, the top embankment layer was almost washed away. However, some part of the top layer can be found on the abutment, and the fill material was found to be sandy (Fig. 2.33). This finding combined with the overflow witnesses' reports could be strong evidences to affirm the occurrence of the overtopping failure.

Fig. 2.32 First investigation trip

Fig. 2.33 Remaining of the Fujinuma main dam from abutment

Fig. 2.34 Samples taken from the middle portion of the dam

- The downstream slope appeared to be damaged severely, as shown in Fig. 2.35. A huge embankment slide can be seen, and most of the dam body on this side was washed away. The downstream slope would have failed first owing to sliding at the breach location. Then, most of the fill material would have been swept away owing to the erosion that induced by the overtopping water. Consequently, the foundation at the downstream side would have been exposed to the surface.

Fig. 2.35 Fujinuma remaining dam

Fig. 2.36 Fill material examining

2.4.2 Investigation of the auxiliary dam

In addition to studying the main dam's failure, we investigated the auxiliary dam as well in order to describe its failure mechanism. In this investigation, we examined the failure location and observed the upstream slope, surrounding area, and foundation. The outcomes are as follows.

- The auxiliary dam experienced upstream sliding failure. Most all of the embankment body was dragged down to the pond. The sliding of the auxiliary dam's upstream slope is believed to be triggered by rapid drawdown resulting from rapid reservoir depletion following failure of the main dam

Fig. 2.37 Upstream failure of the auxiliary dam

Fig. 2.38 Rapid drawdown sliding of the auxiliary dam

2.4.3 Investigation of the reservoir's rim and reservoir

This study also extends our interests on the failure of the rim as well as the reservoir condition after the earthquake as components of dam structure. In some cases, the main dam remains safe but cannot be operated owing to the failure of other components, which makes the study of such components important. The investigation was conducted around the rim in the South area of the dam and in the reservoir at the same location. The outcomes are as follows.

- The reservoir rims failed owing to the upstream sliding failure triggered by rapid drawdown.
- A visual investigation of reservoir showed the existence of the sandy soil around the rim of the pond. However, it was difficult to determine whether this sand was a result of liquefaction or weathering of the rock within the rim.

Fig. 2.39 Sliding of the reservoir rim due to the rapid drawdown

Fig. 2.40 Investigating the cause of the dam failure

Fig. 2.41 Failure of the reservoir’s rim

Fig. 2.42 Fujinuma reservoir after its failure

2.4.4 Damaged area

To understand the harmful force resulting from the dam failure, we investigated the affected area surrounding the dam. The investigation involved reconnaissance starting from the breach location of the main dam, go further to the the downstream side along the flow direction of the river channel and ending at the village affected by the flood due to dam failure. The observations might provide information on how to design a better evacuation plan for dealing with future dam failures or alternative mitigation techniques that could reduce the loss of life and property. The outcomes are as follows.

- The failure caused a flood that washed away 19 houses and damaged others, disabled a bridge, and blocked roads with debris. Seven bodies were discovered after searches began at dawn, and one person was declared missing.
- The river channel was covered by debris from the dam failure
- The river downstream was blocked by debris
- The huge overflow of water damaged nearby structures

Fig. 2.43 River channel coverage by debris from the dam failure

Fig. 2.44 River downstream had been brock by the debris

Fig. 2.45 Huge amount overflows water causing damage to the structure nearby

Fig. 2.46 Guard rail was bend after subjected to the inundate flow

Fig. 2.47 Guard rail was bend after subjected to the inundate flow

2.4.5 Possible failures phenomenon

Regards to the site investigations and comments made by Dr. Sutthisak and team, these assumptions are possible to described failures phenomenon as follow.

- As it has been reported by many authors and our observation, the fill material of the upper embankment consist of sandy material and not well constructed says it was bad in quality. By these reason, due to the strong and long duration of excitation the fill material then continuously loss its strength. Thereafter the sliding occurred at the upper layer on the upstream slope or on both sides. However, the evidence of sliding at downstream side at this level could not be found due to the dam breach that washed away most evidence on downstream side. Thereafter, the crest was settled in sliding shape and erosion of water in pond become severe effect and causing the total settle to this fill level. As it begun, the dam is starting to breach.
- The settlement is higher in upper layer due to the sand compaction by strong shacking, until its reach the reservoir level and follow by overtopping failure.
- Of course, as it is appeared, the dam consists of the concrete protection on upstream side. These concrete slabs and their components are huge in weight, due to their weight at the time of earthquake, the interaction between these contacts play also an important role. This weight might cause great inertia force acting in both direction and might drag this weak upper portion to the pond.
- Gathering the weak upper portion and also strong shaking with long duration might cause a commutative permanent displacement. Expanded on the side and settle in the middle then some sliding occurred due to its instability then at some level the couple failure phenomenon then take place like sliding–overtopping failure.

2.5 Ground motion records

In order to gain insight the failure of the dam, it is important to investigate the ground motion records near the dam's site. According to the 2011 Tohoku earthquake, number of ground motion records at the station which located near the dam site are provided by K–Net and KiK–net that operated by NIED [17]. In this study, there are 5 earthquake records were selected to gain a deep understanding of the earthquake characteristic around the site. The selected records are the motions from the KiK–net's station FKSH08, FKSH09, FKSH11 and from K–Net's station FKS017 and FKS018. The location of each station was shown in Fig. 2.48 along with the dam location. The closet station is the FKSH08 which is about 2 km from the site.

The motion records of each station were shown in Figs. 2.49–2.63(a). Each station contains three components that is the record of the wave in East–West direction (E–W), the North–South direction (N–S) and the vertical direction (U–D), respectively. It can be seen that most of the wave forms are in similar trend except the record obtained from station FKSH08, which is a bit far from the earthquake epicenter, the amplitude is lower than the

other cases. The records show that the earthquake excitation contains a high amplitude and long duration.

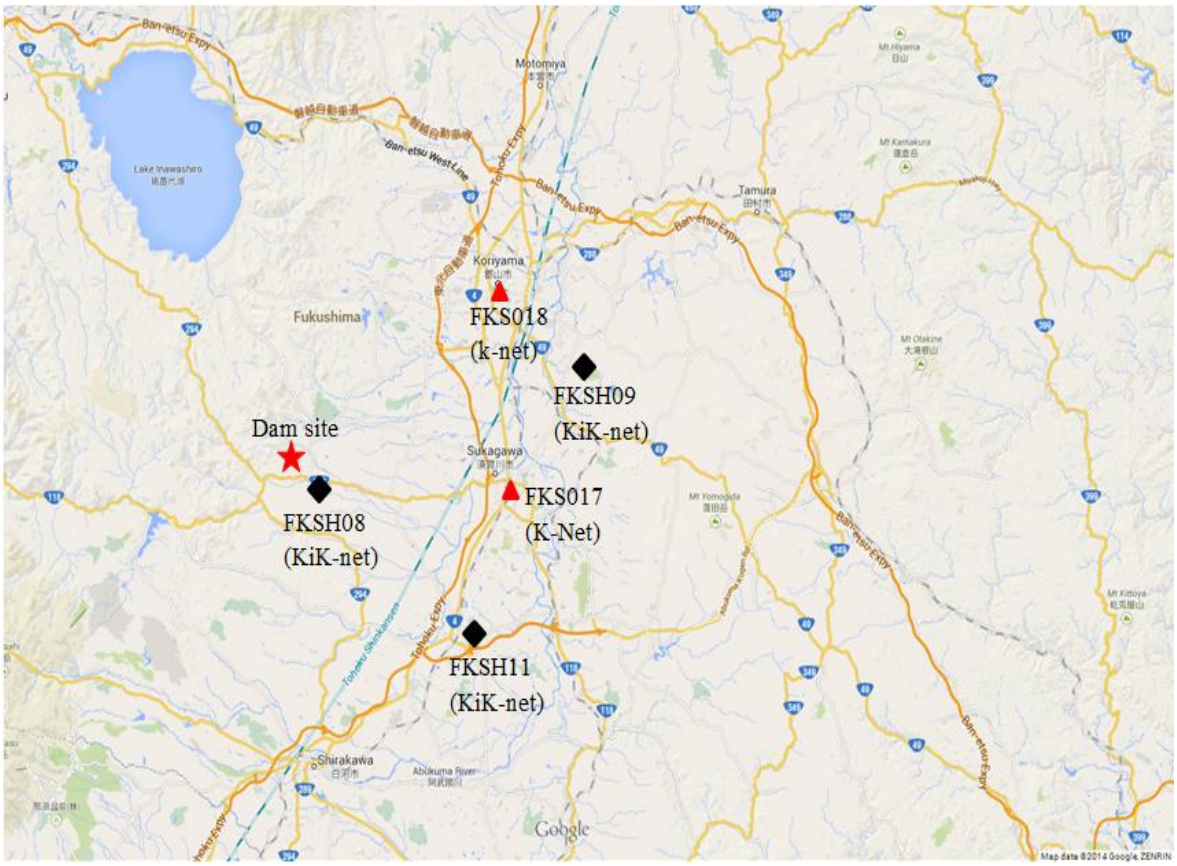

Fig. 2.48 (a) Location of the earthquake record stations and Fujinuma dam (©2014 Google. Map data. © Google. ZENRIN)

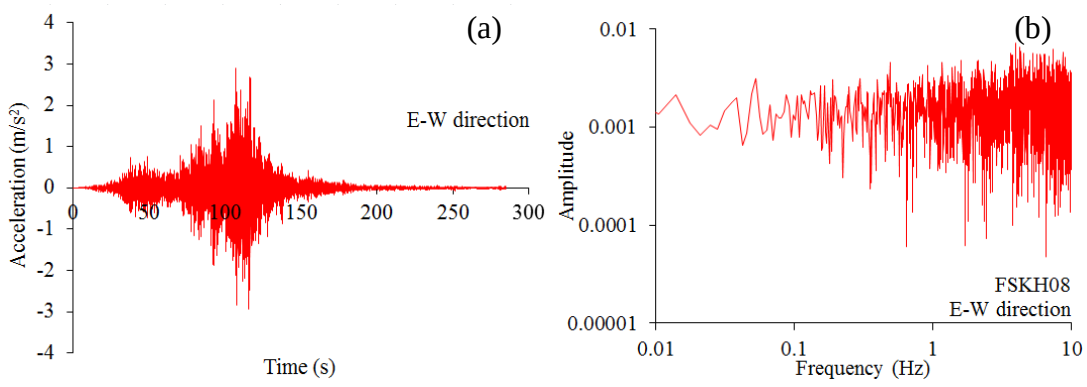

Fig. 2.49 (a) Earthquake record (b) Fourier spectrum (FKSH08 E–W direction)

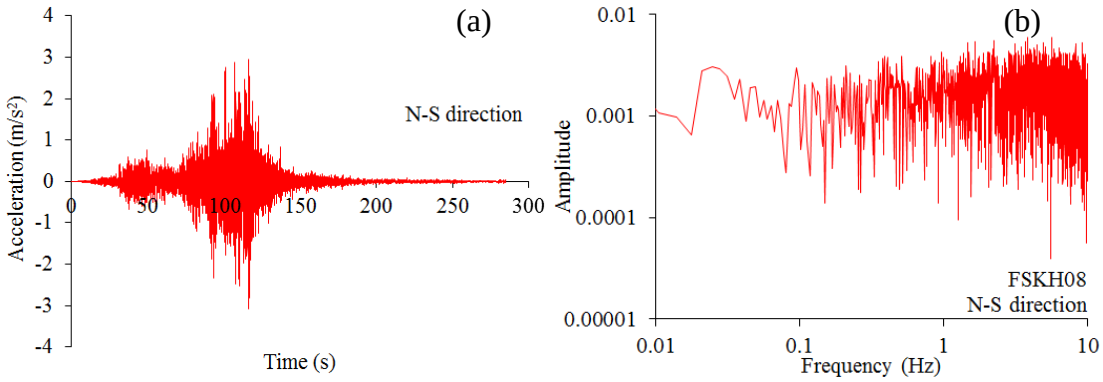

Fig. 2.50 (a) Earthquake record (b) Fourier spectrum (FKSH08 N–S direction)

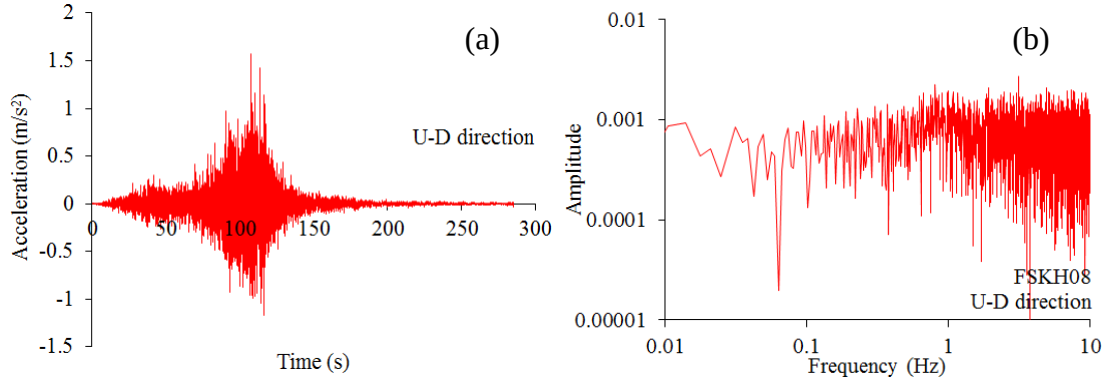

Fig. 2.51 (a) Earthquake record (b) Fourier spectrum (FKSH08 U–D direction)

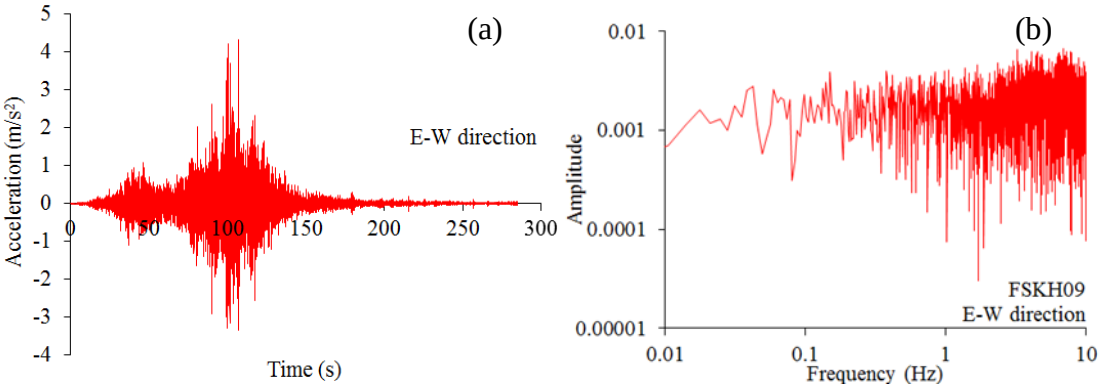

Fig. 2.52 (a) Earthquake record (b) Fourier spectrum (FKSH09 E–W direction)

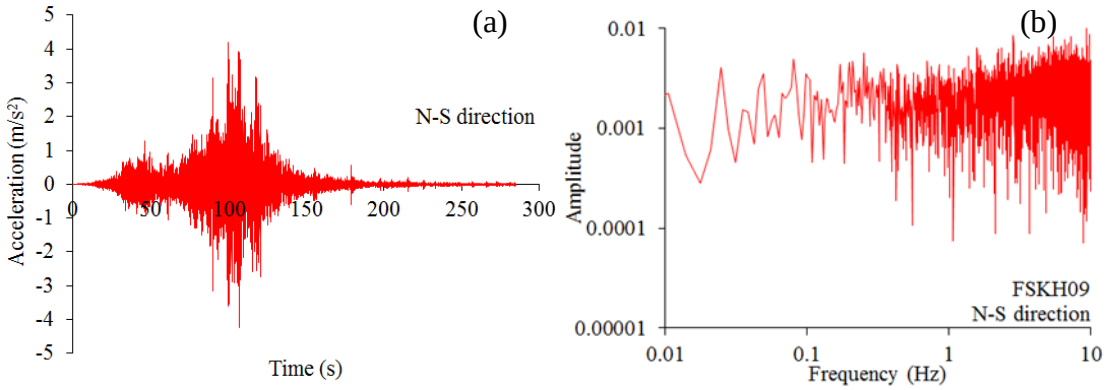

Fig. 2.53 (a) Earthquake record (b) Fourier spectrum (FKSH09 N–S direction)

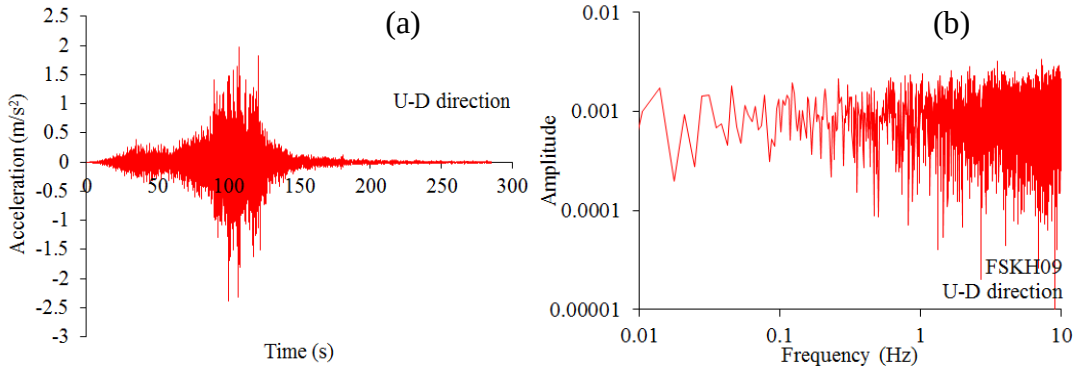

Fig. 2.54 (a) Earthquake record (b) Fourier spectrum (FKSH08 U–D direction)

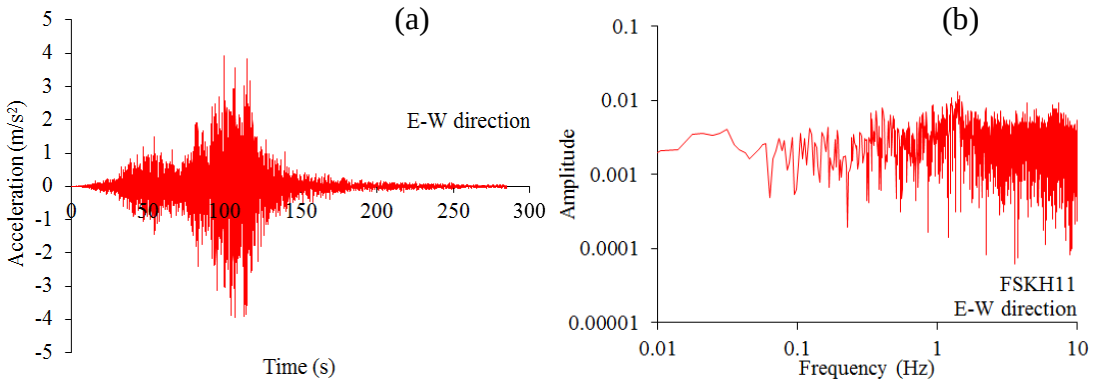

Fig. 2.55 (a) Earthquake record (b) Fourier spectrum (FKSH11 E–W direction)

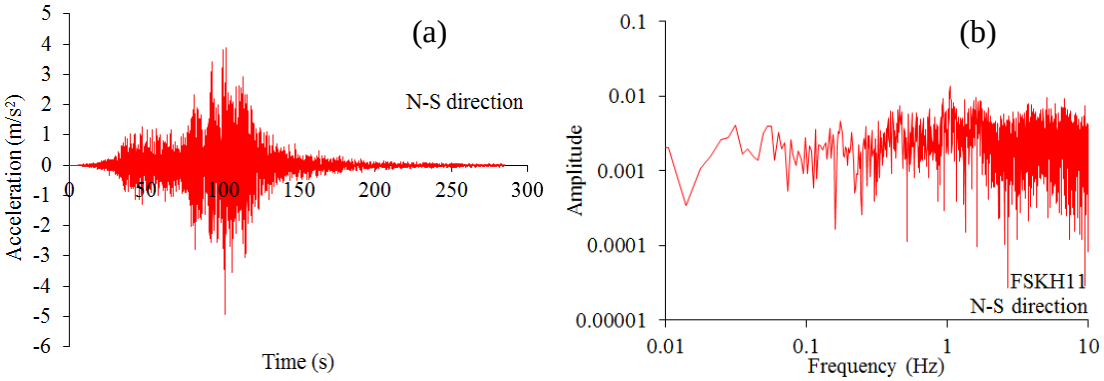

Fig. 2.56 (a) Earthquake record (b) Fourier spectrum (FKSH11 N–S direction)

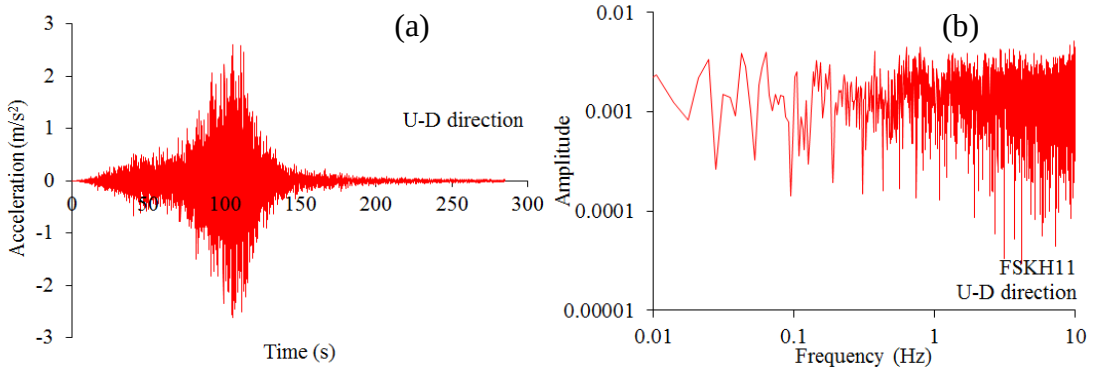

Fig. 2.57 (a) Earthquake record (b) Fourier spectrum (FKSH11 U–D direction)

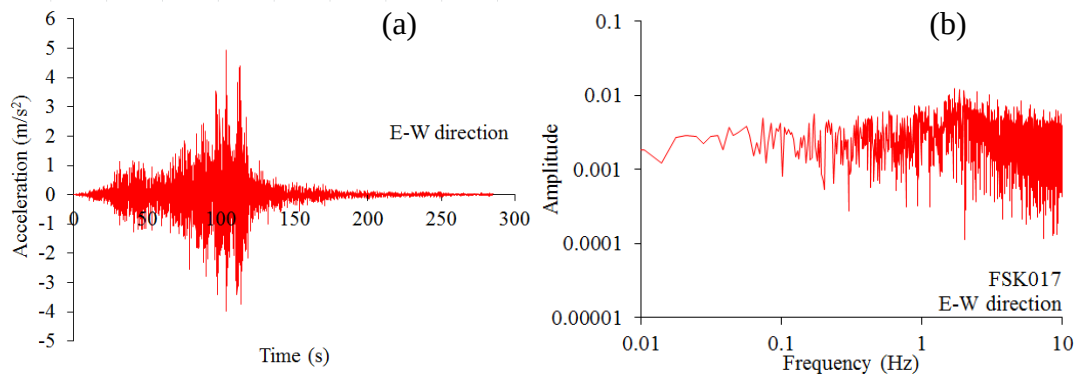

Fig. 2.58 (a) Earthquake record (b) Fourier spectrum (FKS017 E–W direction)

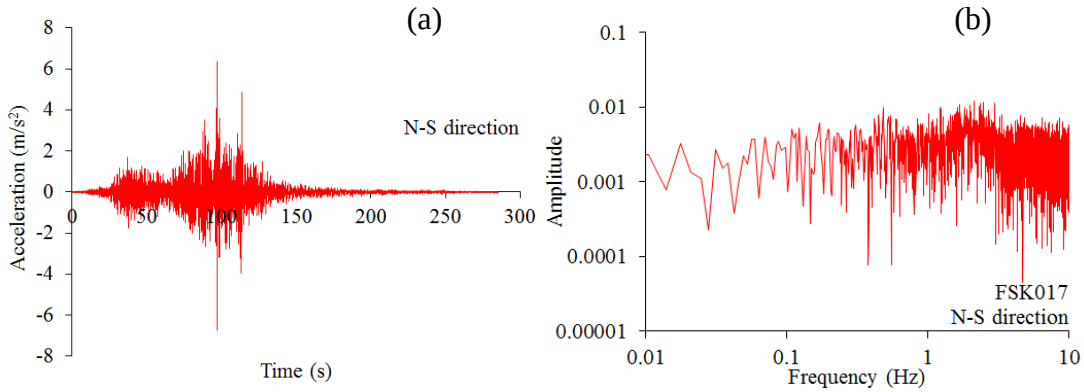

Fig. 2.59 (a) Earthquake record (b) Fourier spectrum (FKS017 N–S direction)

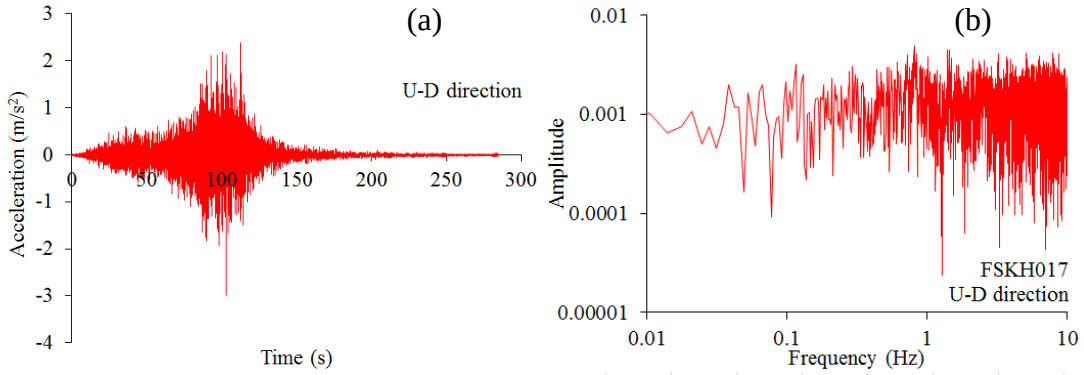

Fig. 2.60 (a) Earthquake record (b) Fourier spectrum (FKS017 U–D direction)

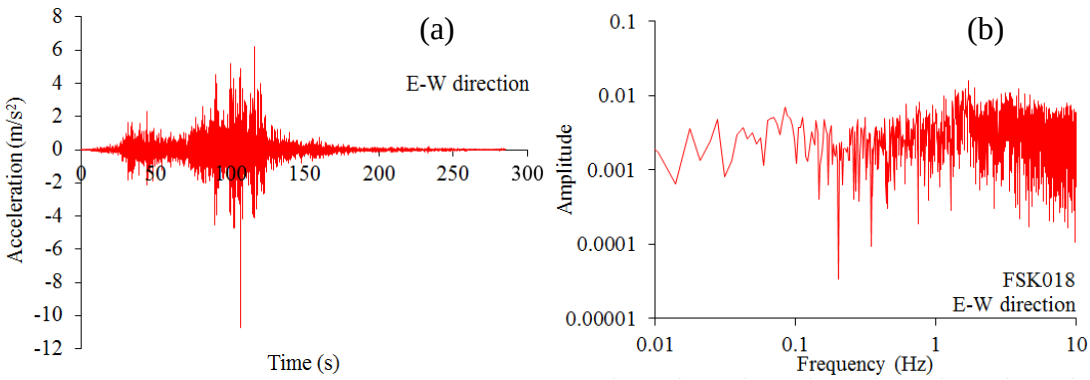

Fig. 2.61 (a) Earthquake record (b) Fourier spectrum (FKS018 E–W direction)

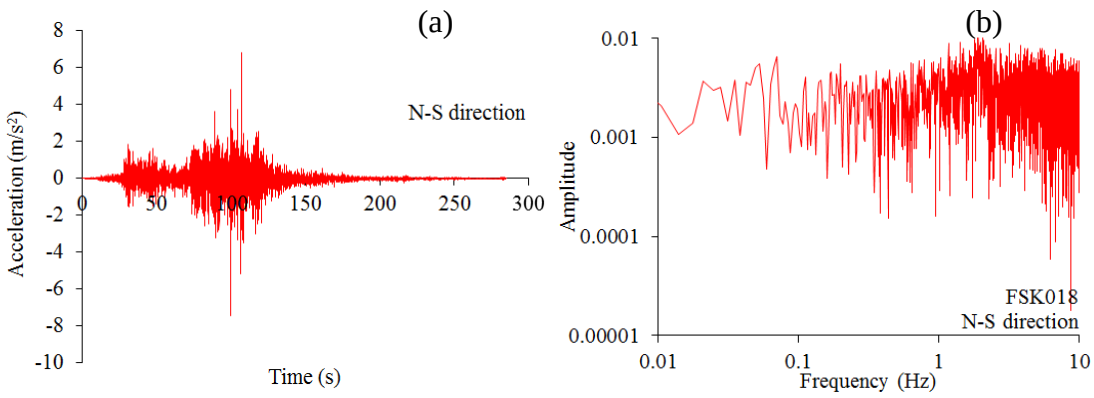

Fig. 2.62 (a) Earthquake record (b) Fourier spectrum (FKS018 N–S direction)

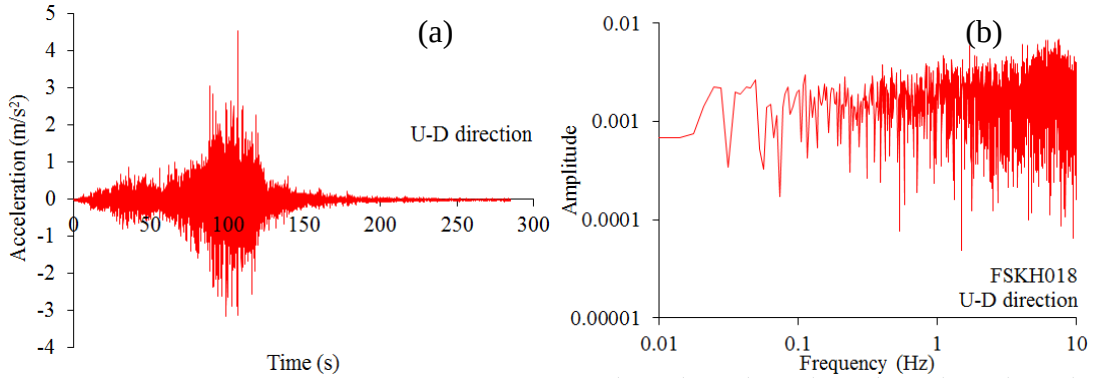

Fig. 2.63 (a) Earthquake record (b) Fourier spectrum (FKS018 U–D direction)

Fig. 2.49–2.63(b) show the Fourier spectrum of all earthquake records. It can be seen that in the horizontal direction which is included the E–W and N–S component, the predominant frequency is in a range between 0.5–3.0 Hz. For the vertical component, it is difficult to indicate the peak amplitude and its corresponding frequency. These Fourier spectrum indicated that the earthquake could characterized in a wideband range that might produce a great response to the structure due to the resonant of the higher mode of vibration.

2.6 Conclusions

From the site investigation, it appears that the dam was breached at the maximum cross section owing to the huge volume of that portion. As per the visual investigation, the remaining of the failed dam, reservoir area, reservoir's rim and also their vicinities, were examined however there is no obvious evidence such as sand boils could be found to confirm the occurrence of liquefaction. Furthermore, in the middle and bottom portions, the material itself does not seem prone to liquefaction.

For laboratory experiments results, it can be summarized that both the middle and bottom layer consist of a high percentage of fine particle sizes whereas the upper part is shown to

consist mainly of sandy materials. And the information on the distribution of small particles was obtained from the study of Tanaka et al. 2012[2]. It can be seen that the clay content (particles smaller than 2 μm) of the middle and bottom portions is about 30% and 10%, respectively. Andrews and Martin 2000[10] summarized that soils are susceptible to liquefaction if they contain less than 10% finer than 2 μm and liquid limit less than 32, soils are not susceptible to liquefaction if they contain greater or equal to 10% finer than 2 μm and liquid limit greater or equal to 32. Accordingly, both the middle and bottom are not susceptible to liquefaction. However, the further study should be conducted in order to obtain more accurate results including liquid limit.

The triaxial test results showed that the parameters of cohesion and friction angle of the bottom and middle portions of the dam are classed as cohesive soil, but that the upper portion is classed as loose material. Furthermore, the modulus of elasticity reveals that at the deeper soil layer, the higher value of its modulus is obtained. The top portion of the dam is shown to have a relatively smaller modulus of elasticity than normally expected for fill materials.

Regards to the visual investigation and laboratory experiments, the failure mechanism might be described as follows.

- For the first scenario, owing to a relatively small elastic modulus of material used to construct the upper portion of the dam and the long duration of strong shaking, the fill material lost its strength. Consequently, sliding occurred in the top layer on the upstream slope or on both sides. Thereafter, the crest was displaced in a sliding pattern. The settlement is deemed to have continued in the same pattern until it reached the reservoir level, following which overtopping failure occurred.
- For another possible scenario, owing to the weak upper portion and the long duration of strong shaking, cumulative permanent displacement could have expanded both sides and caused settlement in the middle, following which sliding occurred owing to instability. Of course, at some certain level, a coupled–failure phenomenon occurred, such as an overtopping–sliding failure.

It is should be noted that by taking samples from the remaining of a collapsed dam represents a difficult task and raises many questions on the reliability of the representativeness of the material properties of the retrieved samples. Therefore, the analyzed results obtained using these data and the further used of this study, should be recognized and aware of this limitation.

Furthermore, it is important to investigate the ground motion records near the dam's site because these records might provide invaluable data in the investigation of the dam's failure. It can be seen that most of the wave forms in are in similar trend except the record of the station which is a bit far from the earthquake epicenter, the amplitude is lower than the other cases. The records show that the earthquake excitation contains a high magnitude and long shaking duration. Also, the Fourier spectrums were presented in this study. These Fourier spectrum indicated that the earthquake could characterized in a wideband range that might produce a great response to the structure.

REFERENCES

[1] K. Ono, S. Kazama, S. Kawagoe, Y. Yokoo, L. Gunawardhana, Possible earthen dam failure mechanisms of Fujinuma reservoir due to the Great East Japan Earthquake of 2011, Hydrological Research Letters 5 (2011) 69–72.

[2] T. Tanaka, F. Tatsuoka, Y. Mohri, Earthquake Induced failure of Fujinuma Dam, International symposium on dams for a changing world, ICOLD, Kyoto, Japan, 6 (2012) 47–52.

[3] Wikipedia. [Online]. Available: /http://en.wikipedia.org/wiki/Fujinuma_dam. [accessed 07/01/12]

[4] BS 1377–5:1990 Methods of test for soils for civil engineering purposes Compressibility, permeability and durability tests

[5] BS 1377–2:1990 Methods of test for soils for civil engineering purposes Classification tests

[6] K. H. Head, Manual of soil laboratory testing, Vol 2, Pentech Press, ISBN 0–7273–1305–3, 1982

[7] Geotechdata. [Online]. Available: http://www.geotechdata.info [accessed 07/01/12]

[8] Japan port and Harbor Association, Technical standards for port and harbor facilities in Japan, (1999) 281–288.

[9] A. Numata, S. Mori, Limits in the gradation curves of liquefiable soils, proceeding of the 13th world conference on earthquake engineering, Canada, (2004) Paper No. 11.

[10] H. B. Seed, I. M. Idriss, Ground motions and soil liquefaction during earthquakes, Earthquake Engineering Research Institute, Berkeley, California, 1982.

[11] D. C. A. Andrews, G. R. Martin, Criteria for liquefaction of silty soils, Proceedings of the 12th World Conference on Earthquake Engineering, New Zealand, (2000).

[12] BS 1377–1:1990, Methods of test for soils for civil engineering purposes General requirements and sample preparation, 1990.

[13] BS 1377–6:1990, Methods of test for soils for civil engineering purposes Consolidation and permeability tests in hydraulic cells and with pore pressure measurement, 1990.

[14] BS 1377–7:1990, Methods of test for soils for civil engineering purposes Shear strength tests (total stress), 1990.

[15] BS 1377–8:1990, Methods of test for soils for civil engineering purposes Shear strength tests (effective stress), 1990.

[16] ASTM D4767 – 04, Standard Test Method for Consolidated Undrained Triaxial Compression Test for Cohesive Soils, ASTM international, 04.09(2005).

[17] National Research Institute for Earth Science and Disaster Prevention (NIED). [Online]. Available: /http://www.kyoshin.bosai.go.jp. [accessed 06.01.12]

CHAPTER III

MICROTREMOR OBSERVATION AT DAM FAILURE SITE

3.1 Introduction

This chapter provides information on the field measurements conducted at the dam site as part of this study. Along with visual investigation, a microtremor test, known as ambient vibration test, was conducted at the dam site to determine the predominant period at the site and the dynamic characteristic of the remainder of the dam. The observation team accessed the site twice for conducting the test. The first investigation was carried out on November 11, 2011, and the second one was carried out on December 12, 2012. This chapter describes the estimation method, observed location, results, and discussion of the results.

A microtremor is a low–amplitude ambient vibration of the ground that can possibly be caused by human activity, wind, or ground movement itself. A microtremor record generally consists of movement information in three dimensions. There are two microtremor–based observation applications: single observation and array observation. Single observation provides information only about site characteristics such as predominant period, whereas array observation can be used for determining the substructure profile. In this study, to acquire the natural frequency and site predominant period, we performed only the single observation. As mentioned, ambient vibration was recorded twice during this study. In the first investigative trip, eight single–site surveys were conducted. In the second trip, three single–site observations were made. The methodology, observation points, results, and discussion of these tests are described in this chapter. Finally, a modal analysis of the remaining dam is presented, and results of the analysis and microtremor observation are compared and discussed.

3.2 Methodology

The procedure of microtremor observation in this study is described through the site and location of the observation points, instrument and measurement as stated below.

3.2.1 Site description

The Fujinuma Dam was an earth–fill dam in Sukagawa City, Fukushima Prefecture, Japan (37°18′07″N 140°11′41″E). It was established on the Ebana River, a tributary of the Abukuma River, 16 km west of the city office of Sukagawa City, as shown in Fig. 3.1(Wikipedia[1]). The structure consisted of two dams: main dam and auxiliary dam. The dam failed on March 11, 2011, after the 2011 Tohoku earthquake. As mentioned, we conducted the microtremor investigation two times. The first microtremor observation was made for both the main dam and the auxiliary dam by conducting eight single–site surveys on November 11, 2011, whereas the latter observations, conducted on December 12, 2012,

which focused only on the main dam with three observation points. The observation points for both the main dam and the auxiliary dam in the first field trip are shown in Fig. 3.2. The observation points in the second trip are shown in Fig. 3.3. The observation points were selected by considering the dam base location and the tip of the remainder of the dam to estimate the resonant period that corresponding to the amplification peak.

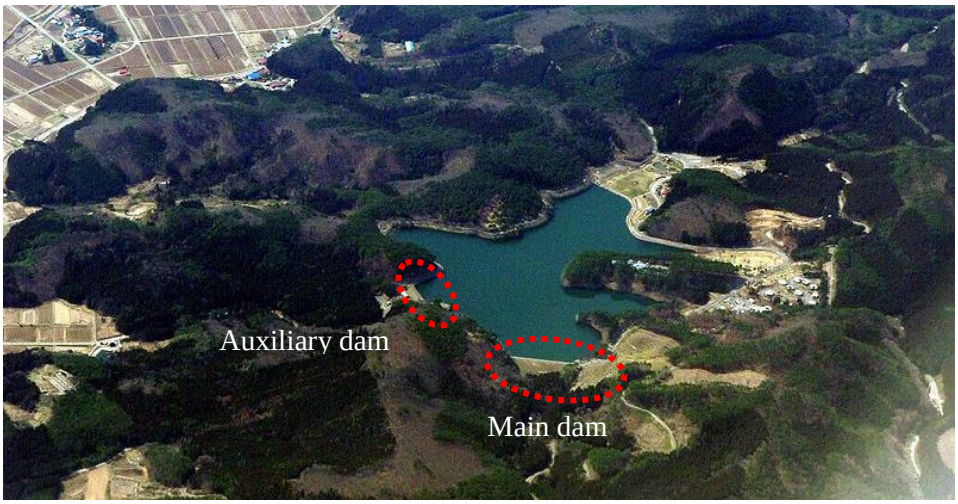

Fig. 3.1 Fujinuma dam and its auxiliary dam

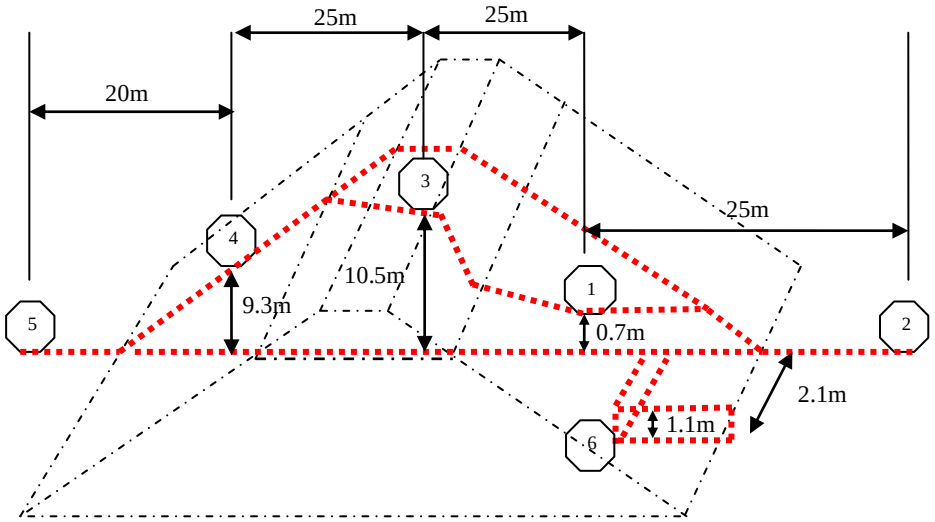

a) Observation points at the main dam

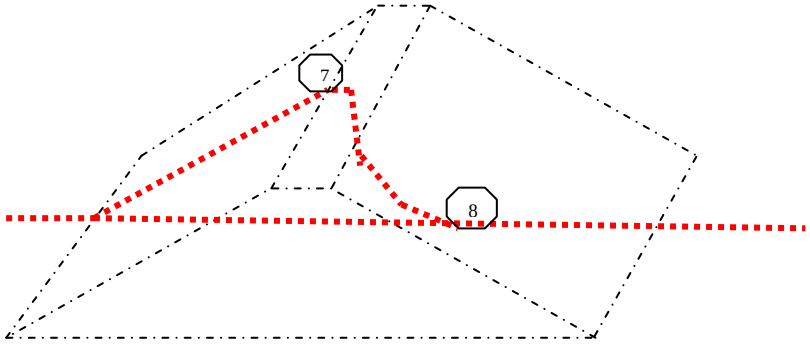

b) Observation points at the auxiliary dam

Fig. 3.2 Observation points 1st trip. a) Main dam. b) Auxiliary dam

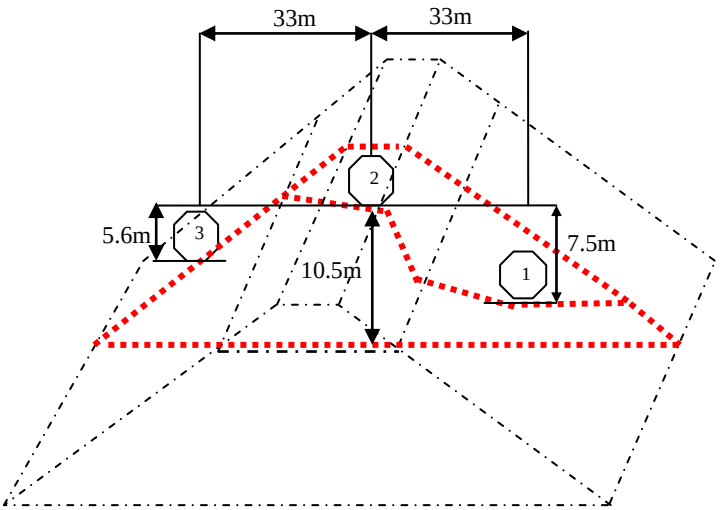

Fig. 3.3 Observation points 2nd trip

3.2.2 Microtremor measurement

The microtremor measurement has been conducted for estimating the site response since it was introduced in the 1950s. It becomes a very useful tool for estimating the predominant periods of subsurface. Generally, to estimate predominant period of ground, there are several techniques can be applied. The simplest one is by using its Fourier amplitude, spectral ratios relative to reference site. After the pioneering work by Kannai and Tanaka (Tokimatsu 1997[2]) many researchers have studied on the applicability and reliability of the microtremor method. However, this method often represents the characteristics of the source rather than the transfer function of a site.

In 1989, Nakamura (Nakamura 1989[3], Nakamura 2000[4], Nakamura 2008[5]) modified microtremor method by introducing the H/V method. In this technique, it was shown that the source effect can be minimized by normalizing the horizontal spectral amplitude with the vertical spectral amplitude. This study indicated that the horizontal to vertical (H/V) spectral ratio of microtremors at a site roughly equals the S–wave transfer function between the ground surface and bedrock at a site. Therefore, the H/V peak frequency at maximum H/V ratio corresponds to the natural frequency of the site and amplification factor, respectively. Due to its cost efficiently and simplicity, this method has been widely used for microtremor observation although it lacks a clear theoretical background.

Equipment

The equipment used in this study is the portable accelerometer data logger GPL–6A3P (Mitutoyo[6]). It is a compact vibration waveform data logger with a built–in vibration detector. The device is best for recording the low frequency range waveform (0.07 Hz to 100Hz). A high resolution A/D converter 24–bit A/D data logger has been used in order to provide a great accuracy. With its portability, it is easy to access any site and easy to conducted the test. Tests of total 8 observation points of the first trip and 3 observation points of the latter were conducted. For each location, the single microtremor observation time was simultaneously measured for the two horizontal (NS–EW) and the vertical components for 10 minutes with a 100 Hz sampling frequency (Rusnardi et al. 2011[7]). On both measurements, the weather was generally cold and sunny with light winds.

Predominant period estimation

In this study, the software, BIDO (I. Cho and T. Tada 2010[8]) was used for data acquisition and preliminary analysis, such as producing plots of time–histories, Fourier spectra, and H/V ratios. A free analysis tool, BIDO was developed for the calculation of Fourier spectra, identification of predominant periods and spectral amplitudes, and for the calculation of H/V ratios. The results were presented in term of Fourier spectral, H/V ratio and the amplification of crest to base ratio.

Fig. 3.4 Distance measurement

Fig. 3.5 Single point microtremor observation

3.3 1st Microtremor investigation

The first set of microtremor observations was recorded during day time on November 11, 2011. These observations aimed to find the predominant period at the site and amplification from the top of remainder of the dam to the base for estimating the natural frequency of both the main dam and the auxiliary dam. Eight sites were selected for observation, of which six were on the main dam and two on the auxiliary dam

3.3.1 Microtremor test records

The microtremor records obtained from each site consisted of one vertical and two horizontal directions. The records for each site are shown in Figs. 3.6–3.15.

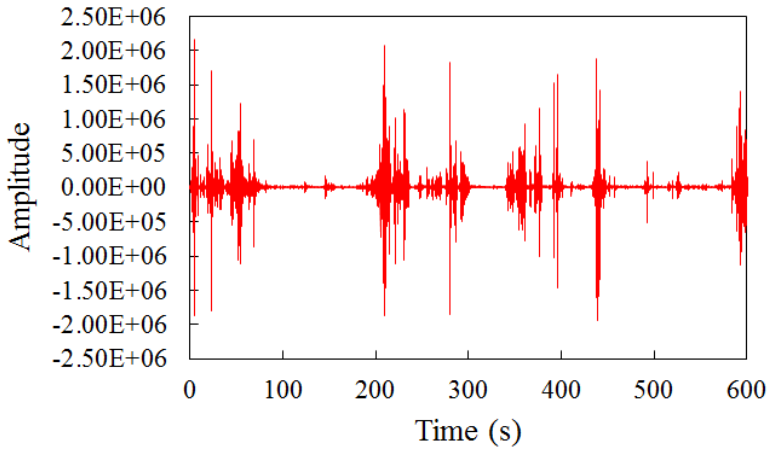

Fig. 3.6 Vertical direction (Sta. 1)

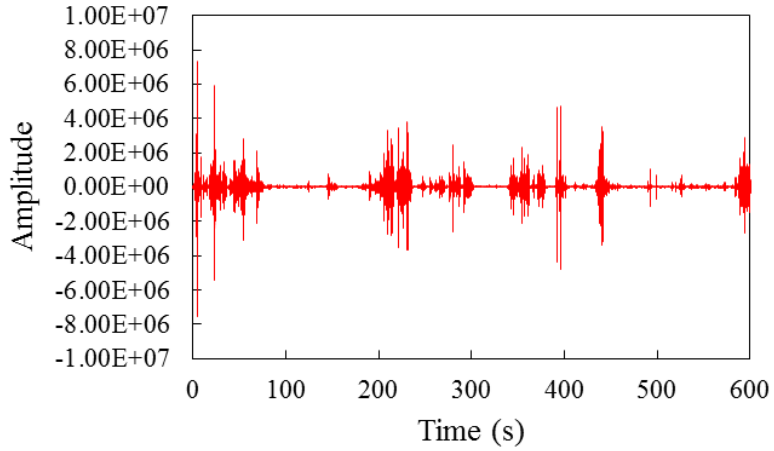

Fig. 3.7 N–S direction (Sta. 1)

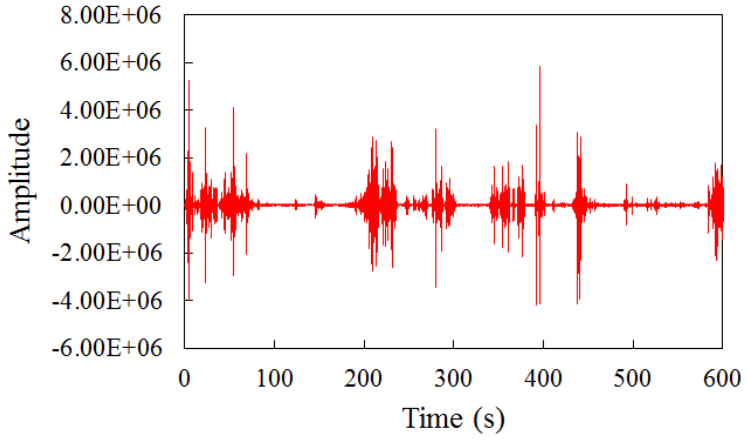

Fig. 3.8 E–W direction (Sta. 1)

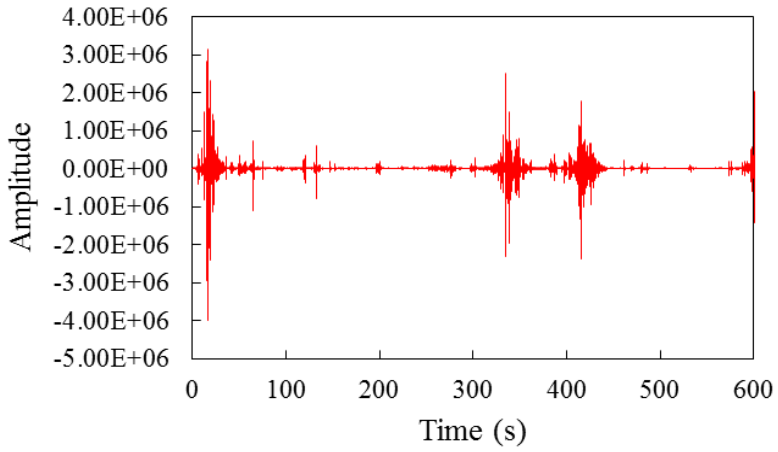

Fig. 3.9 Vertical direction (Sta. 2)

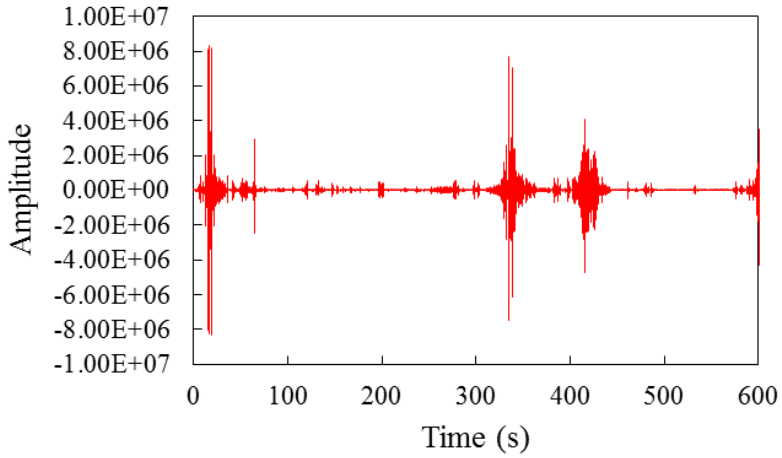

Fig. 3.10 N–S direction (Sta. 2)

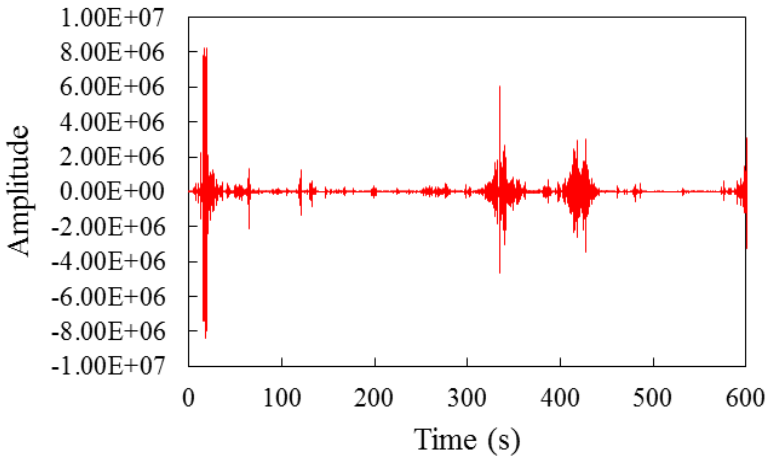

Fig. 3.11 E–W direction (Sta. 2)

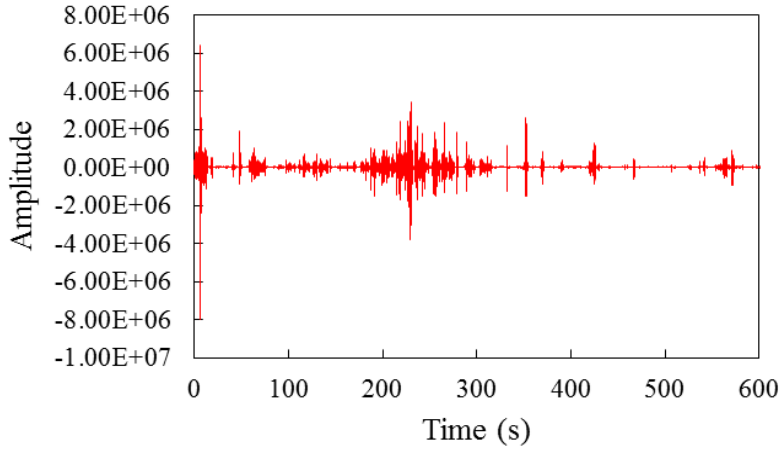

Fig. 3.12 Vertical direction (Sta. 3)

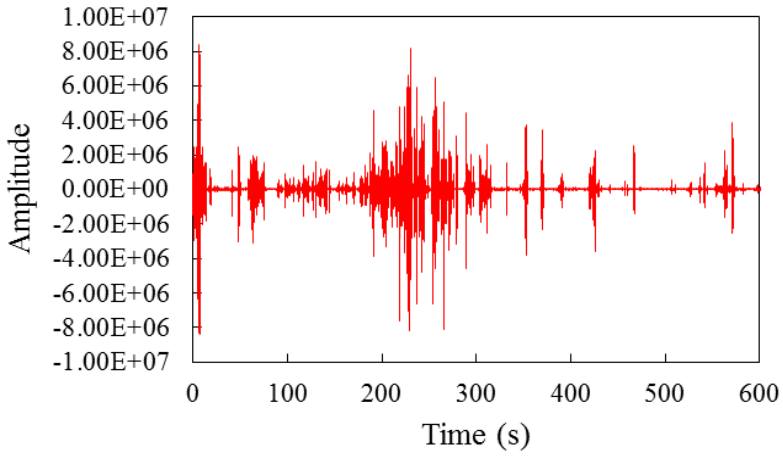

Fig. 3.13 N–S direction (Sta. 3)

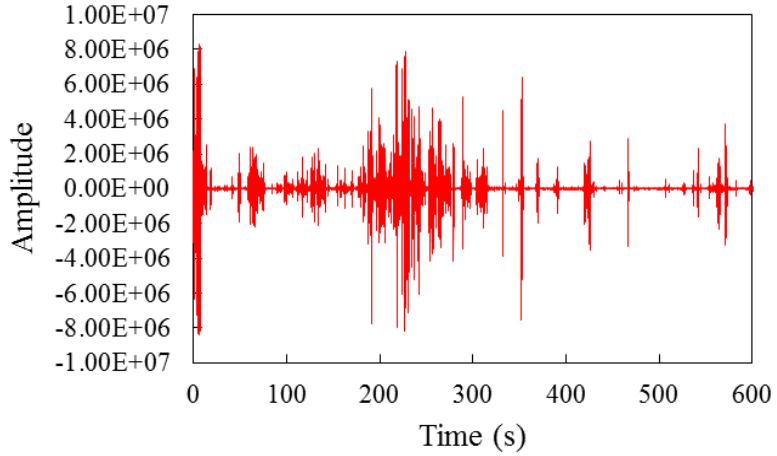

Fig. 3.14 E–W direction (Sta. 3)

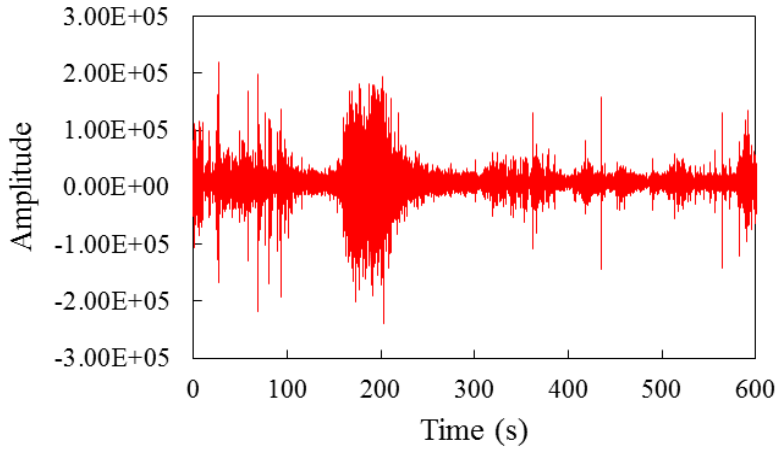

Fig. 3.15 Vertical direction (Sta. 4)

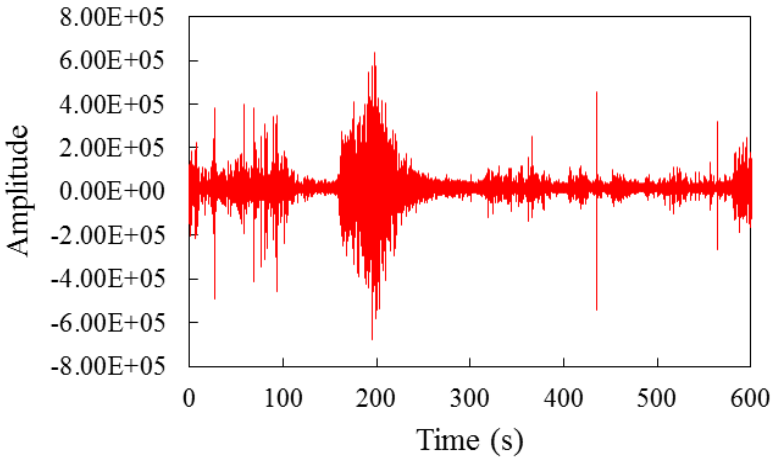

Fig. 3.16 N–S direction (Sta. 4)

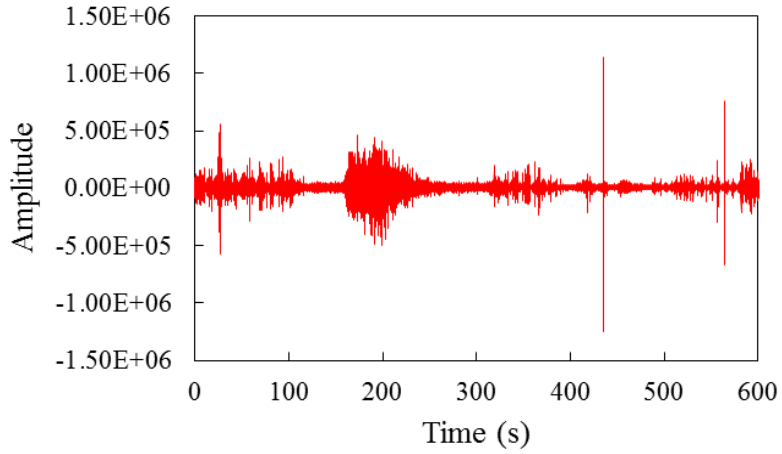

Fig. 3.17 E–W direction (Sta. 4)

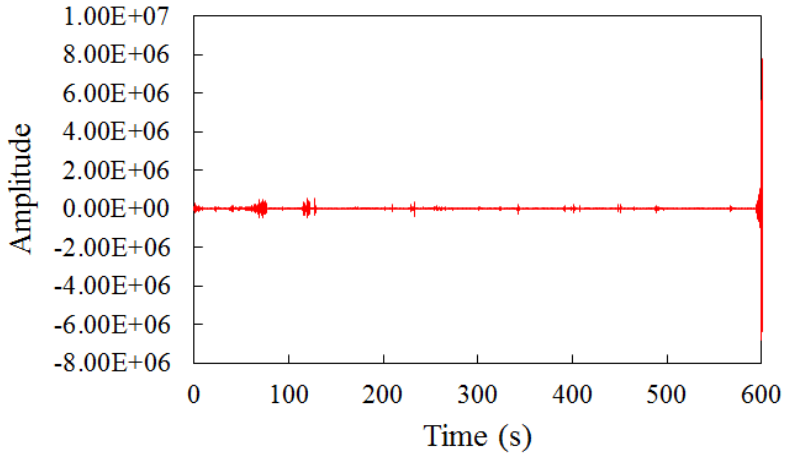

Fig. 3.18 Vertical direction (Sta. 5)

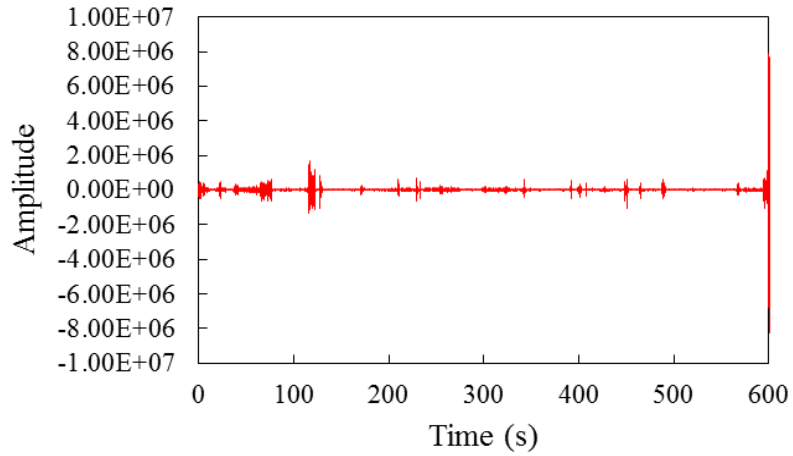

Fig. 3.19 N–S direction (Sta. 5)

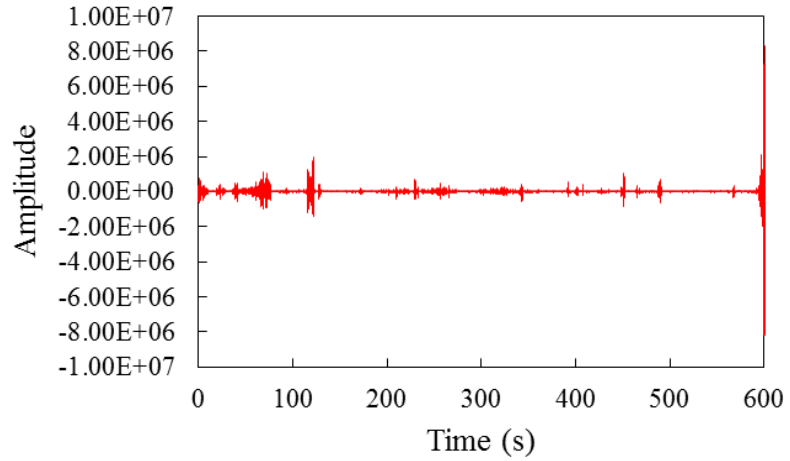

Fig. 3.20 E–W direction (Sta. 5)

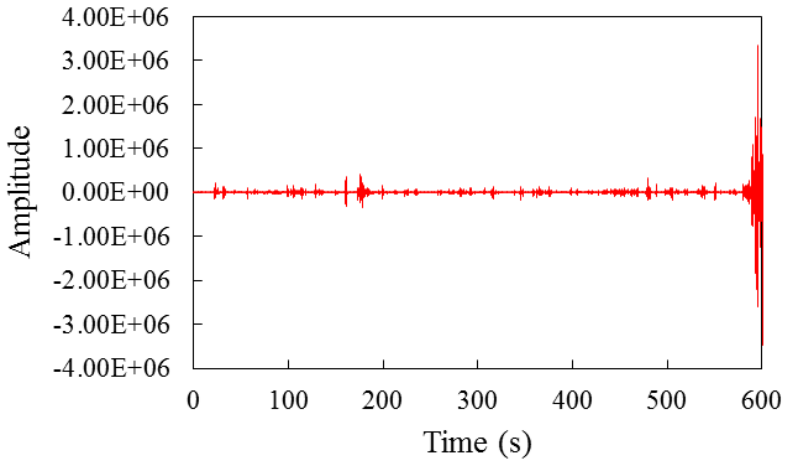

Fig. 3.21 Vertical direction (Sta. 6)

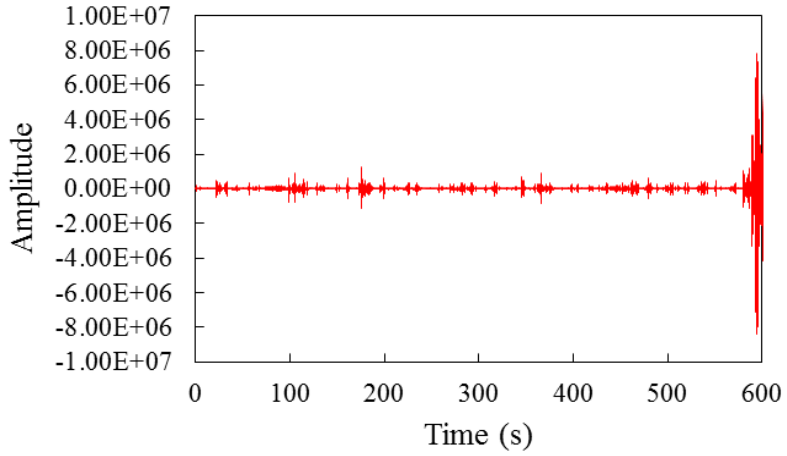

Fig. 3.22 N–S direction (Sta. 6)

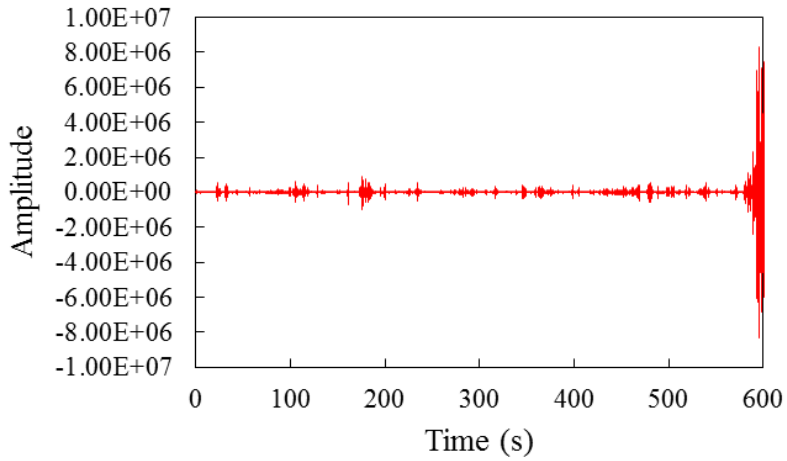

Fig. 3.23 E–W direction (Sta. 6)

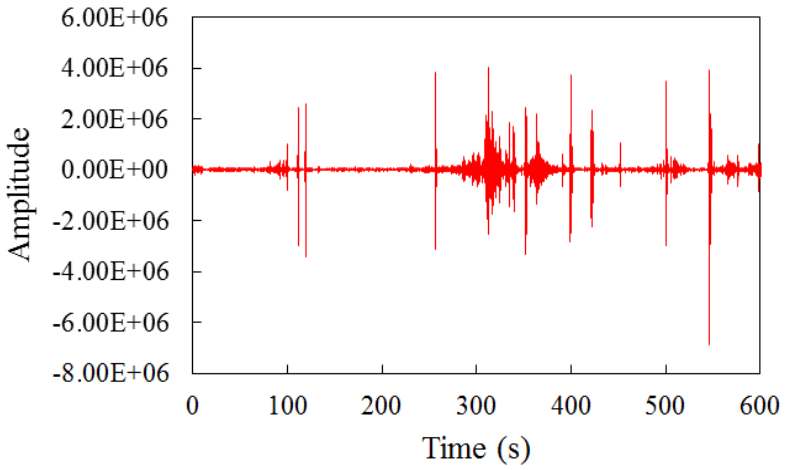

Fig. 3.24 Vertical direction (Sta. 7)

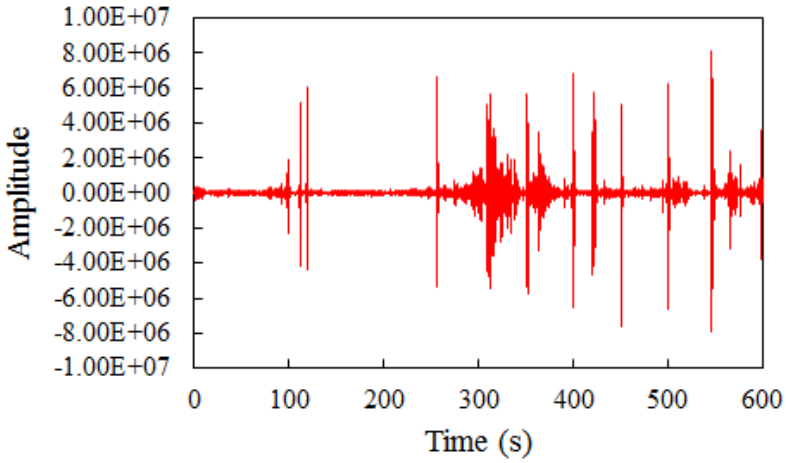

Fig. 3.25 N–S direction (Sta. 7)

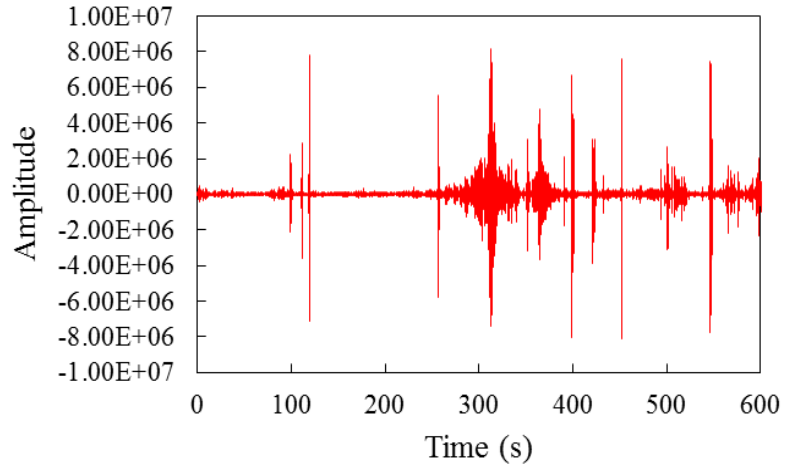

Fig. 3.26 E–W direction (Sta. 7)

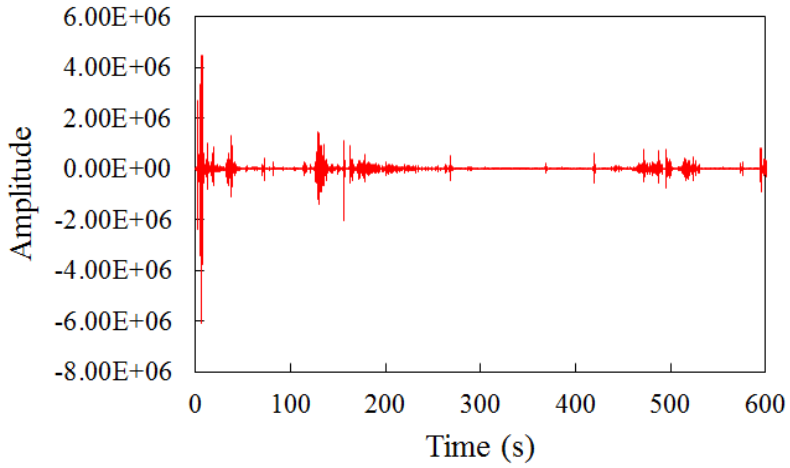

Fig. 3.27 Vertical direction (Sta. 8)

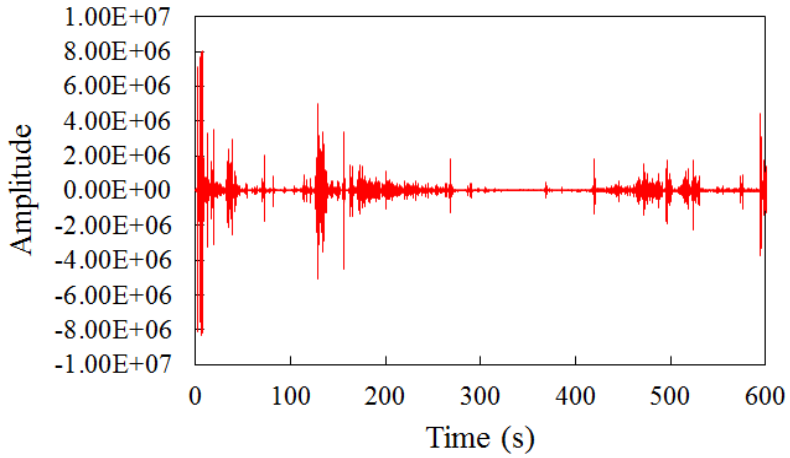

Fig. 3.28 N–S direction (Sta. 8)

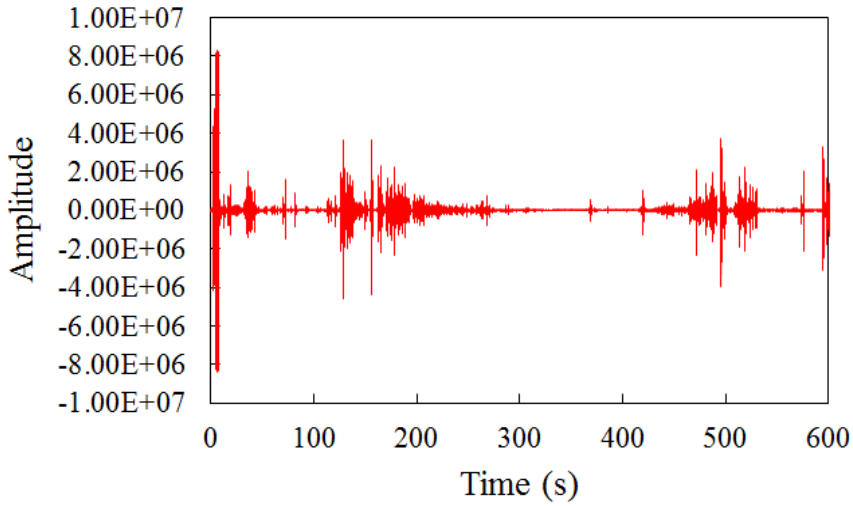

Fig. 3.29 E–W direction (Sta. 8)

3.3.2 The microtremor test results

The microtremor test results obtained from the Fujinuma dam site are divided into three parts: 1) the power spectrum for each observation point in three translational directions (vertical and two horizontal directions), 2) H/V ratio, and 3) amplification ratio of observation points and the assumed dam's basement. The results are presented below:

Power spectrum

Table 3.1 lists the power spectrum results in terms of the predominant period in the three translational directions for each observation point. The power spectrum results of all directions yield an almost similar peak range. It can be seen that for the horizontal components (N–S and E–W), it is difficult to select the peaks within the short period. However, roughly, the peaks were ranged between 0.2 and 0.4 s. For the long period, the peaks were clearly located at about 2.0 s. The vertical component yielded almost the same results as those obtained from the horizontal components. However, for the short period, the corresponding period of the peaks seems to be slightly lower, ranging between 0.2 and 0.3 s.

Table 3.1 Power spectrum

STA	**U–D**		**N–S**		**E–W**	
	Short – period	**Long– period**	**Short – period**	**Long– period**	**Short – period**	**Long– period**
1	0.3–0.4	2	0.3–0.4	2	0.3–0.4	2
2	0.2	2	0.2	2	0.2	2
3	0.2–0.3	2	0.3–0.4	2	0.3–0.4	2
4	0.2–0.3	1.6	0.3–0.4	2	0.3–0.4	2
5	0.3–0.4	2	0.3–0.4	2	0.3–0.4	2
6	0.1, 0.2–0.3	2	0.1, 0.2–0.3	2	0.1	2
7	0.2	2	0.2	2	0.2	2
8	0.2–0.3	2	0.2–0.3	2	0.2–0.3	2

H/V ratio

The H/V ratios are presented in terms of the predominant period. The H/V curves for each station are shown in Figs. 3.30–3.37. All figures show a similar trend, especially for the long period, in which the peak is clearly located at about 2.0 s. For short period range, several peaks can be seen, which may be considered as noise. However, at some stations, the peak corresponding to the short period can be selected clearly.

The estimated predominant periods of all stations are listed in Table 3.2. It can be seen that the predominant period for this site ranged between 2.0 and 3.0 s, which is considered as a long–period site characteristic. For the tip, which was estimated at Sta 3, the resonant period was about 2.0 s, and for the base, the resonant period was about 3.0 s with lower amplitude. In the case of the auxiliary dam, the resonant periods of the tip and base were about 2.0 s.

Note that, in general to determine site's predominant period, the microtremor test should be conducted only on the ground surface. In this study, we conducted the tests based on the remaining dam's shape to obtain its natural frequency. Hence, it must be recognized that the results on H/V ratio obtained in this study were the trial study on its application and they may not represent the actual predominant period of the estimated site.

Table 3.2 Predominant period

STA		**1**	**2**	**3**	**4**	**5**	**6**	**7**	**8**
H/V	Short–period	0.3–0.4	0.4	0.4	0.3–0.5	0.2	0.2–0.3	0.2–0.3	0.2–0.3
ratio	Long–period	2	2	2	2–3	2	2	2	2

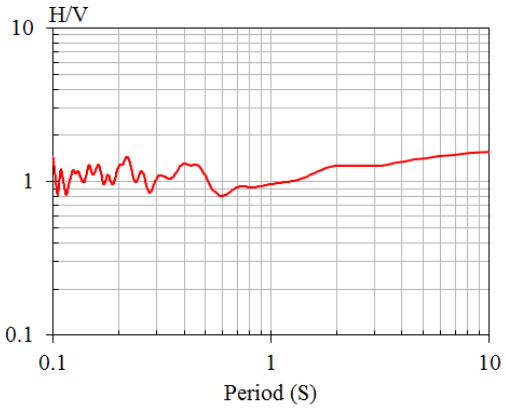

Fig. 3.30 H/V ratio for Sta 1

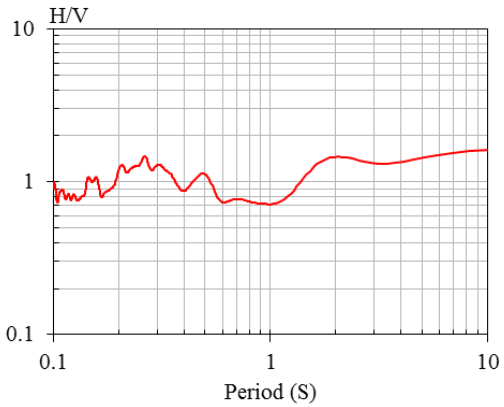

Fig. 3.31 H/V ratio for Sta 2

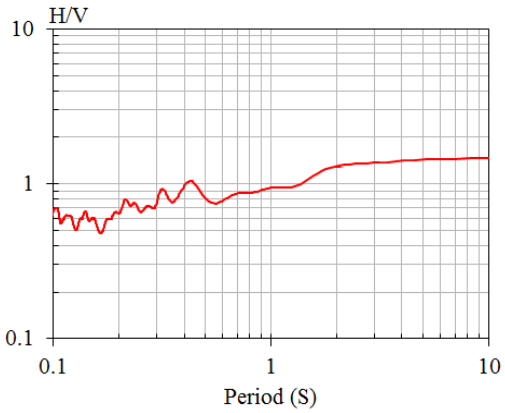

Fig. 3.32 H/V ratio for Sta 3

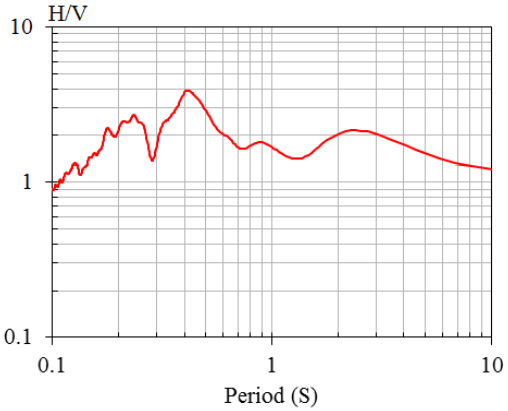

Fig. 3.33 H/V ratio for Sta 4

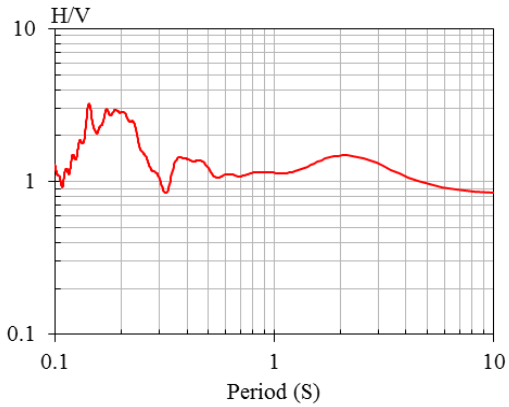

Fig. 3.34 H/V ratio for Sta 5

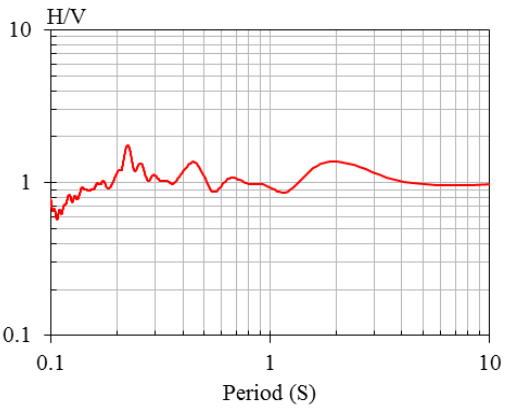

Fig. 3.35 H/V ratio for Sta 6

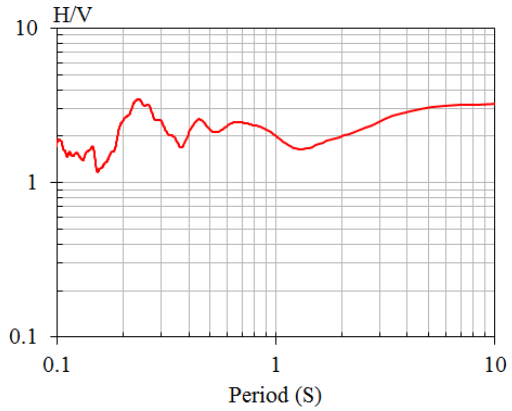

Fig. 3.36 H/V ratio for Sta 7

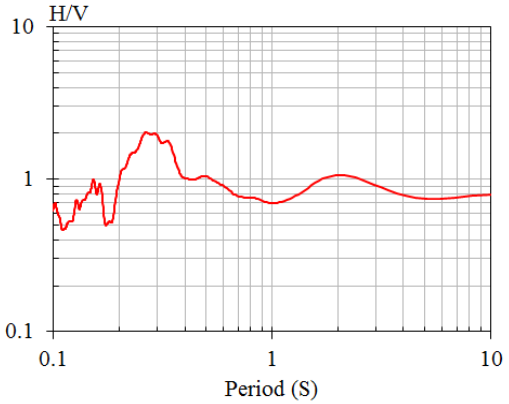

Fig. 3.37 H/V ratio for Sta 8

3.3.3 Adjustment of microtremor records to dam orientation

The previous section provided information on the predominant period of the site. However, to acquire information about the natural frequency of the dam, the raw records needed to be adjusted to match with the dam orientation in both the latitudinal and longitudinal directions (Fig. 3.38). The latitudinal direction of the dam is about 47° from the North, and its longitudinal direction is 43° from the North. In the case of the auxiliary dam, the latitudinal direction is 75° from the North. The information provided from this point forward is mainly related to the natural frequency of the dam. The results are presented in terms of the H/V and amplification ratios of the Fourier spectrum that taken from the crest to the base.

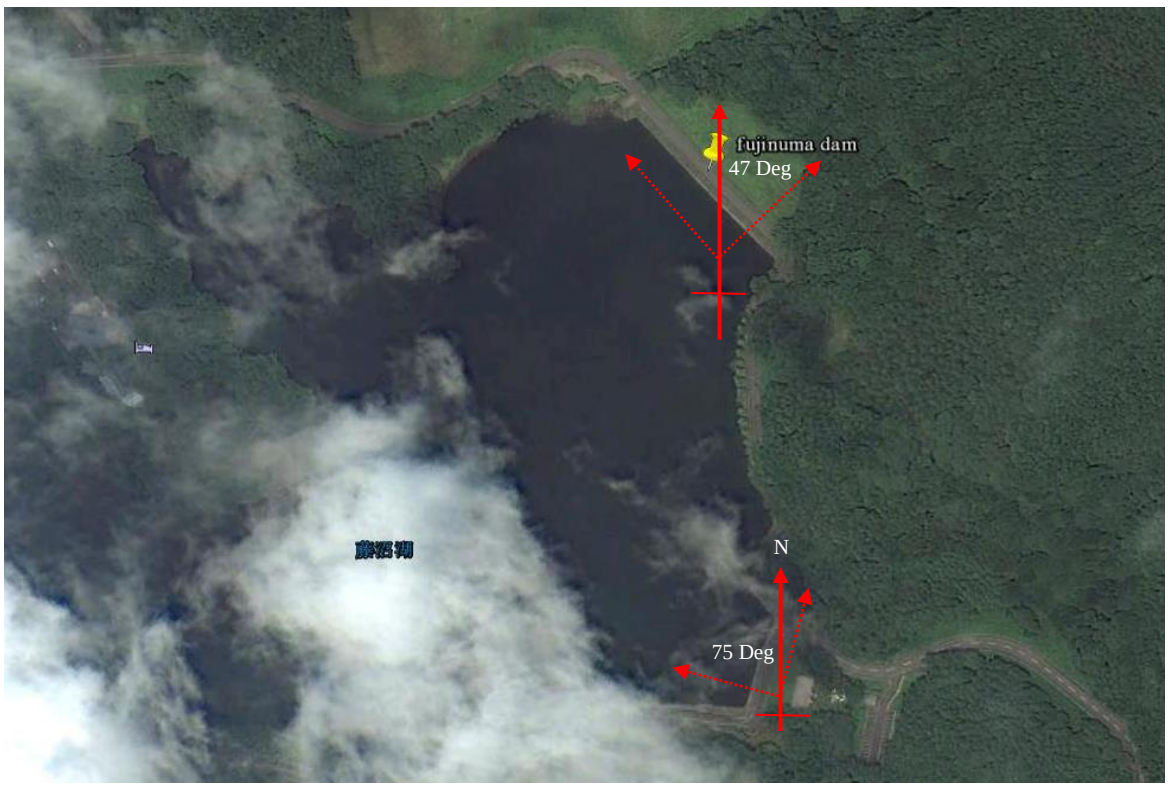

Fig. 3.38 Dam's orientation

H/V ratio with respect to dam orientation

The H/V ratio results are presented in terms of the predominant period. The H/V curves of each station are shown in Figs. 3.39–3.46. Most figures show a similar trend, especially in the long period, in which the peak can be seen clearly at about 2.0–3.0 s. Sta 4 was the only exception, and the peak there was at 0.6 s. In short period range, several peaks can be seen which may considered as noise. However, at some stations, the peak corresponding to the short period can be clearly selected. The estimated predominant periods of all stations are listed in Table 3.3. It can be seen that the predominant period for the site ranges between 2.0 and 3.0 s, which is considered as a long–period site characteristic. For the tip, which was estimated to be at Sta 3, the resonant period was about 2.0 s, and the resonant period at the base (Sta 6) was about 3.0 s with lower amplitude.

As mentioned earlier, the results on H/V ratio provided in this study were the trial study on its application and they may not represent the actual site's predominant period.

Table 3.3 Predominant period

STA		**1**	**2**	**3**	**4**	**5**	**6**	**7**	**8**
H/V	Short–period	0.1–0.5	0.3–0.5	0.3–0.6	0.6	0.3–0.4	0.2	0.2	0.2–0.3
ratio	Long–period	2	2	2	–	3	3	3	3

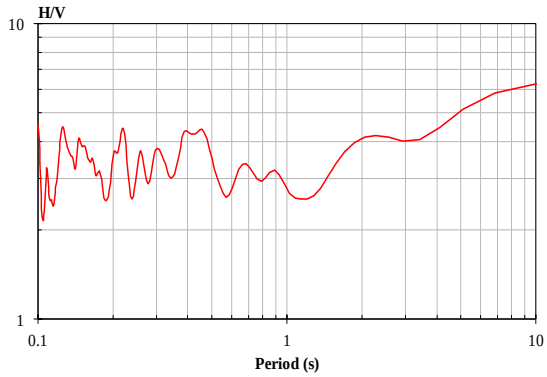

Fig. 3.39 H/V ratio for Sta 1

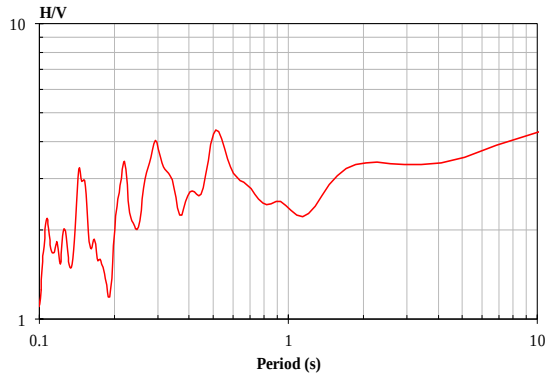

Fig. 3.40 H/V ratio for Sta 2

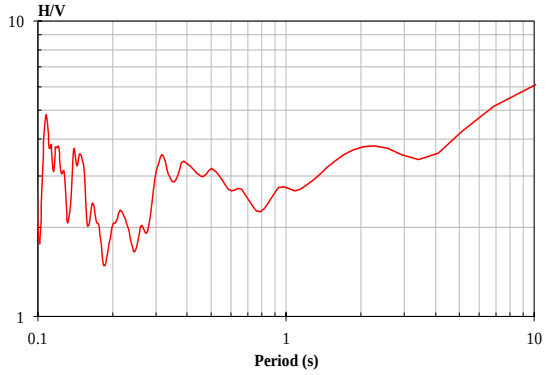

Fig. 3.41 H/V ratio for Sta 3

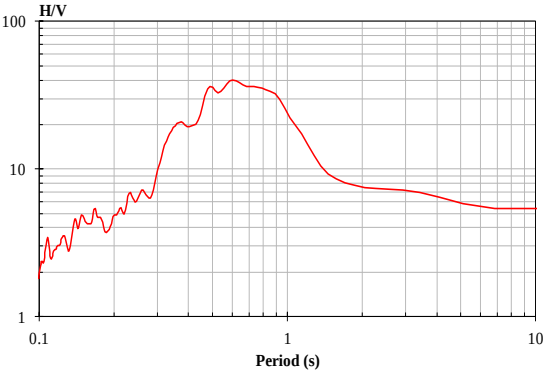

Fig. 3.42 H/V ratio for Sta 4

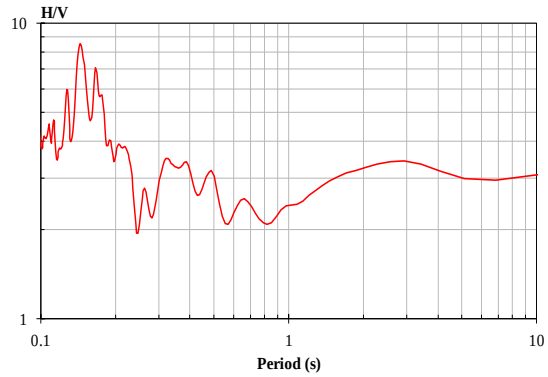

Fig. 3.43 H/V ratio for Sta 5

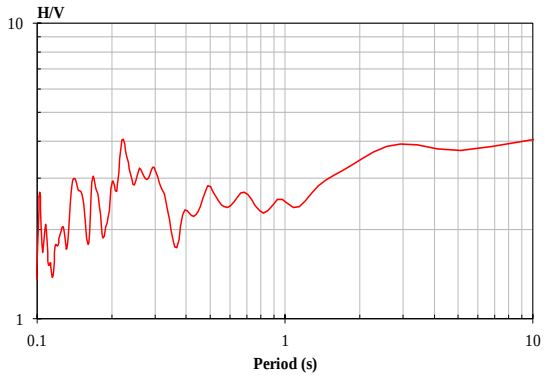

Fig. 3.44 H/V ratio for Sta 6

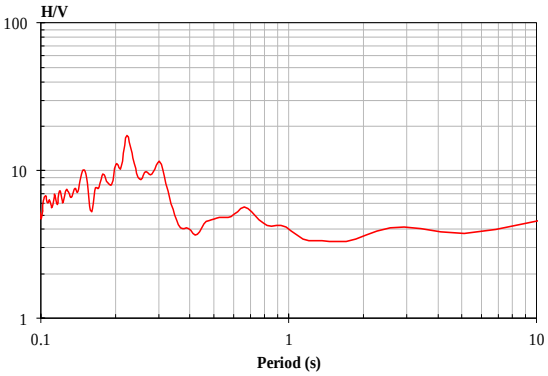

Fig. 3.45 H/V ratio for Sta 7

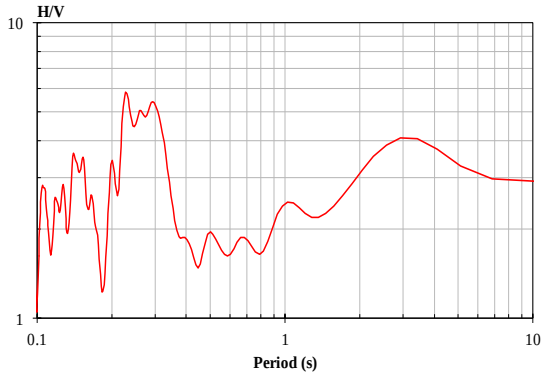

Fig. 3.46 H/V ratio for Sta 8

Amplification ratio

One possible method of estimating the natural frequency is to determine the resonant period from maximum amplification ratio. The amplification ratio in this study refers to the ratio of the Fourier spectrum taken at the crest to the Fourier spectrum of the dam's foundation. In this case, several locations were assumed as the dam's base. The top of the remaining dam structure was assumed as its tip. The locations of the observation points with the corresponding descriptions for the main dam and auxiliary dam are shown in Figs. 3.47 and 3.48, respectively. The results of each case are shown in Figs. 3.49–3.53. The results are expressed in terms of the crest to base amplification ratio and its corresponding period.

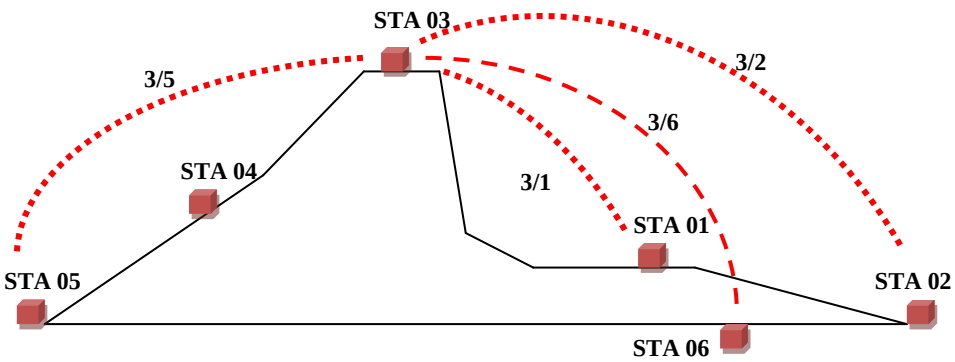

Fig. 3.47 Main dam and its observation points

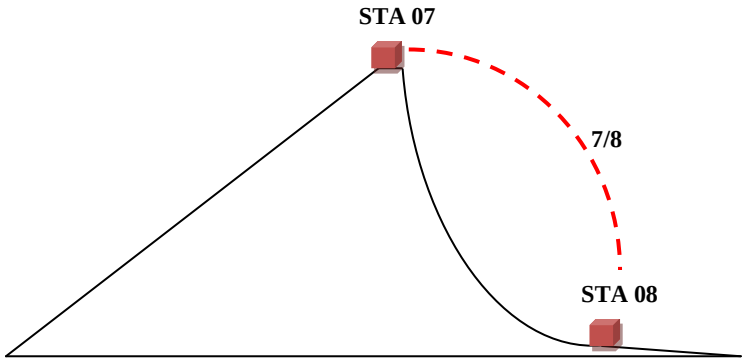

Fig. 3.48 Auxiliary dam and its observation points

The amplification of crest to base in the latitudinal direction is very important to this study because it refers to the dam's primary movement during the earthquake and is the first natural mode shape of the dam. This information can be used for comparing with the results obtained from frequency analysis of the remaining dam using numerical simulation, as well as to understand the possibilities of dam behavior under excitation. The amplification of crest to base in the latitudinal direction for all stations is shown in Figs. 3.49–3.53. Most cases yield a similar result, and it can be seen that the peak ratio is most likely between 0.3–0.6 s.

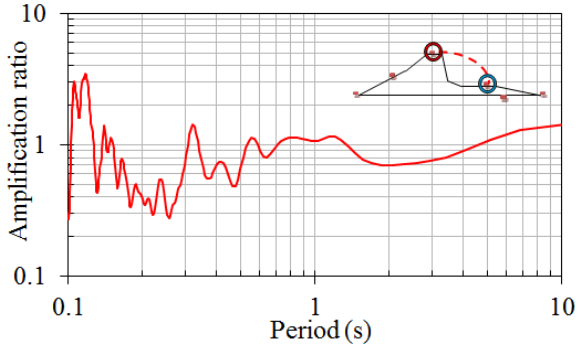

Fig. 3.49 H/V ratio for Sta 3/1

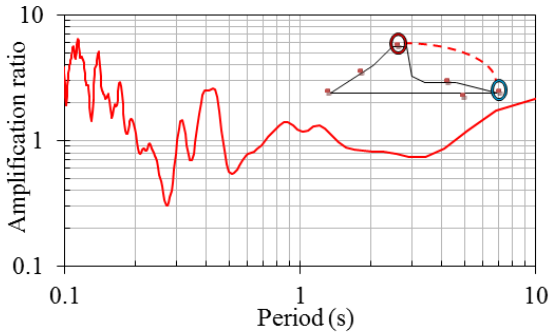

Fig. 3.50 H/V ratio for Sta 3/2

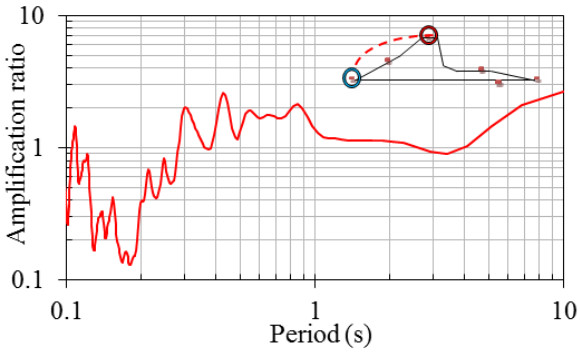

Fig. 3.51 H/V ratio for Sta 3/5

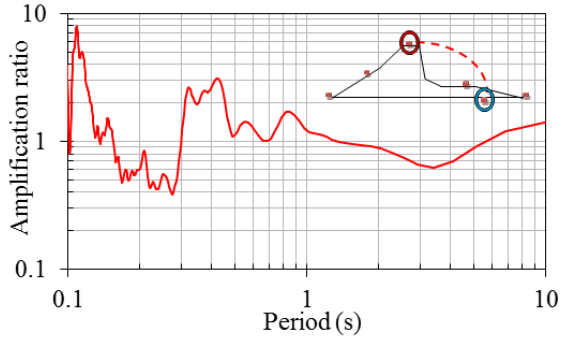

Fig. 3.52 H/V ratio for Sta 3/6

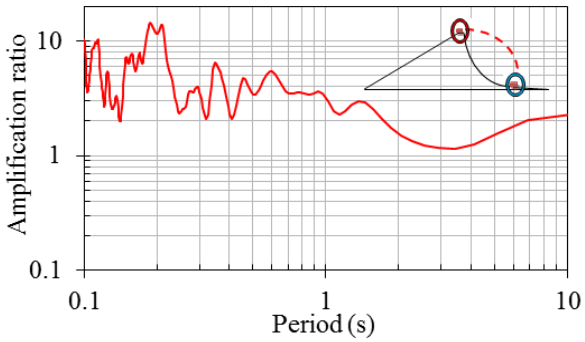

Fig. 3.53 H/V ratio for Sta 7/8

Table 3.4 lists the amplification ratios of remaining dam's tip and the assumed dam's base in terms of the maximum amplification ratio and its corresponding period. It can be seen that the predominant period for this site was ranged between 0.2–0.5 s, which is considered as the remaining dam's fundamental period. For the tip to base (Sta 3/Sta 6) ratio, the resonant period was about 0.43 s.

Table 3.4 Amplification ratio

Sta	**Results**	
	$Ratio_{MAX}$	**Period**
3/1	1.6	0.22
3/2	2.6	0.45
3/5	2.7	0.42
3/6	3.1	0.43
7/8	10.1	0.21

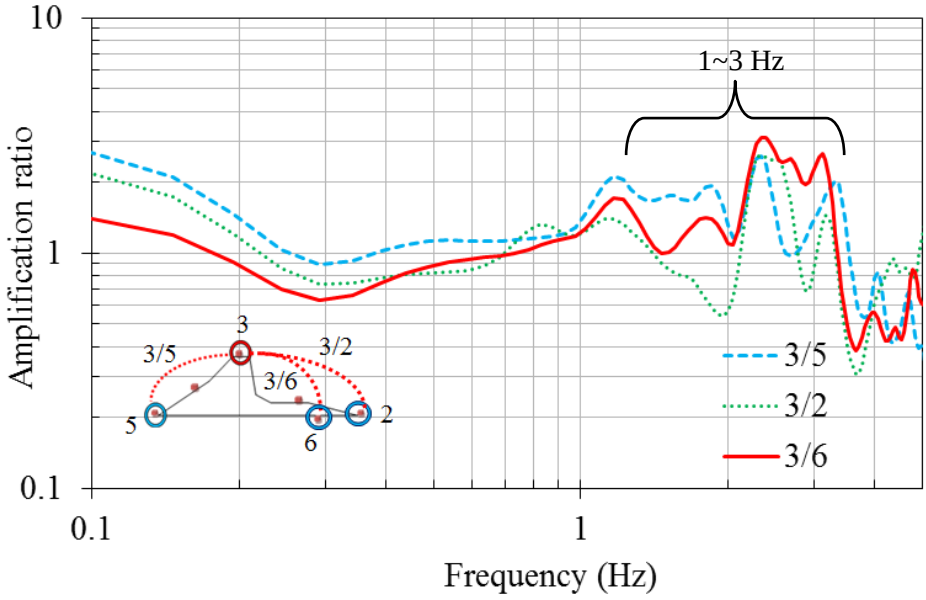

Fig. 3.54 Crest to base amplification ratio

Figure 3.54 shows the ratios of the amplification recorded at the top of the remaining dam to those recorded at three locations near the dam base, i.e., 3/5, 3/2 and 3/6. From the microtremor test results, it can be seen that in the latitudinal direction, the amplification ratio is within 1–3 Hz range.

3.4 2nd Microtremor investigation

The second set of microtremor observations were recorded during day time on December 6, 2012. The purpose of this test was to find out the ratio of amplification at the top of the remaining dam to that at the base for estimating the natural frequency of the dam. Although the first observation provided the data of our interest, the second observation was conducted for the sake of comparison and for reiterating the results. Three sites were selected for observation: the top and the assumed bases on both the upstream and downstream sides.

3.4.1 Microtremor test records

The microtremor records obtained from each site consisted of one vertical and two horizontal directions. The records for each site are shown in Figs. 3.55–3.63.

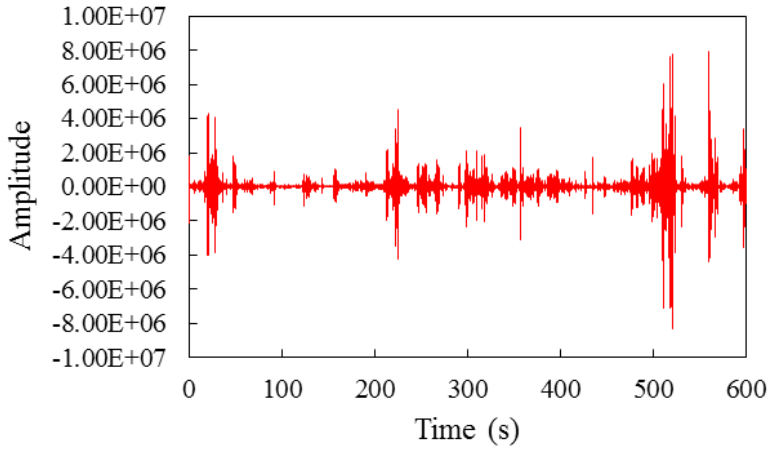

Fig. 3.55 Upstream–Downstream direction (Sta. 1)

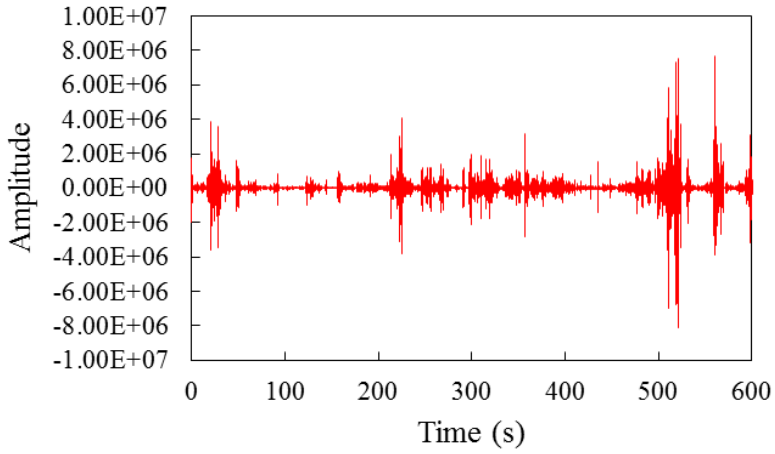

Fig. 3.56 Longitudinal direction (Sta. 1)

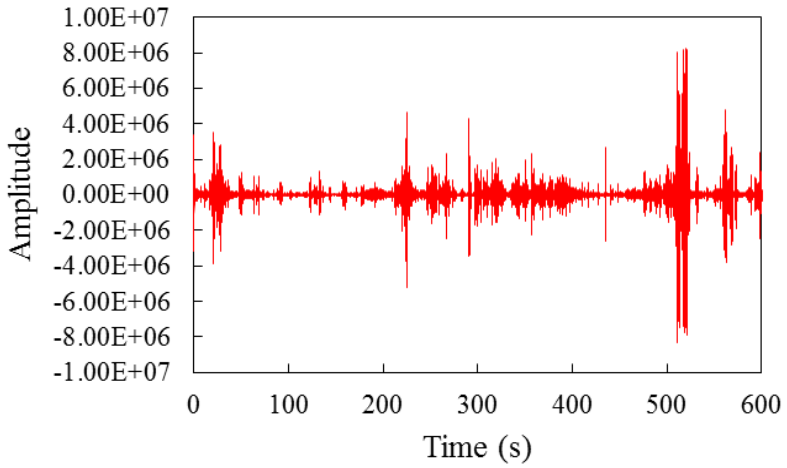

Fig. 3.57 Vertical direction (Sta. 1)

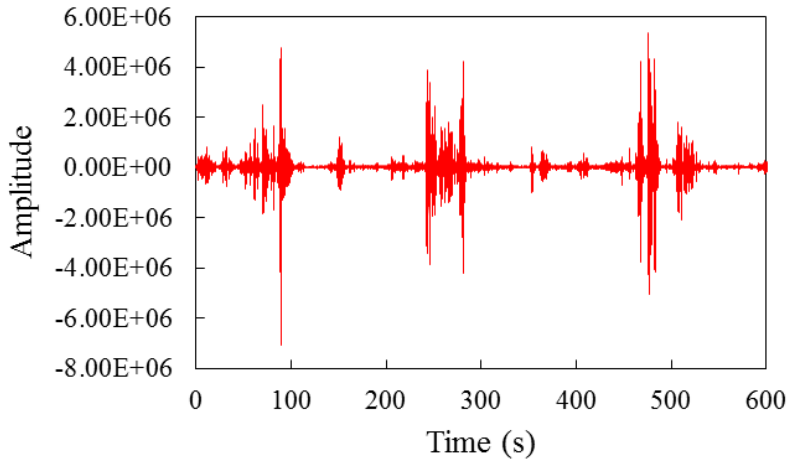

Fig. 3.58 Upstream–Downstream direction (Sta. 2)

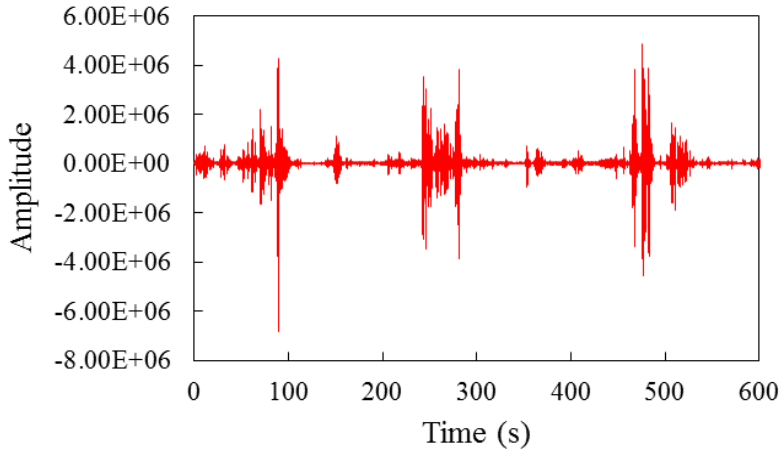

Fig. 3.59 Longitudinal direction (Sta. 2)

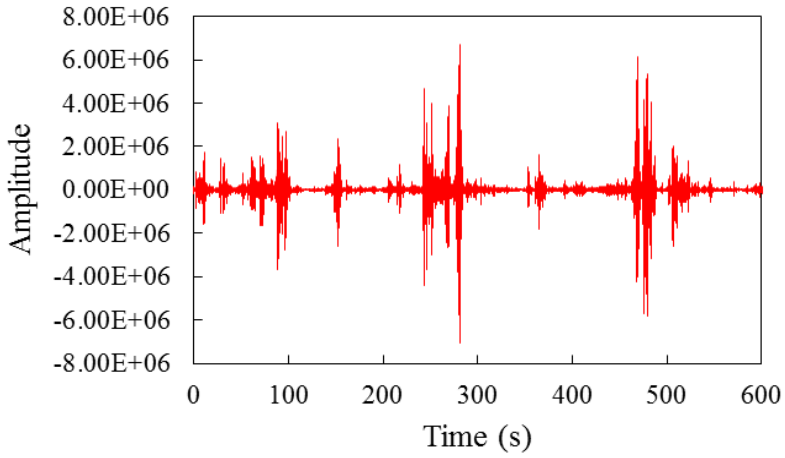

Fig. 3.60 Vertical direction (Sta. 2)

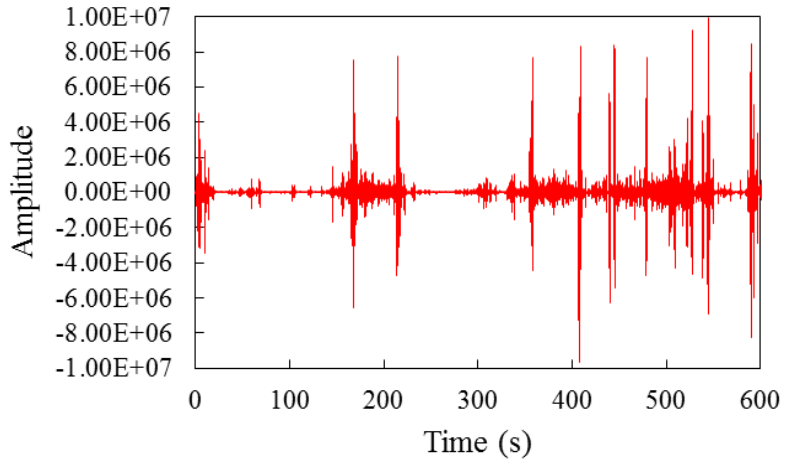

Fig. 3.61 Upstream–Downstream direction (Sta. 3)

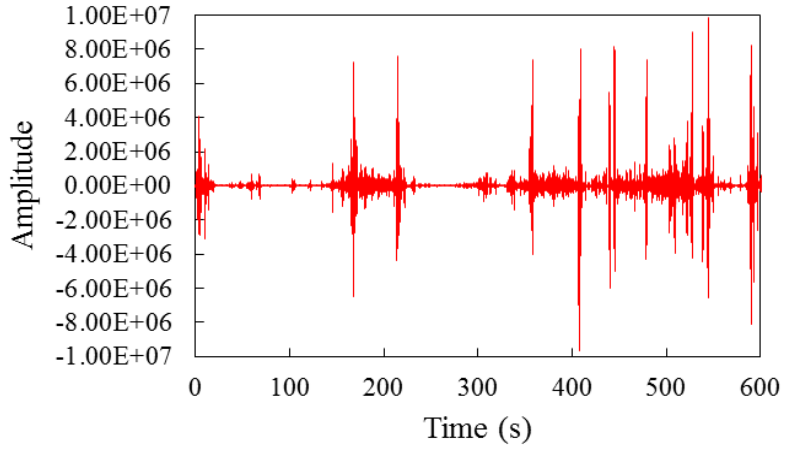

Fig. 3.62 Longitudinal direction (Sta. 3)

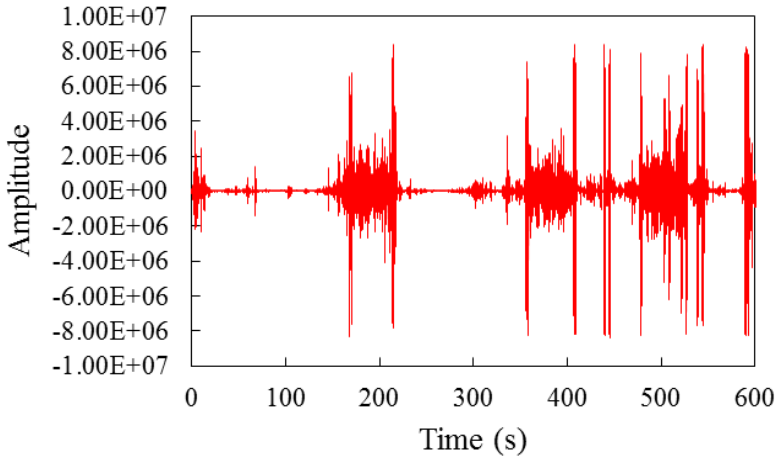

Fig. 3.63 Vertical direction (Sta. 3)

3.4.2 Microtremor test results

Fourier spectral analysis was performed on these records to estimate the spectrum of each site. Thereafter, the amplification ratio was determined to find the effect on the dam's resonance. The amplification ratio was determined from the top of the remaining dam with reference to the base, and according to this estimation, the period corresponding to the peak amplitude indicates the predominant period of such a structure. The results show only the amplification ratio in the latitudinal direction.

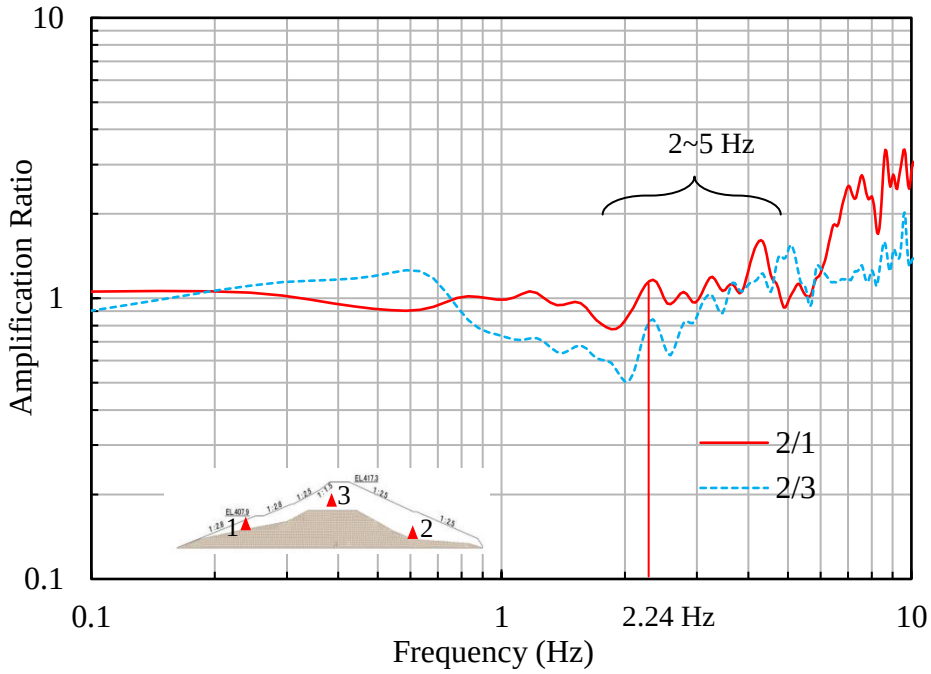

Fig. 3.64 Amplification ratio

Fig. 3.64 shows the amplification ratio that was taken from the top of the remaining dam to two locations near the dam base of the upstream and downstream slopes, defined as 2/1 and 2/3, respectively. By considering crest to base amplification ratio, it can be seen that in the latitudinal direction, the amplification ratio is within the range of 2–5 Hz. However, the

estimated predominant frequencies that we interested should be a fundamental mode, from the results, the first peak of 2.24 Hz was selected as a remaining dam natural frequency. Also, the dam is a long period structure then it might assure the selected natural frequency. Through this, the surveyed predominant period can be used as the data for verifying the dam model, in the study of the dynamic behavior of the dam in the further works.

3.5 Modal analysis of remaining dam

3.5.1 Remaining dam model

In order to verify the finite element model of the Fujinuma dam, the model of the remaining dam was proposed. The remaining dam model was approximately modeled based on the visual investigation at the dam site. The cross section of the remaining dam model is defined in Fig. 3.65. The height of the dam is 13.0 m with the crest width of about 14.7 m. the material properties used for the dam model were obtained from the laboratory experiments as mentioned in Chapter 2. The model was analyzed under plane strain condition and quadrilateral finite elements were used. The boundary conditions were restrained in the horizontal and vertical directions at the bottom of the model. The dam's body was classified into two portions: middle and bottom, while the upper portion assumed to be washed away owing to the dam's failure. The Young modulus is assumed to be constant in any of the three portions of the dam. In this study, for the modal analysis, the dam was analyzed under the empty reservoir condition. This model was used to determine the dam mode shape and its corresponding natural frequency, and for verification against the microtremor observations.

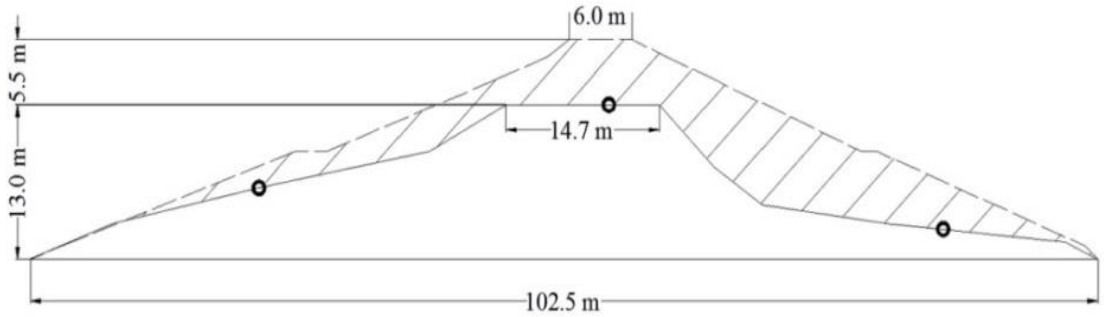

Fig. 3.65 Remaining dam model

3.5.2 Frequency analysis results

Modal analysis was conducted to extract the natural frequency and its corresponding mode shape. In this study, remaining dam model was analyzed. In Fig. 3.66, the result of the modal analysis is shown. The natural frequency is 2.35 Hz for the translational mode in the horizontal direction.

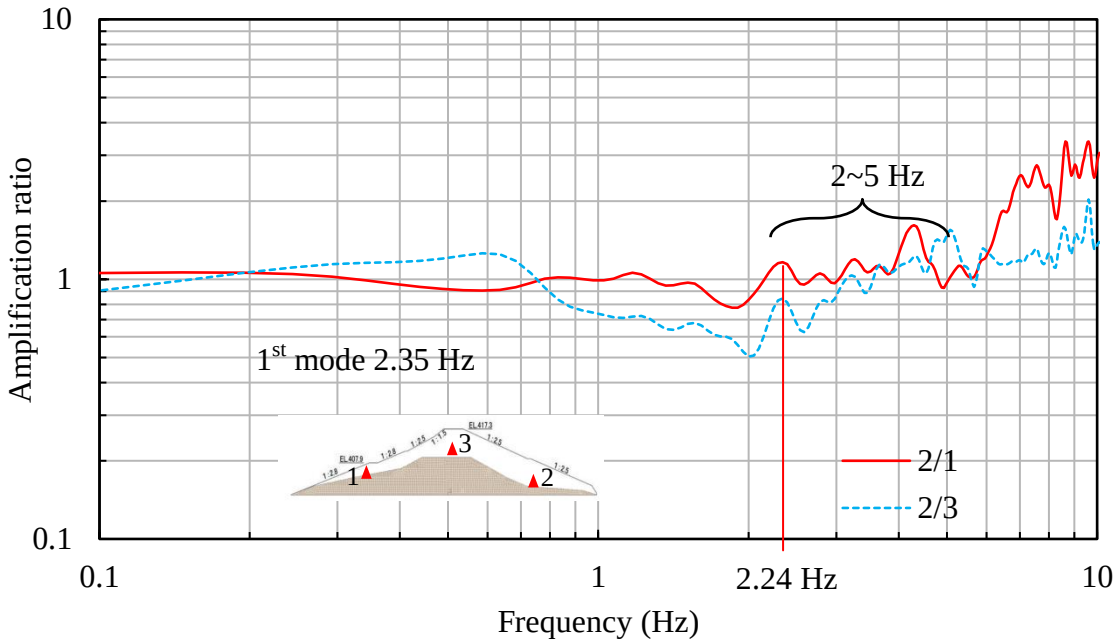

Fig. 3.66 Amplification ratio

Fig. 3.66 shows the amplification ratio that was taken from the top of the remaining dam to two locations near the dam base of the upstream and downstream slopes, defined as 2/1 and 2/3, respectively. By comparing the numerical results with microtremor test results, it can be seen that in the latitudinal direction, the amplification ratio is within the range of 2–5 Hz. The results obtained from the modal analysis of the remaining dam agree well with field observations in relation to the vibration in the latitudinal direction. Therefore, the estimated predominant frequencies of the original dam then can be reliably estimated by applying the same material properties used in the remaining dam model. It should be noted also that as the soils possibly subject to the large strain at the time of the dam failure that may cause degraded values of the shear modulus. As a result, the natural frequency of both microtremor test of the remains dam and the modal analysis result of the actual dam model may be different from the current results if the actual material properties can be acquired.

3.6 Conclusions

The microtremor observations conducted in this study aimed to determine the site's predominant period as well as the dam's natural frequency. A single microtremor observation was conducted at the dam site on both the remainder of the main dam and the remainder of the auxiliary dam. The results show that the predominant period of the dam location is 0.2–0.5 for the short period range and 2.0–3.0 for the long period range.

As the priority of the microtremor measurement in this study is to obtain the natural frequency of the remaining dam by using the amplification ratio taken from the Fourier spectrum at the remaining dam's tip to the Fourier spectrum at its basement. The results on the H/V ratio provided in this study were just only the trial on its application. Therefore, it

must be recognized that the results on the H/V ratio may not represent the actual site's predominant period.

The natural frequency of the remainder of the main dam is about 2–5 Hz in the upstream–downstream direction. The natural frequency of the remainder of the auxiliary dam is about 2 Hz. In addition, a numerical simulation of the remaining dam was performed to extract the fundamental mode and its frequency for verifying the model as well as the properties obtained from laboratory experiments. The results show that the natural frequency obtained from the numerical simulation is about 2.35 Hz in the upstream–downstream direction, which is in good agreement with the microtremor observation. Therefore, the material properties are suitable for modeling the original dam and performing dynamic analysis of the dam.

REFERENCES

[1] Wikipedia. [Online]. Available: /http://en.wikipedia.org/wiki/Fujinuma_dam. [accessed 07/01/12]

[2] K. Tokimatsu, Geotechnical Site Characterization Using Surface Wave. Proceeding of the 1st International Conference on Earthquake Geotechnical Engineering, 3 (1997) 1333–1367.

[3] Y. Nakamura, A Method for Dynamic Characteristics Estimation of Subsurface Using Microtremor on the Ground Surface, Quarterly Report of RTRI, 30(1)(1989) 25–33.

[4] Y. Nakamura, Clear identification of fundamental idea of Nakamura's technique and its applications, Proceeding of the 12th World Conference on Earthquake Engineering, Auckland, New Zeland, (2000).

[5] Y. Nakamura, On the H/V spectrum, Proceeding of the 14Th World Conference on Earthquake Engineering, Beijing, China, October 12–17, (2008).

[6] Mitutoyo. [Online]. Available: /http:// www.mitutoyo.co.jp [accessed 07/01/12]

[7] R. Rusnardi, Kiyono, Y. Ono, Estimation of Earthquake Ground Motion in Padang, Indonesia, International Journal of GEOMATE, 1(1) (2011)71–77.

[8] I. Cho and T. Tada, Bido English manual version 2.0, BIDO 2.0, November, 2010.

CHAPTER IV

DYNAMIC ANALYSIS OF EARTH DAM AND POSSIBLE RETROFITTING TECHNIQUES

4.1 Introduction

Geotechnics problems inevitably deal with the coupled mechanics of soil and water. Study of dam failure is such issue, and it requires nonlinear finite element analysis at finite–strain to simulate the failure. At present, methods for the nonlinear finite element analysis of porous media at finite deformation can be found widely. Using this advanced technique, many constitutive laws can be well established, thus resulting in better descriptions of the actual nonlinear behaviors of soil structures. Although the small–strain formulation might seem to have less potential, it still plays an important role in the verification of finite–strain formulation, which lacks an analytical solution. Within the small–strain regime, finite deformation analysis can be verified with small–strain analysis. Furthermore, owing to its nonlinearity and complexity, finite deformation analysis entails longer calculation times than small–strain analysis. With respect to small–strain problems, the results obtained from small deformation analysis yield an accurate approximation of both the analytical solution and finite strain analysis. Thus, it seems to be benefit for applying both formulations in the proper problem as for small–and finite–strain, respectively.

In this chapter, we review porous media theory. The basic requirement for governing the coupled soil–water formulation and the relevant governing equation are presented. The constitutive law applied in this study is then stated. Thereafter, the small–strain finite element formulation is presented. Finally, Newmark's method is introduced as a global solution algorithm for solving the general finite element equations of motion. Thereafter, dynamic analysis of the Fujinuma dam is presented. The dam's dynamic behavior under earthquake excitation is expressed. The failure mechanism of Fujinuma dam is summarized based on the small–strain analysis and facts. Moreover, seismic retrofitting techniques for this dam are introduced and discussed.

4.2 Implementation of the u–p finite element code at infinitesimal strain

Many materials are used in construction. Recent structures could be built from the most common material such as soil, rock, and wood to complex materials such as reinforced concrete or metal alloys. Soil is one of the simplest materials on Earth, and it has been used as a construction material since ancient times. Although it is one of the elementary materials on this planet, understanding the actual behavior of soil is one of the most challenging research tasks. Unlike steel or concrete, soil is a porous material that consists of soil particles, water, and air. The combined behavior of these elements requires considerable understanding of all relevant topics. After the contribution of Biot 1941[1] and Terzaghi 1943[2], many researchers developed finite element codes for the mixture in the

small–strain regime. For example, Morrison 1995[3] SAGA family of finite element codes, Zienkiewicz and Shiomi 1984[4], and Settari and Price 1984[5] were implemented. To develop the finite element formulation for the mixture, the behaviors of both soil and water, as well as the interactions among them, should be known for setting up the governing equation.

4.2.1 Governing equation

The basic principle in soil mechanic is the effective stress that was introduced by Terzaghi, in 1925(Terzaghi and Peck, 1967[6]). Accordingly, the effective stress can be calculated by subtraction of the pore pressure from the total stress by

$$\sigma' = \sigma - u \quad \text{(Eq. 4.1)}$$

where σ is the total stress, σ' is the effective stress and u is the pore pressure.

In respect of the flow of water in soil, Darcy's law is seems to be fit to described the pore movement in soil. Darcy's law states that the volume of flow of the pore fluid through a porous medium per unit time is proportional to the rate of change of excess fluid pressure with distance. The constant of proportionality includes the viscosity of the fluid and the intrinsic permeability of the soil. For the simple case of a horizontal tube filled with soil

$$Q = \frac{-kA}{\mu}\frac{\Delta P}{L} \quad \text{(Eq. 4.2)}$$

The total discharge, Q (having units of volume per time, e.g., ft³/s or m³/s), is proportional to the intrinsic permeability, k, the cross sectional area, A, and rate of pore pressure change, ΔP with distance, L, and inversely proportional to the dynamic viscosity of the fluid, μ. The negative sign is needed because fluids flow from high pressure to low pressure. Darcy velocity, the seepage velocity can be defined as

$$\boldsymbol{v}^s = \varphi \boldsymbol{v}^t = \varphi(\boldsymbol{v}^{if} - \boldsymbol{v}^{is}) \quad \text{(Eq. 4.3)}$$

where φ is fraction v^{if} and v^{is} is intrinsic velocity of fluid and solid, respectively.

Volume fraction

The simply soil model could be defined as mixture which consists of solid and fluid. To implement the relationship among them the volume fraction is therefore introduced. The volume of soil element can be written as

$$V = V_s + V_f \quad \text{(Eq. 4.4)}$$

where $\varphi^s = \frac{V_s}{V}$ and $\varphi^f = \frac{V_f}{V}$, we have

$$\varphi^s + \varphi^f = 1 \quad \text{(Eq. 4.5)}$$

To establish the finite element formulation for mixture, the definition of stress for soil material is required to introduce the effective stress in 2 dimensions which can be written as

$$\boldsymbol{\sigma} = \boldsymbol{\sigma}' + \boldsymbol{m}p,\ \boldsymbol{m} = \{1 \quad 1 \quad 0\}^T \tag{Eq. 4.6}$$

Balance of mass

Mass of the mixture consists of the mass of the solid, m_s and the mass of fluid, m_f which can be described as follow

$$m_s = \int_{\phi_t(u)} \rho_s(1-\varphi)dv \tag{Eq. 4.7}$$

$$m_f = \int_{\phi_t(u)} \rho_f \varphi dv \tag{Eq. 4.8}$$

where ρ_s and ρ_f is the density of the solid and fluid, respectively.

By taking time derivative of Eq. 4.7 and Eq. 4.8, we have

$$\frac{Dm_s}{Dt} = \frac{\partial[\rho_s(1-\varphi)]}{\partial t} + div[\rho_s(1-\varphi)\mathbf{v}^{is}] = 0 \tag{Eq. 4.9}$$

$$\frac{Dm_f}{Dt} = \frac{\partial(\rho_f\varphi)}{\partial t} + div(\rho_f\varphi\mathbf{v}^{if}) = 0 \tag{Eq. 4.10}$$

or

$$\frac{\partial[\rho_s(1-\varphi)]}{\partial t} + div[\rho_s(1-\varphi)\mathbf{v}^{is}] = 0 \tag{Eq. 4.11}$$

$$\frac{\partial(\rho_f\varphi)}{\partial t} + div(\rho_f\varphi\mathbf{v}^{if}) = 0 \tag{Eq. 4.12}$$

Multipling Eq. 4.12 with ρ_f/ρ_s and substitute into Eq. 4.11, we obtain

$$\rho_f\left(\frac{\partial(1-\varphi)}{\partial t} + \frac{\partial\varphi}{\partial t}\right) + \rho_f\frac{\partial\left(\varphi\left(\boldsymbol{v}^{if}-\boldsymbol{v}_i^{is}\right)\right)}{\partial x_i} + \rho_f\frac{\partial \boldsymbol{v}_i^{is}}{\partial x_i} + n\dot{\rho_f} + \frac{(1-\varphi)\rho_f}{\rho_s}\dot{\rho}_s = 0 \tag{Eq. 4.13}$$

Let,

$$\dot{\boldsymbol{w}} := \boldsymbol{v}^s = \varphi(\boldsymbol{v}^{if} - \boldsymbol{v}^{is}) \tag{Eq. 4.14}$$

and based on the small–strain assumption, the infinitesimal strain of solid phase ε_{ij}^s is defined as follow

$$\varepsilon_{ij}^s = \frac{1}{2}\left(\frac{\partial u_i}{\partial x_j} + \frac{\partial u_j}{\partial x_i}\right) = \frac{1}{2}\left(u_{i,j} + u_{j,i}\right) \tag{Eq. 4.15}$$

Hence,

$$\frac{\partial v_i^{is}}{\partial x_i} = v_{i,i}^{is} = \dot{\varepsilon}_{i,i}^s = 0 \tag{Eq. 4.16}$$

Substituting Eq. 4.14 and Eq. 4.16 into Eq. 4.13 and dividing by ρ_f yield,

$$\dot{w}_{i,i} + \dot{\varepsilon}^s_{i,i} + \varphi \frac{\dot{\rho}_f}{\rho_f} + \frac{(1-\varphi)}{\rho_s}\dot{\rho}_s = 0 \qquad \text{(Eq. 4.17)}$$

Let us assume that the compressibility of solid and fluid grain particles is much smaller than that of the solid skeleton, so $\dot{\rho}_s$ and $\dot{\rho}_f$ become 0. Thus, we have

$$\dot{w}_{i,i} + \dot{\varepsilon}^s_{i,i} = 0 \qquad \text{(Eq. 4.18)}$$

or

$$div(\dot{\boldsymbol{u}}) + div(\dot{\boldsymbol{w}}) = 0 \qquad \text{(Eq. 4.19)}$$

Balance of Momentum

For solid phase, we have

$$\int_s \boldsymbol{t}^s\, ds + \int_v \boldsymbol{f}^s\, dV + \int_v \boldsymbol{h}^s\, dV = \frac{d}{dt}\int_v \rho_s(1-\varphi)\boldsymbol{v}^{is}\, dV \qquad \text{(Eq. 4.20)}$$

and for fluid phase, we have

$$\int_s \boldsymbol{t}^f\, ds + \int_v \boldsymbol{f}^f\, dV + \int_v \boldsymbol{h}^f\, dV = \frac{d}{dt}\int_v \rho_f \varphi \boldsymbol{v}^{if}\, dV \qquad \text{(Eq. 4.21)}$$

where $\boldsymbol{f}^s$and $\boldsymbol{f}^f$ are continuous body force per unit volume for the solid and fluid phase in V, respectively, $\boldsymbol{t}^s$and $\boldsymbol{t}^f$ are traction vetors for the solid and fluid phase on the surface S of an arbitrary volume V, respectively. The interaction between the solid phase and the fluid phase, we have $\boldsymbol{h}^s$ and $\boldsymbol{h}^f$ which are the force per unit volume exerted by the fluid phase on the solid phase and the force per unit volume exerted by the solid phase on the fluid phase, respectively. The $\boldsymbol{h}^s$and $\boldsymbol{h}^f$are equal in magnitude but opposite in direction, we have $\boldsymbol{h}^s + \boldsymbol{h}^f = 0$ therefore.

The total traction vector is defined as

$$\boldsymbol{t}^f + \boldsymbol{t}^s = \boldsymbol{t} \qquad \text{(Eq. 4.22)}$$

where $\boldsymbol{t}^f = \boldsymbol{n}\cdot\boldsymbol{\sigma}^f$, and $\boldsymbol{t}^s = \boldsymbol{n}\cdot\boldsymbol{\sigma}^s$, $\boldsymbol{n}$ is the unit normal to the surface, and $\boldsymbol{\sigma}^f$and $\boldsymbol{\sigma}^s$ is the stress of the fluid and solid phase, respectively.

By using the divergence theorem to transform the surface integral to volume integral, and using Reynold's transportation theorem. Hence, for solid phase, we have

$$\int_V [div(\boldsymbol{\sigma}^s) + \boldsymbol{f}^s + \boldsymbol{h}^s]dV = \int_V \rho_s(1-\varphi)\frac{d\boldsymbol{v}^{is}}{dt}dV \qquad \text{(Eq. 4.23)}$$

and for fluid phase

$$\int_V [div(\boldsymbol{\sigma}^f) + \boldsymbol{f}^f + \boldsymbol{h}^f]dV = \int_V \rho_f \varphi \frac{d\boldsymbol{v}^{if}}{dt}dV \qquad \text{(Eq. 4.24)}$$

Accordingly, the above two equations can be rewritten as

$$div(\boldsymbol{\sigma}^s) + \boldsymbol{f}^s + \boldsymbol{h}^s = \rho_s(1-\varphi)\frac{d\boldsymbol{v}^{is}}{dt} \quad \text{(Eq. 4.25)}$$

$$div(\boldsymbol{\sigma}^f) + \boldsymbol{f}^f + \boldsymbol{h}^f = \rho_f\varphi\frac{d\boldsymbol{v}^{if}}{dt} \quad \text{(Eq. 4.26)}$$

To obtain the balance of the momentum of the mixture, we have

$$\boldsymbol{f} = \boldsymbol{f}^f + \boldsymbol{f}^s = \rho_f\varphi\boldsymbol{g} + \rho_s(1-\varphi)\boldsymbol{g} = \rho\boldsymbol{g} \quad \text{(Eq. 4.27)}$$

where $\boldsymbol{g}$ is the acceleration due to gravity.

and

$$\boldsymbol{h}^s + \boldsymbol{h}^f = 0 \quad \text{(Eq. 4.28)}$$

By doing a summation of Eq. 4.25 and Eq. 4.26, the balance of the momentum of the mixture is written as

$$div(\boldsymbol{\sigma}) + \boldsymbol{f} = \rho_f\varphi\frac{d\boldsymbol{v}^{if}}{dt} + \rho_s(1-\varphi)\frac{d\boldsymbol{v}^{is}}{dt} \quad \text{(Eq. 4.29)}$$

$$div(\boldsymbol{\sigma}) + \boldsymbol{f} - \rho\ddot{\boldsymbol{u}} = 0 \quad \text{(Eq. 4.30)}$$

From Eq. 4.14, we got

$$\frac{d\boldsymbol{v}^{if}}{dt} = \frac{d\boldsymbol{v}^{is}}{dt} + \frac{\ddot{\boldsymbol{w}}}{\varphi} \quad \text{(Eq. 4.31)}$$

By substituted Eq. 4.31 into Eq. 4.29, we have

$$div(\boldsymbol{\sigma}) + \boldsymbol{f} = \rho_f\varphi\left(\frac{d\boldsymbol{v}^{is}}{dt} + \frac{\ddot{\boldsymbol{w}}}{\varphi}\right) + \rho_s(1-\varphi)\frac{d\boldsymbol{v}^{is}}{dt} = \rho_f\ddot{\boldsymbol{w}} + \rho\frac{d\boldsymbol{v}^{is}}{dt} \quad \text{(Eq. 4.32)}$$

Therefore, the governing equation of the equilibrium of the mixture can be written as

$$div(\boldsymbol{\sigma}) + \boldsymbol{f} = \rho_f\varphi\left(\frac{d\boldsymbol{v}^{is}}{dt} + \frac{\ddot{\boldsymbol{w}}}{\varphi}\right) + \rho_s(1-\varphi)\frac{d\boldsymbol{v}^{is}}{dt} = \rho_f\ddot{\boldsymbol{w}} + \rho\ddot{\boldsymbol{u}} \quad \text{(Eq. 4.33)}$$

To solve the coupled solid–fluid problem, another governing equation from the balance of momentum for fluid phase is required,

$$-grad(\varphi p) + \varphi\rho_f\boldsymbol{g} + \boldsymbol{h}^f = \varphi\rho_f\ddot{\boldsymbol{u}} + \rho_f\ddot{\boldsymbol{w}} \quad \text{(Eq. 4.34)}$$

where

$$\boldsymbol{h}^f = -\varphi(\rho_f g\boldsymbol{i}) \quad \text{(Eq. 4.35)}$$

where **i** is the hydraulic gradient, Darcy's law states

$$\boldsymbol{v}^s = \dot{\boldsymbol{w}} = \boldsymbol{k}\boldsymbol{i} \quad \text{(Eq. 4.36)}$$

where **k** is the hydraulic conductivity (permeability) matrix,

$$\boldsymbol{h}^f = -\varphi(\rho_f g \boldsymbol{k}^{-1}\dot{\boldsymbol{w}}) \quad \text{(Eq. 4.37)}$$

Substitute Eq. 4.37 into Eq. 4.34 and divide by porosity φ we obtain

$$-\frac{1}{\varphi}\boldsymbol{grad}(\varphi p) + \rho_f \boldsymbol{g} - (\rho_f g \boldsymbol{k}^{-1}\dot{\boldsymbol{w}}) = \rho_f \ddot{\boldsymbol{u}} + \frac{\rho_f}{\varphi}\ddot{\boldsymbol{w}} \quad \text{(Eq. 4.38)}$$

The acceleration of fluid considers being much smaller than that the acceleration of solid, therefore the acceleration of fluid is negligible. Thus Eq. 4.38 becomes

$$-\frac{1}{\varphi}\boldsymbol{grad}(\varphi p) + \rho_f \boldsymbol{g} = (\rho_f g \boldsymbol{k}^{-1}\dot{\boldsymbol{w}}) + \rho_f \ddot{\boldsymbol{u}} \quad \text{(Eq. 4.39)}$$

For homogeneous behavior, $grad(\varphi) = 0$, thus

$$\dot{\boldsymbol{w}} = -\boldsymbol{k}\left(\frac{\boldsymbol{grad}p}{\rho_f g} - \frac{\boldsymbol{g}}{g}\right) - \frac{1}{g}\boldsymbol{k}\ddot{\boldsymbol{u}} \quad \text{(Eq. 4.40)}$$

4.2.2 Finite element formulation

Weak form

Since there are two types of unknown, the solid displacement and the pore pressure, in the u–p formulation; two trial function spaces, $\boldsymbol{u}$ and $\boldsymbol{p}$, and two weighting function spaces, $\delta\boldsymbol{u}$ and $\delta\boldsymbol{p}$, are introduced as follow:

Multiply Eq. 4.30 by $\delta\boldsymbol{u}$ and integrate over Ω

$$\int_\Omega \delta\boldsymbol{u}\cdot(div(\boldsymbol{\sigma}) + \boldsymbol{f} - \rho\ddot{\boldsymbol{u}})d\Omega = 0 \quad \text{(Eq. 4.41)}$$

Perform integration by parts on, Eq. 4.41 becomes

$$\int_\Omega \delta\boldsymbol{u}\rho\cdot\ddot{\boldsymbol{u}}d\Omega + \int_\Omega \nabla(\delta\boldsymbol{u}):\boldsymbol{\sigma}d\,\Omega = \int_\Omega \delta\boldsymbol{u}\cdot\boldsymbol{f}d\Omega + \int_{\Gamma t}\delta\boldsymbol{u}\cdot\boldsymbol{t}d\Gamma \quad \text{(Eq. 4.42)}$$

For fluid phase, multiply Eq. 4.19 by $\delta\boldsymbol{p}$ and integrate over Ω, then

$$\int_\Omega \delta\boldsymbol{p}\cdot\big(div(\dot{\boldsymbol{u}}) + div(\dot{\boldsymbol{w}})\big)d\Omega = 0 \quad \text{(Eq. 4.43)}$$

where

$$\dot{\boldsymbol{w}} = -\boldsymbol{k}\left(\frac{\boldsymbol{grad}p}{\rho_f g} - \frac{\boldsymbol{g}}{g}\right) - \frac{1}{g}\boldsymbol{k}\ddot{\boldsymbol{u}}\ in\ \Omega \quad \text{(Eq. 4.44)}$$

Therefore, the weak form is presented as follow

$$\int_\Omega \delta\boldsymbol{u}\rho\cdot\ddot{\boldsymbol{u}}d\Omega + \int_\Omega \nabla(\delta\boldsymbol{u}):\boldsymbol{\sigma}d\,\Omega = \int_\Omega \delta\boldsymbol{u}\cdot\boldsymbol{f}d\Omega + \int_{\Gamma t}\delta\boldsymbol{u}\cdot\boldsymbol{t}d\Gamma \quad \text{(Eq. 4.45)}$$

$$\int_\Omega \delta\boldsymbol{p}\cdot\big(div(\dot{\boldsymbol{u}}) + div(\dot{\boldsymbol{w}})\big)d\Omega = 0 \quad \text{(Eq. 4.46)}$$

where

$$\dot{\boldsymbol{w}} = -\boldsymbol{k}\left(\frac{\boldsymbol{grad}p}{\rho_f g} - \frac{\boldsymbol{g}}{g}\right) - \frac{1}{g}\boldsymbol{k}\ddot{\boldsymbol{u}}\ in\ \Omega \quad \text{(Eq. 4.47)}$$

4.2.3 Matrix form

The effect between the solid and fluid phase was carried out through a u–p formulation; the governing equation of motion of 2D coupled solid–fluid problem can be written as shown in Eq. 4.48 and Eq. 4.49.

$$[L]^{\mathrm{T}}\boldsymbol{\sigma} - \rho\mathbf{b} + \rho\ddot{\mathbf{u}} = \mathbf{0} \quad \text{(Eq. 4.48)}$$

$$\mathbf{m}^{\mathrm{T}}\dot{\boldsymbol{\varepsilon}} = div\hat{\mathbf{v}} + \left(\frac{n}{K_w}\right)\dot{p} \quad \text{(Eq. 4.49)}$$

where the total stresses $\boldsymbol{\sigma}$, the body loads $\mathbf{b}$, and the acceleration $\ddot{\mathbf{u}}$ are time dependent with the differential operator L given as

$$[L]^{\boldsymbol{T}} = \begin{bmatrix} \partial/\partial \mathrm{x} & 0 & \partial/\partial \mathrm{y} \\ 0 & \partial/\partial \mathrm{y} & \partial/\partial \mathrm{x} \end{bmatrix} \quad \text{(Eq. 4.50)}$$

In addition,

$$\boldsymbol{\sigma} = \boldsymbol{\sigma}' + \mathbf{m}p,\ \mathbf{m} = \{1 \quad 1 \quad 0\}^{\mathrm{T}} \quad \text{(Eq. 4.51)}$$

$$\hat{\mathbf{v}} = -\mathbf{k}\big(gradp - \rho_w(\mathbf{b} - \ddot{\mathbf{u}})\big)/\rho_w g \quad \text{(Eq. 4.52)}$$

in which the relevant parameters are effective stress $\boldsymbol{\sigma}'$, pore pressure p, total stress $\boldsymbol{\sigma}$, coefficient of permeability $\mathbf{k}$, density of water ρ_w, and gravitational acceleration g.

To introduce the matrix form the shape function is required. The displacement can be defined as $\{\mathbf{u}^{\mathrm{n}}\}$

$$\mathbf{u} = [N]\{\mathbf{u}^{\mathrm{n}}\} \quad \text{(Eq. 4.53)}$$

By introducing Eq. 4.28 into Eq. 4.28, we obtained.

$$\int_{\mathrm{v}}[N]^{\mathrm{T}}([L]^{\mathrm{T}}\boldsymbol{\sigma} - \rho\mathbf{b} + \rho\ddot{\mathbf{u}})\,\mathrm{dV} = \mathbf{0} \quad \text{(Eq. 4.54)}$$

From Eq. 4.54 the first term can be divided into two parts which are traction force and the derivative of the stress as shown in Eq. 4.55

$$\int_{\mathrm{v}}[N]^{\mathrm{T}}[L]^{\mathrm{T}}\boldsymbol{\sigma}\,\mathrm{dV} = \int_{\mathrm{s}}[N]^{\mathrm{T}}\,\mathbf{t}\mathrm{dS} - \int_{\mathrm{v}}([L][N])^{\mathrm{T}}\boldsymbol{\sigma}\,\mathrm{dV} \quad \text{(Eq. 4.55)}$$

where traction force can be defined as the product of pressure and unit vecter perpendicular to the surface

$$\mathbf{t} = \boldsymbol{\sigma}^{\mathrm{T}} \cdot \mathbf{n} \quad \text{(Eq. 4.56)}$$

Hence, the Eq. 4.54 becomes.

$$-\int_{\mathrm{v}}([L][N])^{\mathrm{T}}\boldsymbol{\sigma}\,\mathrm{dV}+\int_{\mathrm{s}}[N]^{\mathrm{T}}\,\mathbf{t}\mathrm{dS}-\int_{\mathrm{v}}[N]^{\mathrm{T}}\rho\mathbf{b}\,\mathrm{dV}+\int_{\mathrm{v}}[N]^{\mathrm{T}}\rho\,\ddot{\mathbf{u}}\mathrm{dV}=\mathbf{0} \qquad \text{(Eq. 4.57)}$$

In this study, the dynamic problem is consider only the force induced by inertia force therefore the body force is then neglect.

$$-\int_{\mathrm{v}}([L][N])^{\mathrm{T}}\delta\boldsymbol{\sigma}\,\mathrm{dV}+\int_{\mathrm{s}}[N]^{\mathrm{T}}\delta\,\mathbf{t}\mathrm{dS}+\int_{\mathrm{v}}[N]^{\mathrm{T}}\rho\delta\,\ddot{\mathbf{u}}\mathrm{dV}=\mathbf{0} \qquad \text{(Eq. 4.58)}$$

The relationship of stress and strain can be written as

$$\mathrm{d}\boldsymbol{\sigma}'=[D]\mathrm{d}\boldsymbol{\varepsilon}=-[D][B]\{\mathbf{u}^{\mathrm{n}}\} \qquad \text{(Eq. 4.59)}$$

The total stress can be described by introducing the pore pressure into Eq. 4.58

$$\delta\boldsymbol{\sigma}=-[D][B]\{\mathbf{u}^{\mathrm{n}}\}+\mathbf{m}\delta\mathrm{p} \qquad \text{(Eq. 4.60)}$$

Hence the finite element formulation for solid partition can be written as

$$\int_{\mathrm{v}}[B]^{\mathrm{T}}([D][B]\{\delta\mathbf{u}^{\mathrm{n}}\}-\mathbf{m}\delta\mathrm{p})\,\mathrm{dV}+\int_{\mathrm{v}}[\mathrm{N}]^{\mathrm{T}}\rho\delta\,\ddot{\mathbf{u}}\mathrm{dV}=-\int_{\mathrm{s}}[\mathrm{N}]^{\mathrm{T}}\delta\,\mathbf{t}\mathrm{dS} \qquad \text{(Eq. 4.61)}$$

Similarly, by introducing the shape function for the pore pressure, we have

$$\boldsymbol{p}=\{N_h\}\{\boldsymbol{p}^n\} \qquad \text{(Eq. 4.62)}$$

Thus, the derivatives of the shape functions for the pore pressure become

$$\boldsymbol{grad}\mathbf{p}=\left[B_p\right]\{\boldsymbol{p}^n\} \qquad \text{(Eq. 4.63)}$$

By introducing Eq. 4.62 and Eq. 4.63 into Eq. 4.61 the matrix form of solid part can be written as.

$$[M^{uu}]\{\delta\ddot{\boldsymbol{u}}^n\}+[K^{uu}]\{\delta\boldsymbol{u}^n\}+[K^{up}]\{\delta p^n\}=\{\delta F\} \qquad \text{(Eq. 4.64)}$$

where

$$[M^{uu}]=\int_v\rho[N]^T[N]dV \qquad \text{(Eq. 4.65)}$$

$$[K^{uu}]=\int_v[B]^T[D]\,[B]dV \qquad \text{(Eq. 4.66)}$$

$$[K^{up}]=\int_v[B]^T\boldsymbol{m}\{N_h\}dV \qquad \text{(Eq. 4.67)}$$

$$\{\delta F\}=\int_s[N]^T\delta\boldsymbol{t}\,dS \qquad \text{(Eq. 4.68)}$$

For the equilibrium of the fluid part, by multiplying Eq. 4.49 with $\{\mathrm{N_h}\}$, the equation then becomes

$$\int_{\mathrm{v}}\{N_h\}^{\mathrm{T}}\left[div\left(\frac{\mathbf{k}}{\rho_{\mathrm{w}}\mathrm{g}}(\boldsymbol{grad}\delta\mathrm{p}+\rho_{\mathrm{w}}\delta\ddot{\mathbf{u}})\right)+\mathbf{m}^{\mathrm{T}}\dot{\boldsymbol{\varepsilon}}-\frac{n}{K_w}\delta\dot{\mathrm{p}}\right]\mathrm{dV}=0 \qquad \text{(Eq. 4.69)}$$

From Darcy's law and by performing Gauss' integration, we obtained

$$\int_{\mathrm{v}}\{N_h\}^{\mathrm{T}} div\left(\frac{\mathbf{k}}{\rho_w \mathrm{g}}(\boldsymbol{grad}\delta\mathrm{p}+\rho_w\delta\ddot{\mathbf{u}})\right)\mathrm{dV}=\int_{\mathrm{s}}\{N_h\}^{\mathrm{T}}\,\delta\mathrm{Q}\mathrm{dS}-\int_{\mathrm{v}}\{B_p\}^{\mathrm{T}}\frac{\mathbf{k}}{\rho_w g}(\boldsymbol{grad}\delta\mathrm{p}+\rho_w\delta\ddot{\mathbf{u}})\mathrm{dV} \quad \text{(Eq. 4.70)}$$

where δQ is the flow rate flowing to take the unit area of the surface, which can be expressed as follows:

$$\delta\mathrm{Q}=\mathbf{n}^{\mathrm{T}}\frac{\mathbf{k}}{\rho_w g}(\boldsymbol{grad}\delta\mathrm{p}+\rho_w\delta\ddot{\mathbf{u}}) \quad \text{(Eq. 4.71)}$$

From Eq. 4.70 and Eq. 4.71, the matrix form of fluid part can be written as.

$$[M^{pu}]\{\delta\ddot{\boldsymbol{u}}^n\}+[K^{up}]^T\{\delta\dot{\boldsymbol{u}}^n\}+[C^{pp}]\{\delta\dot{\boldsymbol{p}}^n\}+[K^{pp}]\{\delta\boldsymbol{p}^n\}=\{\delta\boldsymbol{F}^p\} \quad \text{(Eq. 4.72)}$$

where

$$[M^{pu}]=\int_v\{B_p\}^T\frac{[k]}{g}[N]dV \quad \text{(Eq. 4.73)}$$

$$[C^{pp}]=\int_v\{N_h\}^T\frac{n}{K_w}\{N_h\}dV \quad \text{(Eq. 4.74)}$$

$$[K^{pp}]=\int_v\{B_p\}^T\frac{[k]}{\rho_w g}\{B_p\}dV \quad \text{(Eq. 4.75)}$$

$$\{\delta\boldsymbol{F}^p\}=\int_s\{N_h\}^T\delta\boldsymbol{Q}\,dS \quad \text{(Eq. 4.76)}$$

Finally, the matrix form of the coupled solid–fluid (u–p) finite element formulation for dynamic problem is

$$\begin{bmatrix}M^{uu} & 0\\ M^{pu} & 0\end{bmatrix}\begin{Bmatrix}\delta\ddot{\boldsymbol{u}}\\ \delta\ddot{\boldsymbol{p}}\end{Bmatrix}+\begin{bmatrix}0 & 0\\ K^{upT} & 0\end{bmatrix}\begin{Bmatrix}\delta\dot{\boldsymbol{u}}\\ \delta\dot{\boldsymbol{p}}\end{Bmatrix}+\begin{bmatrix}K^{uu} & K^{up}\\ 0 & K^{pp}\end{bmatrix}\begin{Bmatrix}\delta\boldsymbol{u}\\ \delta\boldsymbol{p}\end{Bmatrix}=\begin{Bmatrix}\delta\boldsymbol{F}\\ \delta\boldsymbol{F}^p\end{Bmatrix} \quad \text{(Eq. 4.77)}$$

4.2.4 Newmark's method

Implicit direct integration technique is applied in this study. Eq 4.77 can be solved using the incremental form of the Newmark's method which can be defined as

$$[M]\Delta\ddot{\boldsymbol{u}}+[C]\Delta\dot{\boldsymbol{u}}+[K]\Delta\boldsymbol{u}=\Delta\boldsymbol{F}_{ext} \quad \text{(Eq. 4.78)}$$

The above equation is applied to obtain the incremental acceleration $\Delta\ddot{\boldsymbol{u}}$, then the incremental velocity and displacement can be determined using the follow equations.

$$\Delta\dot{\boldsymbol{u}}=\Delta t\ddot{\boldsymbol{u}}+(\gamma\Delta t)\Delta\ddot{\boldsymbol{u}} \quad \text{(Eq. 4.79)}$$

$$\Delta\boldsymbol{u}=\Delta t\dot{\boldsymbol{u}}+\frac{1}{2}\Delta t^2\ddot{\boldsymbol{u}}+(\Delta t^2\beta)\Delta\ddot{\boldsymbol{u}} \quad \text{(Eq. 4.80)}$$

where γ and β is the constant for conducting the numerical calculation, in this study, the

average acceleration method is used. Therefore, $\gamma = {}^{1}/_{2}$ and $\beta = {}^{1}/_{4}$ was applied, respectively.

By introducing Eq. 4.79 and Eq. 4.80 into Eq. 4.78, we obtain Eq. 4.81 which is simply implemented and therefore used in the to obtain the solution of the Eq. 4.77 in this study.

$$[\hat{M}]\Delta\ddot{\boldsymbol{u}} = -[K](\Delta t\dot{\boldsymbol{u}} + \Delta t^2\beta\ddot{\boldsymbol{u}}) - [C](\Delta t\ddot{\boldsymbol{u}}) - \Delta\boldsymbol{F}_{ext} \quad \text{(Eq. 4.81)}$$

where

$$[\hat{M}] = [K](\Delta t^2\beta) - [C]\left(\frac{\Delta t}{2}\right) + [M] \quad \text{(Eq. 4.82)}$$

4.3 Site description and input motions

4.3.1 Fujinuma dam

The Fujinuma dam was an earth–fill embankment dam in Sukagawa city, Fukushima prefecture, Japan. It was established on the Ebana river, a tributary of the Abukuma river, 16 km west of the city office of Sukagawa city (37°18′07″N, 140°11′41″E)(Wikipedia[7]). The dam was constructed in 1937 and it was completed in 1949 after construction was halted due to World War II. The dam served the primary purpose of water supply for irrigation. The typical cross section of the main dam and its layout were shown in Figs. 4.1 and 4.2. The dam was 18.5 m in height and 133 m in long embankment–type with a structural volume of 99,000 m^3 and a crest width of 6 m. Also, there is an auxiliary dam with a height of about 6 m and length of approximately 60 m. The dam sat at the head of a 8.8 km^2 drainage area and its reservoir had a capacity of 1,504,000 m^3.

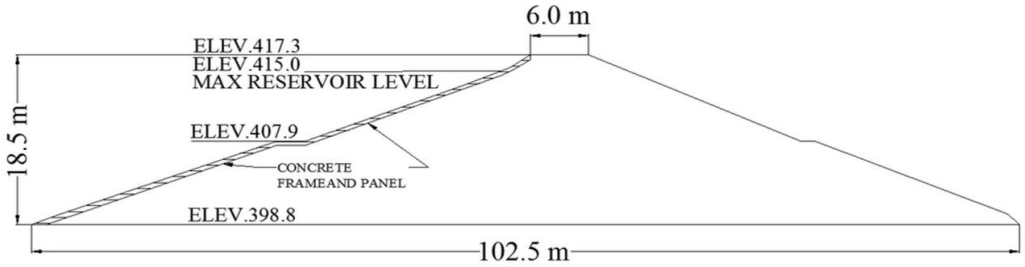

Fig. 4.1 Typical cross section of the main dam

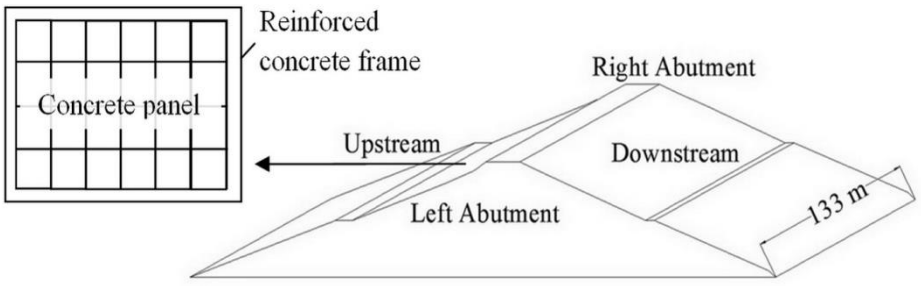

Fig. 4.2 Main dam layout

In this study, 956 triangular 15–noded elements with three–point Gaussian integration, a second-order polynomial interpolation for the displacements, and a first–order interpolation for the pore water pressure were used. Two dam models have been proposed for this study. The first model is a simplified version of the original shape of the Fujinuma dam's typical section and in this study the effect of the concrete frames and panels, and the interaction among them and dam is not taken into account (Fig. 4.3), and the latter is based on the remains of the failed dam following the site investigation (Chapter 3). The first model was used for conducting a dynamic analysis to acquire the dynamic behavior and failure mechanism. The second dam model was used to determine the dam mode shape and natural frequency, and for verification against the microtremor observations. The modal analysis was conducted using ANSYS code [8].The foundation was modeled by extending a 10–m–thick layer 100 m either side of the center. The boundary conditions were restrained in the horizontal and vertical directions at the bottom of the model. For both edges, the boundary conditions were fixed only in the lateral direction and were free in the vertical direction. To avoid the effects of wave reflection on the boundary, an absorbent boundary was applied at both ends and at the bottom of the boundary. The dam's body was classified into three portions: upper, middle, and bottom. The Young modulus is assumed to be constant in any of the three portions of the dam. In this study, for the dynamic analysis, the dam was analyzed under the maximum reservoir condition. The effect of reservoir pressure on the upstream face was applied as static pressure acting on the upstream slope in a direction perpendicular to the upstream face. To acquire the initial stress condition, the static and seepage analyses were conducted in advance. Dynamic analysis was performed using the Plaxis FE code [9].

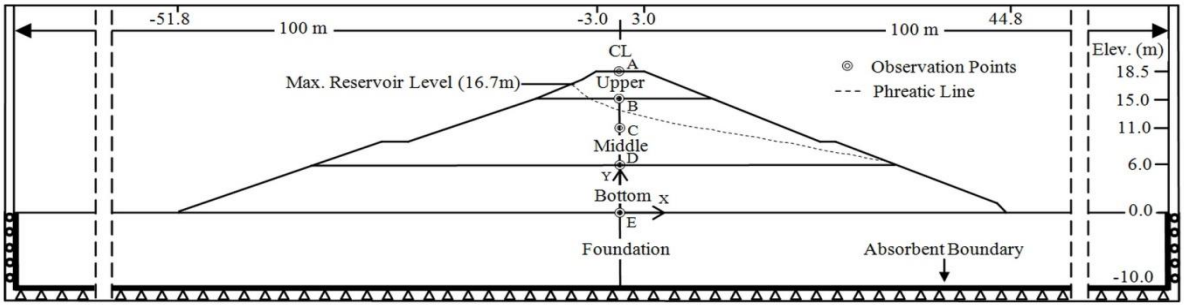

Fig. 4.3 Original dam model

4.3.2 Input motions

The 2011 Tohoku earthquake, or the so–called Great East Japan Earthquake, was a magnitude 9.0 (Mw) undersea megathrust earthquake off the Pacific coast of Japan, which occurred on 11 March 2011. The epicenter was about 70 km east of the Oshika Peninsula, in Miyagi prefecture, at a depth of approximately 32 km (JMA[10]). It was one of the most powerful earthquakes in the world since the establishment of the modern recording system. The ground motion records obtained from Station FKS017 and FKSH08, Sukagawa, Fukushima prefecture, Japan, was provided by the Kyoshin network and Kiban Kyoshin network that operated by the National Research Institute for Earth Science and Disaster

Prevention [11]. These data were observed about 15 km and 2 km away from the dam site, respectively. Furthermore, Hata et al. 2011 [12] also investigated the simulated ground motion at the dam site. They estimated the ground motion for the dam site by microtremor observation by using the site effect substitution method. These motions were used in the dynamic analysis of the dam. The peak ground acceleration a_{max} was 4.198, 3.10 and 4.25 m/s^2 for the observed motion, observed motion 2 and simulated motion, respectively (Fig. 4.4 a, b and e). The spectra of both motions are shown in Fig. 4c, d and f. The predominant period of all motions was 2.71, 2.23 and 2.96 Hz, respectively. The smoothed spectra of motions were also introduced by applying a 50–period moving average (50 per.Mov.Avg.) as shown in Fig. 4.4c, d and f. The predominant period of both motions was therefore 2.73, 2.23 and 4.40 Hz, respectively. In addition, to verify the effects of the phase of ground motion, the opposite wave forms of observed motion and simulated motions were also used as additional input motions for this study.

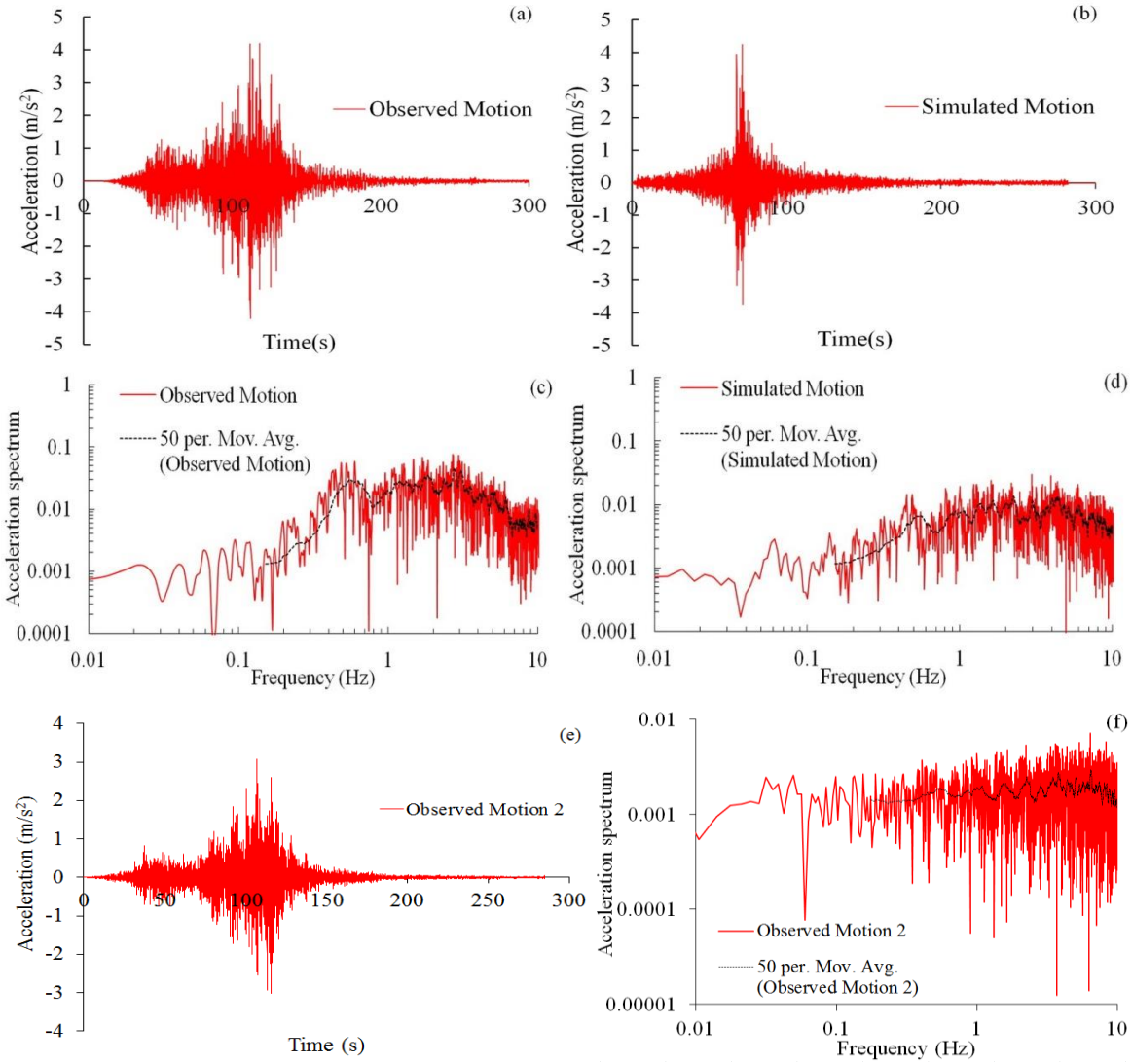

Fig. 4.4 Input motions. (a) Observed motion at FKS017 15 km from the dam site. (b) Simulated motion at the dam site [29]. (c) Spectrum of observed motion. (d) Spectrum of simulated motion. (e) Observed motion 2 at FKSH08 2 km from the dam site. (f) Spectrum of observed motion 2

4.3.3 Material properties

In fact, the soil behavior is nonlinear and to accurately reproduce the stress-strain relationship during dynamic load, it required the advanced constitutive law along with the finite element formulation at large deformation. As it is a preliminary study, the simple elastic–perfectly plastic model was applied and later the further analyzed will be conducted using the nonlinear finite element code and compared with current results. The behavior of the dam materials is described using the Mohr–Coulomb soil model, which is an elastic–perfectly plastic model with a yield surface whose elastic behavior is defined by isotropic elasticity through a linear Young's modulus E and Poisson ratio υ. In this study, the representative modulus of elasticity was applied using the initial stiffness of the actual soil's stress-strain curve obtained from the triaxial test. Actually, the smaller value of the primarily modulus of elasticity at larger strain can be selected however as the samples have been taken from the failed dam that might encountered the degradation of the modulus so the initial stiffness was applied in this study. The model has yield surfaces defined by cohesion c and friction angle ϕ. The generalization of the Coulomb friction failure law is then defined by

$$\tau = c - \sigma_n \tan\phi \qquad \text{(Eq. 4.83)}$$

In which τ : magnitude of the shearing stress, σ_n : normal stress, c : cohesion and ϕ : angle of internal friction. The Mohr–Coulomb failure surface is often expressed in terms of the invariants p, q, r as follow.

$$\left[(1/\sqrt{3})\sin(\theta + \pi/3) - (1/3)\tan\phi\cos(\theta + \pi/3)\right]q - p\tan\phi = c \qquad \text{(Eq. 4.84)}$$

where

$$\left.\begin{aligned} p &= \sigma_{ii}/3, \\ q &= \left(\sigma_{ii}\sigma_{jj} - \sigma_{ji}\sigma_{ij}\right)/2, \\ r &= det\sigma, \\ \theta &= (1/3)\arccos[(r/q)^3] \end{aligned}\right\} \qquad \text{(Eq. 4.85)}$$

The plastic flow rule used in this study was carried out using the associate flow rule in which the dilatancy angle is exactly the same value as the friction of angle so the same surface is applied for the normalized plastic rule.

The cyclic soil behavior of the simple elastic–perfectly plastic is illustrated in Fig.4.5. It can be seen that for stress states that fall within the yield surface, the behavior is purely elastic and all strains are reversible as showed at point A–B in Fig. 4.5. Thereafter, if the system was loaded further until it reached or exceeded the yield surface, the plastic strain or irreversible strain is occurred as defined as point B–C in Fig. 4.5. At this stage, the total strain is a combination between elastic and plastic strain which is defined as point C in Fig. 4.5. And if the system is unloaded, the elastic strain is then reduced and finally vanished, left only plastic strain when the system is at rest condition (Fig. 4.5 C–D). Similarly, when reloaded the system, the behavior is repeated from A–D in Fig .4.5 as mentioned earlier.

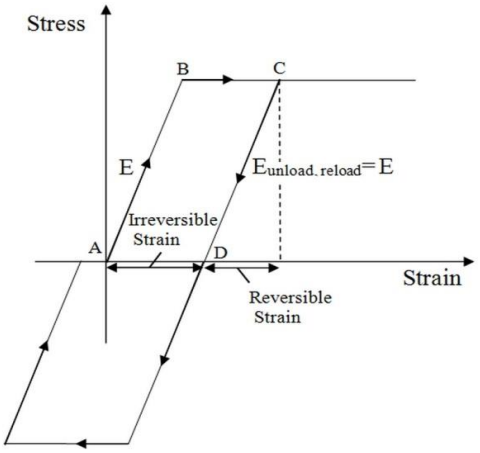

Fig. 4.5 The cyclic soil behavior using the simple elastic–perfectly plastic constitutive law

In dynamic analysis, this model produced elastic behavior without the hysteretic damping. In order to include the soil's damping characteristics, the Rayleigh damping is applied therefore. Biggs, 1964[13] suggested that for geological materials, the minimum critical damping ratio commonly falls in the range of 2% to 5%. Also, many researchers (Chen and Harichandran 2001[14], Anastasiadis et al. 2004[15], Chakraborty and Choudhury 2009[16]) conducted the dynamic analyses of an earth dam and applied the damping ratios of about 5% to 6%. Also, by using Mohr–Coulomb which is included the plasticity model, when the failure surface is reached the energy is subsequently dissipated though plastic deformation. Therefore, Rayleigh damping was assumed in the dynamic analysis by considering 5% damping in the frequency range of 1.64–2.45 Hz.

The parameters of dam material were mainly obtained from the laboratory experiments as mentioned earlier in Table 4.1 while the properties of the foundation were assumed. Each parameter used in the analysis can be described as the following. The dry and saturated unit weight was defining mass for the element located in dry and saturated area, respectively. Permeability or hydraulic conductivity was described fluid movement through porous media. In elastic range, modulus of elasticity, E indicated the relationship between stress and strain within the elastic region while Poisson's ratio, υ provided information on the effect of load in one direction to the deformation in other directions. Shear strength parameters, cohesion, c and friction of angle, ϕ are used to form the yield surface for this model. Lastly, by considering slightly compressibility of water, the rate of excess pore pressure is defined as K_w/n, in which K_w is the bulk modulus of water and n is the soil porosity.

Table 4.1 Soil properties

Materials	**Layer**	γ_{dry} **(kN/m^3)**	γ_{sat} **(kN/m^3)**	$k_y \cong k_x/4$ **(m/s)**	E **(GPa)**	K_w/n **(GPa)**	υ	C' **(kPa)**	ϕ' **deg**
Dam body	Bottom	16.0	18.00	$5.5x10^{-7}$	50.0	1.87	0.3	18.4	31
	Middle	14.0	16.00	$5.5\ x10^{-7}$	30.0	1.12	0.3	7.80	32
	Upper	16.0	18.00	$5.5\ x10^{-7}$	17.5	0.65	0.3	0.0	37
Foundation		30.0			300.0		0.2		

4.4 Analysis results

Analysis' results are expressed mainly consist of the modal analysis and the dynamic analysis. In the modal analysis, the fundamental mode shape and its corresponding frequency is presented. In case of the dynamic analysis, the dam's behaviours during the earthquake excitation using input motions are presented.

4.4.1 Modal analysis

Modal analysis is conducted to extract the natural frequency and its corresponding mode shape. In this study, two dam models were analyzed. Both cases were analyzed under the empty reservoir condition. In Fig. 4.6, the results of the modal analysis are shown. The natural frequency is 1.64 and 2.45 Hz for the first two modes, respectively. For the remaining dam model, the natural frequency is 2.35 Hz for the translational mode in the horizontal direction.

Fig. 4.7 shows the amplification ratio that was taken from the top of the remaining dam to two locations near the dam base of the upstream and downstream slopes, defined as 2/1 and 2/3, respectively. By comparing the numerical results with microtremor test results, it can be seen that in the latitudinal direction, the amplification ratio is within the range of 2–5 Hz. The results obtained from the modal analysis of the remaining dam agree well with field observations in relation to the vibration in the latitudinal direction. Therefore, the estimated predominant frequencies of the original dam are 1.64 and 2.45 Hz. The comparison between the natural frequency of the remains dam obtained from the microtremor observation and the modal analysis of the original dam model shows that the natural frequency of the actual dam model is less than the microtremor test. This is due to the geometry of the original dam which the dam's height is higher while the remains dam is plump in shape. It should be noted also that as the soils possibly subject to the large strain at the time of the dam failure that may cause degraded values of the shear modulus. As a result, the natural frequency of both microtremor test of the remains dam and the modal analysis result of the actual dam model may be different from the current results if the actual material properties can be acquired.

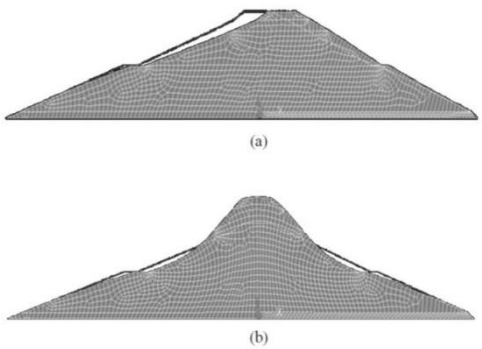

Fig. 4.6 Natural frequency. (a) 1st mode: 1.64 Hz (horizontal direction). (b) 2nd mode: 2.45 Hz (vertical direction)

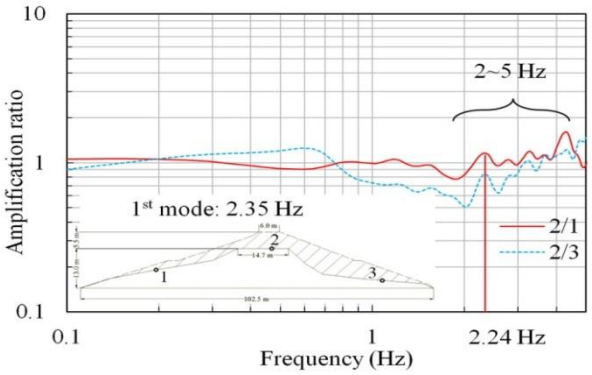

Fig. 4.7 Amplification ratio

4.4.2 Dynamic analysis

Dynamic analysis is performed to provide the possible behaviour of the dam during an earthquake. The results were expressed through the acceleration, displacement, shear strain, excess pore pressure and tension crack.

Acceleration

Results show that larger maximum crest acceleration can be obtained using inverse phase of the observed and simulated motions. Therefore, the acceleration contours at the time when the maximum acceleration reached the dam crest are shown in Figs. 4.8 and 4.9 for the observed and its inverse phase motions, respectively. By using the observed motion, the maximum crest acceleration is determined to be 7.42 m/s^2 and 8.56 m/s^2 accelerating towards the upstream direction at the time of 104.45 s and 111.60 s for normal and inverse phase motion, respectively. In case of the observed motion 2, the maximum crest acceleration is determined to be 7.06 m/s^2 accelerating towards the upstream direction at the time of 107.76 s (Fig. 4.10). For the simulated earthquake, the maximum crest acceleration is 7.60 m/s^2 acting towards the upstream direction at the time of 72.78 s (Fig. 4.11). Similarly, for its inverse phase, the crest experienced the maximum acceleration moving towards the upstream side with a magnitude of about 7.65 m/s^2 at 71.24 s (Fig. 4.12).

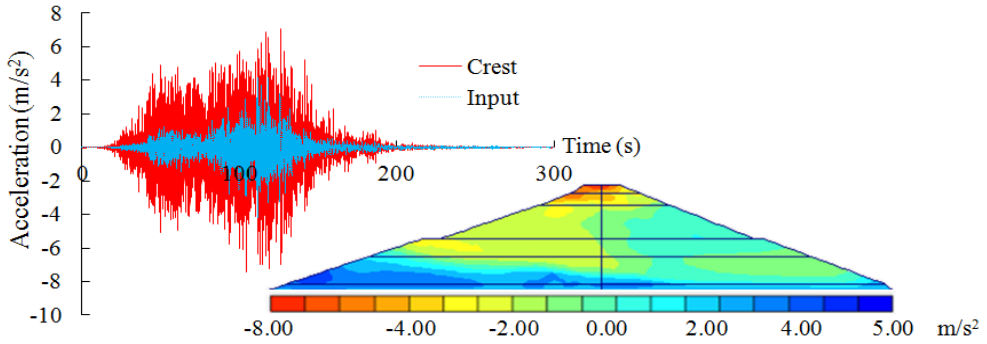

Fig. 4.8 Acceleration contours using the observed motion (actual dam model)

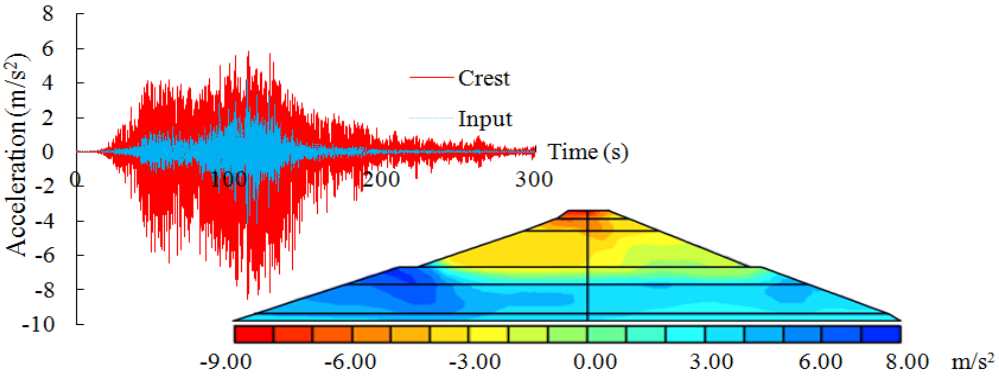

Fig. 4.9 Acceleration contours using the inverse phase of observed motion (actual dam model)

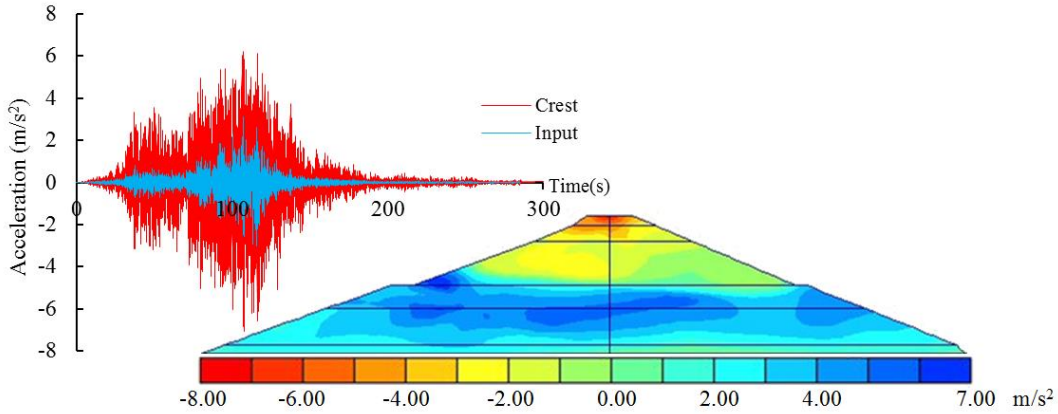

Fig. 4.10 Acceleration contours using the observed motion 2 (actual dam model)

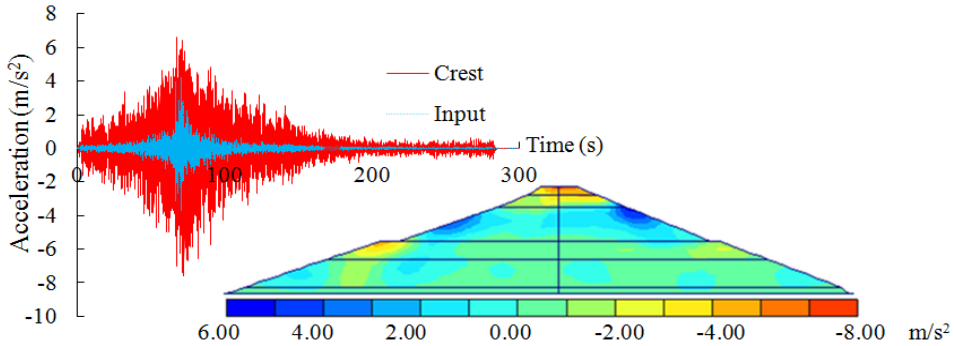

Fig. 4.11 Acceleration contours using the simulated motion (actual dam model)

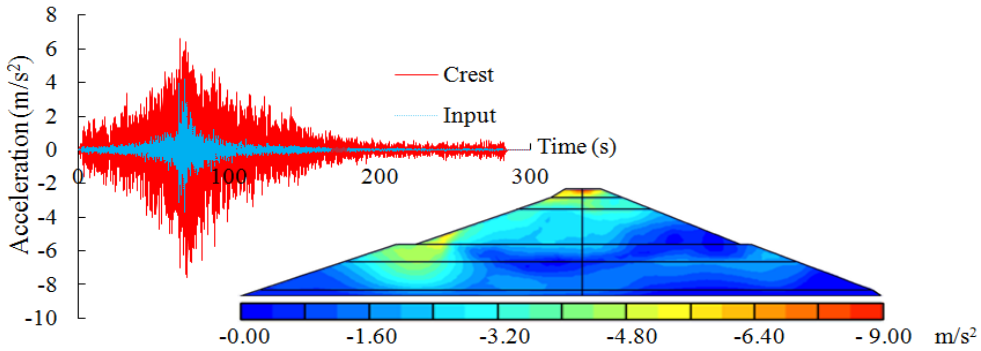

Fig. 4.12 Acceleration contours using the inverse phase of simulated motion (actual dam model)

The observed motion contains high–amplitude waves for a longer duration than the simulated motion. This generates a great response throughout the dam body resulting from significant inertial force acting on the dam. This causes a great amount of plastic deformation and eventually the dam failure owing to the loss of freeboard. In addition, regarding to the spectrum of the observed motion, it can be seen that this motion is characterized by a wide band. Therefore, it might possible induced resonance in the dam and caused a higher response. In contrast, the observed motion 2 and simulated motion contain high-amplitude waves only for a comparatively short period; thus, this does not contribute a sufficient effect to cause large movement and settlement of the dam.

For all motions, it can be seen that the acceleration at the dam crest is amplified significantly. The maximum amplification ratio taken from the crest to the base is 1.76, 2.28 and 1.79 for the observed motion, observed motion 2 and simulated motion, respectively. To verify the effects of the phase of ground motion, the opposite waveforms were used as input motions and amplification ratios of 2.03 and 1.80 were obtained for the observed and simulated ground motions, respectively. This indicates that the response is very sensitive to input ground motion.

Displacement

Deformation can be used for the evaluation of the safety of the dam due to freeboard loss. The results are expressed through its deformed shape and the displacement curve with respect to time at various heights along the dam centerline.

Fig. 4.13 shows the deformed mesh at 104.19 s and its corresponding displacement curves when subjected to the observed motion. It can be seen that the entire dam body was moved in the downstream direction. As time increases, plastic deformations were accumulated. This caused the permanent horizontal displacement Ux of 2.95 m, and crest settlement Uy reached 1.80 m at 104.19 s; this is considered as the point of dam failure due to the loss of freeboard. Settlements at other observation points yield a similar tendency, but the settlements were less with decreasing dam height. In addition, the deformed meshes and deformation curves in both directions, at the end of the shaking using the inverse phase of the observed motion, observed motion 2, simulated ground motion and its inverse phase motion, are shown in Figs. 4.14–4.17. These indicate that both horizontal and vertical displacements fluctuated during the earthquake and settled continuously at a rapid rate, and then remained constant until the end of the excitation. The permanent horizontal displacement of the dam was 3.40 m (upstream side), 0.38 m, 0.30 m, and 0.42 m for the inverse phase of the observed motion, observed motion 2, simulated, and inverse phase of simulated motion, respectively. The vertical displacement at the dam crest reached 2.90 m, 0.72 m, 0.63 m, and 0.60 m for the inverse phase of the observed motion, observed motion 2, simulated, and inverse phase of simulated motion, respectively. As a result, by considering overtopping failure, the dam was able to withstand safely the simulated input motion except for the case of using the inverse phase of the observed motion, for which overflow is expected to occur. However, the performance of a fill dam based on the performance based design concept (Tani et al. 2009[19]) recommended that the safety factor of 2.0 should be taken into account due to the simple constitutive law and the numerical analysis's error. Accordingly, it is recommended that the settlement of the crest should not exceed 1.0 m so the allowable settlement should be limited at 0.5 m. Also, in case of the observed motion 2, the upstream edge and downstream edge of the crest was settled by 0.92 m, when considering of taking the safety factor of 2.0 and FEMA 2005, the dam was not safe due to the loss of freeboard as well.

According to the facts, the dam experienced overflow and subsequent breach. The one possible cause is that the significant settlement of the dam body led to the loss of freeboard. Thus, the observed motion does reflect the actual failure mechanism of the dam, whereas the simulated motion does not. However, all cases show that settlement is high,

especially in the upper portion of the dam owing to its softness. For the changed phase, the observed motions show the significant effect of creating the displacement obtained from the normal and inverse phase, to be in opposite directions.

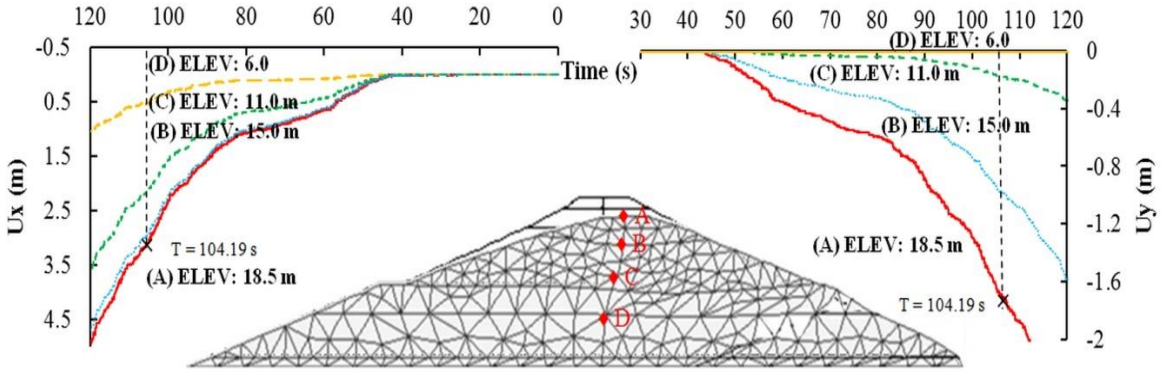

Fig. 4.13 Deformed mesh at 104.19 s using observed motion

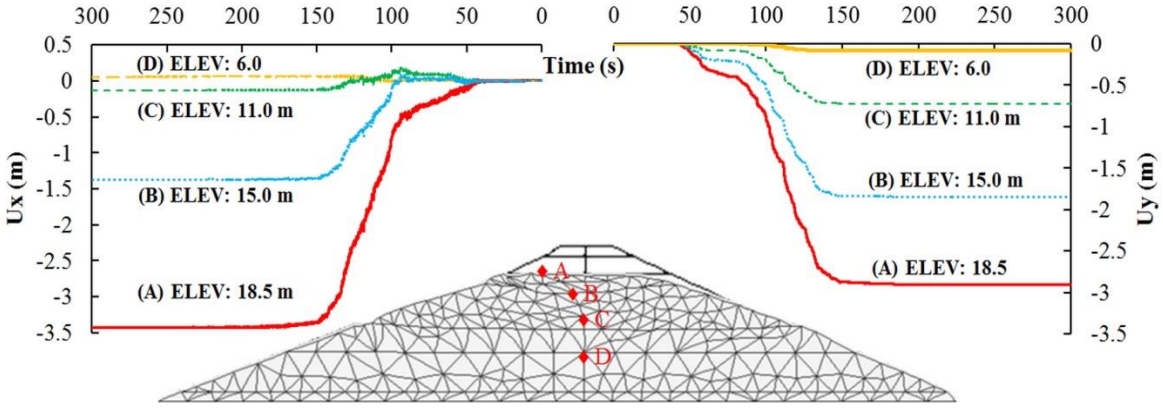

Fig. 4.14 Deformed mesh at end of the analysis using inverse phase of observed motion

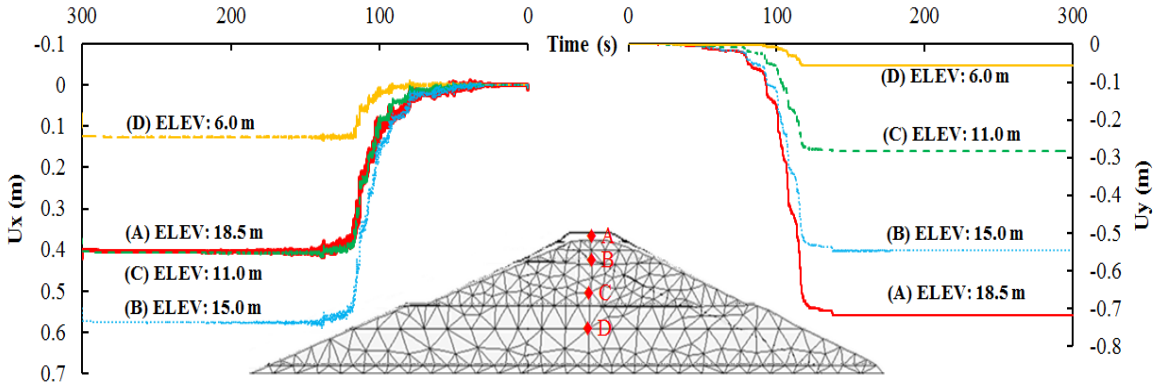

Fig. 4.15 Deformed mesh at end of the analysis using inverse phase of observed motion 2

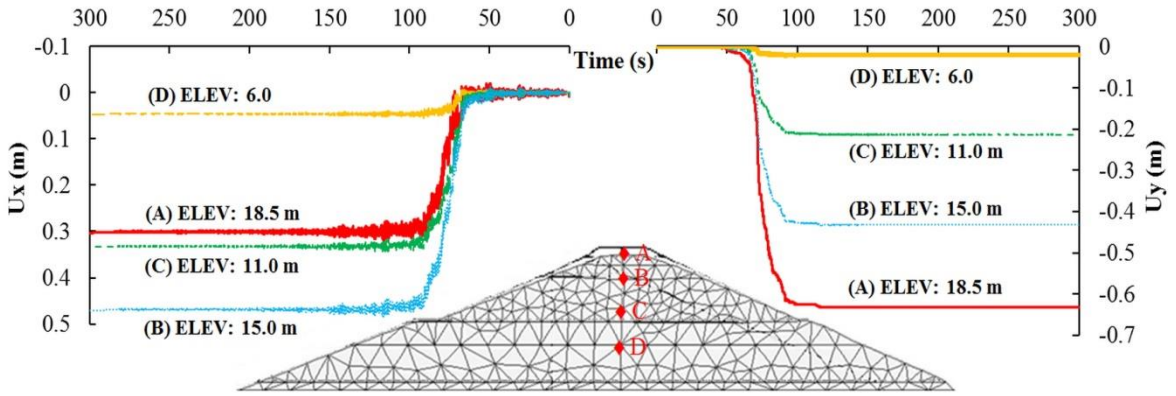

Fig. 4.16 Deformed mesh at end of the analysis using simulated motion

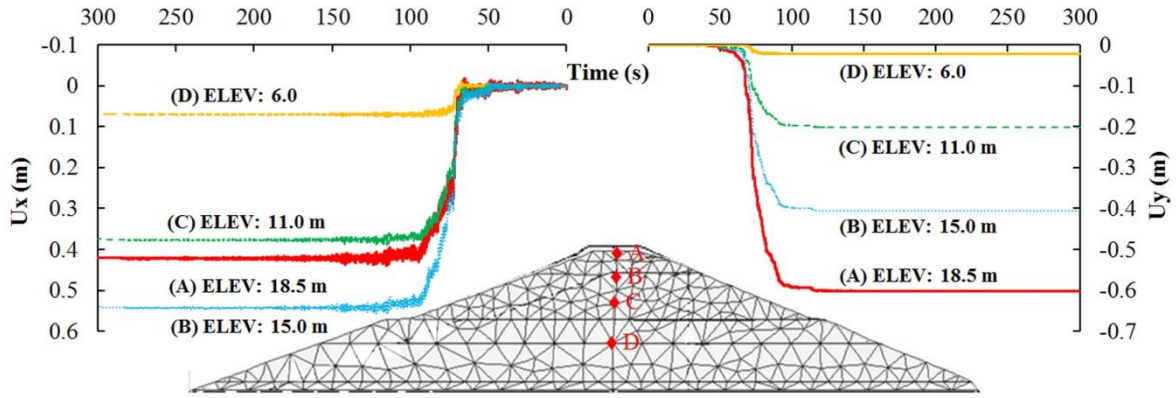

Fig. 4.17 Deformed mesh at end of the analysis using inverse phase of simulated motion

Shear strain

Shear strain provides information for understanding the location within the dam body that might be damaged severely during the earthquake excitation.

Shear strain contours for various times obtained using the observed motion are shown in Fig. 4.18. Most of the dam body experienced an insignificant rate of shear strain. It can be seen that initially, large shear strains occurred in the upper portion, especially on the upstream side. Thereafter, the occurrences of large shear strain can be observed clearly on both sides of the dam in the middle and bottom portions of the downstream slope. This excessive level of shear strain may indicate a possible cause for the dam failure. Similarly, shear strain contours obtained from the remaining motions, yield almost the same pattern as the previous motion (Figs. 4.19–4.22). However, the exception is when using an inverse phase of the observed motion, for which large shear strains can be seen on the upstream slope instead of on the downstream slope.

The sequence of dam failure has been reported by previous researchers. Initially, the dam experienced excessive deformation or a slide on the upper portion of the upstream slope. This, together with a subsequent large slide that occurred on the downstream face, yielded a loss of freeboard and triggered the overflow that resulted in the breaching of the dam.

Most numerical results show good agreement with this scenario, except for the case of using the inverse of the observed motion, which exhibited large strain appearing mainly on the upstream slope. The simulated motions also yield good agreement, but only with a smaller value of shear strain.

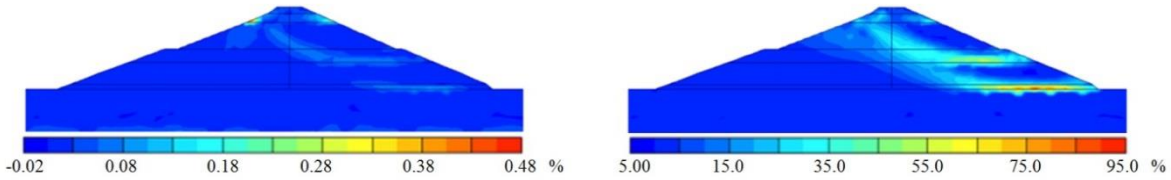

Fig. 4.18 Shear strain contours at 40 s and at 104.19 s using observed motion

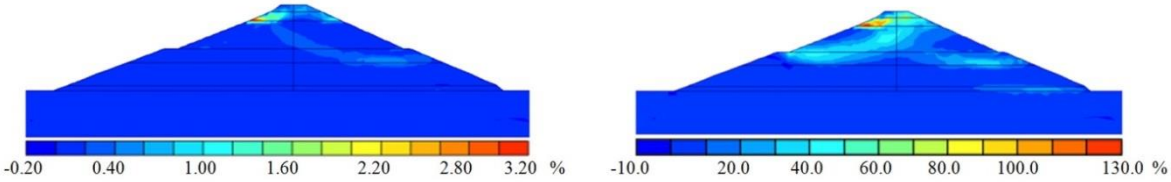

Fig. 4.19 Shear strain contours at 40 s and at the end of motion using observed motion (inverse phase)

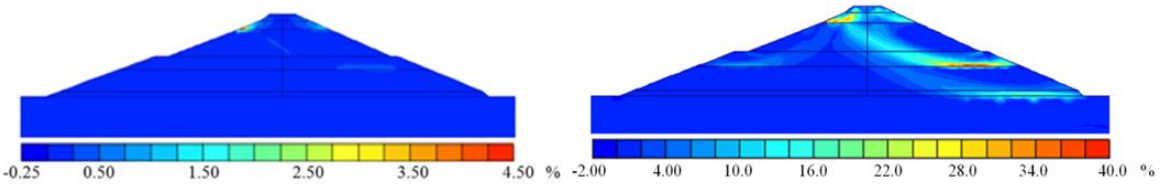

Fig. 4.20 Shear strain contours at 40 s and at the end of motion using observed motion 2

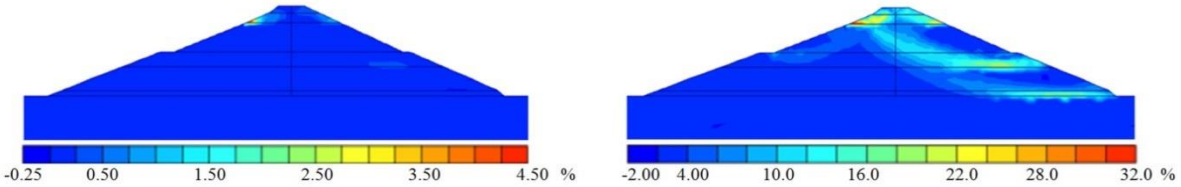

Fig. 4.21 Shear strain contours at 40 s and at the end of motion using simulated motion

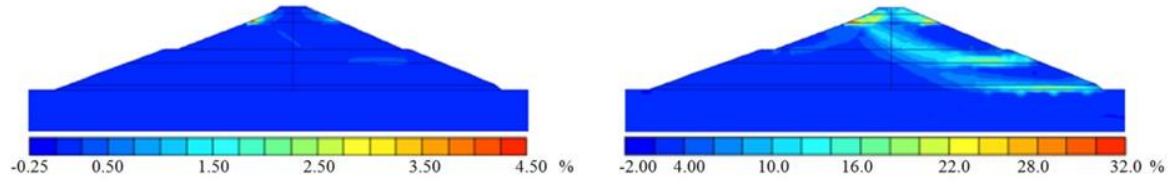

Fig. 4.22 Shear strain contours at 40 s and at the end of motion using simulated motion (inverse phase)

In addition, the mean effective stress and shear stress for the observed point A, B and C were shown in Figs. 4.23 and 4.24(B in magnified). It can be seen that the stress path was

fluctuated regard to the earthquake excitation and when the shear stress reached the Mohr–Coulomb failure surface at the corresponding mean effective stress, the further load was caused the plastic deformation while the stress value was kept constant at the yield point. For point C, as it subjected to the positive pore pressure, the effective stress at the end of earthquake became higher than its initial condition. In contrast, for point A (Fig. 4.24), it showed that at the end of the shaking the mean effective stress was reduced. And at point B, even there is a little change in effective stress but the shear stress almost reached the failure envelope after the earthquake. Therefore, it may indicated the instability such particular location and the sliding was expected to occur.

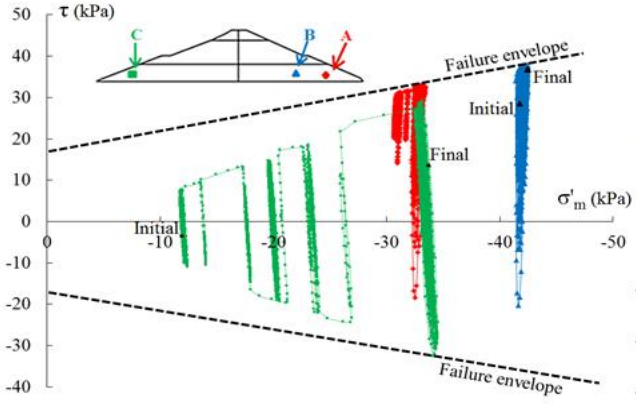

Fig. 4.23 Stress path

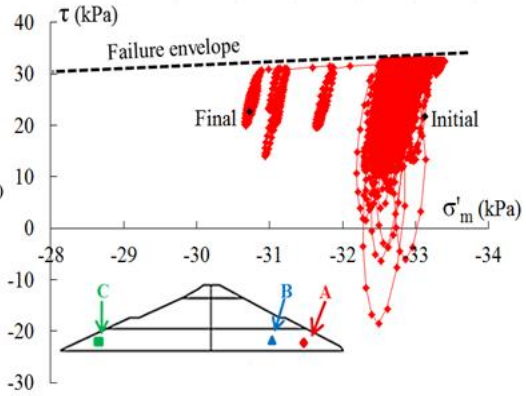

Fig. 4.24 Stress path

Excess pore pressure

The distribution of the excess pore pressure within the dam body and the records of the observation point A and B at 104.19 s using the observed motion are shown in Fig. 4.25. It can be seen that the excess pore pressure developed mostly at the downstream side. The maximum excess pore pressure was about 90 kPa and it can be found near the dam's base close to the dam center line. Besides, the suction or the positive excess pore pressure can be found on the upstream face and within dam's body on the upstream side. It can be seen that from the time history curves of the excess pore pressure at the observation point A and B that the build-up pore pressure was fluctuated at the early period of the shaking and then kept constant until the end of the excitation. The maximum excess pore pressure obtained from the observation point A and B was about 48 kPa and 18 kPa, respectively. In case of using inversed phase of the observed motion, the distribution of the excess pore pressure shows that the build–up pore pressure was mostly concentrated on the upstream side. The maximum excess pore pressure was about 90 kPa which can be found at the lower portion of the dam. On the other hand, on the downstream side, the excess pore pressure found to be in a range of 10–30 kPa and also the suction can be found at the downstream face.

For the Observed motion 2, the excess pore pressure found to be small throughout the dam body. The maximum build–up pore pressure was about 40 kPa which can be found at the lower portion of the dam. For both the simulated and inversed phase of the simulated motion, the similar trends were obtained. The excess pore pressure found to be scattered within the dam body. The upstream side experienced the build–up pore pressure of about

20–40 kPa. Whilst, the downstream side gained greater values of the excess pore pressure especially at the lower portion of the dam. The maximum excess pore pressure was about 80 kPa for both motions.

The results show that most of the dam body experienced the build–up pore pressure that was not high enough to equal the effective stress and trigger the total loss of the soil strength. The maximum ratio taken from the excess pore pressure to initial effective stress (EP/EF) was 0.9 that can be found in some parts within the downstream side while the most of the dam's body gained insignificant ratio. However, in particular locations such as on the downstream side where the effective stress found to be small, the reduction of shear strength can be fairly high and led to significant permanent deformation on those areas.

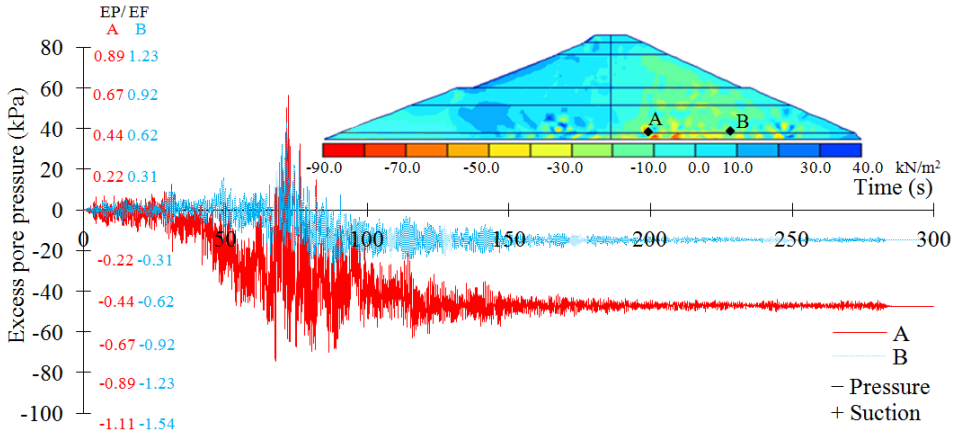

Fig. 4.25 Excess pore pressure

Tension crack

A tension crack is an extension fracture caused by tensile stress. Soil material normally has low tensile strength, and therefore it is possible for any small tensile stress, which might be a product of stretching deformation or positive pore pressure, to cause a tension crack in the soil structure. Besides, the materials used in this study, the middle and bottom, showed fairly high cohesion values which are prone to cracking. Therefore, this phenomenon is important and should be taken into account in this study. This crack provides information that might be useful for understanding the failure mechanism of the failed dam. The occurrence of tension cracks could initiate sliding or internal erosion of the dam structure.

In the analysis, it is possible to capture the tension crack during the shaking duration by illustrating the location in which the tensile stress does exceed the tensile strength. Fig. 4.26 summarizes the zone of the tension crack that occurred throughout the time of the analysis for both the observed and the simulated motion. It can be seen from both cases that the tension crack occurred similarly within the same location. This crack appeared clearly in the middle portion and at the toe for both sides. However, the tension crack on the upstream slope seems to penetrate deeper into the dam body. From this evidence, it would appear that sliding and internal erosion could be triggered, thereafter causing the failure of the dam. In addition, the recorded minimum principal stress σ_3' for the observed

points was shown in Fig. 4.26. It can be seen that the minimal principal stress was fluctuated during the shaking and when it reached 0 kPa which considering as tension cut–off, the further load in tension was caused the stretching plastic deformation, that in fact can lead to the tension crack in fill material, while the stress remained 0 kPa.

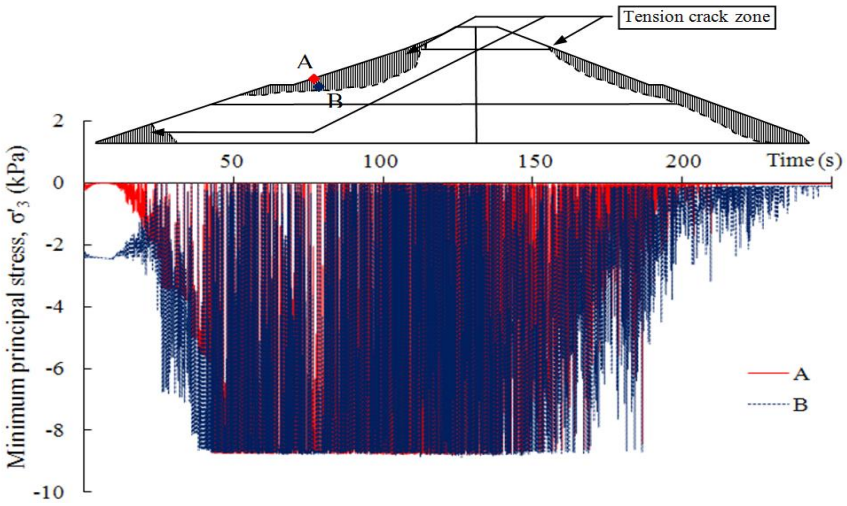

Fig. 4.26 Tension crack zone

4.5 Possible rehabilitation methods

Since, the knowledge on the earthquake engineering have been well established, concerned groups are now raising the awareness on the safety of their structures including dam. Therefore, many researchers (Perlea et al. 2004[17], Fade et al. 2008[18] and Tani et al. 2009[19]) proposed the possible seismic retrofitting methods for embankment dam such as adding downstream berms, increasing freeboard, enlarging a dam, replacing improper soil, enhancing drainage system, establishing an emergency action plan or even considering for no action. The suggestion and discussion for each retrofitting methods were presented. Eventually, the most proper technique has been recommended along with the comparison between other mitigations.

Among all, for strengthening soil structure, geogrid is now becoming popular due to its effectiveness. Previous researches (Wulandari and Tjandra 2006[20], Moradi et al. 2013[21]) conducted the study on the geogrid reinforced embankment. The results demonstrated that the geogrid could improve the stability of the embankment with comparatively higher than other conventional methods.

4.5.1 Proposed FE models

For studying the possible retrofitting method, there are five mitigations were proposed and analyzed to find out the proper mitigation for the studied dam. In dynamic analysis of these retrofit dam models, only simulated motion was used as input motion because it is quite difficult to compare each retrofitting methods when using the vigorous observed motion. The retrofitting techniques presented in this study are as the followings; 1) adding berm to the downstream slope by the half of the dam's height (hereafter, Retrofit 1). Retrofit 1

model is shown in Fig. 4.27a; 2) adding berm to the downstream slope by the same height of the original dam (hereafter, Retrofit 2). Retrofit 2 model is illustrated in Fig. 4.27b. For both the Retrofit 1 and 2 models, the amount of the added soil volume was about 20% of the actual dam volume and its properties were considered to be the same as the middle soil layer used in the original dam body; 3) enlarge dam by increasing dam height and adding downstream berm (hereafter, Retrofit 3). Retrofit 3 model is shown in Fig. 4.27c. The actual dam was enlarged by increasing crest height by 3.5 m, doubling the crest width and also adding downstream berm which total added soil volume was about 40% of the original dam volume; 4) lowering reservoir level (hereafter, Retrofit 4). Retrofit 4 model is exactly the same model with the original dam model except the level of the reservoir surface reduced by 10% (15.0 m) as shown in Fig. 4.27d; 5) geogrid reinforced dam (hereafter, Retrofit 5), some modifications were made. Geogrids were applied in the dam body with 3 m spacing between each layer form the bottom to the crest that resulting in a total of 7 geogrid layers (Fig. 4.28). The geogrid was modeled as a cable element which is considered only the axial rigidity and can only resist tensile force. In all retrofit models, the upper portion of the dam were replaced by the material that applied in the middle portion of the dam which considered as one of the strengthening methods for this dam except in the Retrofit 4 which is all material properties were kept as the original. In case of geogrid, the material properties were obtained from previous researchers [20, 21]. The geogrid parameters were defined only in term of axial rigidity, EA and tensile strength (Table 4.2).

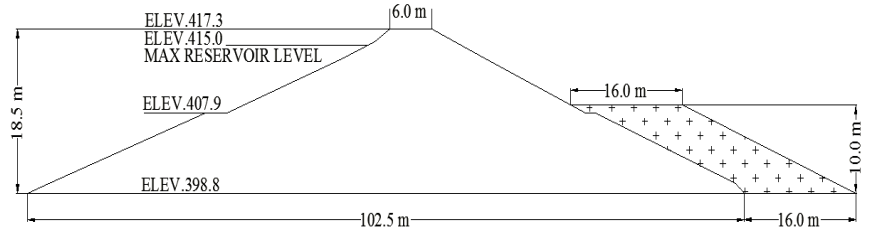

(a) Retrofit 1

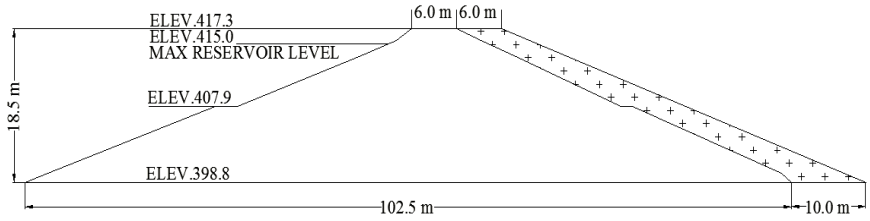

(b) Retrofit 2

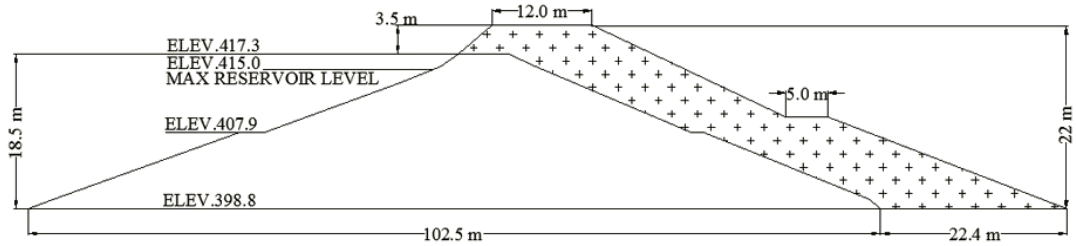

(c) Retrofit 3

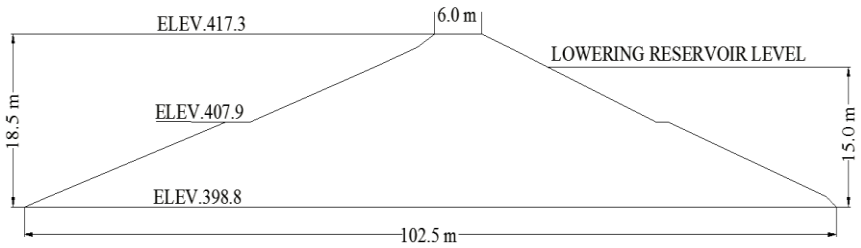

(d) Retrofit 4

Fig. 4.27 Retrofit dam models. (a) Retrofit 1. (b) Retrofit 2. (c) Retrofit 3. (d) Retrofit 4

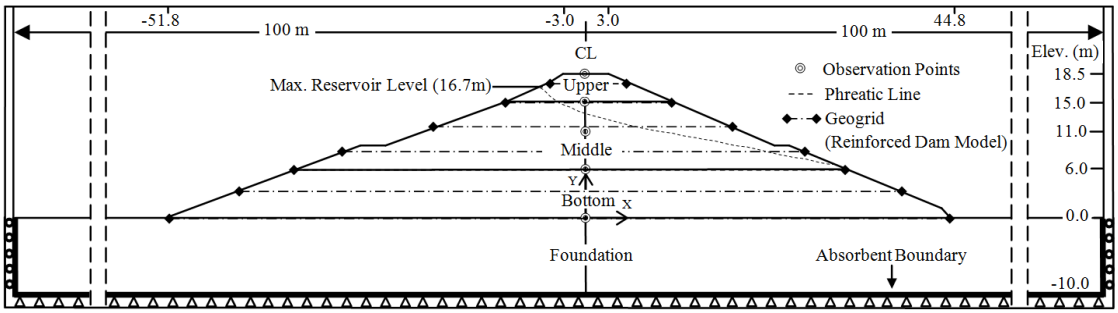

Fig. 4.28 Retrofit 5

Table 4.2 Geogrid Material properties

Material	Axial stiffness, EA (kN/m)	Tensile strength (kN/m)
Geogrid	$1.0x10^5$	200.0

4.5.2 Modal analysis results

Modal analysis is conducted to extract the natural frequency and its corresponding mode shape. All cases were analyzed under the empty reservoir condition. The result of the modal analysis of the actual dam model shows that the natural frequency is 1.64 and 2.45 Hz for the first two modes, respectively. The natural frequency of all retrofit dam models is therefore 1.76–2.61 Hz, 1.67–2.50 Hz, 1.40–2.14 Hz, 1.64–2.45 Hz and 1.77–2.65 Hz, respectively. The summaries of all proposed models were shown in Table 4.3.

Table 4.3 Summaries of the natural frequency of the proposed models

Model	Actual	Remaining	Retrofit 1	Retrofit 2	Retrofit 3	Retrofit 4	Retrofit 5
Mode 1	1.64 Hz	2.35 Hz	1.76 Hz	1.67 Hz	1.40 Hz	1.64 Hz	1.77 Hz
Direction	Horizontal						
Mode 2	2.45 Hz		2.61 Hz	2.50 Hz	2.14 Hz	2.45 Hz	2.65 Hz
Direction	Vertical						

4.5.3 Dynamic analysis results

A dynamic analysis is performed to determine the possible behavior of the dam during an earthquake. The results were expressed through acceleration, deformation, shear strain, excess pore pressure and tension crack.

Acceleration

For the retrofit models, all cases were analyzed by using the simulated motion only. The summaries of the crest acceleration with its direction and the maximum crest to base amplification ratio were shown in Table 4.4. The results showed that the maximum crest acceleration can be seen from the Retrofit 1 which is determined to be 9.63 m/s^2 accelerating towards the upstream direction. Whilst, the lowest maximum crest acceleration belongs to the Retrofit 4 that is about 8.11 m/s^2 acting toward the upstream side. For all cases, it can be seen that the crest acceleration is amplified obviously. The highest maximum amplification ratio taken from the crest to the base is 2.20 while the lowest is 1.91 using the Retrofit 1 and Retrofit 4, respectively.

The results show that the actual dam model is less sensitive to the excitation than the reinforced dam models. This is due to the higher rigidity provided in the retrofit models and also the actual model could easily displace and dissipate the energy from the earthquake excitation.

Table 4.4 Summaries of the acceleration of the proposed models

Model	**Actual**	**Retrofit 1**	**Retrofit 2**	**Retrofit 3**	**Retrofit 4**	**Retrofit 5**
Crest acceleration (m/s^2)	7.60	9.63	8.60	8.80	8.11	8.48
Direction (Upstream, U) (Downstream, D)	U	U	U	D	U	U
Amplification ratio	1.79	2.20	2.02	2.05	1.91	2.0

Deformation

In case of retrofit models, the permanent horizontal displacement at the dam crest was 0.57, 0.28, 0.005, 0.10 and 0.47 m for the Retrofit model 1 to 5, respectively. And, the settlement at the dam crest obtained using the Retrofit model 1 to 5, was 0.49, 0.22, 0.19, 0.57 and 0.39 m, respectively (Fig. 4.29). As a result, by considering overtopping failure, all models were able to withstand the simulated motion. However, due to uncertainty in the numerical analysis and the material model together with the previous study on the performance of a fill dam based on the performance based design concept (Tani et al. 2009[19]) suggested that the safety factor of 2.0 should be taken into account. Accordingly, it is recommended that the settlement of the crest should not exceed 1.0 m so the allowable settlement should be limited at 0.5 m. Therefore, all retrofit cases are able to satisfy this criterion except the actual dam model and the Retrofit 4.

The summaries of deformation using all models were shown in Table 4.5. By comparing

the actual dam model and the retrofit models, it can be summarized that the minimum crest settlement was obtained from the Retrofit 3 which is 70.1% dropped from the actual model. According to this, the effective retrofit methods are ranked from the Retrofit 3, Retrofit 2 and Retrofit 5 while the others not seem to be as effective as these three techniques in order to reduce the crest settlement.

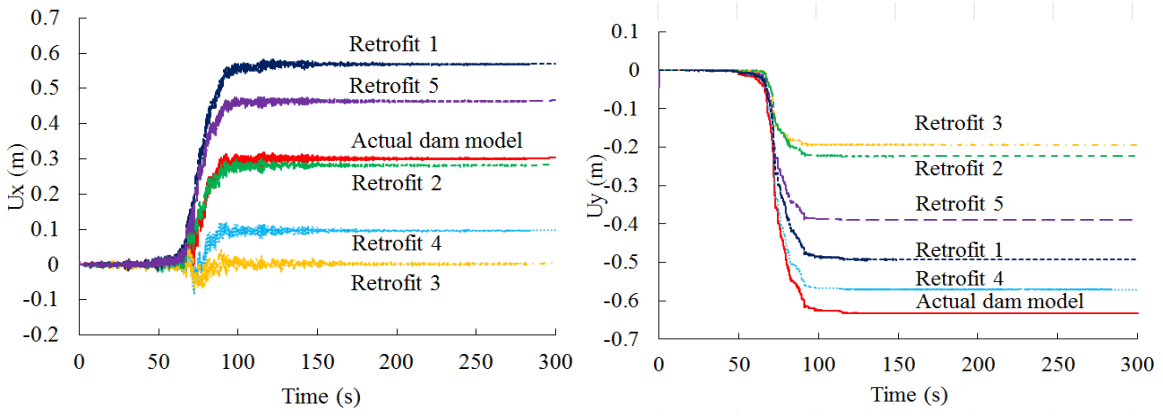

Fig. 4.29 Deformation curves at end of the motion using the simulated motion (all models)

Table 4.5 Summaries of the deformation of the proposed models

Model		**Actual**	**Retrofit 1**	**Retrofit 2**	**Retrofit 3**	**Retrofit 4**	**Retrofit 5**
Crest Deformation (m)							
Direction	Ux	0.30	0.57	0.28	0.005	0.10	0.47
	Uy	-0.65	-0.49	-0.22	-0.19	-0.57	-0.39
%	Ux	–	90.4	5.21	98.3	66.9	38.3
different	Uy	–	24.2	65.5	70.1	12.2	53.7

Shear strain

Shear strain contours at the end of the excitation obtained from the actual model and the Retrofit model 1 to 4 are shown in Figs. 4.30 and 4.31, respectively. Also, Shear strain contours of the Retrofit 5 for various times were shown in Fig. 4.32. Similarly, the same trend can be seen in the retrofit models but in smaller values and shear strain at the top portion appear to be vanished except only for the Retrofit 4 which the shear strain at the upper portion still can be observed. By comparing the actual dam model with all retrofit dam models, it can be drawn that the maximum value of shear strain obtained from retrofit dam models were greatly dropped by using the Retrofit model 2, 3 and 5. Therefore, Some of the proposed methods for retrofitting the dam are seems to be an effective measure for strengthening this structure especially it can solve a problem on the large shear strain at the top portion effectively.

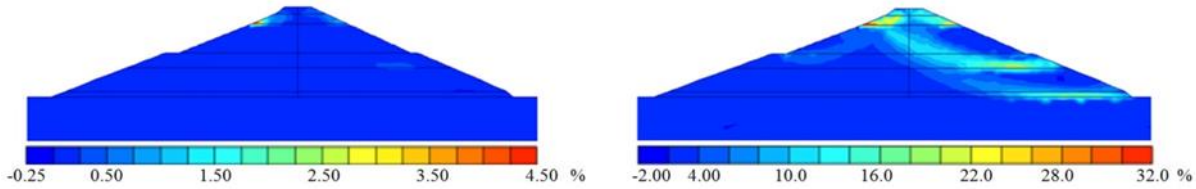

Fig. 4.30 Shear strain contours at 40 s and at the end of motion using the observed motion (actual dam model)

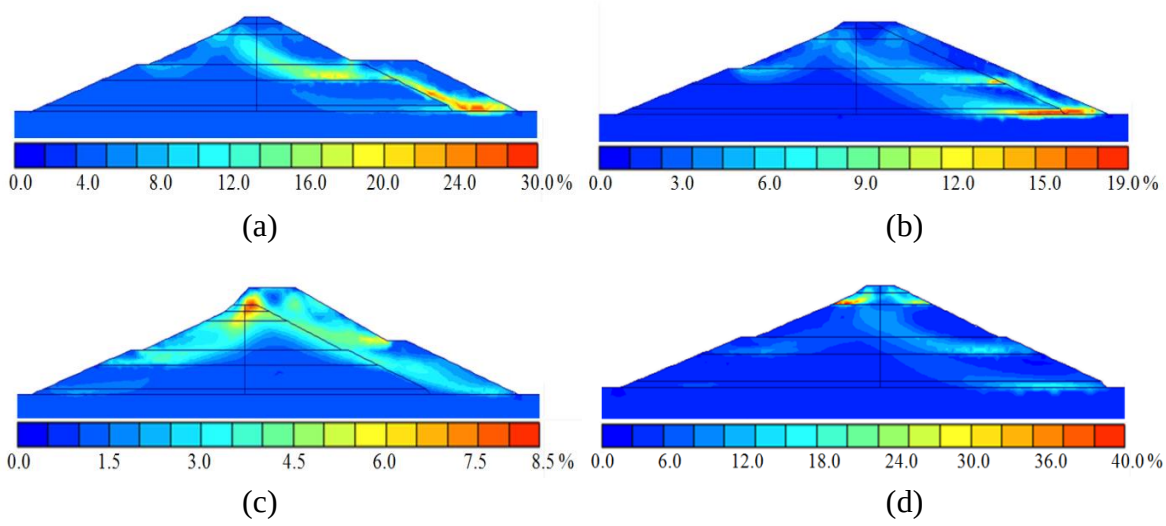

Fig. 4.31 Shear strain contours at the end of motion using the simulated motion.

(a) Retrofit 1. (b) Retrofit 2. (c) Retrofit 3. (d) Retrofit 4

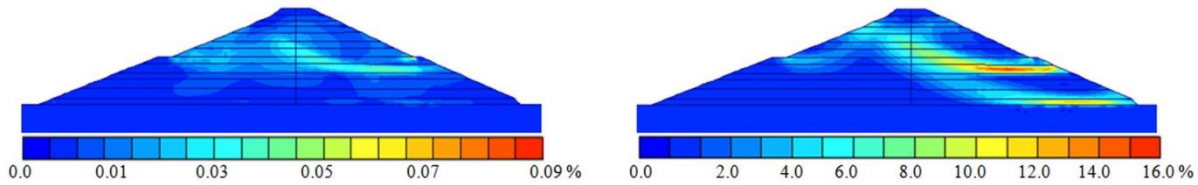

Fig. 4.32 Shear strain contours at 40 s and at the end of motion using geogrid reinforced dam model

Excess pore pressure

The distribution of the excess pore pressure within the dam body obtained from the Retrofit model 1to 5 are shown in Figs. 4.33–4.37. It can be seen that the excess pore pressure developed mostly at the lower portion of the upstream and downstream side. The maximum excess pore pressure was about 50 kPa for the Retrofit 1 to 3 and 70 kPa for Retrofit 4 and 5. Besides, the suction or the positive excess pore pressure can be found on the upstream face and downstream face. The results show that most of the dam body experienced the build–up pore pressure that was not high enough to equal the effective stress and trigger the total loss of the soil strength. The maximum ratio taken from the excess pore pressure to initial effective stress (EP/EF) was 0.9 for the Retrofit 1, 2, 4 and 5,

and 0.8 for the Retrofit 3 which this maximum ratio can be found in some parts within the downstream side while the most of the dam's body gained insignificant ratio. However, in particular locations such as on the lower portion of the dam where the effective stress found to be small, the reduction of shear strength can be fairly high and led to significant permanent deformation on those areas.

By comparing to the actual dam model, it can be seen that all retrofit models gave a slightly lower value of the built–up pore pressure. The most effective measure for reducing the effect of built–up pore pressure is the Retrofit 4 and 5. Even though they experienced the higher value of the maximum of the excess pore pressure than the rest, in most area within dam body, these models experienced smaller excess pore pressure.

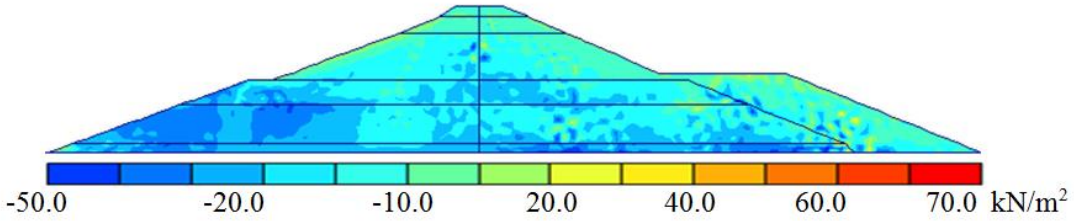

Fig. 4.33 Excess pore pressure of Retrofit 1

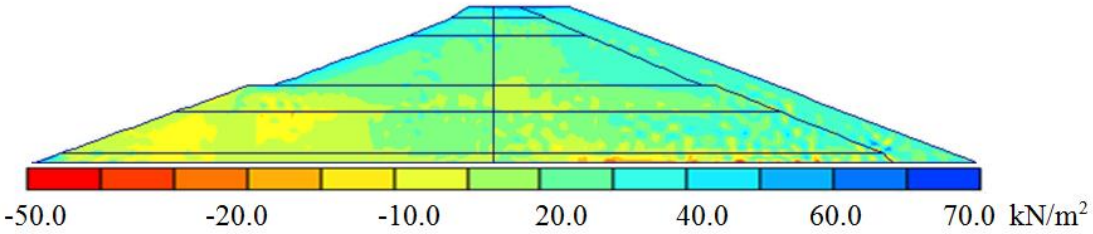

Fig. 4.34 Excess pore pressure of Retrofit 2

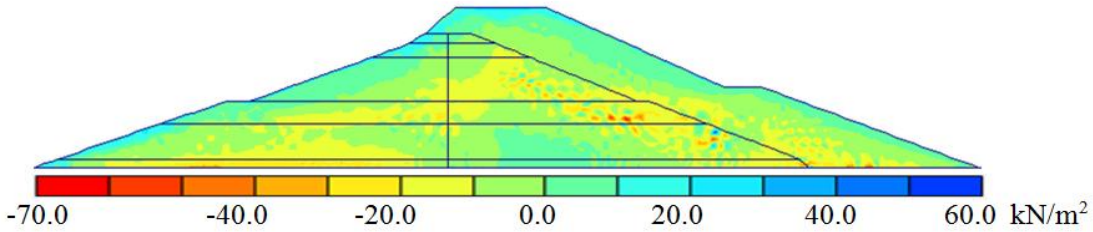

Fig. 4.35 Excess pore pressure of Retrofit 3

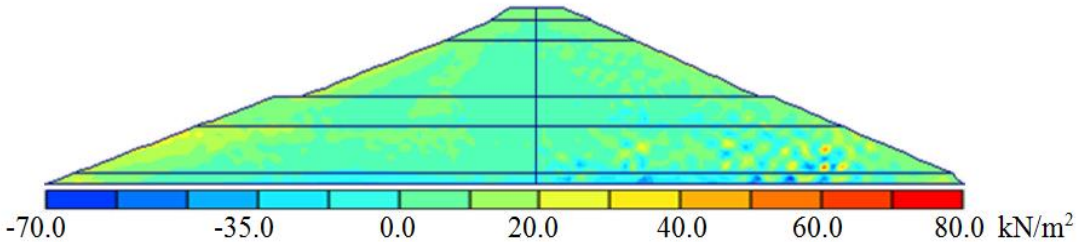

Fig. 4.36 Excess pore pressure of Retrofit 4

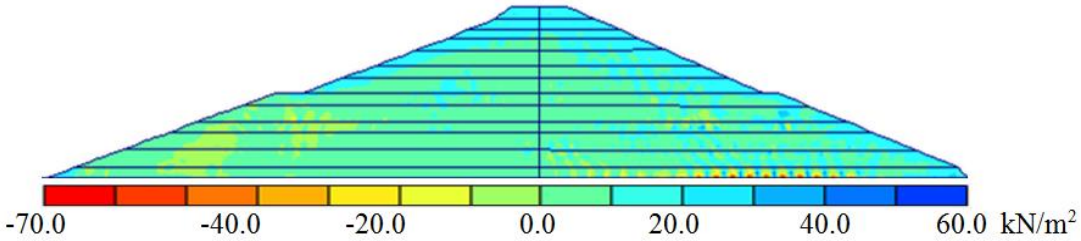

Fig. 4.37 Excess pore pressure of Retrofit 5

Tension crack

Regarding the retrofit models, tension cracks occurred similarly within the same location to the actual dam model. However, for reinforced dam models, the depth of tensile cracks appears to be shallower than the actual dam model and also the tensile cracks can be found at the upper portion and crest.

Possible mitigation for resisting the observed ground motion

In real situation, when the dam experienced the long duration earthquake like the observed motion used in the studied of the failure of the actual dam, only each mitigation measure might not be enough to preserve the dam from its failure. The combination of those techniques may be necessity in order to ensure seismic safety of the studied dam and being able to resist this energetic quake.

The possible measure for encountering the powerful shaking of the observed motion proposed in this study is a combination of various techniques as following. The actual dam was enlarged by increasing crest height by 3.5 m, doubling the crest width and also adding downstream berm which total added soil volume was about 40% of the original dam volume and geogrids were applied in the dam body with 1 m spacing between each layer form the bottom to the crest that resulting in a total of 23 geogrid layers. The installation pattern of the geogrid was shown in Fig. 4.38. In addition, to reduce the effect of the build–up pore pressure that might cause the reduction of shear strength, the seepage cut–off wall was applied at the dam centerline along the dam's height.

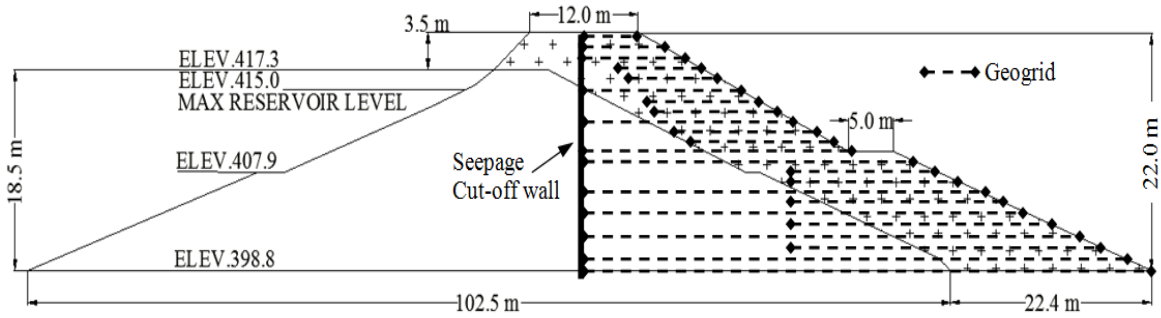

Fig. 4.38 Possible retrofitting method for resisting the observed motion

The proposed measure for the Fujinuma dam was analyzed using the observed motion. In this study, the geogrid and the cut–off wall was assumed to be not produce any chance in dynamic characteristic of the proposed dam model. Therefore, the first two fundamental natural frequency of the proposed dam model is 1.40–2.14 Hz that is equal to the Retrofit 3 model. The dynamic analysis results showed that the maximum crest acceleration is 8.80 m/s^2 toward downstream. The horizontal and vertical displacement at the dam's crest found to be 1.83 m and 1.98 m, respectively. The comparison between the results on the displacement field using the actual dam model and the proposed dam model were shown in Fig. 4.39. For the shear strain, the large shear strain can be found at the middle height of the dam with a smaller value than that in the actual dam model (Fig. 4.40). The excess pore pressure can be found at the downstream side especially at the dam's center line. The maximum excess pore pressure was about 100 kPa. The maximum ratio taken from the excess pore pressure to initial effective stress (EP/EF) was 0.8 for proposed model which this maximum ratio can be found at the middle portion near the dam's center line on the downstream side while the most of the dam's body gained insignificant ratio. However, due to the great value of effective stress, the proposed model was not vulnerable to liquefy (Fig. 4.41). In summary, the proposed model was capable to withstand the gigantic power of the observed motion as the crest settlement was not high enough to cause the overtopping failure (Freeboard length = 5.3 m). However, it might experience the large shear strain that might subsequently cause the slope instability and cracks. Even though, results showed that the dam was not failed, the large settlement did take place which might cause damages to the proposed dam.

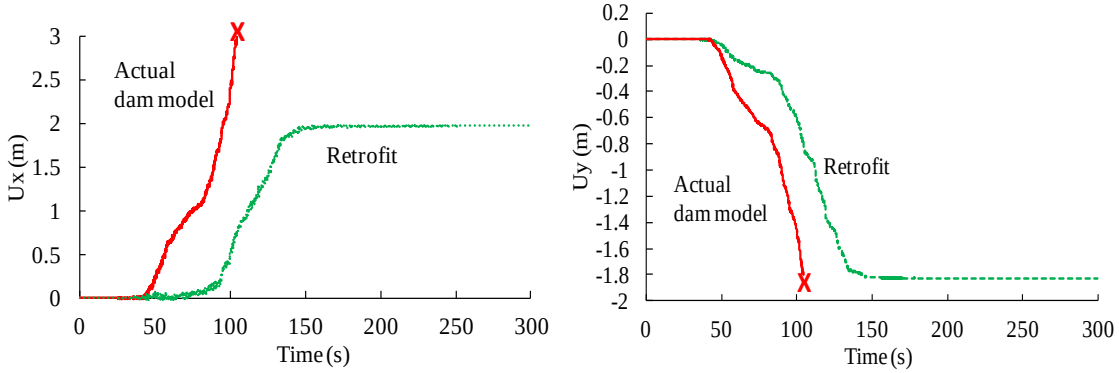

Fig. 4.39 Deformation curves at end of the dynamic analysis using the observed motion

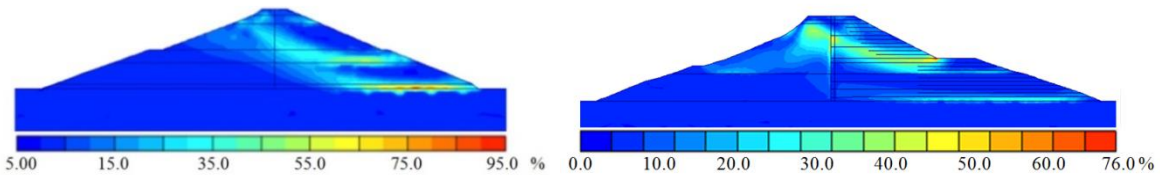

Fig. 4.40 Comparison of shear strain between the actual model at 104.19 s and retrofit model at the end of motion

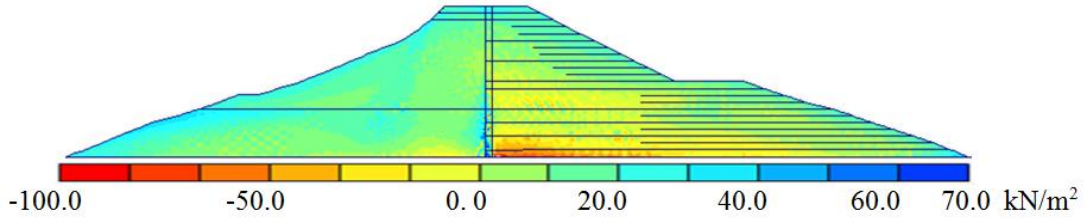

Fig. 4.41 Excess pore pressure of proposed method for resisting the observed motion

4.6 Conclusions and discussions

The numerical simulation results obtained using the observed motion show that the dam was subjected to the high amplitude and long duration earthquake. Also, the spectrum of the earthquake motion is characterized by a wide band that possibly induced resonance in the dam. Thus, the dam experienced significant amplifications throughout the dam body and this led to the great driving inertia force. In addition, with a long duration of shaking, the build-up pore pressure was then developed within the dam's body especially in the lower portion of the downstream side. Although, the excess pore pressure was not high enough to match the effective stress and trigger the liquefaction in those particular locations, soils might experience the reduction of the shear strength at the locations where the effective stress is small. Accordingly, large shear strain can be observed initially on the top portion of the dam and later the large shear strains can be found on the downstream side. Regards to the sliding patterns that occurred in the top portion and on the downstream slope, the dam was settled and the plastic deformation was then accumulated and become large until the dam's crest reached the reservoir level. Therefore, the dam failed owing to the loss of freeboard that might later cause the breaching of the dam. Furthermore, in all cases, large shear strains were observed initially in the upper portion of the upstream slope, following which large shear strains commenced on the downstream side. These, together with tension cracks, might evidently indicate the cause of the sliding failure of the dam slope. In addition, these sliding patterns exhibit good agreement with the facts gathered from field observations.

Several other failure mechanisms could describe the failure of the Fujinuma dam, such as the effect of the interaction between the concrete face and the dam, or the interaction between the reservoir and the dam. However, these effects were not taken into account in this study.

Through this study, it can be seen that the quality of compacting material in the upper portion might be one possible reason for the dam failure, which brought about such a disaster to those who lived downstream. Thus, this study demonstrates that it is very important not only to design a dam that is capable of withstanding future quakes, but that the investigation and maintenance of existing dams are crucial for continued seismic safety.

Although the numerical simulation results obtained in this study could describe the failure mechanism of the dam, this simulation is based on the small strain assumption. To gain insight into the failure mechanism of the soil structure, which is most likely to be within a large deformation regime, it is recommended to consider the effect of geometrical nonlinearity. Therefore, to address this suggestion, the development of the FE code for solving the problem at finite strain is recommended. Thus, the failure mechanism of the dam could be analyzed properly and results acquired that are more reliable. In addition, to describe other possible failure mechanisms, the material nonlinearity or other advanced constitutive laws and the proper fluid–structure interaction should be taken into account in future works.

There are five retrofitting techniques have been introduced in this study. Those methods were proposed in order to find out the suitable mitigation for retrofitting the existing dam that could possibly be applied for the similar cases in future for preventing the dam from its failure. Those retrofitting methods are; 1) Retrofit 1, added downstream berm by half of the dam's height; 2) Retrofit 2, added downstream berm by the same of the dam's height; 3) Retrofit 3, enlarged and increased dam height; 4) Retrofit 4, lowered reservoir level; and 5) Retrofit 5, applied geogrid reinforcement layers. All retrofit models were analyzed using the simulated motion because it is difficult to compare the results using the observed motion.

The results clearly indicated that the Retrofit 3, Retrofit 2 and Retrofit 5 are seem to be effective measures for reducing the risk of failure of this studied dam. Above all, the Retrofit 3 found to be most effective way for retrofitting the studied dam especially in case of existing dam due to its simplicity and also the crest settlement found to be smallest among other techniques. By raising the dam height and adding downstream berm, these together made this retrofit dam could safely resist the simulated motion. The Retrofit 2 also experienced a small crest settlement by just only expanded the crest width and added downstream berm by the same height of the original dam. The Retrofit 5 or geogrid reinforced model found also to be a good measure as it could reduce the crest settlement as well as the shear strain which is much smaller than that observed in the actual dam model. However, in case of retrofitting the existing dam, the Retrofit 2 and 3 are more appropriate as it is quite simply to construct while the geogrid reinforcement seems to be suitable for new constructing dam.

In real situation, when the dam experienced the long duration earthquake like the observed motion used in the studied of the failure of the actual dam, only each mitigation measure might not be enough to preserve the dam from its failure. The combination of those techniques may be necessity in order to ensure seismic safety of the studied dam and being able to resist this energetic quake.

In summary, the proposed model was capable to withstand the gigantic power of the observed motion as the crest settlement was not high enough to cause the overtopping failure (Freeboard length = 5.3 m). However, it might experience the large shear strain that might subsequently cause the slope instability and cracks. Even though, results showed that

the dam was not failed, the large settlement did take place which might cause damages to the proposed dam.

Most mitigation techniques proposed here in this study were mainly focused on the structural strengthening. Yet, the best solution needs to take into account of many factors like; workability, economy and the important of the dam, effect to downstream site, for selecting the most suitable method for each case. Therefore, where compromised between the retrofitting method, cost and the accepted damage level could be met, other measures such as early planning, establishing inundate map and making evacuation plan or even "no action" might considered to be possible mitigation for this dam as well.

Through this study, it can be seen that there is always a risk for those people who lived near the dam site especially at downstream side. The Fujinuma dam was an existing dam which constructed in the past when the modern seismic design was not yet established. Also, the seismic safety evaluation of this dam using the state of the art techniques was not conducted. In fact, this study presented only one case, there are still numerous of existing fill dams were needed to be evaluate their seismic safety to ensure the safety of people and their properties. Therefore, the seismic safety evaluation of existing dams is crucial and indeed urgent. Otherwise, when future quake strikes it might bring about a disaster to those who live downstream. Thus, this study demonstrates that it is very important not only to design a dam that is capable of withstanding future quakes, but the investigation, maintenance and mitigation of existing dams are vital for seismic safety of dam

REFERENCES

[1] M.A. Biot, General theory of three–dimensional consolidation, Journal of Applied Physics, 12 (1941) 155-164.

[2] K. Terzaghi, Theoretical Soil Mechanics, John Wiley and Sons, New York, 1943.

[3] C. S. Morrison, The development of a modular finite element program for analyses of soil–structure interaction, Doctoral Dissertation, Geotechnical Engineering Division, Department of Civil Engineering, Virginia Polytechnic Institute and State University, Blacksburg, 1995.

[4] O. C. Zienkiewicz and T. Shiomi, Dynamic behavior of saturated porous media; The generalized Biot formulation and It's numerical solution. International Journal for Numerical and Analytical Methods in Geomechanics, 8(1984) 71–96.

[5] A. Settari and H. S. Price, Simulation of hydraulic fracturing in low permeability reservoirs, SPE Journal, (1984)141–152

[6] K. Terzaghi, R. Peck, Soil Mechanics in Engineering Practice (second ed.), Wiley, New York, 1967.

[7] Wikipedia. [Online]. Available: /http://en.wikipedia.org/wiki/Fujinuma_Dam. [accessed 07/01/12]

[8] Japan Meteorological Agency (JMA). [Online]. Available:

/http://www.jma.go.jp/en/quake/ [accessed 06.07.12]

[9] National Research Institute for Earth Science and Disaster Prevention (NIED). [Online]. Available: /http://www.kyoshin.bosai.go.jp. [accessed 06.01.12]

[10] Y. Hata, S. Nakamura, A. Nozu, Seismic waveform evaluation at the Fujinuma Dam for the 2011 off the Pacific coast of Tohoku Earthquake–Application of site effect substitution method to a huge subduction earthquake, Journal of Structural Engineering, JSCE, 58A (2011) 250–263.

[11] ANSYS., ANSYS Structural Analysis Guide, ver. 14.5, 2010.

[12] R. B. J. Brinkgreve, P. A. Vermeer, Plaxis ver. 7, Material models manual, Balkema, Rotterdam, 1998.

[13] J. M. Biggs, Introduction to Structural Dynamics. New York, McGraw–Hill, 1964.

[14] M.T. Chen, Harichandran, Response of an earth dam to spatially varying earthquake ground motion, Journal of Engineering Mechanics, 127, No. 9, (2001) 932–939.

[15] A. Anastasiadis, N. Klimis, K. Makra, B. Margaris, On seismic behaviour of a 130 m high rockfill dam: an integrated approach. Proceeding of the 13th Conference on Earthquake Engineering,Vancouver, Canada, 2933 (2004).

[16] D. Chakraborty, D. Choudhury, Investigation of the Behavior of Tailings Earthen Dam Under Seismic Conditions. American Journal of Engineering and Applied Sciences 2, 3, (2009) 559–564.

[17] V. Perlea, D. Mathews and W. Empson, Evaluation of alternatives for earthquake hazard mitigation of an embankment dam in Kansas. Proceeding of the 13th world conference on earthquake engineering, Vancouver, B.C., Canada, August 1–6, 1895(2004).

[18] M. Fade, M. Yazdani and A. Azad, Seismic retrofit of embankment dams based on dynamic nonlinear analyses, Proceeding of the 12th international conference of international association for computer methods and advances in geomechanics(IACMAG), October 1–6, Goa, India, (2008).

[19] S. Tani, S. Tsukuni and T. Shiomi, Performance of a fill dam based on the performance–based design concept and study of a seismic retrofitting method, Journal of Soils and foundations, 49(6)(2009)841–851.

[20] P. S Wulandari and D. Tjandra, Determination of optimum tensile strength of geogrid reinforced embankment. Proceeding of the International Civil Engineering Conference "Towards Sustainable Civil Engineering Practice", Surabaya, August 25–26, (2006).

[21] G. Moradi, A. Abdolmaleki, M. Ahmadvand and H. Ghadami. Stabilization of rock slopes using geosynthetic materials as new approach and its comparison with conventional methods. International symposium on advances in science and technology, Bandar–abbas, iran, 7–8 march, (2013).

CHAPTER V

FINITE ELEMENT FORMULATION OF POROUS MEDIA AT FINITE STRAIN

5.1 Introduction

The failure of the Fujinuma dam is known to be the first complete dam breakdown in Japan. Therefore, it is very important to determine the cause of failure and learn as much as possible from this event for minimizing the effects of such disasters and protecting other existing dams against future quakes. As mentioned, infinitesimal–strain analysis is valid only for small–strain problems. When deformation approaches the finite regime, the results obtained using the small–deformation approach are unreliable. As mentioned in Chapter 4, finite element codes for infinitesimal strain have been implemented by many researchers (for example, Lewis and Schrefler 1998[1], Zienkiewicz et al. 1998[2]). Although these codes are widely applied in both academic and practice, their limitations are recognized, especially when the strain is large. To overthrow such limitations, finite–strain finite element formulations for solids and structures have been developed and implemented by interested groups (Hibbitt et al. 1970[3], Bathe et al. 1975[4], Bathe and Ozdemir 1976[5], Gabriel and Bathe 1995[6], Bathe 1996[7], Crisfield 1997[8], etc.). Subsequently, researchers (Diebels and Ehlers 1996[9], Li et al. 2004[10], Regueiro and Ebrahimi 2010[11], Heider 2012[12], Sun et al. 2013[13], etc.) developed and implemented finite–strain finite element formulations for porous media. The code proposed herein is based mainly on the works of Li et al. 2004[10] and Regueiro and Ebrahimi 2010[11].

To implement a finite–strain finite element code, a formulation for determining the finite strain of porous media is developed. By deriving the governing equations to fix the reference or current coordinates and consider the solid and fluid as separate, the mixed formulation of both phases with respect to the reference coordinates is then presented. The formulation of finite deformation is most likely similar to the small–strain version but with some different assumptions, which explained in detail in this chapter.

The proposed code should be tested to verify the accuracy of the solution. Therefore, the result of the finite–strain finite element code is compared with the result of the analytical solution and small–strain finite element code within the small–strain regime. Given that generally, the effect of finite deformation is required to be considered in the failure analysis soil structures such as dams because the deformation involved can be very large. Then, dynamic analysis of the Fujinuma dam was performed using both small– and finite–strain finite element codes. Comparisons between the results obtained using finite– and small–strain finite element codes were then made.

This chapter first introduces the governing equation for porous media at finite–strain. Then, the finite–strain formulation is developed and presented in the weak form and finally with finite element formulation and its matrix form. Since, the finite element code at

finite–strain is developed, the verification against the analytical solutions is performed for both static and dynamic problems. Then, the dynamic analysis of Fujinuma dam using the proposed code is presented. Finally, the results, discussion, and comparison between small– and finite–strain finite element analyses are presented.

5.2 Implementation of the nonlinear u–p finite element code at finite strain

To develop the finite–strain finite element code, finite continuum mechanics and a governing equation for porous media are developed with the aim of establishing a governing formulation for this problem. Then, the weak form, final finite element formulation, and its matrix form are presented.

5.2.1 Governing equation

In nonlinear continuum mechanics, the reference configuration and current configuration are utmost important. For any motion defined in space, could be assumed as a continuum within a set of configurations. For each material point $\boldsymbol{X}$, we associate Lagrangian displacement, velocity and acceleration fields $\boldsymbol{u(X,t)}$, $\boldsymbol{v(X,t)}$ and $\boldsymbol{a(X,t)}$(Fig. 5.1).

$$\boldsymbol{u}(\boldsymbol{X},t) = \boldsymbol{x} - \boldsymbol{X} \qquad \text{(Eq. 5.1)}$$

$$\boldsymbol{v}(\boldsymbol{X},t) = \frac{\partial \boldsymbol{\phi}(\boldsymbol{X},t)}{\partial t} \qquad \text{(Eq. 5.2)}$$

$$\boldsymbol{a}(\boldsymbol{X},t) = \frac{\partial^2 \boldsymbol{\phi}(\boldsymbol{X},t)}{\partial t^2} \qquad \text{(Eq. 5.3)}$$

where $\boldsymbol{x} = \boldsymbol{\phi}(\boldsymbol{X},t)$, and $\boldsymbol{X}$ are the positions of material point $\boldsymbol{X}$ in the current and reference configurations, respectively. At any spatial point x now occupied by $\boldsymbol{X}$, we also associate fluid particles that completely fill up the voids of $\boldsymbol{X}$, with Eulerian velocity in the presence of diffusion given by

$$\overline{\mathbf{v}} = \overline{\mathbf{v}}(\boldsymbol{x},t) \neq \boldsymbol{v}(\boldsymbol{X},t) \qquad \text{(Eq. 5.4)}$$

If $\overline{\boldsymbol{v}} = \boldsymbol{v}$, then the fluid and solid phase move together as one body leading to a so–called undrained motion.

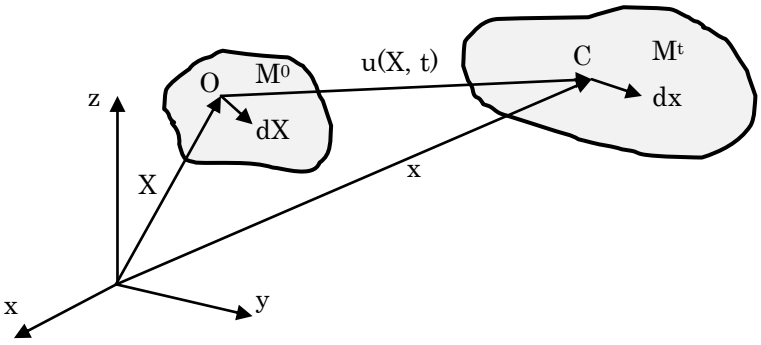

Fig. 5.1 motion of continuum

The deformation gradient $\boldsymbol{F}$ is the derivative of each component of the deformed $\boldsymbol{x}$ vector with respect to each component of the reference $\boldsymbol{X}$ vector. For the displacement $d\boldsymbol{x}$ of any point can be written as

$$d\boldsymbol{x} = \boldsymbol{x}(\boldsymbol{X} + d\boldsymbol{X}) - \boldsymbol{x}(\boldsymbol{X}) \quad \text{(Eq. 5.5)}$$

and the deformation gradient is then

$$\boldsymbol{F} = \frac{\partial \boldsymbol{x}}{\partial \boldsymbol{X}} \quad \text{(Eq. 5.6)}$$

Deformation tensors, unlike the small–strain where engineering strain could be simply applied, the deformation tensors used in finite–strain continuum mechanics, are the right and left Cauchy–Green deformation tensors.

The right Cauchy–Green deformation tensor defined as:

$$\boldsymbol{C} = \boldsymbol{F}^T \cdot \boldsymbol{F} \quad \text{(Eq. 5.7)}$$

Therefore, to evaluate the local displacement from the rigid body displacement, the concept of finite strain is introduced. The strains for large deformation is the Lagrangian finite strain tensor or known as the Green–Lagrangian strain tensor which can be written as

$$\boldsymbol{E} = \frac{1}{2}(\boldsymbol{C} - \boldsymbol{I}) \quad \text{(Eq. 5.8)}$$

For the current configuration, the Eulerian–Almansi finite strain tensor is applied which defined as

$$\boldsymbol{e} = \frac{1}{2}(\boldsymbol{I} - \boldsymbol{b}^{-1}) \quad \text{(Eq. 5.9)}$$

where

$$\boldsymbol{b} = \boldsymbol{F} \cdot \boldsymbol{F}^T \quad \text{(Eq. 5.10)}$$

and the relationship between the Green–Lagrangian strain tensor and the Eulerian–Almansi finite strain tensor is written as

$$\boldsymbol{E} = \boldsymbol{F}^T \boldsymbol{e}\, \boldsymbol{F} \quad \text{(Eq. 5.11)}$$

From this point forward, the operators divergence and gradient were specified in both current and reference configurations. Therefore, **grad** and **GRAD** represent the gradient operator for the current and reference configuration, respectively. And, div and DIV stand for the divergence operators for the current and reference configuration, respectively.

Balance of Mass

Denote that m_s and m_f is the mass of solid grains and fluid particles, respectively. The mass densities of solid grains and fluid particles by ρ_s and ρ_f, respectively, the total mass of mixture in an arbitrary deformed configuration are given by the volume integrals

$$m_s = \int_{\phi_t(u)} \rho_s(1-\varphi)dv \quad \text{(Eq. 5.12)}$$

$$m_f = \int_{\phi_t(u)} \rho_f \varphi dv \quad \text{(Eq. 5.13)}$$

Let $\frac{\boldsymbol{D}}{\boldsymbol{Dt}}$ denote the material time derivative, take the material time derivatives and localize the results from the argument of arbitrary, we get

$$\frac{\boldsymbol{D}m_s}{\boldsymbol{D}t} = \frac{\partial[\rho_s(1-\varphi)]}{\partial t} + div[\rho_s(1-\varphi)\boldsymbol{v}] = 0 \quad \text{(Eq. 5.14)}$$

for the solid phase, and

$$\frac{\boldsymbol{D}m_f}{\boldsymbol{D}t} = \frac{\partial(\rho_f\varphi)}{\partial t} + div(\rho_f\varphi\overline{\boldsymbol{v}}) = 0 \quad \text{(Eq. 5.15)}$$

for the fluid phase, where div is the spatial divergence operator, $\overline{\boldsymbol{v}}$ is intrinsic velocity of fluid phase. Note that the convected terms follow the motions of the respective constituent materials through their intrinsic velocities.

If instead of following the motion of each phase, the motion of the solid phase alone is followed, the total time derivatives with respect to the solid phase motion may take different forms. Let $\frac{\boldsymbol{D}m_s}{\boldsymbol{D}t}$ denote the total time derivative with respect to the solid phase motion, then for solid phase the total derivative is identical to the material derivative.

However, for the fluid phase the total time derivative of m_f following the solid phase motion is not zero, but instead represents the rate of fluid mass accumulation in the moving volume of the solid phase, and thus

$$\frac{\boldsymbol{D}m_f}{\boldsymbol{D}t} = \frac{dm_f}{dt} + \int_{\phi_t(\partial u)} \boldsymbol{q}\cdot\boldsymbol{n}da = 0 \quad \text{(Eq. 5.16)}$$

$$\frac{\partial(\rho_f\varphi)}{\partial t} + div(\rho_f\varphi\overline{\boldsymbol{v}} + \boldsymbol{q}) = 0 \quad \text{(Eq. 5.17)}$$

where $\boldsymbol{q}$ is the mass rate flow per unit current surface area, and $\boldsymbol{n}$ is the outward unit normal vector to the same surface area. The surface flux $\boldsymbol{q}$ is related to the solid and fluid velocities via expression

$$\boldsymbol{q} = \rho_f\tilde{\boldsymbol{v}}, = \tilde{\boldsymbol{v}} = \varphi\boldsymbol{v}^r, \boldsymbol{v}^r = \overline{\boldsymbol{v}} - \boldsymbol{v} \quad \text{(Eq. 5.18)}$$

where $\boldsymbol{v}^r$ is the relative velocity of the fluid phase to the solid phase and $\tilde{\boldsymbol{v}}$ is the superficial Darcy's velocity. By expanding equations Eq. 5.12 and Eq. 5.13, we have

$$-\frac{d\varphi}{\partial t} + (1-\varphi)\frac{1}{\rho_s}\frac{d\rho_s}{dt} + (1-\varphi)div\boldsymbol{v} = 0 \quad \text{(Eq. 5.19)}$$

for solid phase, and for the fluid phase as

$$\frac{d\varphi}{\partial t} + \frac{\varphi}{\rho_s}\frac{d\rho_f}{dt} + \varphi\text{div}\boldsymbol{v} + \frac{1}{\rho_f}div(\rho_f\tilde{\boldsymbol{v}}) = 0 \quad \text{(Eq. 5.20)}$$

In Eq. 5.20 $\frac{d\rho_f}{dt}$ is the total rate of change of mass density of the fluid phase contained in the solid skeleton volume and thus does not necessarily describe the deformation of the same fluid particles. By adding the last two equations, it gives the total mass conservation for the mixture which is

$$\mathrm{div}\dot{\mathbf{u}} + \frac{1}{\rho_f} div\left(\rho_f \tilde{\mathbf{v}}\right) + (1-\varphi)\frac{1}{\rho_s}\frac{d\rho_s}{dt} + \frac{\varphi}{\rho_s}\frac{d\rho_f}{dt} = 0 \qquad \text{(Eq. 5.21)}$$

for the incompressible solid and fluid, Eq. 5.21 becomes

$$div\boldsymbol{v} + div\tilde{\boldsymbol{v}} = 0 \qquad \text{(Eq. 5.22)}$$

Balance of momentum

For the solid phase, from Eq. 4.6, the definition of the effective stress, the linear momentum balance equation in the absence of momentum supplies due to chemical reaction with fluid takes the form

$$\int_{\phi_t(u)} \rho_s(1-\varphi)\cdot \boldsymbol{g} dv + \int_{\phi_t(u)} \boldsymbol{h}_s dv + \int_{\phi_t(u)} n\cdot \boldsymbol{\sigma}' da = \frac{\boldsymbol{D}}{\boldsymbol{D}t}\int_{\phi_t(u)} \rho_s(1-\varphi)\boldsymbol{v} dv$$

$$\equiv \int_{\phi_t(u)} \rho_s(1-\varphi)\mathbf{a} dv \qquad \text{(Eq. 5.23)}$$

where $\boldsymbol{g}$ is the vector of gravity acceleration, $\boldsymbol{h}_s$ is the flow–induced body force arising from the frictional drag of the fluid phase on the solid matrix, and

$$\boldsymbol{a}(\boldsymbol{X},t) = \frac{\partial^2 \boldsymbol{\phi}(\boldsymbol{X},t)}{\partial t^2} \equiv \frac{\partial \boldsymbol{v}(\boldsymbol{X},t)}{\partial t} + \boldsymbol{v}\cdot \mathbf{grad}(\boldsymbol{v}) \qquad \text{(Eq. 5.24)}$$

is the material acceleration of the solid phase. Note the second part of Eq. 5.23 is derived by Reynold's transport theorem and balance of solid mass. Eq. 5.24, **grad** denotes the spatial gradient operator and partial differentiation, is carried out with either $\boldsymbol{X}$ and $\boldsymbol{x}$ held fixed depending on the argument carried by the variable being differentiated. Eq. 5.23 thus localizes to

$$\rho_s(1-\varphi)\boldsymbol{g} + \boldsymbol{h}_s + div\boldsymbol{\sigma}' = \rho_s(1-\varphi)\boldsymbol{a} \qquad \text{(Eq. 5.25)}$$

Similarly, for the fluid phase the momentum balance equation can be written as

$$\int_{\phi_t(u)} \rho_f \varphi \boldsymbol{g} dv + \int_{\phi_t(u)} \boldsymbol{h}_f dv + \int_{\phi_t(u)} \boldsymbol{n}\cdot \boldsymbol{p}_w da = \frac{\boldsymbol{D}}{\boldsymbol{D}t}\int_{\phi_t(u)} \rho_f \varphi \overline{\mathbf{v}} dv \equiv \int_{\phi_t(u)} \rho_f \varphi \overline{\mathbf{a}} dv \qquad \text{(Eq. 5.26)}$$

where $\boldsymbol{h}_f$ *is* reactive body force exerted by the solid matrix on the fluids, and

$$\overline{\boldsymbol{a}}(\boldsymbol{X},t) = \frac{\partial \overline{\boldsymbol{v}}(\boldsymbol{X},t)}{\partial t} + \overline{\boldsymbol{v}}\cdot \mathrm{grad}(\overline{\boldsymbol{v}}) \qquad \text{(Eq. 5.27)}$$

is the material acceleration of the fluid phase. Because of the Eulerian description of the fluid flow, it would not be practical to identify each and every fluid material particle and

describe their motions for purpose of evaluating the fluid material acceleration, and thus, Eq. 5.27 is the only recourse. The localization of Eq. 5.26 now takes the form

$$\rho_f \varphi \boldsymbol{g} + \boldsymbol{h}_f + div\boldsymbol{p}_w = \rho_f \varphi \overline{\boldsymbol{a}} \qquad \text{(Eq. 5.28)}$$

Note that since $\boldsymbol{h}_s$ and $\boldsymbol{h}_f$ are a pair of internal forces, which naturally will not affect the mixture as a whole, $\boldsymbol{h}_s + \boldsymbol{h}_f = 0$. By substituting Eq. 5.25 into Eq. 5.28 gives

$$\rho \boldsymbol{g} + div\boldsymbol{\sigma} = \rho_s(1-\varphi)\boldsymbol{a} + \rho_f \varphi \overline{\boldsymbol{a}} = \rho \boldsymbol{a} + \rho_f \varphi \boldsymbol{a}^r \qquad \text{(Eq. 5.29)}$$

where

$$\rho = \rho_s(1-\varphi) + \rho_f \varphi \qquad \text{(Eq. 5.30)}$$

is the total saturated mass density of the solid–fluid mixture, and

$$\boldsymbol{a}^{\mathrm{r}} = \overline{\boldsymbol{a}} - \boldsymbol{a} \qquad \text{(Eq. 5.31)}$$

is the relative material acceleration of the fluid phase relative to the solid phase. In the u–p formulation, we assume $\boldsymbol{a}^{\mathrm{r}} \approx 0$, Eq. 5.30 becomes

$$\rho \boldsymbol{g} + div\boldsymbol{\sigma} = \rho \ddot{\boldsymbol{u}} \qquad \text{(Eq. 5.32)}$$

5.2.2 Finite element formulation

The governing equations for the strong formulation of the problem in spatial coordinates are stated as follows:

$$div\boldsymbol{\sigma} + \rho \boldsymbol{b} = \rho \ddot{\boldsymbol{u}} \qquad \text{(Eq. 5.33)}$$

$$div\boldsymbol{v} + div\tilde{\boldsymbol{v}} = 0 \qquad \text{(Eq. 5.34)}$$

where

$$\hat{\boldsymbol{v}} = -\boldsymbol{k} \cdot \boldsymbol{grad} h$$

$$\hat{\boldsymbol{t}} = \boldsymbol{\sigma}^T \cdot \boldsymbol{n} \qquad on\ \partial_t \phi(\boldsymbol{B})$$

$$\hat{\boldsymbol{u}} = \boldsymbol{u} \qquad on\ \partial_u \phi(\boldsymbol{B})$$

$$\hat{q} = -\hat{\boldsymbol{v}} \cdot \boldsymbol{n} \qquad on\ \partial_q \phi(\boldsymbol{B})$$

$$\hat{h} = h \qquad on\ \partial_u \phi(\boldsymbol{B})$$

Weak form finite element formulation

To obtain the weak formulation, the trial solution spaces are defined:

$$\boldsymbol{\eta} = \{\boldsymbol{\eta}: \phi(\boldsymbol{B}) | \boldsymbol{\eta} = 0 \quad on\ \partial_u \phi(\boldsymbol{B})\}$$

$$\boldsymbol{\psi} = \{\boldsymbol{\psi}: \phi(\boldsymbol{B}) | \boldsymbol{\psi} = 0 \quad on\ \partial_u \phi(\boldsymbol{B})\}$$

Multiplying $\boldsymbol{\eta}$, $\boldsymbol{\psi}$ into Eq. 5.33–Eq. 5.34 and integrate over the current configuration

$$\int_{\phi_t(\beta)} \boldsymbol{\eta} \cdot div\boldsymbol{\sigma}\, dv + \int_{\phi_t(\beta)} \rho\boldsymbol{\eta} \cdot \boldsymbol{b}\, dv = \int_{\phi_t(\beta)} \rho\boldsymbol{\eta} \cdot \ddot{\boldsymbol{u}}\, dv \qquad \text{(Eq. 5.35)}$$

$$\int_{\phi(\beta)} \boldsymbol{\psi} div\boldsymbol{v} dv + \int_{\phi(\beta)} \boldsymbol{\psi} div\hat{\boldsymbol{v}} dv = 0 \qquad \text{(Eq. 5.36)}$$

for the solid phase.

By introducing the effective stress expression, we obtained

$$\boldsymbol{G}(\boldsymbol{u}, \boldsymbol{\rho_w}, \boldsymbol{\eta}) = \int_{\phi_t(\beta)} \big(grad\boldsymbol{\eta} : \boldsymbol{\sigma}' - div\boldsymbol{\eta}\boldsymbol{p}_w - \rho\boldsymbol{\eta} \cdot (\boldsymbol{b} - \ddot{\boldsymbol{u}})\big) dv - \int_{\phi_t(\beta)} \boldsymbol{\eta} \cdot \hat{\boldsymbol{t}} ds = 0$$

(Eq. 5.37)

and fluid phase, from $\dot{J} = Jdiv\boldsymbol{v}$ and integrated using integration by parts on term $\int_{\phi(\beta)} \psi div\hat{\mathrm{v}}\mathrm{dv}$ in Eq. 5.36 we obtained

$$\boldsymbol{H}(\boldsymbol{u}, \boldsymbol{p}_w, \boldsymbol{\psi}) = \int_{\phi(\beta)} \left(\boldsymbol{\psi} \frac{\dot{J}}{J} - \boldsymbol{grad\psi} \cdot \tilde{\boldsymbol{v}}\right) dv - \int_{\partial_q \phi(\beta)} \psi\, \hat{\boldsymbol{q}} ds = 0 \qquad \text{(Eq. 5.38)}$$

By taking the derivation of Eq. 5.37 and Eq. 5.38, we have

$$\boldsymbol{G}(\boldsymbol{u} + \delta\boldsymbol{u}, p_w + \delta p_w, \boldsymbol{\eta}) = G(\boldsymbol{u}, \boldsymbol{p}_w, \boldsymbol{\eta}) + \frac{\partial \boldsymbol{G}}{\partial \boldsymbol{u}} \cdot \delta\boldsymbol{u} + \frac{\partial \boldsymbol{G}}{\partial \boldsymbol{p}_w} \delta\boldsymbol{p}_w = 0 \qquad \text{(Eq. 5.39)}$$

$$\boldsymbol{H}(\boldsymbol{u} + \delta\boldsymbol{u}, p_w + \delta p_w, \psi) = H(\boldsymbol{u}, \boldsymbol{p}_w, \boldsymbol{\psi}) + \frac{\partial \boldsymbol{H}}{\partial \boldsymbol{u}} \cdot \delta\boldsymbol{u} + \frac{\partial \boldsymbol{H}}{\partial \boldsymbol{p}_w} \delta\boldsymbol{p}_w = 0 \qquad \text{(Eq. 5.40)}$$

A constitutive relation for the mechanical deformation of the solid matrix must also be specified. The alternative forms (Borja and Alarcon, 1995[1]) of the effective stress equation is defined as

$$\boldsymbol{P} = \boldsymbol{P}' - \mathbf{p}_\mathrm{w} \boldsymbol{F}^{-T} \qquad \text{(Eq. 5.41)}$$

$$\boldsymbol{S} = \boldsymbol{S}' - \mathbf{p}_\mathrm{w} \boldsymbol{C}^{-1} \qquad \text{(Eq. 5.42)}$$

where $\boldsymbol{P}$ and $\boldsymbol{S}$ refer to the first and second Piola–Kirchhoff stress tensors, respectively; $\boldsymbol{P}'$ and $\boldsymbol{S}'$ are the effective the first and second Piola–kirchhoff stress tensors, respectively; $\boldsymbol{F}$ is the deformation gradient; $\boldsymbol{C} = \boldsymbol{F}^T \cdot \boldsymbol{F}$ is the right Cauchy–Green deformation tensor. The effective stress tensors **P**, **S** and $\boldsymbol{\sigma}$ are given by the relations $\boldsymbol{S} = \boldsymbol{F}^{-1} \cdot \boldsymbol{P} = \boldsymbol{F}^{-1} \cdot \boldsymbol{\sigma} \cdot \boldsymbol{F}^{-T}$ for the effective stress tensor $\boldsymbol{S}'$, and additive decomposition of the form

$$\boldsymbol{S} = \boldsymbol{S}_{inv} + \boldsymbol{S}_{vis} \qquad \text{(Eq. 5.43)}$$

is postulated, where $\boldsymbol{S}_{inv}$ and $\boldsymbol{S}_{vis}$ are inviscid and viscous parts of $\boldsymbol{S}$, respectively. For the inviscid part, a compressible Neo–Hookean hyperelastic material is assumed for the large deformation analysis. The stored energy function of a compressible Neo–Hookean hyperelastic material can be written as (Bonet and Wood, 1997[2])

$$\Psi = \frac{\mu}{2}(\boldsymbol{I_c} - 3) - \mu \ln J + \frac{\lambda}{2}(\ln J)^2 \quad \text{(Eq. 5.44)}$$

where λ and μ are lame's constants, J is the Jacobian determinant of the deformation gradient $\boldsymbol{F}$, ($J = \det \boldsymbol{F}$) and $\boldsymbol{I_c}$ is the first invariant of the right Cauchy–Green deformation tensor $\boldsymbol{C}$ ($\boldsymbol{I_c} = tr\boldsymbol{C} = \boldsymbol{C}:\boldsymbol{I}$).

Thus, the inviscid effective stress can be obtained from

$$\boldsymbol{S'}_{inv} = 2\frac{\partial \Psi}{\partial C} = \mu \boldsymbol{1} + (-\mu' + \lambda' \ln J)\boldsymbol{C}^{-1} \quad \text{(Eq. 5.45)}$$

For the viscous part, we consider a Kelvin solid and postulate the following form

$$\boldsymbol{S'}_{vis} = \alpha \boldsymbol{C}:(\frac{1}{2}\dot{\boldsymbol{C}}) \quad \text{(Eq. 5.46)}$$

Where α is a viscous damping parameter of the solid matrix, and $\boldsymbol{C}$ is the fourth order Lagrangian tangential elasticity tensor which takes the form

$$\boldsymbol{C} = 4\frac{\partial^2 \Psi}{\partial \boldsymbol{C} \partial \boldsymbol{C}} = \lambda' \boldsymbol{C}^{-1} \otimes \boldsymbol{C}^{-1} + 2(\mu' - \lambda' \ln J)\boldsymbol{I}_{C^{-1}} \quad \text{(Eq. 5.47)}$$

where $\boldsymbol{I}_{C^{-1}} = \partial(\boldsymbol{C}^{-1})/\boldsymbol{C}$ is rank four tensor with components. Applying a push forward on all four indices of C, the Eulerian or spatial elasticity tensor $\boldsymbol{C}$ can be expressed in terms of the effective Lame's constants λ' and μ' as,

$$c_{ijkl} = \lambda' \delta_{ij}\delta_{kl} + 2\mu' \left(\frac{\delta_{ik}\delta_{jl} + \delta_{il}\delta_{jk}}{2}\right) \quad \text{(Eq. 5.48)}$$

Where $\lambda' = \frac{\lambda}{J}$ and $\mu' = \frac{\mu - \lambda \ln J}{J}$

Note that in case of small strains where *J = 1*, then, and the standard fourth order tensor used in linear elastic analysis is recovered.

To obtain the weak form, the above expression of the constitutive relationship and the following terms are required.

$$dv = JdV, \boldsymbol{grad\eta} = \frac{\partial \boldsymbol{\eta}}{\partial \mathbf{x}} = \frac{\partial \boldsymbol{\eta}}{\partial \mathbf{X}} \cdot \frac{\partial \mathbf{X}}{\partial \mathbf{x}} = \boldsymbol{GRAD\eta} \cdot \boldsymbol{F^{-1}}$$

$$div\boldsymbol{\eta} = \boldsymbol{GRAD\eta}:\boldsymbol{F^{-T}}, \boldsymbol{\rho} = \frac{\mathbf{1}}{J}\boldsymbol{\rho_0}$$

Thus, we obtained

$$\boldsymbol{G}(\boldsymbol{u}, \boldsymbol{p}_w, \boldsymbol{\eta}) = \int_\beta \{(\boldsymbol{F}^T \cdot \boldsymbol{GRAD\eta}) : \boldsymbol{S'} - J\boldsymbol{p}_w(\boldsymbol{GRAD\eta} : \boldsymbol{F}^{-1}) - \rho_0 \boldsymbol{\eta} \cdot (\boldsymbol{b} - \ddot{\boldsymbol{u}})\} dV - \int_{\partial_t \beta} \boldsymbol{\eta} \cdot \widehat{\boldsymbol{T}} dS = 0 \quad \text{(Eq. 5.49)}$$

for solid phase. Similarly, for fluid phase we obtained

$$\mathbf{H}(\boldsymbol{u}, \boldsymbol{p}_w, \boldsymbol{\psi}) = \int_\beta \boldsymbol{\psi} \dot{j} dV - \int_\beta \{(\boldsymbol{GRAD}\boldsymbol{\psi} \cdot \boldsymbol{F}^{-1}) \cdot J\tilde{\boldsymbol{v}}\} dv - \int_{\partial_q \beta} \boldsymbol{\psi} \widehat{\boldsymbol{Q}} dS = 0 \quad \text{(Eq. 5.50)}$$

By expanding the Eq. 5.49 and Eq. 5.50, the final weak form can be written as

$$\delta \boldsymbol{G} = \int_\beta (\boldsymbol{F}^T \cdot \boldsymbol{GRAD}\,\boldsymbol{\eta}) : \boldsymbol{C}^{ep} : (\boldsymbol{F}^T \cdot \boldsymbol{GRAD}\delta\boldsymbol{u})\, dV + \int_\beta \boldsymbol{GRAD}\boldsymbol{\eta} : (\boldsymbol{S}' \oplus \mathbf{1}) : \boldsymbol{GRAD}\,\delta\boldsymbol{u}\, dV - \int_\beta J\, \boldsymbol{p}_w (\boldsymbol{GRAD}\,\boldsymbol{\eta} : \boldsymbol{F}^{-T})(\boldsymbol{GRAD}\,\delta\boldsymbol{u} : \boldsymbol{F}^{-T})\, dV - \int_\beta J (\boldsymbol{GRAD}\,\boldsymbol{\eta} : \boldsymbol{F}^{-T})\delta\boldsymbol{p}_w\, dV + \int_\beta J\, \boldsymbol{p}_w (\boldsymbol{GRAD}\,\boldsymbol{\eta} \cdot \boldsymbol{F}^{-1})^T : (\boldsymbol{GRAD}\,\delta\boldsymbol{u} \cdot \boldsymbol{F}^{-1})\, dV - \int_\beta J\, \boldsymbol{\rho}_w (\boldsymbol{GRAD}\,\delta\boldsymbol{u} : \boldsymbol{F}^{-T})\boldsymbol{\eta} + \int_\beta J\boldsymbol{\rho}_w (\boldsymbol{GRAD}\delta\boldsymbol{u} : \boldsymbol{F}^{-T})\boldsymbol{\eta} \cdot \ddot{\boldsymbol{u}} dV + \int_\beta J\rho\boldsymbol{\eta} \cdot \delta\ddot{\boldsymbol{u}} dV$$

(Eq. 5.51)

$$\delta \boldsymbol{H} = \int_\beta \boldsymbol{\psi}\, \dot{J}\, (\boldsymbol{GRAD}\delta\boldsymbol{u} : \boldsymbol{F}^{-T})\, dV + \int_\beta \boldsymbol{\psi} J\, (\boldsymbol{GRAD}\delta\dot{\boldsymbol{u}} : \boldsymbol{F}^{-T}) dV + \int_\beta (\boldsymbol{GRAD}\boldsymbol{\psi} \cdot \boldsymbol{F}^{-1}) \cdot \frac{\boldsymbol{k}}{\rho_w g} \cdot (\boldsymbol{GRAD}\,\delta\boldsymbol{p}_w \cdot \boldsymbol{F}^{-1}) J\, dV - 2\int_\beta (\boldsymbol{GRAD}\boldsymbol{\psi} \cdot \boldsymbol{F}^{-1}) \cdot sym\left[\frac{\boldsymbol{k}}{\rho_w g} \cdot (\boldsymbol{GRAD}\delta\boldsymbol{u} \cdot \boldsymbol{F}^{-1})^T\right] \cdot (\boldsymbol{GRAD}\,\boldsymbol{p}_w \cdot \boldsymbol{F}^{-1})\, J\, dV + \int_\beta (\boldsymbol{GRAD}\,\boldsymbol{\psi} \cdot \boldsymbol{F}^{-1}) \cdot \frac{\boldsymbol{k}}{\rho_w g} \cdot (\boldsymbol{GRAD}\,\boldsymbol{p}_w \cdot \boldsymbol{F}^{-1})(\boldsymbol{GRAD}\,\delta\boldsymbol{u} : \boldsymbol{F}^{-T})\, JdV - \int_\beta (\boldsymbol{GRAD}\boldsymbol{\psi} \cdot \boldsymbol{F}^{-1}) \cdot \{(\boldsymbol{GRAD}\boldsymbol{p}_w \cdot \boldsymbol{F}^{-1}) - (\boldsymbol{GRAD}\delta\boldsymbol{u} : \boldsymbol{F}^{-T})\mathbf{1}\} \cdot \boldsymbol{k} \cdot \frac{\boldsymbol{G}}{g} JdV$$

(Eq. 5.52)

5.2.3 Matrix form

The matrix equations require representations of **u** and $\mathbf{p_w}$ in terms of the basis functions or shape functions. These are given by introducing the following interpolation functions for the unknowns of the solid displacement field **u** and the pore fluid pressure $\mathbf{p_w}$. Let

$$\delta\mathbf{u} = [N]\{\delta\mathbf{u}^{\mathrm{ne}}\} \quad \text{(Eq. 5.53)}$$

$$\mathbf{GRAD}\delta\mathbf{u} = [B]\{\delta\mathbf{u}^{\mathrm{ne}}\} \quad \text{(Eq. 5.54)}$$

$$\delta\mathbf{p}_{\mathrm{w}} = [N_{\mathrm{h}}]\{\delta\mathbf{p}_{\mathrm{w}}{}^{\mathrm{me}}\} \quad \text{(Eq. 5.55)}$$

$$\mathbf{GRAD}\delta\mathbf{p}_{\mathrm{w}} = [B_h]\{\delta\mathbf{p}_{\mathrm{w}}{}^{\mathrm{me}}\} \quad \text{(Eq. 5.56)}$$

Similarly, for the trial function defined as follows

$$\boldsymbol{\eta} = [N]\{\boldsymbol{\eta}^{\mathrm{ne}}\} \quad \text{(Eq. 5.57)}$$

$$\mathbf{GRAD}\boldsymbol{\eta} = [B]\{\boldsymbol{\eta}^{\mathrm{ne}}\} \quad \text{(Eq. 5.58)}$$

$$\boldsymbol{\psi} = [N_h]\{\boldsymbol{\psi}^{\mathrm{me}}\} \quad \text{(Eq. 5.59)}$$

$$\mathbf{GRAD}\boldsymbol{\psi} = [B_h]\{\boldsymbol{\psi}^{\mathrm{me}}\} \quad \text{(Eq. 5.60)}$$

where

$$\mathbf{GRAD}\delta\mathbf{u} = \left(\frac{\partial\delta\mathbf{u_1}}{\partial\mathbf{X_1}}\ \frac{\partial\delta\mathbf{u_1}}{\partial\mathbf{X_2}}\ \frac{\partial\delta\mathbf{u_1}}{\partial\mathbf{X_3}}\ \frac{\partial\delta\mathbf{u_2}}{\partial\mathbf{X_1}}\ \frac{\partial\delta\mathbf{u_2}}{\partial\mathbf{X_2}}\ \frac{\partial\delta\mathbf{u_2}}{\partial\mathbf{X_3}}\ \frac{\partial\delta\mathbf{u_3}}{\partial\mathbf{X_1}}\ \frac{\partial\delta\mathbf{u_3}}{\partial\mathbf{X_2}}\ \frac{\partial\delta\mathbf{u_3}}{\partial\mathbf{X_3}}\right)^{\mathrm{T}} \quad \text{(Eq. 5.61)}$$

Substitute Eq. 5.53–Eq. 5.60 into Eq. 5.33 and Eq. 5.34, we obtained

$$\begin{aligned}\mathbf{G}(\mathbf{u},\mathbf{p}_{\mathrm{w}},\boldsymbol{\eta}) &= \{\boldsymbol{\eta}^{\mathrm{ne}}\}^{\mathrm{T}}\int_{\beta_{\mathrm{e}}}\Big(([F][B])^{\mathrm{T}}\mathbf{S}' - \mathrm{J}\mathbf{p}_{\mathrm{w}}[B]^{\mathrm{T}}\{\mathbf{F}^{-\mathrm{T}}\} - \int_{\beta_{\mathrm{e}}}\rho_0[N]^{\mathrm{T}}\mathbf{b} \\ &+ \rho_0[N]^{\mathrm{T}}[N]\{\ddot{\mathbf{u}}^{\mathrm{ne}}\}\Big)\,\mathrm{dV} - \{\boldsymbol{\eta}^{\mathrm{ne}}\}^{\mathrm{T}}\int_{\partial_{\mathrm{t}}\beta_{\mathrm{e}}}[N]^{\mathrm{T}}\widehat{\mathbf{T}}\,\mathrm{dS}\end{aligned} \quad \text{(Eq. 5.62)}$$

$$\begin{aligned}\mathbf{H}(\mathbf{u},\mathbf{p}_{\mathrm{w}},\boldsymbol{\psi}) &= \{\boldsymbol{\psi}^{\mathrm{me}}\}^{\mathrm{T}}\int_{\beta_{\mathrm{e}}}[N_h]^{\mathrm{T}}\mathrm{j}\,\mathrm{dV} - \{\boldsymbol{\psi}^{\mathrm{me}}\}^{\mathrm{T}}\int_{\beta_{\mathrm{e}}}([F^{-T}][B_h])^{\mathrm{T}}\mathrm{J}\tilde{\mathbf{v}}\,\mathrm{dV} \\ &- \{\boldsymbol{\psi}^{\mathrm{me}}\}^{\mathrm{T}}\int_{\partial_{\mathrm{q}}\beta_{\mathrm{e}}}[N_h]^{\mathrm{T}}\widehat{\mathbf{Q}}\,\mathrm{dS}\end{aligned} \quad \text{(Eq. 5.63)}$$

Governing equations of the matrix formulation then defined as follow

$$[M^{UU}]\{\delta\ddot{\mathbf{u}}^{\mathrm{n}}\} + [K^{UU}]\{\delta\mathbf{u}^{\mathrm{n}}\} + [K^{UP}]\{\delta\mathbf{p}_{\mathrm{w}}^{\mathrm{m}}\} = \left\{\mathbf{F}^{\mathrm{int}} - \mathbf{F}^{\mathrm{ext}}\right\} \quad \text{(Eq. 5.64)}$$

$$[K^{UP}]^{\mathrm{T}}\{\delta\dot{\mathbf{u}}^{\mathrm{n}}\} + [K^{PU}]\{\delta\mathbf{u}^{\mathrm{n}}\} + [K^{PP}]\{\delta\mathbf{p}_{\mathrm{w}}^{\mathrm{m}}\} = \left\{\mathbf{H}^{\mathrm{int}} - \mathbf{H}^{\mathrm{ext}}\right\} \quad \text{(Eq. 5.65)}$$

or

$$\begin{bmatrix}M^{UU} & 0\\ 0 & 0\end{bmatrix}\begin{Bmatrix}\delta\ddot{\mathbf{u}}\\ \delta\ddot{\mathbf{p}}\end{Bmatrix} + \begin{bmatrix}0 & 0\\ K^{UP^T} & 0\end{bmatrix}\begin{Bmatrix}\delta\dot{\mathbf{u}}\\ \delta\dot{\mathbf{p}}\end{Bmatrix} + \begin{bmatrix}K^{UU} & K^{UP}\\ K^{PU} & K^{PP}\end{bmatrix}\begin{Bmatrix}\delta\mathbf{u}\\ \delta\mathbf{p}\end{Bmatrix} = \begin{Bmatrix}\mathbf{F}^{\mathrm{int}} - \mathbf{F}^{\mathrm{ext}}\\ \mathbf{H}^{\mathrm{int}} - \mathbf{H}^{\mathrm{ext}}\end{Bmatrix} \quad \text{(Eq. 5.66)}$$

where

$$[M^{UU}] = \textstyle\sum_{\mathrm{e}}[A_e]^{\mathrm{T}}\int_{\beta_{\mathrm{e}}}J\rho[N]^T[N]\mathrm{dV}[A_e] \quad \text{(Eq. 5.67)}$$

$$[K^{UU}] = [K_1^{UU}] + [K_2^{UU}] + [K_3^{UU}] + [K_4^{UU}] + [K_5^{UU}] + [K_6^{UU}] \quad \text{(Eq. 5.68)}$$

$$[K_1^{UU}] = \textstyle\sum_e[A_e]^T\int_{\beta_e}\{[F][B]\}^T[C]\,\{[F][B]\}dV[A_e] \quad \text{(Eq. 5.69)}$$

$$[K_2^{UU}] = \textstyle\sum_e[A_e]^T\int_{\beta_e}[B]^T[\sum][B]\,dV[A_e] \quad \text{(Eq. 5.70)}$$

$$[K_3^{UU}] = \textstyle\sum_e[A_e]^T\int_{\beta_e}J\rho_w\,[\bar{N}]^T\mathbf{b}\{\{F^{-T}\}^T[B]\}\,dV[A_e] \quad \text{(Eq. 5.71)}$$

$$[K_4^{UU}] = \sum_e [A_e]^T \int_{\beta_e} J\mathbf{p}_w\, [B]^T \{F^{-T}\}\{F^{-T}\}^T [B] dV [A_e] \quad \text{(Eq. 5.72)}$$

$$[K_5^{UU}] = \sum_e [A_e]^T \int_{\beta_e} J\mathbf{p}_w \{[F^{-1}][B]\}^T \left\{\left[\hat{F}^{-T}\right][B]\right\} dV [A_e] \quad \text{(Eq. 5.73)}$$

$$[K_6^{UU}] = \sum_e [A_e]^T \int_{\beta_e} J\rho_w\, [\bar{N}]^T \{\ddot{\mathbf{u}}\}\{\{F^{-T}\}^T [B]\} dV [A_e] \quad \text{(Eq. 5.74)}$$

$$[K^{UP}] = -\sum_e [A_e]^T \int_{\beta_e} J\{\{F^{-T}\}^T [B]\}^T [N_h] dV \left[A_{pe}\right] \quad \text{(Eq. 5.75)}$$

$$\left\{\mathbf{F}^{\text{int}}\right\} = \sum_e [A_e]^T \int_{\beta_e} (([F][B])^T \mathbf{S}' - J\mathbf{p}_w [B]^T \{F^{-T}\} + \rho_0 [N]^T [N]\{\ddot{\mathbf{u}}^{\text{ne}}\})\, dV$$

(Eq. 5.76)

$$\{\mathbf{F}^{\text{ext}}\} = \sum_e [A_e]^T \left[\int_{\beta_e} \rho_0 [N]^T \mathbf{b}\, dV + \int_{\partial_t \beta_e} [N]^T \hat{\mathbf{T}}\, dS\right] \quad \text{(Eq. 5.77)}$$

$$[K^{PU}] = [K_1^{PU}] - \frac{1}{\rho_w g}[K_2^{PU}] + \frac{1}{\rho_w g}[K_3^{PU}] - [K_4^{PU}] + [K_5^{PU}] \quad \text{(Eq. 5.78)}$$

$$[K_1^{PU}] = \sum_e \left[A_{pe}\right]^T \int_{\beta_e} [N_h]^T \{F^{-T}\}^T [B] \dot{J}\, dV [A_e] \quad \text{(Eq. 5.79)}$$

$$[K_2^{PU}] = \sum_e \left[A_{pe}\right]^T \int_{\beta_e} ([F^{-T}][B_h])^T [A] \left(\left[\hat{F}^{-T}\right][B]\right) J dV [A_e] \quad \text{(Eq. 5.80)}$$

$$[K_3^{PU}] = \sum_e \left[A_{pe}\right]^T \int_{\beta_e} ([F^{-T}][B_h])^T \{P\}(\{F^{-T}\}^T [B])\, J dV [A_e] \quad \text{(Eq. 5.81)}$$

$$[K_4^{PU}] = \sum_e \left[A_{pe}\right]^T \int_{\beta_e} ([F^{-T}][B_h])^T [W] \left(\left[\hat{F}^{-T}\right][B]\right) J\, dV [A_e] \quad \text{(Eq. 5.82)}$$

$$[K_5^{PU}] = \sum_e \left[A_{pe}\right]^T \int_{\beta_e} ([F^{-T}][B_h])^T \{W\}(\{F^{-T}\}^T [B]) J\, dV [A_e] \quad \text{(Eq. 5.83)}$$

$$[K^{PP}] = \frac{1}{\rho_w g} \sum_e \left[A_{pe}\right]^T \int_{\beta_e} ([F^{-T}][B_h])^T [k] ([F^{-T}][B_h]) J dV \left[A_{pe}\right] \quad \text{(Eq. 5.84)}$$

$$\left\{\mathrm{H}^{\text{int}}\right\} = \sum_e \left[A_{pe}\right]^T \left[\int_{\beta_e} [N_h]^T \dot{J}\, dV - \int_{\beta_e} ([F^{-T}][B_h])^T J \tilde{\mathbf{v}}\, dV\right] \quad \text{(Eq. 5.85)}$$

$$\{\mathrm{H}^{\text{ext}}\} = \sum_e \left[A_{pe}\right]^T \int_{\partial_q \beta_e} [N_h]^T \hat{\mathbf{Q}}\, dS \quad \text{(Eq. 5.86)}$$

$$\begin{bmatrix} F_{11} & F_{12} \\ F_{21} & F_{22} \end{bmatrix} = \begin{bmatrix} \frac{\partial x}{\partial X} & \frac{\partial y}{\partial X} \\ \frac{\partial x}{\partial Y} & \frac{\partial y}{\partial Y} \end{bmatrix} \quad \text{(Eq. 5.87)}$$

$$\{\mathrm{F}^{-\mathrm{T}}\} = \begin{Bmatrix} \mathrm{F}_{11}^{-1} \\ \mathrm{F}_{21}^{-1} \\ \mathrm{F}_{12}^{-1} \\ \mathrm{F}_{22}^{-1} \end{Bmatrix} \quad \text{(Eq. 5.88)}$$

$$[\bar{N}] = \begin{bmatrix} N_1 & 0 & N_n & 0 \\ 0 & N_1 & \cdots & 0 & N_n \end{bmatrix} \quad \text{(Eq. 5.89)}$$

$$[F] = \begin{bmatrix} F_{11}[I] & F_{12}[I] \\ F_{21}[I] & F_{22}[I] \end{bmatrix} \quad \text{(Eq. 5.90)}$$

$$[F^{-1}] = \begin{bmatrix} F_{11}^{-1} & F_{21}^{-1} & 0 & 0 \\ 0 & 0 & F_{11}^{-1} & F_{21}^{-1} \\ F_{12}^{-1} & F_{22}^{-1} & 0 & 0 \\ 0 & 0 & F_{12}^{-1} & F_{22}^{-1} \end{bmatrix} \quad \text{(Eq. 5.91)}$$

$$\left[\hat{F}^{-T}\right] = \begin{bmatrix} F_{11}^{-1} & F_{21}^{-1} & 0 & 0 \\ F_{12}^{-1} & F_{22}^{-1} & 0 & 0 \\ 0 & 0 & F_{11}^{-1} & F_{21}^{-1} \\ 0 & 0 & F_{12}^{-1} & F_{22}^{-1} \end{bmatrix} \quad \text{(Eq. 5.92)}$$

$$[\Sigma] = \begin{bmatrix} [S'] & [0] \\ [0] & [S'] \end{bmatrix} \quad \text{(Eq. 5.93)}$$

$$[B_h] = \begin{bmatrix} \frac{\partial N_1}{\partial X} & 0 & \frac{\partial N_n}{\partial X} & 0 \\ 0 & \frac{\partial N_1}{\partial Y} & \cdots & 0 & \frac{\partial N_n}{\partial Y} \end{bmatrix} \quad \text{(Eq. 5.94)}$$

$$\{\mathrm{Z}\} = [F^{-T}][B_h]\{\mathbf{p}_\mathrm{w}\} \quad \text{(Eq. 5.95)}$$

$$[A] = \begin{bmatrix} 2k_{11}Z_1 & k_{22}Z_2 & k_{22}Z_2 & 0 \\ 0 & k_{11}Z_1 & k_{11}Z_1 & 2k_{22}Z_2 \end{bmatrix} \quad \text{(Eq. 5.96)}$$

$$\{\mathrm{P}\} = \begin{Bmatrix} \mathrm{k}_{11}\mathrm{Z}_1 \\ \mathrm{k}_{22}\mathrm{Z}_2 \end{Bmatrix} \quad \text{(Eq. 5.97)}$$

$$[\mathrm{W}] = \begin{bmatrix} k_{11}\frac{G_1}{g} & k_{22}\frac{G_2}{g} & 0 & 0 \\ 0 & 0 & k_{11}\frac{G_1}{g} & k_{22}\frac{G_2}{g} \end{bmatrix} \quad \text{(Eq. 5.98)}$$

$$\{\mathrm{W}\} = \begin{Bmatrix} \mathrm{k}_{11}\frac{\mathrm{G}_1}{\mathrm{g}} \\ \mathrm{k}_{22}\frac{\mathrm{G}_2}{\mathrm{g}} \end{Bmatrix} \quad \text{(Eq. 5.99)}$$

$$[k] = \begin{bmatrix} k_{11} & 0 \\ 0 & k_{22} \end{bmatrix} \quad \text{(Eq. 5.100)}$$

$$\{\delta\mathbf{u}^{\mathrm{ne}}\} = [A_e]\{\delta\mathbf{u}^{\mathrm{n}}\} \quad \text{(Eq. 5.101)}$$

$$\{\delta\mathbf{p}_\mathrm{w}{}^{\mathrm{me}}\} = [A_{pe}]\{\delta\mathbf{p}_\mathrm{w}{}^{\mathrm{m}}\} \quad \text{(Eq. 5.102)}$$

5.2.4 Implicit direct integration technique for solving nonlinear problem

Implicit direct integration technique is applied in this study. Eq. 5.66 can be solved using the Newmark's method with Newton–Raphson iteration (Bathe and Baig 2005[14] and Chang 2004[15]). The residual force **R**, can be defined as

$$\boldsymbol{R} = \mathbf{F}^{\text{ext}} - \mathbf{F}^{\text{int}} - [K]\left(\Delta t\boldsymbol{v} + \frac{1}{2}\Delta t^2\boldsymbol{a}\right) - [C](\Delta t\boldsymbol{a}) \quad \text{(Eq. 5.103)}$$

By given displacement $\boldsymbol{u}_{t-1}, \boldsymbol{v}_{t-1}, and\ \boldsymbol{a}_{t-1}$ at time $t-1$, the $\boldsymbol{u}_t, \boldsymbol{v}_t, and\ \boldsymbol{a}_t$ are determined using the following equations

$$\tilde{\boldsymbol{u}}_t = \boldsymbol{u}_{t-1} + \Delta t\boldsymbol{v}_{t-1} + \frac{1}{2}\Delta t^2\boldsymbol{a}_{t-1} \quad \text{(Eq. 5.104)}$$

$$\tilde{\boldsymbol{v}}_t = \boldsymbol{v}_{t-1} + \Delta t\boldsymbol{v}_{t-1} + \Delta t\boldsymbol{a}_{t-1} \quad \text{(Eq. 5.105)}$$

Then,

$$\boldsymbol{u}_t = \tilde{\boldsymbol{u}}_t + \beta\Delta t^2\boldsymbol{a}_t \quad \text{(Eq. 5.106)}$$

$$\boldsymbol{v}_t = \tilde{\boldsymbol{v}}_t + \frac{1}{2}\Delta t\boldsymbol{a}_t \quad \text{(Eq. 5.107)}$$

$$\boldsymbol{R}_{i+1} = \mathbf{F}^{\text{ext}}(t_{i+1}) - \mathbf{F}^{\text{int}}(t_{i+1}) - [K]\left(\Delta t\boldsymbol{v}_t + \frac{1}{2}\Delta t^2\boldsymbol{a}_t\right) - [C](\Delta t\boldsymbol{a}_t) = 0 \quad \text{(Eq. 5.108)}$$

In this study, the constant γ and β is ½ and ¼ (average acceleration method), respectively. To obtain the solution of the above equation, the Newton–Raphson method is applied. Now we have the $\boldsymbol{R}_{i+1}$ as the right hand side of the equilibrium equation, the solution $\Delta\boldsymbol{a}$ can be obtained using the left hand side equation which can be defined as

$$[K^{eff}]\Delta\boldsymbol{a} = \boldsymbol{R}_{i+1} \quad \text{(Eq. 5.109)}$$

where

$$[K^{eff}] = [M] + [C]\frac{\Delta t}{2}\boldsymbol{v}_t + [K]\frac{1}{2}\Delta t^2\boldsymbol{a}_t \quad \text{(Eq. 5.110)}$$

Convergence criteria

Convergence criteria are a measure to obtained solution that satisfies equilibrium. In this study, three criteria are used in order to control the accuracy of the numerical calculation for each load and time step. Generally, the convergence criteria are usually based on the norm of the displacements (total or incremental), Residuals force and Energy (product of residual and displacement). Normally, it is recommended to apply a combination of the three criteria because the displacement based itself could be misleadingly satisfied by a slow convergence rate. Besides, Residual based criteria are most reliable as it is possible to check that the equilibrium has been achieved within a specified tolerance in the current increment. Also, the energy based criteria that use both displacements and residuals are the alternative choice. The norm of those three convergence criteria can be expressed as

follow.

$$\|U\|_2 = \sqrt{\left(\sum_{i=1}^{n} |u_{t+1} - u_t|^2\right)} \leq \text{TOL} \quad \text{(Eq. 5.111)}$$

$$\|R\|_2 = \sqrt{\left(\sum_{i=1}^{n} |R|^2\right)} \text{ or} \sqrt{\left(\sum_{i=1}^{n} |F_{ext} - F_{int}|^2\right)} \leq \text{TOL} \quad \text{(Eq. 5.112)}$$

$$\|E\|_2 = \sqrt{\left(\sum_{i=1}^{n} |R \cdot U|^2\right)} \leq \text{TOL} \quad \text{(Eq. 5.113)}$$

The convergence criteria and tolerances (TOL) must be carefully selected. By selecting an over rigorous tolerance value, it costs an extremely unnecessary calculation time. On the other hand, by choosing too loose tolerance value, it produces inaccurate approximation. Thus, the tolerances should be selected in such way that it could provide accurate results yet economical solutions.

5.3 Verification and numerical examples

The finite element method is a procedure for obtaining an approximate solution to a specific problem by applying numerical methods. It is crucial to ensure the accuracy of the proposed code before apply it in research work or in the practical field, as well as to determine the limitations of the proposed code. Generally, small–strain finite element code can be verified against the corresponding analytical solution. However, in the finite–strain case, it is difficult to find an exact solution. Therefore, the accuracy of the code can be verified against the small–strain solution as well as against the analytical solution within the small–strain region. In this study, the proposed code was verified for both static and dynamic problems. Therefore, the results obtained using the proposed code, infinitesimal–strain finite element code, and analytical solution were compared.

5.3.1 Static verification problem

The verification was conducted following the study of Li et al. 2004[10]. A numerical example involving the consolidation of a two–dimensional porous media layer was used for verifying the code. The dimensions of the numerical model are 1 m × 10 m (width × height). The boundary condition is fixed at the bottom mesh and restrained only in the horizontal direction on both sides. The flow boundary is impervious on all sides, with the exception of the top mesh, which is considered as the draining part. For static problems, a surcharge load was applied along the top of the numerical model under various loads of 40 kPa, 2 MPa, 4 MPa, and 8 MPa. The numerical model and the properties applied in this analysis are shown and listed in Fig. 5.2 and Table 5.1, respectively. The surcharge load is shown in Fig. 5.3.

According to this consolidation problem, a steady–state analytical solution of consolidated vertical displacement for a linear elastic solid phase can be written as follows:

$$\Delta H = wH_0/\lambda + 2\mu \quad \text{(Eq. 5.114)}$$

where ΔH is the vertical displacement, λ and μ is lame constant, H_0 is the height of the model and w is the surcharge load.

Table 5.1Conditions and properties

Parameter	**Cases**	
	Static	Harmonic
F(kPa)	40, 2000, 4000,8000	1.5(1-cos(ωt))
λ(MPa)	29	8.4, 28.85
μ(MPa)	7	5.6, 19.23
k(m/s)	0.1	0.01
ω(rad/s)	NA	50
ρ_s (kg/m^3)	2700	2700
ρ_w (kg/m^3)	1000	1000
n_s	0.58	0.58
n_f	0.42	0.42
H (m)	10	20
K_f (GPa)	22	22

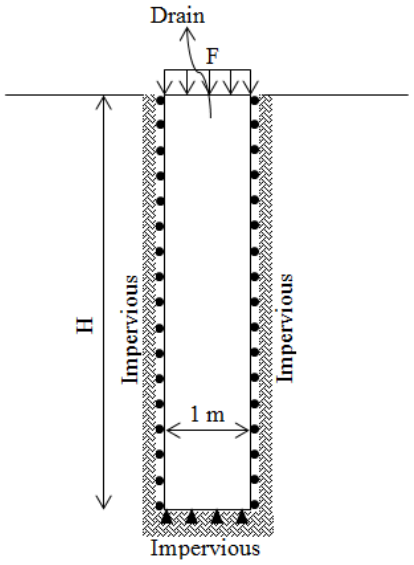

Fig. 5.2 Numerical model

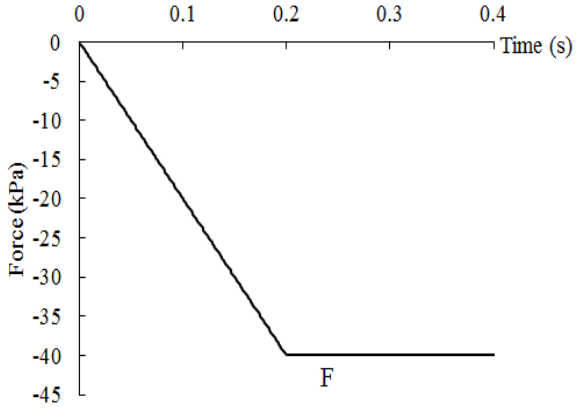

Fig. 5.3 Applied load in static problem

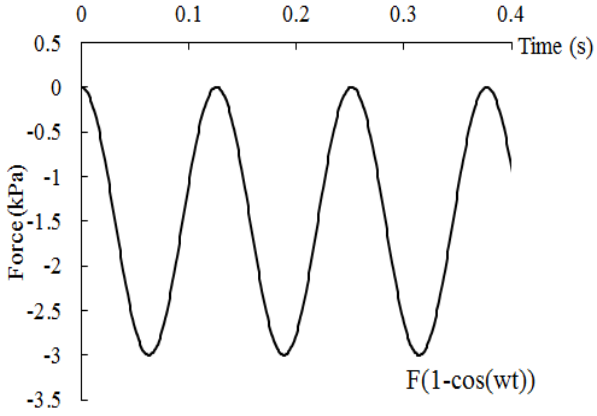

Fig. 5.4 Applied load in dynamic problem

5.3.2 Dynamic verification problem

The verification problem was solved based on the work of Regueiro and Ebrahimi, 2010[11]. The similar numerical model as a static verification problem and all conditions are applied in this study. For the dynamic problem, a harmonic load was applied at the top of the mesh as the surcharge load. The load function, model's dimension and its properties are listed and shown in Table 5.1 and Fig. 5.4. The analytical solution was obtained from the study of Simon et al. 1984[16] and De Boer et al. 1993[17], which are as follows:

$$u(Z,t) = \frac{1}{\sqrt{a}(\lambda+2\mu)} \int_0^t f(\tau - t) e^{-\left(\frac{b}{2a}\right)\tau} I_0 \left(\frac{b\sqrt{\tau^2 - aZ^2}}{2a}\right) H\left(\tau - \sqrt{a}Z\right) d\tau \quad \text{(Eq. 5.115)}$$

$$p(Z,t) = \frac{1}{\left(n^f\right)^2(\lambda+2\mu)} \left[n^s n^f \rho^f L_{,tt}(Z,t) + S_v L_{,t}(Z,t)\right] \quad \text{(Eq. 5.116)}$$

$$\sigma'(Z,t) = \frac{b}{2\sqrt{a}} \int_0^t f(\tau - t) e^{-\left(\frac{b}{2a}\right)\tau} I_1 \left(\frac{b\sqrt{\tau^2 - aZ^2}}{2a}\right) \frac{Z}{\sqrt{\tau^2 - aZ^2}} H\left(\tau - \sqrt{a}Z\right) d\tau$$

$$+ H\left(\tau - \sqrt{a}Z\right) f\left(\tau - \sqrt{a}Z\right) e^{-\left(\frac{b}{2\sqrt{a}}\right)Z} \quad \text{(Eq. 5.117)}$$

where

$$s_v = \frac{\left(n^f\right)^2 \rho^f g}{k} \quad \text{(Eq. 5.118)}$$

$$a = \frac{(n^s)^2 n^f \rho^f + \left(n^f\right)^2 n^s \rho^s}{\left(n^f\right)^2(\lambda+2\mu)} \quad \text{(Eq. 5.119)}$$

$$b = \frac{s_v}{(n^f)^2(\lambda+2\mu)} \quad \text{(Eq. 5.120)}$$

$$L(Z,t) = \int_0^t Q(t - \tau) G(Z,t) d\tau \quad \text{(Eq. 5.121)}$$

$$Q(t) = \frac{1}{\sqrt{a}} \int_0^t f(\tau - t) e^{-\left(\frac{b}{2a}\right)\tau} I_0 \left(\frac{b}{2a}\tau\right) d\tau \quad \text{(Eq. 5.122)}$$

$$G(Z,t) = \frac{1}{\sqrt{a}} e^{-\left(\frac{b}{2a}\right)t} I_0 \left(\frac{b\sqrt{\tau^2 - aZ^2}}{2a}\right) H\left(\tau - \sqrt{a}Z\right) - \frac{1}{\sqrt{a}} e^{-\left(\frac{b}{2a}\right)t} I_0 \left(\frac{b}{2a}t\right) \quad \text{(Eq. 5.123)}$$

$u(Z,t)$Vertical displacement, $f(t)$ loading function, $I_n(Z)$ modified Bessel's function of n[th] order, $H(t)$ Heaviside function, $p(Z,t)$ excess pore pressure, $\sigma'(Z,t)$ effective stress and k hydraulic conductivity.

5.3.3 Verification results

The results show that in the static problem, when the applied load is 40 kPa (infinitesimal – strain), the results obtained from the finite–strain finite element code show good agreement with the results of both the small–strain finite element code and the analytical solution (Fig. 5.5). Under larger loads of 2 MPa, 4 MPa, and 8 MPa, the results obtained using the small–strain finite element code approached that of the analytical solution, while the finite–strain finite element code yielded a smaller response. As the larger load was applied, the greater difference between the results of the finite–strain finite element code and that of the small–strain finite element code was obtained (Fig. 5.6).

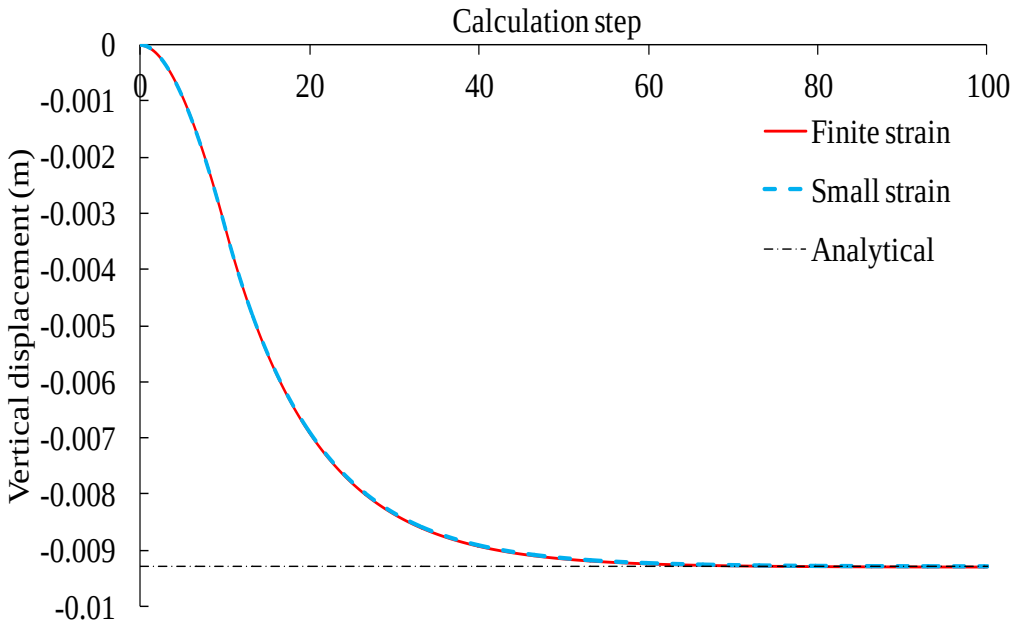

Fig. 5.5 Verification results of static problem when applied 40 kPa

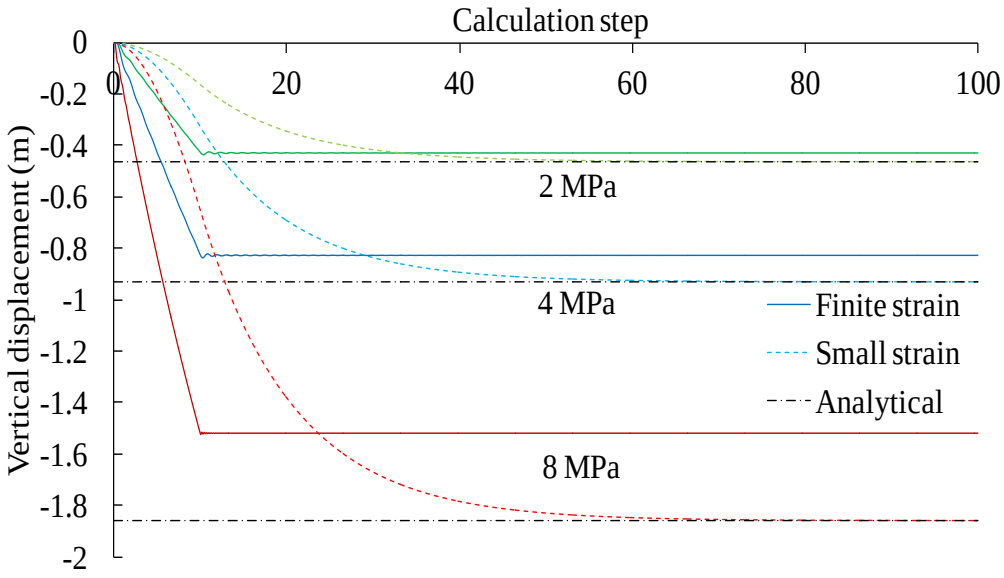

Fig. 5.6 Verification results of static problem when applied 2, 4 and 8 MPa

For the dynamic problem, Fig. 5.7 shows the vertical displacements of the observation points at z = 0.0 m, 1.0 m, and 2.0 m from the model surface of the finite–strain finite element code, small–strain finite element code, and analytical solution. It can be seen that the vertical displacement of the observation points were settled continuously and were clearly in harmonic form at the shallow level, but this harmonic wave form could hardly be recognized when the observation depth increased. In terms of displacement, under a small harmonic load, the vertical displacement obtained using the finite–strain finite element code is in good agreement with the results of both the small–strain finite element code and the analytical solution.

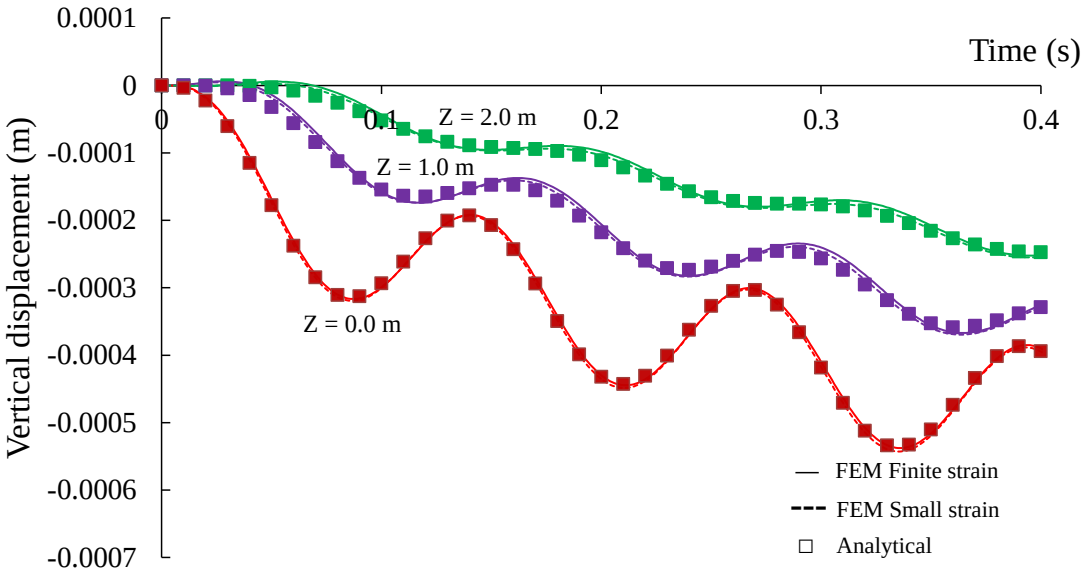

Fig. 5.7 Vertical displacements when subjected to harmonic loading

A plot of effective stress values obtained using the finite–strain finite element code, small–strain finite element code, and analytical solution are shown in Fig. 5.8. It can be seen that the results obtained using the finite–strain finite element code were perfectly matched with the results obtained using the small–strain finite element code and analytical solution. The effective stress increases as the depth of the observation point increases. The vertical effective stress of the observation points were clearly in harmonic wave form at the shallow depth, and these harmonic forms tended to vanish at deeper level.

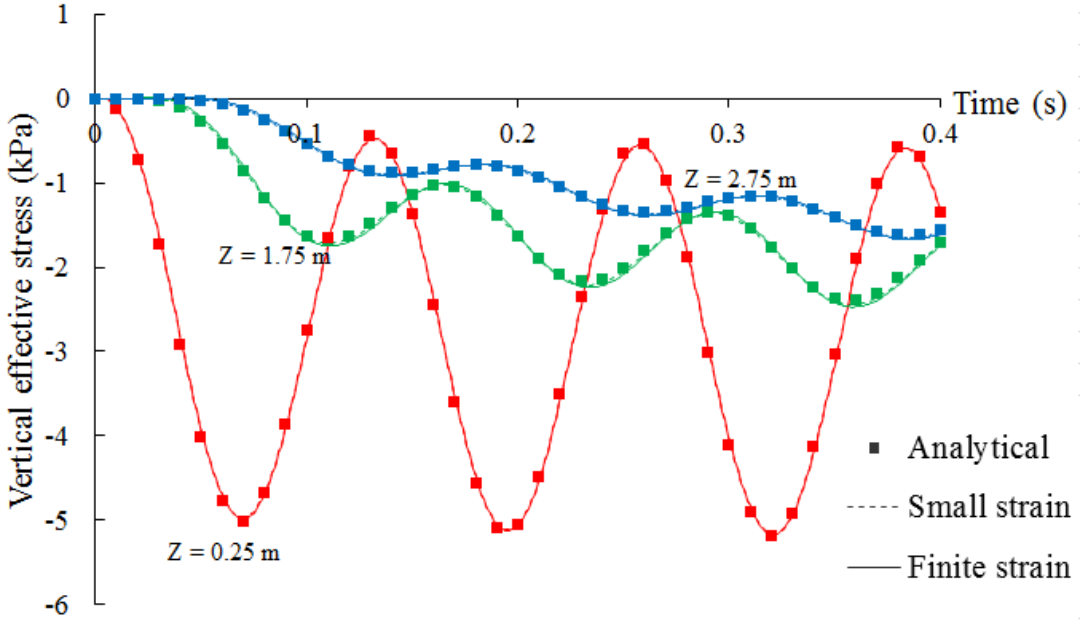

Fig. 5.8 Vertical effective stress

The excess pore pressures at the observation points Z = 0.0 m, 1.0 m, 2.0 m, and 3.5 m obtained using the finite–strain finite element code and the small–strain finite element code are shown in Fig. 5.9. The result shows that under a small harmonic load, the excess pore pressure obtained using the finite–strain finite element code is in good agreement with that obtained using the small–strain finite element code. It can be seen that at the deeper observation point, the higher excess pore pressure is obtained.

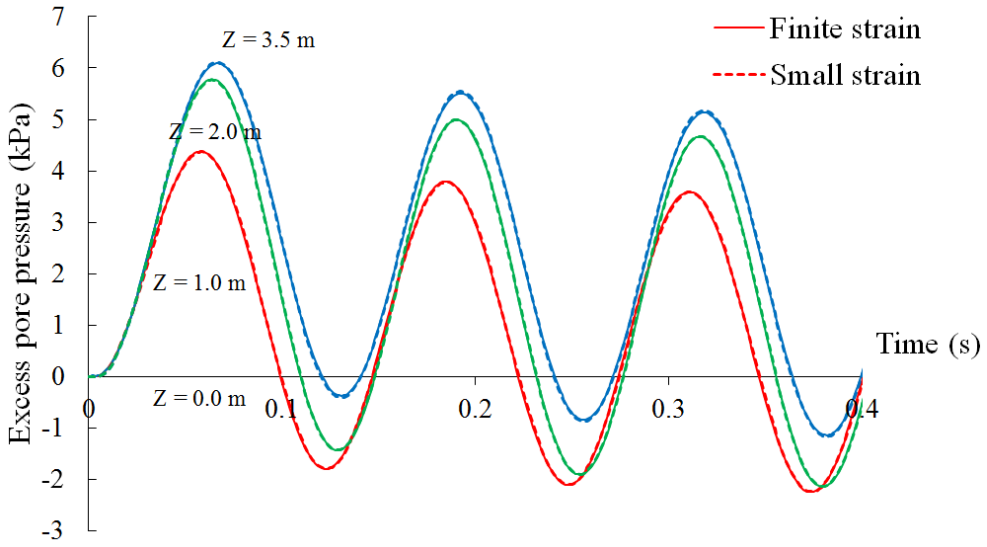

Fig. 5.9 Excess pore pressure

Given that the results of both the static and dynamic problems obtained using the proposed code is in good agreement with the analytical solution and the results of the small–strain finite element code in all aspects, the proposed code can be developed further to include the advanced constitutive law and applied to the analysis of earth dams or any geotechnical problems.

5.4 Analysis of the Fujinuma dam

5.4.1 Site description and input motion

The dam of interest here is Fujinuma dam, which has been described in Chapter 4, section 2. 2. The same information was used for the analysis described in this Chapter. However, in the current code, only the elastic constitutive law is applicable. Thus, analysis and comparison between the results of the small–strain finite element code and the finite–strain finite element code using elastic properties are presented.

In this study, as a preliminary step, a generated harmonic wave was used as the input motion, as shown in Fig. 5.10, instead of real ground motion record, because when using the 2011 Tohoku earthquake, the computational cost of the current code rose drastically. The peak ground acceleration a_{max} is 3.00 m/s^2 with 15 s of shaking duration.

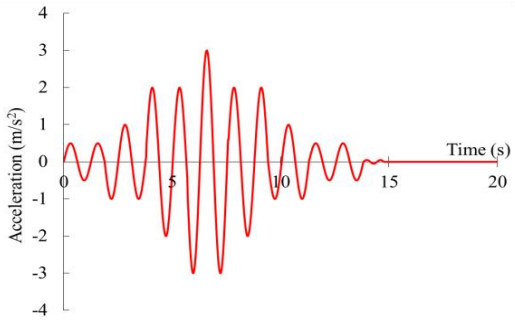

Fig. 5.10 Input motion

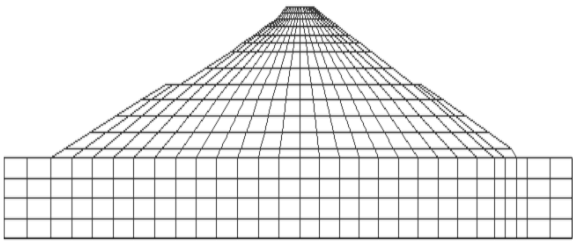

Fig. 5.11 Fujinuma dam model

5.4.2 FE model

In this study, 456 rectangular four–node elements with four–point Gaussian integration, first–order polynomial interpolation for displacement, and first–order interpolation for the pore water pressure were used. The dam model is a simplified version of the original shape of the Fujinuma dam's typical section, and in this study, the effect of the concrete frames and panels, as well as the interaction among them and dam, are not taken into account (Fig. 5.11). The foundation was modeled by extending a 10–m–thick layer, 100 m on either side of the center. The boundary conditions were restrained in the horizontal and vertical directions at the bottom of the model. For both edges, the boundary conditions were fixed only in the lateral direction and were free in the vertical direction. The dam body was classified into three portions: upper, middle, and bottom. The Young modulus was assumed to be constant in all three portions of the dam. For dynamic analysis, the dam was analyzed under the undrained condition, and neglected the effect of reservoir pressure and the initial stress. All elements in the model were assumed to be under the saturated condition.

5.4.3 Analysis results and discussions

Dynamic analysis is performed to provide information on the behaviour of the dam during an earthquake. The results were expressed through the acceleration, displacement, shear strain and excess pore pressure. The comparison between results obtained from finite–strain finite element code and infinitesimal–strain finite element code were presented.

Acceleration

The analysis results obtained using both small–strain and finite–strain finite element code shows that; the maximum crest acceleration obtained from the small–strain finite element code is 6.75 m/s^2 accelerating towards the upstream direction, while the finite–strain finite element code gives the maximum crest acceleration of about 7.10 m/s^2 acting toward the upstream side (Fig. 5.12). The results show that the finite–strain finite element code gives a close approximation to the small–strain finite element code. Even, minor differences can be seen in the responses using both small–and finite–strain finite element code, by

considering a whole picture both codes yield good agreement.

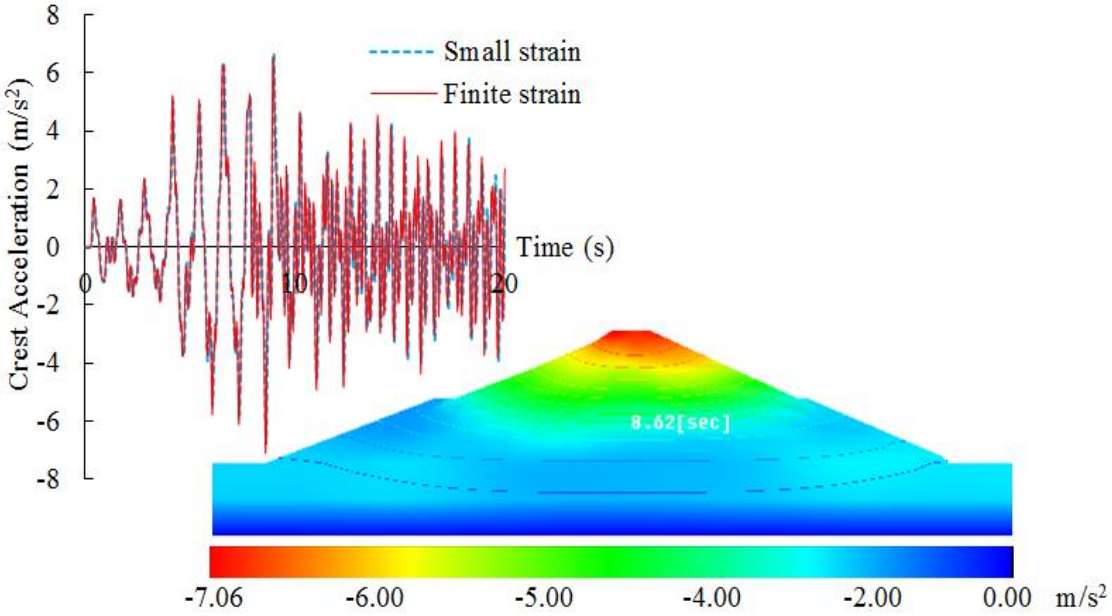

Fig. 5.12 Acceleration

Displacement

The results are expressed through the displacement curves with respect to time at the dam's crest along with the deformed mesh.

Fig. 5.13 shows the displacement curves using both small–and finite–strain finite element code along with the deformed mesh at 8.0 s. The maximum crest's vertical displacement Uy is 0.0012 m at 15.66 s, and the maximum crest's horizontal displacement Ux is 0.0716 m at 6.6 s moving toward the upstream side. In case of finite–strain finite element code, the maximum vertical displacement at the dam crest was 0.00124 m at 19.34 s and the maximum horizontal displacement at the dam crest was 0.0715 m at 6.6 s (upstream side). All curves indicated that both horizontal and vertical displacements fluctuated during the earthquake until the end of the excitation.

By comparing small–strain and finite–strain finite element code, it can be summarized that; for the maximum crest settlement, the finite strain code predicted a slightly higher value than the small–strain code, in case of the maximum horizontal displacement, the small–strain code gave a bit higher value than the finite–strain code. In overall, both codes yield a similar tendency and are in good agreement with only small difference which is expected due to the different formulations.

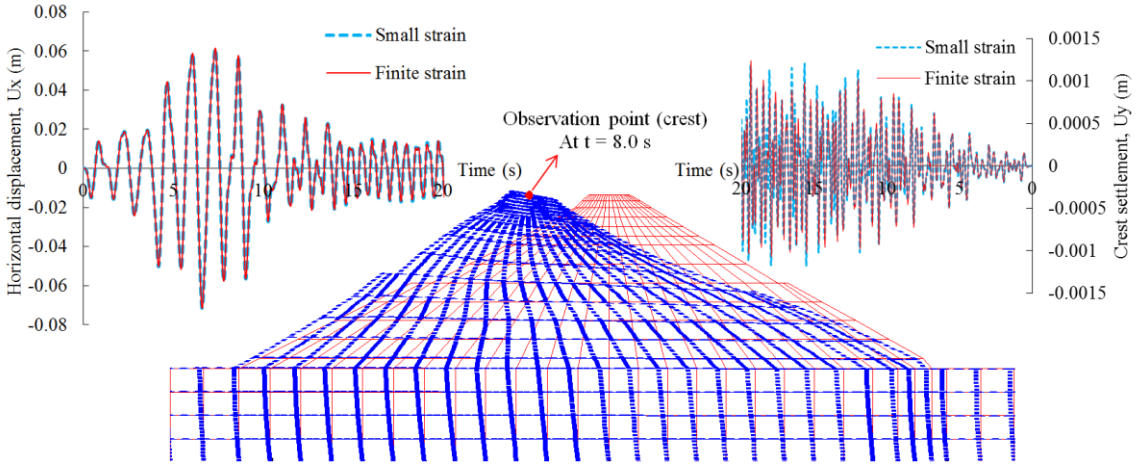

Fig. 5.13 Displacement

Excess pore pressure

The excess pore pressure of the observation points at various location of the dam's body using the finite–strain and infinitesimal–strain finite element code are shown in Fig. 5.14. It can be seen that the excess pore pressure developed mostly at the lower portion of the downstream side. The maximum excess pore pressure was about 48 kPa and 43 kPa for the finite–strain and infinitesimal–strain finite element code, respectively. It can be seen that from the time history curves of the excess pore pressure that the build–up pore pressure was fluctuated until it reached the end of the excitation.

By comparing small–strain and finite–strain finite element code, as a whole both codes yield a similar tendency and are in good agreement with only small difference which is expected due to the different formulations.

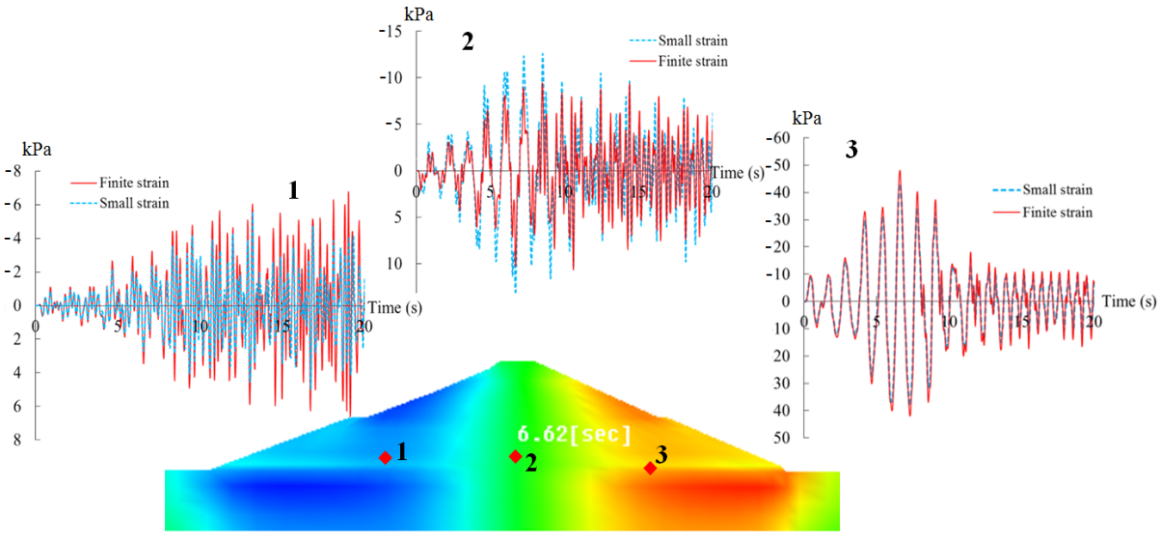

Fig. 5.14 Excess pore pressure

5.5 Conclusions

The finite element code for coupled solid–fluid at finite strain for static and dynamic problems has been proposed. The governing equation, finite element formulation and its matrix form have been presented in this study. The code is currently developed for only for elastic regime as its preliminary step. In this study, the proposed code has been verified with the static and dynamic problem. In static verification problem, when applied 40 kPa load (infinitesimal–strain), the result obtained from the finite–strain finite element code yield good agreement with both small–strain finite element code and the analytical solution. Then, when applied larger loads of 2 MPa, 4 MPa and 8 MPa, the results obtained from small–strain finite element code approached the analytical while the finite–strain finite element code, gave a smaller response which agree well with the finite–strain's assumption. In dynamic problem, the surcharge load was applied at the top of the soil column model with a harmonic load. The results of the vertical displacement, vertical effective stress and excess pore pressure obtained from the finite–strain finite element code, small–strain finite element code and the analytical solution are in good agreement. Therefore, the proposed code can be developed further to include the more advanced constitutive law and then applied to the geotechnical problems.

Thereafter, the proposed code was used to estimate the response of the Fujinuma dam when subjected to a dynamic load. A generated harmonic wave was applied to the Fujinuma dam model to estimate its response and compare with the results obtained using the infinitesimal–strain finite element code. By comparing the results of the small– and finite–strain finite element codes, it can be said that the maximum crest settlement, horizontal displacement, acceleration, and excess pore pressure obtained using the finite–strain finite element code are in good agreement with that obtained using the small–strain finite element code.

As the proposed code is not yet complete (some parts such as the damping term have not yet been included), incorrect parts or mistakes must be found and addressed to ensure that the code is reliable and can applied to relevant further study or research. In addition, in future works, descriptions of other possible failure mechanisms, material nonlinearity, or other advanced constitutive laws, as well as the proper fluid–structure interaction, should be considered.

REFERENCES

[1] R. W. Lewis, B. A. Schrefler, The finite element method in the static and dynamic deformation and consolidation of porous media, John Wiley and Sons, New York, 1998.

[2] O.C. Zienkiewicz, A.H.C. Chan, M. Pastor, B.A. Schrefler, T. Shiomi, Computational geomechanics with special reference to earthquake engineering, John Wiley and Sons, Chichester, 1998.

[3] H. D. Hibbitt, P. V. Marcal and J. R. Rice, A finite element formulation for problems of large strain and large displacement, International Journal of Solids Structures, 6(1970) 1069–1086.

[4] K.J. Bathe, E. Ramm and E.L. Wilson, Finite Element Formulations for Large Deformation Dynamic Analysis, International Journal for Numerical Methods in Engineering, 9(1975)353–386.

[5] K.J. Bathe and H. Ozdemir, Elastic–Plastic Large Deformation Static and Dynamic Analysis, Computers & Structures, 6 (2)(1976) 81–92.

[6] G. Gabriel and K.J. Bathe, Some Computational Issues in Large Strain Elasto–Plastic Analysis, Computers & Structures, 56 (2/3)(1995)249–267.

[7] K. J. Bathe, Finite Element Procedures, Prentice-Hall, MA: Klaus–Jürgen Bathe, 1996

[8] M. A. Crisfield Non–linear finite element analysis of solids and structures, volume 2, John Wiley & Sons Ltd, Baffins Lane, Chichester, England, 1997.

[9] S. Diebels, W. Ehlers, Dynamic analysis of a fully saturated porous medium accounting for geometrical and material non–linearities, International Journal for numerical methods in Engineering, 39 (1996) 81-97.

[10] C. Li, R.I. Borja, R.A. Regueiro, Dynamics of porous media at finite strain, Computation Methods in Applied Mechanics and Engineering, 193 (2004) 3837–3870.

[11] R.A. Regueiro, D. Ebrahimi, Implicit dynamic three–dimensional finite element analysis of an inelastic biphasic mixture at finite strain Part 1: Application to a simple geomaterial, Computer Methods in Applied Mechanics and Engineering 199 (2010) 2024–2049

[12] Y. Heider, Saturated Porous Media Dynamics with Application to Earthquake Engineering, Yousef Heider's Dissertation Report No II–25, University of Stuttgart, Stuttgart, Germany, 2012.

[13] W. C. Sun, J. T. Ostien and A. G. Salinger, A stabilized assumed deformation gradient finite element formulation for strongly coupled poromechanical simulations at finite strain, International Journal for Numerical and Analytical Methods in Geomechanics. (2013) Published online in Wiley Online Library (wileyonlinelibrary.com). DOI: 10.1002/nag.2161

[14] K. J. Bathe and M. M. I. Baig, On a Composite Implicit Time Integration Procedure for Nonlinear Dynamics, Computers & Structures, 83(2005) 2513–2534.

[15] S. Y. Chang, Studies of Newmark method for solving nonlinear systems: (i) basic analysis , Journal of the Chinese Institute of Engineers, 27(5)(2004) 651–662.

[16] B. R. Simon, O. C. Zlenklewlcz, D. K. Paul, An analytical solution for the transient response of saturated porous elastic solids, International Journal for Numerical and Analytical Methods in Geomechanics, 8 (1984) 381–398.

[17] R. de Boer, W. Ehlers and Z. Liu, One–dimensional transient wave propagation in fluid–saturated incompressible porous media, Archive of Applied Mechanics, 63 (1993) 59–72.

CHAPTER VI

CONCLUSIONS AND RECOMMENDATIONS

6.1 Conclusions

The main objective of this research is to develop an appropriate procedure for evaluating the seismic safety of earth dam. Also, this study aimed to find out the cause of the Fujinuma dam failure following the 2011 Tohoku earthquake by conducting the site investigation, laboratory experiment and numerical simulation. Furthermore, to determine the proper rehabilitation methods for particular dam, various mitigation techniques were introduced. Lastly, as it is recognized that in the study of the failure of soil structure, the coupled solid–fluid finite element code at large deformation found to be most suitable for analyzing this type of problems. Hence, the implementation of such code was provided in this study.

6.1.1 Failure of the Fujinuma dam

Site investigation and possible failure mechanism

As per the visual investigation, the remaining of the failed dam, reservoir area, reservoir's rim and also their vicinities, were examined however there is no obvious evidence such as sand boils could be found to confirm the occurrence of liquefaction. Furthermore, in the middle and bottom portions, the material itself does not seem prone to liquefaction.

According to laboratory experiments, it can be summarized that both the middle and bottom layer consist of a high percentage of fine particle sizes whereas the upper part is shown to consist mainly of sandy materials. The distribution of small particles showed that the clay content (particles smaller than 2 μm) of the middle and bottom portions is about 30% and 10%, respectively which are not susceptible to liquefaction as they contain greater or equal to 10% finer than 2 μm. Accordingly, both the middle and bottom are not susceptible to liquefaction. The triaxial test results showed that the parameters of cohesion and friction angle of the bottom and middle portions of the dam are classed as cohesive soil, but that the upper portion is classed as loose material. Furthermore, the modulus of elasticity reveals that the deeper the soil layer is, the higher its modulus becomes. The top portion of the dam is shown to have a relatively smaller modulus of elasticity than normally expected for fill materials.

Regards to the visual investigation and laboratory experiments, the failure mechanism might be described as follows.

- For the first scenario, owing to a relatively small elastic modulus of material used to construct the upper portion of the dam and the long duration of strong shaking, the fill material lost its strength. Consequently, sliding occurred in the top layer on the upstream slope or on both sides. Thereafter, the crest was displaced in a sliding

pattern. The settlement is deemed to have continued in the same pattern until it reached the reservoir level, in which the overtopping failure took place.

- For another possible scenario, owing to the weak upper portion and the long duration of strong shaking, cumulative permanent displacement could have expanded both sides and caused settlement in the middle, following which sliding occurred owing to instability. Of course, at some certain level, a coupled–failure phenomenon occurred, such as an overtopping–sliding failure.

Microtremor observation

The microtremor observation in this study was conducted in order to determine site predominant period and also the natural frequency of the dam. The results show that the predominant period of the dam location is within the range of 0.2–0.5 for short period and 2–3 for long period range. For the natural frequency of the remaining of the main dam is range about 2–5 Hz in the upstream downstream direction. Also, the numerical simulation of the remaining dam has been conducted in order to verify the dam's representative model and the properties obtained from the laboratory experiments. The results show the natural frequency obtained from finite element is about 2.35 Hz in the upstream–downstream direction therefore it yield good agreement with the microtremor observation. So, the numerical model and material properties are proper for representing the original dam and also for conducting the dynamic analysis of the dam.

Numerical simulation

The dynamic analysis of the dam obtained using the observed motion showed that the dam was subjected to the high amplitude and long duration earthquake. Also, the spectrum of the earthquake motion is characterized by a wide band that possibly induced resonance in the dam. Thus, the dam experienced significant amplifications throughout the dam body and this led to the great driving inertia force. In addition, with a long duration of shaking, the build-up pore pressure was then developed within the dam's body especially in the lower portion of the downstream side. Although, the excess pore pressure was not high enough to match the effective stress and trigger the liquefaction in those particular locations, soils might experience the reduction of the shear strength at the locations where the effective stress is small. Accordingly, large shear strain can be observed initially on the top portion of the dam and later the large shear strains can be found on the downstream side. Regards to the sliding patterns that occurred in the top portion and on the downstream slope, the dam was settled and the plastic deformation was then accumulated and become large until the dam's crest reached the reservoir level. Therefore, the dam failed owing to the loss of freeboard that might later cause the breaching of the dam. Furthermore, in all cases, large shear strains were observed initially in the upper portion of the upstream slope, following which large shear strains commenced on the downstream side. These, together with tension cracks, might evidently indicate the cause of the sliding failure of the dam slope. In addition, these sliding patterns exhibit good agreement with the facts gathered from field observations.

Through this study, it can be seen that the quality of compacting material in the upper portion might be one possible reason for the dam failure, which brought about such a

disaster to those who lived downstream. Thus, this study expressed that it is very important not only to design a dam that is capable of withstanding future quakes, but that the investigation and maintenance of existing dams are crucial for continued seismic safety.

6.1.2 Possible rehabilitation techniques

There are five retrofitting techniques have been introduced in this study. Those retrofitting methods are; 1) Retrofit 1, added downstream berm by half of the dam's height; 2) Retrofit 2, added downstream berm by the same of the dam's height; 3) Retrofit 3, enlarged and increased dam height; 4) Retrofit 4, lowered reservoir level; and 5) Retrofit 5, applied geogrid reinforcement layers. All retrofit models were analyzed using the simulated motion.

The results clearly indicated that the Retrofit 3, Retrofit 2 and Retrofit 5 are seem to be effective measures for reducing the risk of failure of this studied dam. Above all, the Retrofit 3 found to be most effective way for retrofitting the studied dam especially in case of existing dam due to its simplicity and also the crest settlement found to be smallest among other techniques. By raising the dam height and adding downstream berm, these together made this retrofit dam could safely resist the simulated motion. The Retrofit 2 also experienced a small crest settlement by just only expanded the crest width and added downstream berm by the same height of the original dam. Even though, the Retrofit 5 or geogrid reinforced model found also to be a good measure as it could reduce the crest settlement as well as the shear strain, in case of retrofitting the existing dam, the Retrofit 2 and 3 are more appropriate as it is quite simply to construct while the geogrid reinforcement seems to be suitable for new constructing dam.

In real situation, when the dam experienced the long duration earthquake like the observed motion used in the studied of the failure of the actual dam, only each mitigation measure might not be enough to preserve the dam from its failure. The proposed model was built using the combination of those techniques. The analysis showed that the proposed model was capable to withstand the gigantic power of the observed motion as the crest settlement was not high enough to cause the overtopping failure (Freeboard length = 5.3 m). However, it might experience the large shear strain that might subsequently cause the slope instability and cracks. Even though, results showed that the dam was not failed, the large settlement did take place which might cause damages to the proposed dam.

Through this study, it can be seen that there are still numerous of existing fill dams were needed to be evaluate their seismic safety to ensure the safety of people and their properties. Therefore, the seismic safety evaluation of existing dams is crucial and indeed urgent. Otherwise, when future quake strikes it might bring about a disaster to those who live downstream. Thus, this study demonstrates that it is very important not only to design a dam that is capable of withstanding future quakes, but the investigation, maintenance and mitigation of existing dams are vital for seismic safety of dam

6.1.3 Finite element code for coupled solid–fluid at finite strain

Eventually, the finite element code for coupled solid–fluid at finite strain for static and dynamic problems has been proposed. The governing equation, finite element formulation and its matrix form have been presented in this study. The code is currently developed for only for elastic regime as its preliminary step. In this study, the proposed code has been verified with the static and dynamic problem. In static verification problem, when applied 40 kPa load (infinitesimal–strain), the result obtained from the finite–strain finite element code yield good agreement with both the small–strain finite element code and the analytical solution. Then, by applied larger loads of 2 MPa, 4 MPa and 8 MPa, the results obtained from the small–strain finite element code approached the analytical while the finite–strain finite element code, gave a smaller response which matched well with the finite–strain's assumption. In dynamic problem, the surcharge load was applied at the top of the soil column model with a harmonic load. The results of the vertical displacement, vertical effective stress and excess pore pressure obtained from the finite–strain finite element code, small–strain finite element code and the analytical solution are in good agreement. Therefore, the proposed code can be developed further to include the more advanced constitutive law and then applied to the geotechnical problems.

Finally, the proposed code has been used to estimate the response of the Fujinuma dam when subjected to the recorded ground motion. In this study, the generated harmonic wave has been applied to the Fujinuma dam model to estimate its response and compare with the finite element code for the infinitesimal–strain. By comparing the small–strain and the finite–strain finite element code, it can be summarized that the maximum crest settlement, horizontal displacement, acceleration and excess pore pressure obtained from the finite–strain finite element code are in good agreement with the small–strain finite element code.

6.2 Recommendations

It is should be noted that by taking samples from the remaining of a collapsed dam represents a difficult task and raises many questions on the reliability of the representativeness of the material properties of the retrieved samples. Therefore, the analyzed results obtained using these data and the further used of this study, should be recognized and aware of this limitation.

Several other failure mechanisms could describe the failure of the Fujinuma dam, such as the effect of the interaction between the concrete face and the dam, or the interaction between the reservoir and the dam. However, these effects were not taken into account in this study.

Although the numerical simulation results obtained in this study could describe the failure mechanism of the dam, this simulation is based on the small–strain assumption. To gain insight into the failure mechanism of the soil structure, which is most likely to be within a large deformation regime, it is recommended to consider the effect of geometrical

nonlinearity. Therefore, to address this problem, the development of the finite element code for solving the problem at finite–strain is done in this study. However, the current code still limit to the only elastic material in order to apply to research works that related to this field, the more advanced constitutive law need to be introduced in the current code. Thus, the failure mechanism of the dam could be analyzed properly and results acquired that are more reliable. In addition, to describe other possible failure mechanisms, the material nonlinearity or other advanced constitutive laws and the proper fluid–structure interaction should be taken into account in future works.

For the proposed code, the code is not completely done several parts need to be added and corrected such as the damping term is not included in current study, the incorrect parts or mistakes must be found out and addressed in order to provide the reliable code and applied to further study or research works that related to this field. In addition, for the future works, to describe other possible failure mechanisms, the material nonlinearity or other advanced constitutive laws and the proper fluid–structure interaction should be taken into account as well.

Most mitigation techniques proposed here in this study were mainly focused on the structural strengthening. Yet, the best solution needs to take into account of many factors like; workability, economy and the important of the dam, effect to downstream site, for selecting the most suitable method for each case. Therefore, where compromised between the retrofitting method, cost and the accepted damage level could be met, other measures such as early planning, establishing inundate map and making evacuation plan or even “no action” might considered to be possible mitigation for this dam as well.